

# **Initiation of Particle Movement in Turbulent Open Channel Flow**

**Manousos S. Valyrakis**

Dissertation submitted to the faculty of the Virginia Polytechnic Institute and State University in  
partial fulfillment of the requirements for the degree of

Doctor of Philosophy

In

Civil and Environmental Engineering

Panayotis Diplas, Chair

Clinton L. Dancey, Co-Chair

John C. Little

Saad A. Ragab

Joseph A. Schetz

February 4, 2011

Blacksburg, Virginia

Keywords: impulse of flow events, extreme value theory modeling, prediction with adaptive  
neuro-fuzzy inference systems, wavelet transform, turbulent flow energy

Copyright © 2011, Manousos Valyrakis

# **Initiation of Particle Movement in Turbulent Open Channel Flow**

Manousos S. Valyrakis

## **ABSTRACT**

The objective of this thesis is to investigate the flow conditions that lead to coarse grain entrainment at near incipient motion conditions. Herein, a new conceptual approach is proposed, which in addition to the magnitude of hydrodynamic force or flow power, takes into account the duration of the flow event. Two criteria for inception of grain entrainment, namely the critical impulse and critical energy concepts, are proposed and compared. These frameworks adopt a force or energy perspective, considering the momentum or energy transfer from each flow event to the particle respectively, to describe the phenomenon.

A series of conducted mobile particle experiments, are analyzed to examine the validity of the proposed approaches. First a set of bench-top experiments incorporates an electromagnet which applies pulses of known magnitude and duration to a steel spherical particle in a controlled fashion, so as to identify the critical level for entrainment. The utility of the above criteria is also demonstrated for the case of entrainment by the action of turbulent flow, via analysis of a series of flume experiments, where both the history of hydrodynamic forces exerted on the particle as well as its response are recorded simultaneously.

Statistical modeling of the distribution of impulses, as well as conditional excess impulses, is performed using distributions from Extreme Value Theory to effectively model the episodic nature of the occurrence of these events. For the examined uniform and low mobility flow conditions, a power law relationship is proposed for describing the magnitude and frequency of occurrence of the impulse events. The Weibull and exponential distributions provide a good fit for the time between particle entrainments. In addition to these statistical tools, a number of Adaptive Neuro-Fuzzy Inference Systems employing different input representations are used to learn the nonlinear dynamics of the system and perform statistical prediction. The performance of these models is assessed in terms of their broad validity, efficiency and forecast accuracy.

Even though the impulse and energy criteria are deeply interrelated, the latter is shown to be advantageous with regard to its performance, applicability and extension ability. The effect of single or multiple highly energetic events carried by certain coherent flow structures (mainly strong sweep events) with regard to the particle response is also investigated.

## **Dedication**

I would like to dedicate the product of this endeavor to my parents (Stavros and Kalliopi) and brother (Alexandros), for their continuous and loving support.

## **Acknowledgements**

First, I would like to thank my advisors, Dr. Panayiotis Diplas and Dr. Clinton L. Dancey for their guidance, patience and support, throughout this project. Among the many skills they helped me cultivate, I am particularly grateful for promoting my independent critical thinking with emphasis on novel and innovative approaches. I would also like to express my sincere gratitude towards the members of my committee, Dr. John C. Little, Dr. Saad A. Ragab and Dr. Joseph A. Schetz, for their encouragement and invaluable experience.

I would like to acknowledge the technical expertise and assistance of Dr. Tanju Akar and Ahmet O. Celik, in planning and conducting many of the flume experiments, as well as Krista Greer for providing data from the electromagnet experiments.

Throughout my studies at Virginia Tech, I have had the fortune to instruct or assist a number of undergraduate and graduate courses, for which I am grateful to Dr. Samuel W. Easterling and Dr. William R. Knocke. I would also like to thank Dr. William E. Cox, Dr. Daniel L. Gallagher and Dr. G.V. Loganathan for being inspiring instructors and Dr. Randel L. Dymond, Dr. Erich T. Hester and Dr. Mark A. Widdowson for their discussions on improving the content of instructed courses.

Out of the many students I have interacted with and also learned from, I would like to thank Mr. Roger Arnold for his enthusiasm in conducting undergraduate research, under my mentoring. I would also like to thank Dr. Linbing Wang and Laura M. Kosoglu with Dr. George M. Filz, for providing access to own software and sharing ideas with regard to its application.

Finally, I would like to thank a number of good friends and fellow professionals, who helped rendering this experience deeper and rewarding: Alexandros Arsalis, Dimitrios Dermisis, Anastasios Peppas, Dr. Sotirios Vardakos, Vasileios Vlachakis, Dr. Haris Volos, and Dr. Oral Yagci.

## Table of Contents

List of Figures.....	x
List of Tables.....	xvii
<b>Chapter 1. Introduction.....</b>	<b>1</b>
1. Overview.. ..	1
2. Organization.....	2
<b>Chapter 2. The role of instantaneous force magnitude and duration on particle entrainment.....</b>	<b>3</b>
Abstract.....	3
1. Introduction.....	4
2. Interpretation of incipient motion condition from a new perspective.....	6
3. Impulse criterion formulation.....	8
3.1. Incipient saltation.....	9
3.1.1. Equation of motion.....	10
3.1.2. Results.....	11
3.2. Incipient rolling.....	14
3.2.1. Equation of motion.....	15
3.2.2. Results.....	17
4. Electromagnet experiments.....	23
4.1. Description of setup and experimental process.....	23
4.2. Results.....	27
5. Discussion.....	28
5.1. Comparison of saltation and rolling thresholds: force-duration representation.....	29
5.2. Comparison of saltation and rolling thresholds: normalized impulse representation.....	33
5.3. Generalization of various degrees of movement.....	35
5.4. Generalization to other grain arrangements.....	38
6. Conclusions.....	38

Appendix.....	39
Notation.....	40
Acknowledgement.....	42
References.....	42

### **Chapter 3. Entrainment of coarse grains in turbulent flows: an Extreme Value Theory**

<b>approach .....</b>	<b>48</b>
Abstract.....	48
1. Introduction.....	49
1.1. Impulse theory.....	51
1.2. Detection of impulse events and determination of $I_{cr}$ .....	53
2. Stochastic modeling of impulses.....	56
2.1. Extreme Value modeling .....	58
2.1.1. Generalized Extreme Value distribution.....	58
2.1.2. Generalized Pareto distribution.....	59
3. Description of setup and experimental process.....	60
4. Analysis and results.....	62
4.1. Frequency magnitude relationship.....	62
4.2. Impulse distribution.....	65
4.3. Distribution of conditional excess impulses.....	67
4.3.1. Application of POT.....	67
4.3.2. Estimation of the GDP parameters and model performance.....	68
4.4. Reliability of grain dislodgement.....	73
4.4.1. Empirical estimation.....	73
4.4.2. Parametric modeling.....	75
5. Discussion.....	77
5.1. Probability of entrainment for an individual particle.....	77
5.2. Extension of the utility of the power law relation to variable grain and flow characteristics.....	80
5.3. Implications for bed load transport.....	82
6. Conclusions.....	84

Notation.....	85
Acknowledgement.....	86
References.....	87

**Chapter 4. Prediction of coarse particle movement with adaptive neuro-fuzzy inference**

<b>systems.....</b>	<b>92</b>
Abstract.....	92
1. Introduction.....	93
2. Framework for the prediction of the onset of particle entrainment .....	94
2.1. Time domain forecasting.....	95
2.2. Frequency domain representation.....	97
2.2.1. Continuous wavelet transform.....	98
2.2.2. Wavelet multiresolution analysis.....	99
3. ANFIS Methodology .....	102
3.1. ANFIS overview.....	102
3.2. Algorithm architecture .....	102
4. Description of setup and experimental method.....	106
5. ANFIS simulations.....	108
5.1. Data preparation .....	108
5.2. Input selection .....	109
6. Discussion.....	110
6.1. ANFIS evaluation.....	110
6.2. ANFIS simulation results.....	112
6.3. Knowledge representation and general applicability.....	114
7. Conclusions.....	115
Notation.....	116
Acknowledgement.....	117
References.....	117

**Chapter 5. Entrainment of coarse particles in turbulent flows: an energy approach.....121**

Abstract.....	121
---------------	-----

1. Introduction.....	122
2. Role of energetic events to grain mobilization .....	124
3. Impulse criterion formulation.....	126
3.1. Incipient saltation.....	128
3.2. Incipient rolling.....	132
4. Incipient entrainment experiments .....	134
4.1. Description of setup and experimental process.....	134
5. Results and discussion.....	136
5.1. Trajectory analysis of rolling particle.....	136
5.2. Comparison of experimental data to theoretical predictions.....	141
5.3. Characteristic features of energetic events resulting in particle entrainment .....	143
5.4. Comparison of saltation and rolling thresholds .....	145
5.5. Comparison of energy criterion to traditional energetic approaches.....	146
6. Conclusions.....	148
Notation.....	149
Acknowledgement.....	150
References.....	150

**Chapter 6. Comparison of event based impulse and energy criteria for the entrainment of coarse particles in turbulent flow.....156**

Abstract.....	156
1. Introduction.....	157
2. Derivation of impulse and energy criteria from first principles.....	158
2.1. Newtonian formulation.....	158
2.2. Lagrangian formulation.....	159
3. Comparison between the impulse and energy criteria.....	162
3.1. Similarities.....	162
3.2. Advantages of energy criterion.....	162
3.3. Application examples.....	163
4. Classification of high energy events with regard to entrainment duration and the coherent flow structures .....	166

4.1. Rapid particle entrainments.....	168
4.2. Slow particle entrainments.....	168
4.3. Incomplete particle entrainments.....	169
5. Discussion: Generalization of the energy criterion.....	170
6. Conclusions.....	171
Acknowledgement.....	173
References.....	174
<b>Chapter 7. Conclusions.....</b>	<b>178</b>
Summary of major findings.....	178

**List of Figures**

**Chapter 2. The role of instantaneous force magnitude and duration on particle entrainment.....3**

**Figure 1.** a) Local particle configuration, showing the uppermost layer of (8mm) glass beads, the LDV measurement volume, the He-Ne beam and the initial and displaced positions of the fully exposed sphere. b) Time series of streamwise LDV measurements ( $u$ ), upstream an exposed mobile grain and instances of observed dislodgements (dashed vertical lines). c) Temporal history of hydrodynamic drag force acting on the exposed grain, as a function of the  $u^2$ . Impulses ( $I_i$  –shaded areas) are events with magnitude greater than the critical force ( $F_{crit}$  –dashed horizontal line) and duration ( $T_i$ ). .....8

**Figure 2.** The two limiting cases of local bed particle geometry, used to describe entrainment by: a) saltation; mobile particle (dashed circle) is initially surrounded by neighboring particles, and b) rolling; mobile particle (dashed circle) is fully exposed to the flow. For both cases the position of the downstream entrained particle, due to mean flow forcing, is depicted with a continuous thick circle, while the path followed is shown with a dot-dashed curve. The critical pulses responsible for the onset of entrainment are also illustrated (shown in the inset).....9

**Figure 3.** Normalized lift force magnitude,  $\hat{F}_L$ , versus normalized impulse duration,  $\hat{T}_{salt}$ , required for particle’s incipient saltation ( $\hat{z}=1$ ).....14

**Figure 4.** Definition sketch for entrainment of particle by rolling, due to drag ( $F_D$ ) and lift ( $F_L$ ) forces. The radial and tangential components of the resultant effective force system are also depicted ( $\Sigma F_\xi$  and  $\Sigma F_\theta$ ). Top view of particle arrangement illustrating the cut plane (dot-dashed line) is provided in the inset.....17

**Figure 5.** Threshold surface predicting the critical pulse characteristics (normalized hydrodynamic drag,  $\Sigma \hat{F}_\theta$ , and lift,  $\Sigma \hat{F}_\xi$ , forces and normalized duration,  $\hat{T}_{roll}$ ) for onset of entrainment.....20

**Figure 6.** Threshold curve of critical drag and duration combinations, for the incipient entrainment of a quartz sphere in water ( $R_m=4$  mm,  $R_b=4$  mm,  $\alpha=0$ ,  $F_L=0$ ).....21

**Figure 7.** Relative error (expressed as the ratio of excess impulse over the imparted impulse) for a range of drag forces.....22

**Figure 8.** Representation of the programmable voltages for the generation of electromagnetic pulses a) by varying the voltage levels for fixed duration and b) by changing the duration for fixed magnitude.....25

**Figure 9.** Plot of threshold curves and  $T_e, V^2$  combinations, for run 4-4. Two critical curves are shown: the first obtained from the best fit of the data points for which entrainment was observed (continuous line) and the second predicted from equation 16 (dashed line, scaled appropriately to account for  $c_i$ ).....26

**Figure 10.** Data points of normalized magnetic force (parameterized by  $\hat{v}^2$ ) and duration,  $\hat{T}_e$ , for which movement was observed, for all the runs. The best fit (dashed) curve and the threshold curve predicted from equation 18 (continuous line) are also shown.....28

**Figure 11.** Classification of the representative modes of incipient motion, depending on the relative magnitude of drag to lift forces normalized by the mobile particle's weight (case of a completely exposed particle with  $R_m= 4$  mm,  $R_b= 4$  mm,  $\alpha=0$ ). The dividing lines are obtained from the appropriate normalization of equations (11a) and (11b). .....30

**Figure 12.** Threshold surfaces indicating the critical drag, lift and duration combinations, for the modes of entrainment by: a) saltation and b) rolling, for the case of an exposed particle ( $R_m = 4$  mm,  $R_m = 4$  mm,  $\alpha=0$ ). The intersection of the saltation and rolling critical surfaces with the vertical cut-plane,  $F_L = 1.5F_R = 0.0045$  N, is emphasized with a thick line, to illustrate the separation between the two modes.....31

**Figure 13.** Threshold curves for movement by saltation or rolling, for the case of an exposed particle ( $R_m= 4$  mm,  $R_b= 4$  mm,  $\alpha=0$ ) and different values of lift force: a)  $F_L=1.5F_R$ , b)  $F_L=1.7F_R$ , c)  $F_L=-1.5F_R$ .....32

**Figure 14.** Critical normalized impulse for full dislodgement versus normalized duration: a) as predicted by saltation theory (dashed line), b) as predicted by rolling theory (continuous line) and c) as a linear best fit of the observed data from electromagnet experiments (dashed-dotted line).....35

**Figure 15.** Generalized threshold curves for saltation, providing different levels of normalized linear grain displacement,  $\hat{z}$ , as a function of the offered impulse characteristics (normalized magnitude,  $\hat{F}_L$ , and duration,  $\hat{T}_{salt}$ ).....37

**Figure 16.** Generalized threshold curves for rolling, providing different levels of normalized angular grain displacement,  $\lambda$ , as a function of the offered impulse characteristics (normalized magnitude, parameterized by  $V^2$ , and duration,  $\hat{T}_e$ ).....37

**Chapter 3. Entrainment of coarse grains in turbulent flows: an Extreme Value Theory approach.....48**

**Figure 1.** Sketch of the temporal history of hydrodynamic force ( $F(t)$ ) acting on a grain (the mean,  $F_m$ , and critical,  $F_{cr}$ , force levels are shown with the dotted and dashed horizontal lines). Impulse events (shaded areas) with magnitude above a critical level ( $I_{cr}$ ) result in complete particle entrainment (vertical dotted line).....53

**Figure 2.** Definition sketch for the local arrangement and forces exerted on a fully exposed mobile particle Inset: Top view of particle configuration illustrating the cut plane (dot-dashed line).....53

**Figure 3.** Representation of hydrodynamic forcing history on a coarse particle: a) as a continuous time series of the drag force,  $F_D \sim u^2$  and b) as a discrete point process of corresponding impulse events and impulse exceedances ( $\xi_i$ , denoted by the thick vertical lines above  $I_{thr}$ ) randomly occurring in time. The threshold impulse level  $I_{thr} (< I_{cr})$  and impulse events associated with particle displacement (stars) are also shown. ....57

**Figure 4.** The probability of particle entrainment ( $P_E$ ) is approximated by the probability of occurrence of extreme impulse events above critical, defined from the probability distribution of impulses, ( $P(I_i > I_{cr})$ ), or from the conditional probability of impulse exceedances ( $P(\xi_i > I_{cr} - I_{thr} | I_{cr} > I_{thr})$ ), using equation (19)).....57

**Figure 5.** Sketch (side view) of the experimental setup (top view shown in the inset), illustrating the possible locations of the mobile particle and its local configuration with a retaining pin.....61

**Figure 6.** Variation of magnitude of impulses normalized with the critical impulse level ( $I_i/I_{cr}$ ) with the mean frequency of their occurrence ( $f_j$ , for run E3) and fitted power-law relationship (the lognormal fit is also shown for comparison).....64

**Figure 7.** Illustration of the dependence of the frequency-magnitude power law relationship (equation 9) of the normalized impulse values on the different flow conditions (E1-E6).....65

<b>Figure 8.</b> Cumulative distribution function of impulse data ( $F(I_i)$ , for run $E3$ ) and corresponding fitted models (equation 10).....	66
<b>Figure 9.</b> Graphical method for selection of optimal $I_{thr}$ , for run $E1$ : a) plot of mean excess over threshold and b) plot of number of exceedances for a range of threshold impulses (dashed lines correspond to the limits of 85% and 97.5% quantiles, defining the range of possible thresholds). The dotted vertical line corresponds to the chosen threshold $I_{thr}=0.005$ ( $m^2/s^2$ ), corresponding to the 90% quantile.....	69
<b>Figure 10.</b> Distribution of the tail of impulses for run $E1$ and threshold corresponding to the 90% quantile ( $I_{thr}=0.005$ ( $m^2/s^2$ )): a) probability of conditional excess impulses and best fit of the GPD model and b) empirical cumulative distribution function (CDF) of conditional excess impulses and the corresponding model fit (equation 7).....	71
<b>Figure 11.</b> Probability density functions predicted by the GPD model, for all flow conditions.....	72
<b>Figure 12.</b> Plot of the empirical survival function, $S(t)$ , estimated employing the nonparametric Kaplan-Meier estimator (equation 14) and best fit curves predicted using the Weibul model (equation 15).....	75
<b>Figure 13.</b> Comparison of the exceedance probability of impulses, $P=P(I_i>I_{cr})$ , predicted using different model distributions with the probability of entrainment of a single particle $P_E$ , using various methods of estimation: a) $P_E=\tau_e/(\tau_e+\tau_w)$ , b) $P_E=f_i/f_E$ , and c) $P_E=f(I_i)/f_C$ .....	80
<b>Figure 14.</b> Conceptual illustration of the utility of impulse concept in defining different levels of grain mobilization: a) no entrainment –the distributions ( $f$ ) of $I_i$ , $I_{cr}$ are apart, and b) threshold of motion characterized by a small but finite probability of grain mobilization or a certain degree of the distributions’ overlap (higher degree of overlap will result in higher transport rates).....	82
 <b>Chapter 4. Prediction of coarse particle movement with adaptive neuro-fuzzy inference systems.....</b>	<b>92</b>
<b>Figure 1.</b> Illustration of forces acting on a fully exposed particle (dashed circle), leading to its entrainment by rolling (following the trajectory $O'B'$ ).....	96

**Figure 2.** Illustration of the continuous wavelet transform of the streamwise velocity  $u$ : a) time history of  $u$  and of the displacement signal  $\Delta x$  (vertical dashed lines show instants of onset of entrainment), b) wavelet coefficient maps of the corresponding signal over a wide range of scales of interest.....99

**Figure 3.** Schematic diagram illustrating the two-level wavelet decomposition of a signal,  $S$ , into approximations ( $A_i$ ) and details ( $D_i$ ), where  $i$ , refers to the level of decomposition of  $S$  or  $A_{i-1}$ ..100

**Figure 4.** Demonstration of the wavelet multiresolution analysis (two-level decomposition) of a fraction of the streamwise velocity signal: a) original signal ( $u$ ) and displacement signal (vertical dashed lines show instants of onset of entrainment), b) level-2 approximation of  $u$ , c) level-1 detail of  $u$ , and d) level-2 detail of  $u$ .....101

**Figure 5.** ANFIS architecture for an  $n$ -input Sugeno model with 2 membership functions per input ( $A_{i,j}$ ,  $j=1,2$ ) and  $N_R$  number of rules (rectangular boxes represent adaptive nodes, circles represent fixed nodes).....105

**Figure 6.** Sketch (side view) of the experimental setup (top view shown in the inset), illustrating the range of possible locations of the mobile particle and the local base particle arrangement with a retaining pin to constrain further entrainment downstream. The targeting locations of the LDV and He-Ne laser are also depicted in relation to the mobile sphere.....106

**Figure 7.** Illustration of the history of predicted normalized particle displacements ( $\Delta x/\Delta x_{max}$ ), for the model with the best performance (U3In). The filled boxes in the timeline below the horizontal axis, correspond to the events when the particle is completely dislodged.....113

**Chapter 5. Entrainment of coarse particles in turbulent flows: an energy approach.....121**

**Figure 1.** Time history of instantaneous flow power ( $P_f \sim u_f^3$ ) exerted on a completely exposed particle. Energetic flow events ( $E_i$  –shaded areas) have instantaneous flow power in excess of the threshold level ( $u_{cr}^3$  –dashed line) lasting for duration ( $T_i$ ). The instant of full entrainment denoted by the dotted vertical line.....126

**Figure 2.** Entrainment of particle by: a) saltation; mobile particle (dashed circle) is initially surrounded by neighboring particles, and b) rolling; mobile particle (dashed circle) is completely exposed to the flow. For both cases the position of the downstream entrained particle, due to mean flow forcing, is depicted with a continuous thick circle, while the path followed is shown

with a dot-dashed curve. Complete entrainment is initiated by energetic events above critical,  $E_{f,i}$ , shown in the inset.....127

**Figure 3.** Representation of energy threshold for entrainment of a 12.6 mm particle in saltation mode by: a) mean specific energy and advection length scale, and b) mean flow power ( $P_f$ ) and duration ( $C_{salt}T_{salt}$ ) combinations.....131

**Figure 4.** Illustration of the energy threshold for entrainment of a 12.6 mm particle in rolling mode by: a) characteristic specific energy ( $\sim u_f^2$ ) and lengthscale combinations, and b) mean flow power ( $P_f$ ) and duration ( $C_{roll}T_{roll}$ ) combinations.....135

**Figure 5.** Representation of the available flow power and corresponding resistance level (dotted curve) for representative cases of particle entrainment: a) relatively short flow event of high energy content, b) long duration of flow event and low energy content, and c) representative case of relatively high  $C_{eff}$ . The vertical dashed line shows the instant of initiation of entrainment.....138

**Figure 6.** Representation of the net power transferred towards the grain's dislodgement (shaded area corresponds to the total offered energy) for representative cases of particle entrainment: a) relatively short flow event of high energy content, b) long duration of flow event and low energy content, and c) representative case of relatively high  $C_{eff}$ . The vertical dashed line shows the instant of initiation of entrainment.....139

**Figure 7.** Representation of the history of the mechanical work performed on the particle until the critical level is reached for representative cases of particle entrainment: a) relatively short duration of flow event and high specific energy, b) long duration of flow event and low specific energy, and c) representative case of relatively high  $C_{eff}$ . The vertical dashed line shows the instant of initiation of entrainment.....140

**Figure 8.** Plot of energy content of flow events ( $C_{roll}u_f^3T_{roll}$ ) against the total duration for entrainment ( $t_{tot}$ ), for experimental run E1, showing also the threshold energy level (dashed line) as predicted from equation (9).....142

**Figure 9.** Relation between the mean velocity of the flow event and the resulting particle velocity (averaged over the duration of dislodgement).....142

**Figure 10.** Distribution of the coefficient of energy transfer,  $C_{eff}$  (values from all experiments).....143

**Figure 11.** Probability distribution of the characteristic lengthscale of the flow events (for all experiments).....144

**Figure 12.** Probability distribution of the energy density of the flow events (for all experiments).....145

**Figure 13.** Mean streamwise velocity profile for the various experimental runs, *E1* to *E7* (only the near bed portion is shown for clarity).....147

**Figure 14.** Plot of rate of occurrence of energetic events showing an almost linear dependence with the frequency of grain entrainments.....148

**Chapter 6. Comparison of event based impulse and energy criteria for the entrainment of coarse particles in turbulent flow.....156**

**Figure 1.** Representation of energy threshold for entrainment (equation 6) of a 12.6 mm particle by a) saltation, and b) rolling, as a function of the average specific energy ( $\sim u_f^2$ ) and lengthscale of the flow event.....165

**Figure 2.** Classification of the energetic flow events (shown with grey, filled circles) based on the duration required for the particle to complete its entrainment ( $t_{tot}$ ). The events depicted with open symbols (del, circle, triangle, square and diamond) correspond to the typical events analyzed in the figure pairs 3a-b, c-d, e-f, g-h, and i-k respectively.....166

**Figure 3. a, c, e, g, i):** Fluctuating velocity components ( $u_f^2$ ,  $v_f^2$  shown as thick continuous and dotted lines, respectively) and corresponding critical streamwise velocity level ( $u_{cr}-u_{f,m}$ , indicated as the horizontal dot-dashed line) for typical entrainment events. Segments of the velocity record with positive  $u_f^2$  and  $v_f^2$  are shaded with blue and red color, while the regions of down-crossings of  $u_f^2$  and  $v_f^2$  are shaded with orange and green color respectively. **b, d, f, h, k):** Characteristic particle trajectories corresponding to the typical cases shown in (a, c, e, g, i). The instant of initiation of particle entrainment is depicted with the dotted vertical line.....173

## List of Tables

<b>Chapter 2. The role of instantaneous force magnitude and duration on particle entrainment.....</b>	<b>3</b>
<b>Table 1.</b> Characteristics of different particle configurations and the best fit curves derived from the data points for which movement was observed.....	25
<b>Chapter 3. Entrainment of coarse grains in turbulent flows: an Extreme Value Theory approach.....</b>	<b>48</b>
<b>Table 1.</b> Summary of flow characteristics for mobile particle flume experiments. ....	62
<b>Table 2.</b> Summary of power-law and Frechet parameters characterizing the magnitude-frequency relation and distribution of impulses, respectively.....	64
<b>Table 3.</b> Summary of the GPD shape ( $\gamma_{GPD}$ ) and scale ( $\sigma_{GPD}$ ) parameters, estimated using maximum likelihood method (MLE -standard errors are shown in parenthesis) and method of moments (MOM), for all experimental runs.....	72
<b>Table 4.</b> Summary of empirical model estimators and Weibull and exponential model parameters and mean time to displacement ( $E_w, E_e$ ), characterizing the survival function for various flow conditions ( $E1-E4$ ).....	75
<b>Chapter 4. Prediction of coarse particle movement with adaptive neuro-fuzzy inference systems.....</b>	<b>92</b>
<b>Table 1.</b> Summary of time averaged local flow characteristics and mean particle entrainment rate for incipient entrainment experiments.....	108
<b>Table 2.</b> Characteristics of selected ANFIS models for each input representation.....	110
<b>Table 3.</b> Evaluation of the selected ANFIS models according to computational time and error indices.....	112
<b>Chapter 5. Entrainment of coarse particles in turbulent flows: an energy approach.....</b>	<b>121</b>
<b>Table 1.</b> Summary of flow characteristics for incipient entrainment experiments.....	134

# Chapter 1. Introduction

## 1. Overview

The dynamic interaction between turbulent fluid forces and solid particles for flows over an erodible boundary constitutes a central problem in earth surface dynamics and engineering. The purpose of this thesis is to investigate the exact conditions under which entrainment of individual coarse particles is initiated. As opposed to traditional criteria employing spatial and temporally averaged flow quantities or more recent approaches considering the effect of instantaneous local flow parameters, an event based approach is adopted here. The cornerstone of this concept is that the intermittent entrainment of sediment particles, at near threshold flow conditions, is the result of flow events of different magnitude and duration, occurring randomly in space and time. The proposed framework provides better understanding of the fundamental process and dynamics of grain entrainment, which is essential for a variety of applications ranging from fluvial hydraulics (e.g. design of stable channel bed and banks and the protection of hydraulic structures against scouring processes), to environmental engineering and stream ecology (e.g. estimation of flushing flow conditions downstream of a reservoir).

## 2. Organization

This thesis is divided into five major chapters (Chapters 2 to 6), each of which is formatted as a self-contained manuscript that has either been accepted, submitted or is under submission to peer reviewed journals. These chapters are nearly identical with the published reprints or submitted versions of the manuscripts, with certain editing variations so as to enhance their presentation and render the whole thesis format more uniform.

In particular, in Chapter 2, impulse is proposed to be a quantity relevant to the initiation of particle entrainment. Hydrodynamic forces of sufficiently high magnitude are shown to be capable of entraining a particle, only when they last long enough. The concept of critical impulse is formulated theoretically for both modes of entrainment, namely saltation and rolling. The general applicability and validity of this criterion is demonstrated via a series of controlled bench-top experiments incorporating a steel sphere displaced in air due to application of electromagnetic pulses of varying magnitude and duration.

Considering impulse as the criterion relevant to particle entrainment, Chapter 3 focuses on the statistical representation of the relatively rare and extreme flow impulses as well as the episodic particle entrainments associated with them, by means of Extreme Value Theory (EVT). The Frechet and the Generalized Pareto Distribution are employed to statistically model the distribution of impulses and the conditional impulses in excess of a high threshold. A power law relationship between the magnitude of impulses and the frequency of their occurrence is found. The time between occurrences of entrainment events is modeled using the Weibull and exponential distributions. A series of mobile grain flume experiments in uniform and low mobility flow conditions are provided to demonstrate the utility and successful application of the presented approach.

In Chapter 4, an attempt is made to model the nonlinear dynamics of particle entrainment to the salient characteristics of the flow events using an Adaptive Neuro-Fuzzy Inference System (ANFIS). A number of different architectures are presented, trained and tested using the time or frequency domain representation of the input (flow history). The efficiency, generalization ability and predictability of the developed models, is demonstrated, proving its utility and versatility over traditional statistical predictive approaches.

Chapter 5 introduces a new criterion for the entrainment of coarse particles by saltation and rolling at near threshold flow conditions, adopting an energy perspective. Similar to the impulse concept this is an event based framework, where emphasis is given on the energy, rather than momentum, supplied from randomly occurring flow events, towards particle entrainment. Threshold energy levels are expressed in terms of important features of the flow events such as the mean flow power and duration or energy density and characteristic length scale. It is shown that the energetic flow events perform mechanical work on a particle at a rate described by the energy efficiency coefficient.

Finally, a comparison of the impulse and energy criteria is presented in Chapter 6. Even though the two event based approaches are interrelated, the energy criterion appears to have certain strengths with respect to its application and extensibility. An example using data from mobile particle flume experiments is provided to demonstrate the extension of the concept from single to multiple flow events where the flow structures and particle dynamics are analyzed.

The major findings of this study are summarized in Chapter 7.

## Chapter 2. The role of instantaneous force magnitude and duration on particle entrainment\*

Manousos Valyrakis,<sup>1</sup> Panayiotis Diplas,<sup>1</sup> Clint L. Dancey,<sup>1</sup> Krista Greer,<sup>1</sup> and Ahmet O. Celik<sup>1</sup>

\*This chapter is a reprint of the published article: Valyrakis, M., P. Diplas, C. L. Dancey, K. Greer, and A. O. Celik (2010), Role of instantaneous force magnitude and duration on particle entrainment, *J. Geophys. Res.*, 115, F02006, doi:10.1029/2008JF001247, reproduced with permission of AGU.

<sup>1</sup>Baker Environmental Hydraulics Laboratory, Department of Civil and Environmental Engineering, Virginia Polytechnic Institute and State University, Blacksburg, Virginia, USA.

### Abstract

A new criterion for the onset of entrainment of coarse sediment grains is presented here. It is hypothesized that not only the magnitude, but also the duration of energetic near bed turbulent events is relevant in predicting grain removal from the bed surface. It is therefore proposed that the product of force and its duration, or impulse, is a more appropriate and universal criterion for identifying conditions for particle dislodgement. This conjecture is investigated utilizing two theoretical models, representative of two modes of entrainment: saltation and rolling. In these models, instantaneous, highly fluctuating turbulent forces are simulated as short-lived pulses of characteristic magnitude and duration, which transfer adequate fluid momentum to the particle, to trigger its entrainment. The analytical solution of the respective equations of motion is employed in deriving representations of threshold conditions, in terms of the impulse characteristics. It is shown that hydrodynamic forces of sufficiently high magnitude are capable of entraining a particle, only when they last long enough so that their impulse exceeds a critical value. To illustrate further the validity of the critical impulse concept, as well as extend and generalize its application to different entrainment levels of an individual grain, a novel experimental setup is utilized. This set up facilitates observations of angular displacement of a steel mobile particle in air due to electromagnetic pulses of different magnitude and duration. The experimentally obtained conditions for partial or complete entrainment support the concept of a critical impulse.

## 1. Introduction

The dynamic interplay between fluctuating turbulent fluid forces and particle dislodgement for flows over an erodible boundary constitutes a central problem in earth surface dynamics and engineering. Soil erosion in riverine, estuarine and aeolian environments provides a good example. One of the first attempts to highlight the importance of turbulence on particle movement, albeit in an elementary way, is attributed to *Varenius* [1664]. Varenius concluded from observations that the random movement of sediment is related to the fluctuating motion of the water in the stream. Since then, a large number of researchers have advocated this point of view based on detailed field, laboratory and other studies [*Leighly*, 1934; *Einstein and El-Samni*, 1949; *Sutherland*, 1967; *Paintal*, 1971b; *Grass*, 1970; *Grass*, 1983; *Apperley and Raudkivi*, 1989; *Nelson et al.*, 1995; *Papanicolaou et al.*, 2001; *Nelson et al.*, 2001; *Sumer et al.*, 2003; *Paiment-Paradis et al.*, 2003; *McEwan et al.*, 2004; *Schmeeckle et al.* 2007]. Evidently, the role of the instantaneous stress tensor is very important, especially at conditions near the threshold of movement. This point has been well demonstrated for both smooth [e.g. *Sutherland*, 1967; *Grass*, 1971; *Sumer et al.*, 2003] and rough boundaries [e.g. *Apperley and Raudkivi*, 1989; *Schmeeckle and Nelson*, 2003], as well as in the presence of bed forms [e.g. *Raudkivi*, 1966; *Nelson et al.* 1993; *Sumer et al.*, 2003; *Paiment-Paradis et al.*, 2003].

In spite of this widespread recognition, attempts to link the characteristics of turbulent flow to particle entrainment have not typically surpassed qualitative descriptions. Even in the very few and most sophisticated cases where researchers have resorted to the solution of the governing flow equations, they have predominantly employed the time-averaged Reynolds equations. This is a reflection of the difficulties in accounting for the intricate ways that turbulence influences, or even dominates, particle threshold conditions. Shields was among the first researchers to formulate a quantitative criterion for inception of grain motion. His empirically obtained diagram [*Shields*, 1936] remains the standard method for identifying threshold of motion conditions and considerable effort has been spent to explain deviations from it, and to devise alternative plots for a variety of flow/sediment cases [e.g. *Bettess*, 1984; *Buffington and Montgomery*, 1997; *Shividchenko and Pender*, 2000; *Paphitis*, 2001; *Paphitis et al.*, 2002]. As of this time, the development of a precise and universal criterion for determining the initiation of sediment movement remains elusive.

To make the problem more manageable, in this study we consider the phenomenon of initiation of motion for particles that are sufficiently large so that  $R_* > 100$ , which corresponds to the Reynolds independent region of Shields' diagram, where  $R_* = u^* D_{50} / \nu$  is the boundary Reynolds number,  $u^*$  the shear velocity,  $D_{50}$  the bed material median size, and  $\nu$  the kinematic viscosity of water. Even under these conditions the scatter of the threshold of motion results reported in the literature [e.g. *Buffington and Montgomery, 1997; Lavelle and Mofjeld, 1987*] exceeds an order of magnitude. The conventional Shields parameter,  $\tau^* = \tau / [g(\rho_s - \rho_f) D_{50}]$ , where  $\tau$  is the boundary shear stress,  $g$  the acceleration of gravity, and  $\rho_f$  and  $\rho_s$  the density of fluid and sediment, respectively, is applicable to averaged en masse entrainment by steady uniform flow, as it has been reported by several researchers [e.g. *Paintal, 1971a; Coleman and Nikora, 2008*]. It is therefore evident that  $\tau^*$ , which represents a temporal, and usually spatial, average of the rapidly fluctuating instantaneous stresses encountered near the boundary, is an incomplete measure of the turbulent flow processes responsible for particle dislodgement. The wide range of grain parameters, such as size and shape, pocket geometry, particle exposure, and bed geometries further complicate the overall picture.

Many researchers, in an effort to overcome the limitations of the approach proposed by Shields, have advocated the important role that peak values in the instantaneous velocity or pressure field in the vicinity of the boundary, and resulting hydrodynamic forces, play on particle dislodgement, particularly for flow conditions near threshold of movement [e.g. *Sutherland, 1967; Hofland et al., 2005; Schmeeckle et al., 2007; Vollmer and Kleinhans, 2007; Gimenez-Curto and Corniero, 2009*]. More details about the role of such peak forces have been provided by *Diplas et al. [2008]*, who demonstrated for the first time that the concept of impulse associated with an energetic turbulent event is the more suitable parameter for determining particle entrainment, by saltation (using theoretical arguments) and rolling (by analyzing experimental data obtained via an electromagnet). The present study seeks to extend and generalize the validity of the impulse concept proposed by *Diplas et al. (2008)* by accounting for a variable slope in the saltation formulation of the problem and by analytically considering the case of particle entrainment via rolling motion. The present results are elaborated further to describe different levels of movement - other than the critical for full entrainment - and corroborated through a series of appropriately designed laboratory experiments.

## 2. Interpretation of incipient motion condition from a new perspective

*Einstein and El Samni* [1949], *Sutherland* [1967] and *Cheng and Clyde* [1972] were among the first researchers who emphasized the role of fluctuating forces, exceeding the temporal mean hydrodynamic force, on inception of particle entrainment. By the traditional interpretation of incipient motion, a sediment grain can be displaced from a particle configuration, if sufficient hydrodynamic force, above a critical level, is applied to it. However, these “extreme” high magnitude turbulent events are usually limited in their duration, which may render them ineffective for completely dislodging a grain from its initial position in the bed matrix. In contrast, turbulent events of not as high magnitude (still exceeding a critical minimum value) but of sufficient duration may transfer enough momentum over this longer duration for the particle to not only initiate motion but be fully displaced from its local arrangement in the bed matrix. This notion implies that the duration of turbulent structures, as well as the magnitude of the force they exert, is of significance when the full displacement of the grain is considered.

In an effort to identify the relationship between local instantaneous forces and particle movement, a laboratory flume experiment was performed at near threshold conditions. A tilting flume 0.6m wide and 20.5m long, located in the Baker Environmental Hydraulics laboratory was used for this purpose. A two-component laser Doppler velocimeter (LDV) with average sampling rate of about 500 Hz, was used to determine the instantaneous streamwise velocity history one diameter upstream and along the centerline of a 12.7 mm diameter spherical Teflon® particle (Figure 1a). The particle is fully exposed, resting on top of four layers of 8mm glass beads. The particle is free to move downstream due to the near bed flow. However, further entrainment is retained by a carefully placed pin, which sends the particle back into its initial local bed configuration, so that a continuous record of displacement events can be obtained (Figure 1b). For a flow having a depth averaged velocity of 0.2 m/s, friction velocity of 0.025 m/s and depth of 7.2 cm, the entrainment rate of the exposed particle was on average close to two full entrainments per minute. A He-Ne laser and photomultiplier were used simultaneously with the LDV to identify and encode the displacement of the mobile sphere, in real-time (Figure 1a). The He-Ne laser beam targets the photomultiplier and is partially blocked by the initially resting particle (Figure 1a). At the displaced position the particle completely blocks the beam affecting the reading of the photomultiplier. In this manner, grain displacement is automatically and

accurately detected. Excerpts from the complete velocity (LDV) and dislodgement (He-Ne) record are shown in Figure 1b. In this figure the instants of full grain dislodgement is indicated with dashed vertical lines. The results from these tests consistently indicated that only a few of the high magnitude local velocity events resulted in full particle dislodgement (examples in Figure 1b are events *B*, *C*, *E* and *F*), even though their magnitude was well in excess of the minimum velocity required for a net unbalanced force on the particle, assuming the standard drag formula parameterization. For example, over the duration (approximately 30 min) of the experiment, only 65 out of 1465 above threshold events resulted in entrainment [Diplas *et al.*, 2008]. Closer observation of the record suggests that although all the velocity spikes have relatively short duration, of the order of several or tens of milliseconds (ms), the ones that did not cause dislodgement appear to be particularly short-lived (e.g. events *A* and *D* in Figure 1b). Apparently, these extreme magnitude, but short-lived, events may initiate grain movement but do not last sufficiently long to fully dislodge it. This vibration or pivoting of a particle has been observed in the laboratory from our own flume experiments and in the field as well [e.g. Garcia *et al.*, 2007].

Given the highly fluctuating nature of turbulent flow, and associated hydrodynamic forces, there is a need to refine the currently used definition for initiation of motion. In addition to a local, instantaneous force magnitude that exceeds a critical value ( $F_{crit}$  – the horizontal dashed line in Figure 1c), particle dislodgement requires that the force be applied for an adequate period of time, to transfer sufficient momentum to the particle to carry it out of its initial grain configuration. Thus as shown in Figure 1c, though both events (*D*, *E*) are strong enough to commence particle movement, only *E* lasts sufficiently long to accomplish dislodgement. A parameter that captures both force magnitude and duration simultaneously is impulse ( $I_i$ ), defined as the integral of the hydrodynamic net force over the duration of the force ( $T_i$ ):

$$I_i = \int_{t_i}^{t_i+T_i} F(t)dt \quad (1)$$

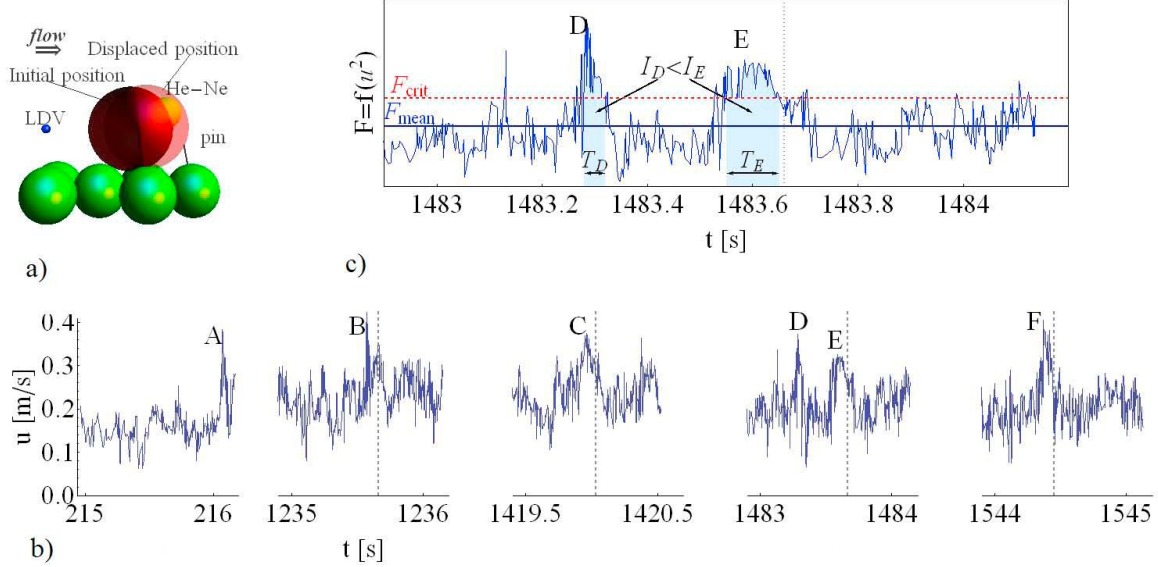


**Figure 1.** a) Local particle configuration, showing the uppermost layer of (8mm) glass beads, the LDV measurement volume, the He-Ne beam and the initial and displaced positions of the fully exposed sphere. b) Time series of steamwise LDV measurements ( $u$ ), upstream an exposed mobile grain and instances of observed dislodgements (dashed vertical lines). c) Temporal history of hydrodynamic drag force acting on the exposed grain, as a function of the  $u^2$ . Impulses ( $I_i$  –shaded areas) are events with magnitude greater than the critical force ( $F_{crit}$  –dashed horizontal line) and duration ( $T_i$ ).

### 3. Impulse criterion formulation

The threshold force characteristics leading to full displacement of a spherical grain by either saltation or rolling is the focus of this paper. Both of these modes have a probability of occurrence, depending on local grain arrangement and flow conditions. For the limiting case of an entirely hidden particle, the forces that may trigger its initially upward movement (or incipient saltation) are lift forces, while for the case of an exposed grain both drag and lift play a role in mobilizing the grain, usually by rolling, for conditions very close to threshold (Figures 2a and 2b, respectively). In the analytical models developed here, dislodgement via saltation is considered accomplished when the grain is lifted a characteristic height, which for saltation of coarse grains in water is of the order of one particle diameter [e.g. *Nino and Garcia, 1994*]. Full dislodgement by rolling is achieved when the grain reaches the topmost location in its local configuration. In both cases the grain reaches a position of higher exposure to the near bed flow which eventually results in its further entrainment downstream.

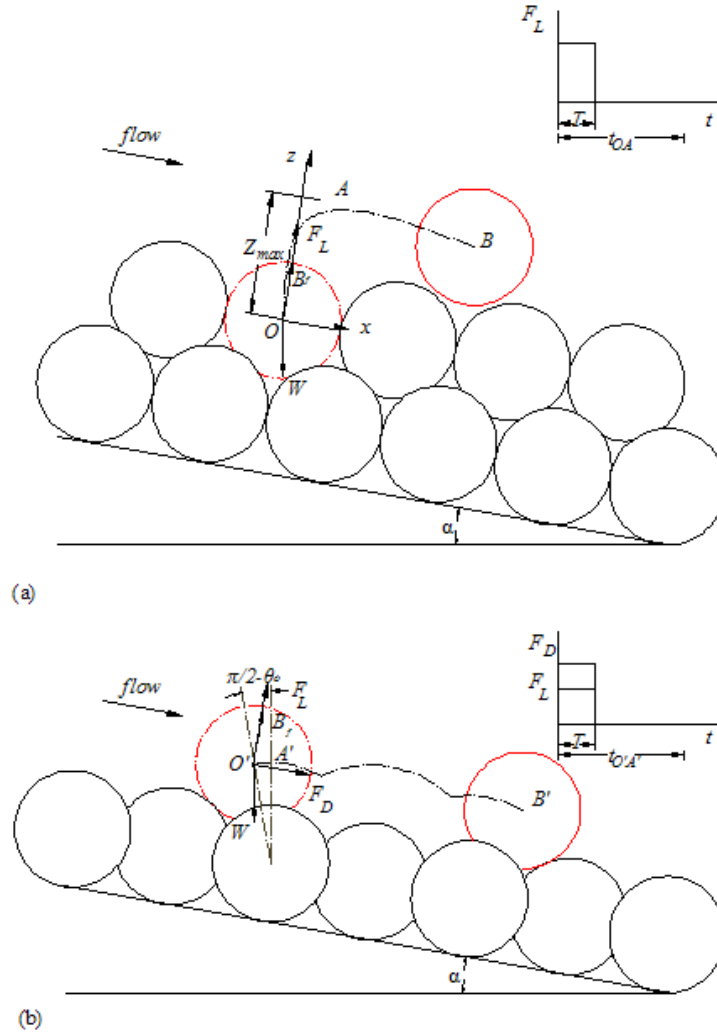


**Figure 2.** The two limiting cases of local bed particle geometry, used to describe entrainment by: a) saltation; mobile particle (dashed circle) is initially surrounded by neighboring particles, and b) rolling; mobile particle (dashed circle) is fully exposed to the flow. For both cases the position of the downstream entrained particle, due to mean flow forcing, is depicted with a continuous thick circle, while the path followed is shown with a dot-dashed curve. The critical pulses responsible for the onset of entrainment are also illustrated (shown in the inset).

### 3.1. Incipient Saltation

The interaction of lift forces with sediment particles has been pursued analytically both from a deterministic [e.g. *Jeffreys, 1929; Benedict and Christensen, 1972; Ling, 1995; Nino et al., 2003*] and probabilistic viewpoint [e.g. *Cheng and Chiew, 1998; Wu and Lin, 2002; Wu and Yang, 2004*] by means of statistical treatment of flow and grain parameters. Saltation of coarse bed material has also been investigated experimentally providing useful statistics such as lift

intensities [Chepil, 1958; Cheng and Clyde, 1972; Mollinger and Nieuwstadt, 1996] and even grain trajectories [Abbott and Francis, 1977; Nino and Garcia, 1994]. Einstein and El-Samni [1949] experimentally measured the lift forces generated due to pressure differences between the top and bottom of hemispheres. They were the first to emphasize the significance of rapidly fluctuating lift forces due to the instantaneous variation of the near rough bed pressure field, varying over a range of the same order of magnitude as the mean lift. More recently, Mollinger and Nieuwstadt [1996] measured directly lift forces on a sphere lying on a smooth bed, finding intensities (ratio of root mean square to mean values) of 2.8. Thus for the accurate prediction of incipient saltation, one should account for such peaks in the applied fluid forces. Here, the above rationale is extended to include not only the peaks in magnitude, but also the duration of the applied fluctuating hydrodynamic lift. This is accomplished by considering the temporal history or duration of such peak events and treating them as square pulses capable of imparting sufficient momentum to the grain to cause its full displacement normal to the boundary.

### 3.1.1. Equation of motion

For the analytical model of grain saltation, spherical particles are considered. The only forces applied upon the grain in its initial position are the hydrodynamic lift and buoyancy forces and its weight (Figure 2a). This is representative of the case when the grain under consideration is surrounded by similar size particles forming a closely packed configuration, rendering hydrodynamic drag ineffective, due to underexposure. In this context, the trajectory of a saltating grain consists of a path that is initially nearly normal to the boundary [Bagnold, 1973]. The more the grain becomes exposed into the flow, the more the drag forces become effective in its downstream entrainment, which results in a projectile-like motion (e.g. path  $OAB$ , in Figure 2a). The initial portion of the trajectory ( $OA$  in Figure 2a) due to the application of an impulsive lift force is modeled here. Consistent with the definition of full displacement by saltation, the particle must reach or exceed a threshold height, of the order of one grain diameter ( $z_{max}=2R_m$ , where  $R_m$  is the radius of the mobile sphere). This may be seen as the minimum required displacement for the grain to pass over neighboring grains of about the same size [Abbott and Francis, 1977]. Lift forces triggering entrainment by saltation are assumed to be of high magnitude ( $F_L$ ) compared to the resisting forces and of relatively short duration ( $T_{salt}$ ) compared

to the response time of the particle or  $t_{OA}$ , which is the time required for the particle to reach the maximum displacement height,  $z_{max}$ . As in *Diplas et al.* (2008) such forcing events can be modeled as square pulses,  $F_L(1-H(t-T_{salt}))$  (shown as an inset in Figure 2a), where  $H(t-T_{salt})$  is the unit step (Heaviside) function, defined by:

$$H(t-T_{salt}) = \begin{cases} 0, & t < T_{salt} \\ 1, & t \geq T_{salt} \end{cases} \quad (2)$$

The equation of motion along the  $z$  direction (using the Cartesian coordinate system shown in Figure 2a), accounting for added mass and variable bed slope,  $\alpha$ , is:

$$V(\rho_s + \rho_f C_m) \frac{d^2 z(t)}{dt^2} = F_L [1 - H(t - T_{salt})] - W \cos \alpha + B_f \quad (3)$$

where  $C_m$  is the added mass coefficient, which equals 0.5 for spheres in water [*Auton*, 1988],  $W = \rho_s V g$ , is the particle's weight,  $V$  its volume ( $V = 4\pi R_m^3 / 3$ ),  $B_f = \rho_f V g \cos \alpha$ , is the buoyancy force (acting normal to the bed surface for uniform or gradually varied flows following *Christensen* [1995]) and  $z(t)$  is the normal to the bed trajectory component of the particle's center of mass at time  $t$ .

### 3.1.2. Results

The analytical solution of equation (3) (e.g. obtained by means of Laplace transforms), is as follows:

$$z(t) = \frac{\cos \alpha (\rho_s - \rho_f) g t^2}{2(\rho_s + \rho_f C_m)} \left[ \frac{F_L}{F_R} \left( 1 - \left( 1 - \frac{T_{salt}}{t} \right)^2 \right) - 1 \right], \text{ for } t \geq T_{salt} \quad (4)$$

with  $F_R = \cos \alpha (\rho_s - \rho_f) V g$ , the sum of resisting forces in  $z$  direction. Equation (4) describes the deceleration phase of the grain after the cessation of impulsive lift force application. The

maximum displacement height,  $z_{max}$ , is obtained from equation (4), considering that at this position the grain has no upwards velocity ( $dz/dt=0$ ):

$$z_{max} = \frac{\cos \alpha (\rho_s - \rho_f) g T_{salt}^2}{2(\rho_s + \rho_f C_m)} \frac{F_L}{F_R} \left[ \frac{F_L}{F_R} - 1 \right] \quad (5)$$

Equation (5) can be used to determine the required duration of the applied lift force,  $F_L$ , given specified dislodgement height,  $z_{max}$ :

$$T_{salt} = \frac{F_R}{F_L} \sqrt{\frac{(\rho_s + \rho_f C_m)}{(\rho_s - \rho_f) g} \frac{2}{\left(1 - \frac{F_R}{F_L}\right)} \frac{z_{max}}{\cos \alpha}} \quad (6)$$

Assuming that full entrainment by saltation occurs for  $z_{max}=2R_m$ , the required duration  $T_{salt}$  becomes:

$$T_{salt} = \frac{F_R}{F_L} \sqrt{\frac{4R_m(\rho_s + \rho_f C_m)}{\cos \alpha (\rho_s - \rho_f) g \left(1 - \frac{F_R}{F_L}\right)}} \quad (7)$$

Utilizing the component of resisting force in  $z$  direction ( $F_R$ ) and the time required for the free fall of the grain from elevation  $h_{max}=2R_m/\cos \alpha$ ,  $t_{ff} = \sqrt{\frac{2h_{max}}{g} \frac{\rho_s + \rho_f C_m}{\rho_s - \rho_f}}$ , equation (5) can be

normalized:

$$\hat{z} = \hat{F}_L^2 \hat{T}_{salt}^2 \left( 1 - \frac{1}{\hat{F}_L} \right) \quad (8)$$

where  $\hat{z} = \frac{z_{max}}{2R_m}$ , is the normalized displacement,  $\hat{F}_L = \frac{F_L}{F_R}$  and  $\hat{T}_{salt} = \frac{T_{salt}}{t_{ff}}$  denote normalized lift force and duration, respectively. Equation (8) may be used to illustrate the significance, of both duration of the applied lift force as well as its magnitude, as shown in Figure 3, for complete

entrainment ( $\hat{z}=1$ ). This normalized threshold curve (Figure 3), represents combinations of normalized lift force and duration which identify events that are barely sufficient to lead to full displacement. Events above the threshold curve lead to complete entrainment of the grain while events below the curve are insufficient to dislodge the grain, according to the definition employed here. The lift force required to dislodge the grain increases in magnitude as its duration decreases, in an almost inverse fashion. A 50% decrease in normalized duration (from 0.50 to 0.25, which for coarse gravel is of the order of tens of milliseconds), requires an 80% increase of lift force magnitude (from 2.5 to 4.5). Near bed turbulent flows exhibit a range of different timescales of coherent structures. Due to the variability in the duration of such turbulent forcing events, prediction of entrainment based solely on criteria relevant to the magnitude of flow alone, cannot be sufficient.

However, the normalized impulse,  $\hat{I}_{salt}$ , which for saltation can be expressed as the product of normalized lift force with normalized duration, is observed to remain almost constant, for infinitesimally small normalized durations (from equation (8):  $\lim_{\hat{T}_{salt} \rightarrow 0} \hat{I}_{salt} = 1$ , for  $z_{max}=2R_m$ ).

For the previously mentioned examples, normalized impulse has a value of 1.25 and 1.125, respectively. While for a range of possible durations, the critical lift forces vary over an order of magnitude (Figure 3), critical impulse exhibits only a small relative change. The significance of this observation becomes more apparent when the variability of the instantaneous fluctuating lift forces is considered. As an example *Schmeeckle and Nelson* [2003] measured “upward events” of magnitude close to six times the average lift force, for the case of a sheltered grain in a gravel bed. Since high normalized lift forces are typical for entrainment by saltation, the constancy of impulse to a value close to one renders it a robust criterion for prediction of this type of movement.

For lower values of normalized lift force (or higher values of normalized duration), the displacement  $z(T_{salt})$  will be greater, considering equations (4) and (7). Higher values of  $z(T_{salt})$  imply greater exposure to the mean flow when the lift has ceased to be applied. Subsequently, the drag force may impart additional momentum for the grain’s entrainment. This observation conceptually illustrates that even in such cases that lie in between pure saltation and pure rolling, the constancy of normalized saltation impulse to a value close to one is not necessarily a conservative approximation.

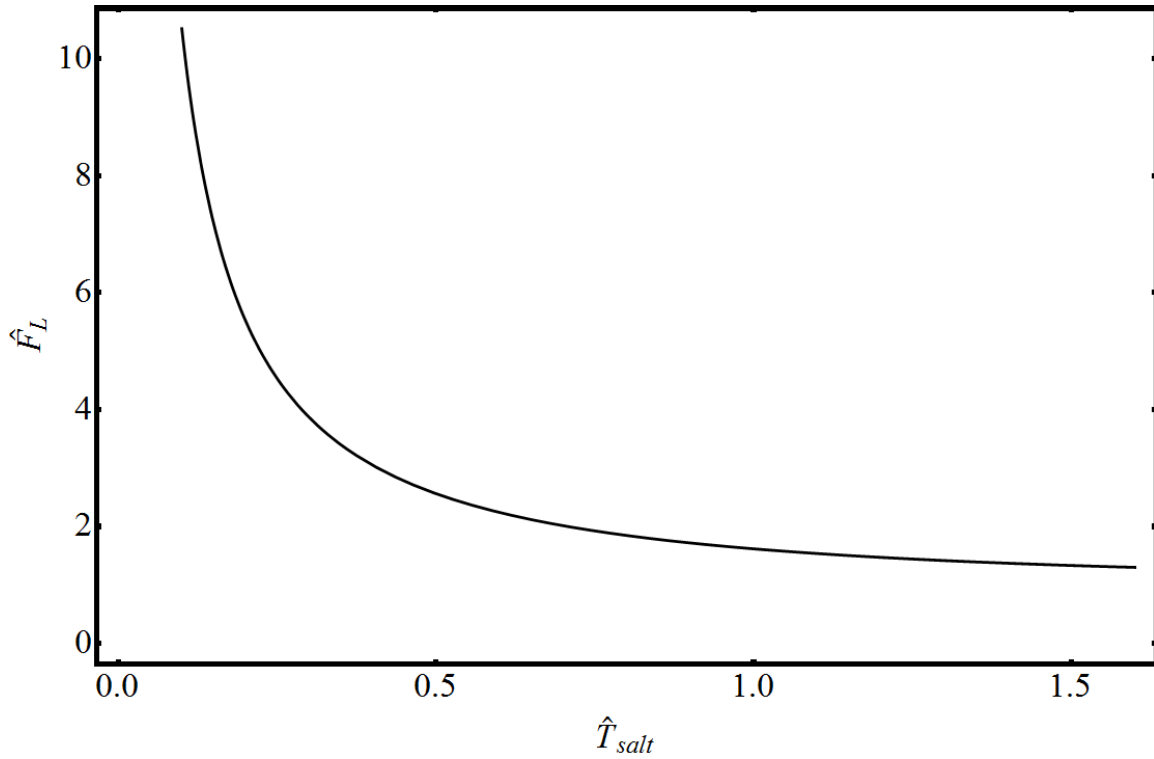


**Figure 3.** Normalized lift force magnitude,  $\hat{F}_L$ , versus normalized impulse duration,  $\hat{T}_{salt}$ , required for particle's incipient saltation ( $\hat{z} = 1$ ).

### 3.2. Incipient Rolling

Similar to saltation, incipient movement of a sediment grain by rolling has also been studied in the past, using either a theoretical deterministic [White, 1940; Coleman, 1967; Komar and Li, 1988; James 1990; Ling, 1995] or stochastic approach [Papanicolaou et al., 2002; Wu and Chou, 2003; Wu and Yang, 2004; Hofland and Battjes, 2006]. Other researchers have experimentally investigated the effect of hydrodynamic forces acting on spherical particles along with the effects of the local grain arrangement or flow parameters, such as relative grain protrusion [Fenton and Abbott, 1977; Chin and Chiew, 1993; Kirchner et al., 1990] and relative flow depth [Shvidchenko and Pender, 2000] and slope [Lam Lau and Engel, 1999; Dey and Debnath, 2000; Gregoretti, 2001; Gregoretti, 2008; Recking, 2009], or solved the equations of motion of individual grains to obtain their trajectories, considering the instantaneous forces acting on them [McEwan and Heald, 2001; Schmeeckle and Nelson, 2003; Valyrakis et al., 2008]. Recently the

effect of turbulent fluctuations of the local velocity and pressure field on sediment mobilization has received a lot of attention [Dancey *et al.*, 2002; Zanke, 2003; Hofland *et al.*, 2005; Schmeeckle *et al.*, 2007; Vollmer and Kleinhans, 2007; Smart and Habersack, 2007]. In the following analysis the role of duration of applied hydrodynamic forces in addition to their magnitude is investigated.

### 3.2.1. Equation of motion

The entrainment of a fully exposed grain in near threshold flow conditions, where hiding effects are minor, is most likely to occur by rolling or sliding, for round or platy particles, respectively. To simplify the analysis spherical particles are considered here and only rolling grain movement is examined. According to the definition of inception of entrainment by rolling, the mobile grain has to reach the topmost position ( $A'$  in Figure 2b), performing an angular displacement,  $\theta = \pi/2 - \theta_0$ , with  $\theta_0$ , the pivoting angle, formed between the horizontal and the lever arm. When the grain reaches the position of maximum exposure ( $A'$ ), it will be entrained further downstream experiencing the near bed turbulent flow (e.g. following the path  $O'A'B'$ , Figure 2b). The relevant forces are the hydrodynamic drag and lift forces ( $F_D$  and  $F_L$  respectively), assumed to act through the barycenter of the exposed sphere, the buoyancy ( $B_f$ ) and the grain's weight ( $W$ ). The local bed topography, along with the polar coordinate system and the forces acting on the protruding grain, are illustrated in Figure 4. The generic case of non-horizontal bed surface ( $\alpha \neq 0$ ) and different radii of exposed ( $R_m$ ) and uniform base ( $R_b$ ) particles is considered, which allows for a wide range of degrees of protrusion that are of practical importance to be investigated. For rolling mode, continuous contact of the mobile particle with the base particles must be retained. This constraint requires:

$$F_{N\xi} \leq 0 \tag{9a}$$

where  $F_{N\xi}$  represents the reaction force, acting normal to the contact surfaces, with direction towards the center of the base particles. The mobilization condition can be expressed as:

$$\frac{d^2\theta}{dt^2} > 0 \quad (9b)$$

*Pigozzi et al.*, 2007, have theoretically shown that the particle follows the minimum resistance path ( $O'A'$ ), rolling between the two downstream supporting particles for the arrangement shown in Figure 2b. Similar to the incipient saltation analysis, the short-lived hydrodynamic forces acting on the mobile sphere can be represented by a step (Heaviside) function of certain duration ( $T_{roll}$ ) and magnitude (Figure 2b inset). Then the equations of motion in polar coordinates,  $\theta$  and  $\xi$ , [e.g. *Schmeeckle and Nelson*, 2003] considering equation (9a), obtain the following form:

$$L_{arm} \left( \frac{7}{5} \rho_s + \rho_f C_m \right) V \frac{d^2\theta}{dt^2} = [F_D \sin(\theta - \alpha) + F_L \cos(\theta - \alpha)][1 - H(t - T_{roll})] + B_f \cos(\theta - \alpha) - W \cos \theta \quad (10a)$$

$$L_{arm} (\rho_s + \rho_f C_m) V \left( \frac{d\theta}{dt} \right)^2 + F_{N\xi} = [F_L \sin(\theta - \alpha) - F_D \cos(\theta - \alpha)][1 - H(t - T_{roll})] + B_f \sin(\theta - \alpha) - W \sin \theta \quad (10b)$$

where  $L_{arm}$ , is the lever arm defined as the distance between the center of gravity ( $O'$ ) and point of rotation ( $D'$ ) of the rolling grain ( $L_{arm} = O'D' = \sqrt{R_m^2 + 2R_m R_b}$ , Figure 4).

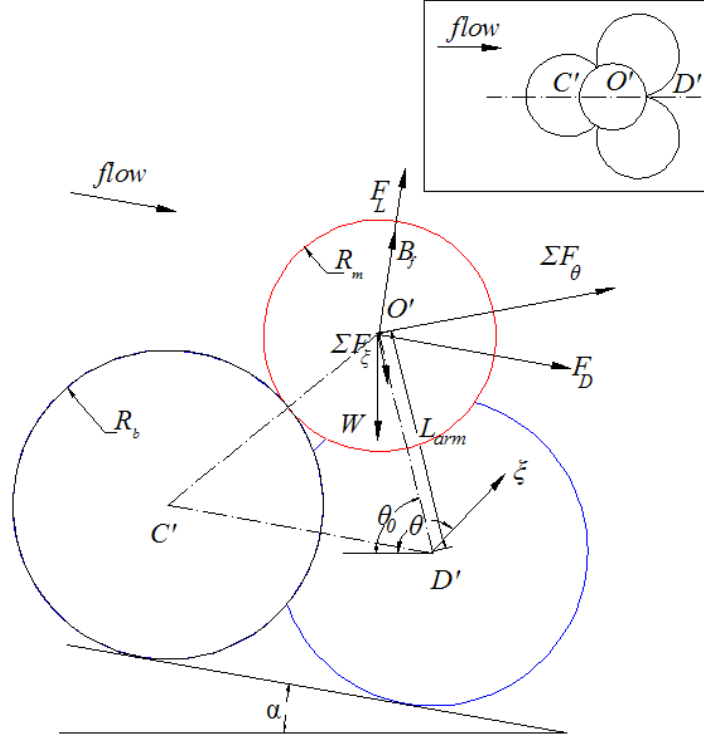


**Figure 4.** Definition sketch for entrainment of particle by rolling, due to drag ( $F_D$ ) and lift ( $F_L$ ) forces. The radial and tangential components of the resultant effective force system are also depicted ( $\Sigma F_\xi$  and  $\Sigma F_\theta$ ). Top view of particle arrangement illustrating the cut plane (dot-dashed line) is provided in the inset.

### 3.2.2. Results

The pure rolling of the grain while retaining contact with the base particles can be described from equation (10a). This occurs only for certain combinations of drag and lift which considering the equilibrium of forces in Figure 4 can be expressed as:

$$\Sigma F_\theta = F_D \sin(\theta_0 - \alpha) + (F_L + B_f) \cos(\theta_0 - \alpha) - W \cos \theta_0 > 0 \quad (11a)$$

$$\Sigma F_\xi = -F_D \cos(\theta_0 - \alpha) + (F_L + B_f) \sin(\theta_0 - \alpha) - W \sin \theta_0 < 0 \quad (11b)$$

where  $\Sigma F_\xi$  and  $\Sigma F_\theta$  represent the sum of forces in the radial,  $\xi$ , and tangential,  $\theta$ , directions at the rest position, respectively.

Pure rolling can be described in two phases; an accelerating phase due to the action of short-lived, high magnitude, hydrodynamic forces and a decelerating one considering only the resisting forces.

If the duration of the acceleration phase ( $t < T_{roll}$ ), is relatively short, small angular displacements will occur ( $\Delta\theta \geq \theta_0$ ). With this approximation the equation (10a), can be linearized to allow for an analytical solution (see Appendix):

$$L_{arm}m_{mod} \frac{d^2(\Delta\theta)}{dt^2} = \Sigma F_\theta - (\Delta\theta)\Sigma F_\xi \geq 0 \quad (12)$$

where  $m_{mod} = (\frac{7}{5}\rho_s + \rho_f C_m)V$ , which holds for  $t < t_{roll}$ . Assuming  $\Delta\theta(t=0)=0$  and  $\Delta\theta'(t=0)=0$ , as the initial conditions the angular displacement,  $\Delta\theta$ , (for  $t < T$ ) is obtained from the solution of equation (12):

$$\Delta\theta = \frac{\Sigma F_\theta}{-\Sigma F_\xi} \left\{ \cosh \left( t \sqrt{\frac{-\Sigma F_\xi}{L_{arm}m_{mod}}} \right) - 1 \right\} \quad (13)$$

At time  $t = T_{roll}$ , when the impulsive forces cease, the particle will have a new position  $\theta(t = T_{roll}) = \theta_0 + \Delta\theta$ , with angular velocity,  $\Delta\theta'(t = T_{roll})$ , calculated by taking the derivative of equation (13):

$$\Delta\theta'(t = T_{roll}) = \frac{\Sigma F_\theta}{\sqrt{L_{arm}m_{mod}} \sqrt{-\Sigma F_\xi}} \sinh \left( T_{roll} \sqrt{\frac{-\Sigma F_\xi}{L_{arm}m_{mod}}} \right) \quad (14)$$

In this analysis, for the sake of simplicity, only the impulsive drag and lift forces responsible for mobilizing the grain are considered. Thus for  $t > T_{roll}$ , the particle decelerates, due to the action of the gravitational force component. The equation of motion in the  $\theta$  direction becomes:

$$L_{arm}m_{mod} \frac{d^2\theta}{dt^2} = B_f \cos(\theta - \alpha) - W \cos \theta \quad (15)$$

According to the definition of entrainment by rolling, the applied impulse has to impart enough momentum so that the grain at time  $t=t_{O'A'}$ , will reach the topmost position,  $\theta(t=t_{O'A'})=\pi/2$ , with zero tangential velocity,  $\Delta\theta'(t=t_{O'A'})=0$ . With these conditions and equations (13) for  $t=T_{roll}$  and (14), the duration of impulse necessary for grain dislodgment, as a function of the force components, particle and local geometry characteristics is obtained from equation (15), by multiplication of all parts with the angular velocity,  $\Delta\theta'$  and subsequent integration (see Appendix):

$$T_{roll} = \sqrt{\frac{L_{arm}m_{mod}}{-\Sigma F_{\xi}}} \operatorname{arc\,sinh} \left( \sqrt{2W\rho_{\theta}} \frac{\sqrt{-\Sigma F_{\xi}}}{\Sigma F_{\theta}} \right) \quad (16)$$

with  $\rho_{\theta} = (1 - \sin \theta_0) \left( \frac{\cos \theta_0}{1 - \sin \theta_0} \sin \alpha + \left( \cos \alpha - \frac{\rho_f}{\rho_s} \right) \right)$ , a coefficient incorporating the effects of initial geometrical arrangement and the relative density of fluid and solid grain. Equation (16) is the counterpart to equation (7) in the saltation analysis, now for rolling. The components of total force in both tangential and radial directions as well as their duration can be normalized utilizing the weight of the grain and the time required for free fall from a height proportional to  $(1 - \sin \theta_0)L_{arm}$ , which is the elevation difference between the initial and topmost positions, respectively. Thus using the normalized variables;

$\hat{T}_{roll} = \frac{T_{roll}}{\sqrt{2L_{arm}(\rho_{\theta}m_{mod}/W)}}$ ,  $\Sigma \hat{F}_{\xi} = \frac{\Sigma F_{\xi}}{W/2\rho_{\theta}}$ ,  $\Sigma \hat{F}_{\theta} = \frac{\Sigma F_{\theta}}{W}$ , equation (16), becomes:

$$\hat{T}_{roll} = \sqrt{\frac{1}{-\Sigma \hat{F}_{\xi}}} \operatorname{arc\,sinh} \left( \frac{\sqrt{-\Sigma \hat{F}_{\xi}}}{\Sigma \hat{F}_{\theta}} \right) \quad (17)$$

The result is shown in Figure 5, as a surface plot of normalized duration  $\hat{T}_{roll}$ ,  $\Sigma \hat{F}_{\xi}$  and  $\Sigma \hat{F}_{\theta}$  which are functions of lift and drag normalized by the weight of the mobile grain. Points at

or above the threshold surface denote combinations of duration, drag and lift force, which will result in complete entrainment by rolling. A weak dependence of  $\hat{T}_{roll}$  for a wide range of negative values of  $\Sigma\hat{F}_\xi$  is observed (Figure 5). This implies that the role of the normalized radial component of the total force is limited to setting a constraint for the ratio of effective hydrodynamic forces, so that movement occurs in rolling mode. However, a rather significant dependence on the normalized tangential component of the resultant forces is seen.  $\Sigma\hat{F}_\theta$  is almost inversely related to  $\hat{T}_{roll}$  (Figure 5), meaning that for increasing magnitude of this component, the required duration for triggering particle motion is reduced. For instance, for the limiting case of  $\Sigma\hat{F}_\xi = 0$ , equation (17) predicts (by application of l'Hopital's rule) that  $\hat{T}_{roll}$  and  $\Sigma\hat{F}_\theta$  are inversely related:

$$\lim_{\Sigma\hat{F}_\xi \rightarrow 0} \hat{T}_{roll} = \frac{1}{\Sigma\hat{F}_\theta} \quad (18)$$

Even though the magnitude of  $\Sigma\hat{F}_\theta$ , may exhibit a variation of more than an order of magnitude, the normalized impulse,  $\hat{I}_{roll}$ , defined as the product of  $\hat{T}_{roll}$  and  $\Sigma\hat{F}_\theta$  retains a constant value of unity, according to equation (18). Similar to the case of entrainment by saltation, the observed constancy or small variation of normalized impulse for a wide range of forcing conditions makes impulse a valuable criterion for coarse grain entrainment prediction.

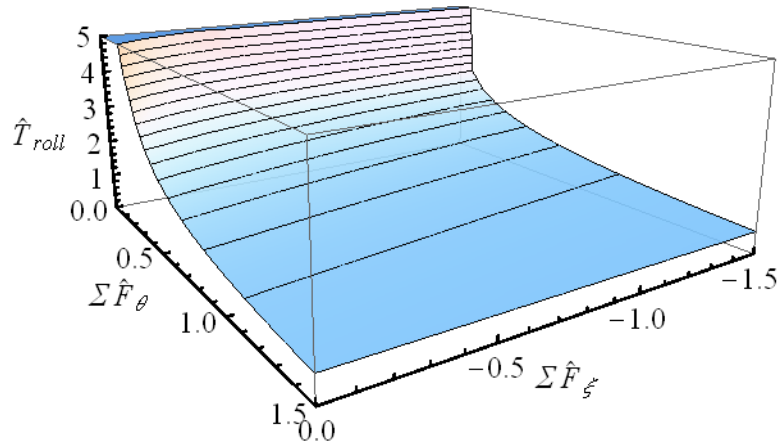


**Figure 5.** Threshold surface predicting the critical pulse characteristics (normalized hydrodynamic drag,  $\Sigma\hat{F}_\theta$ , and lift,  $\Sigma\hat{F}_\xi$ , forces and normalized duration,  $\hat{T}_{roll}$ ) for onset of entrainment.

The threshold conditions for complete grain entrainment are highly dependent on the local particle configuration, such as lever arm and pivoting angle as shown from equation (16). A practical dimensional example is provided in the following. For instance, assume an 8 mm quartz sphere ( $\rho_s = 2650 \text{ kg/m}^3$ ), submerged in water ( $\rho_f = 1000 \text{ kg/m}^3$ ), resting on an arrangement of three closely packed base particles of the same radius (8 mm), with zero bed slope ( $\alpha = 0$ ). For different levels of lift force the critical combinations of drag force and duration are determined from equation (16), while satisfying the constraints for rolling mode. The relation between drag force magnitude and duration for zero lift force is plotted in Figure 6, for a range of durations. Similar to the case of entrainment by saltation, only combinations of the driving force (here drag) and duration which fall above the threshold curve correspond to complete entrainment.

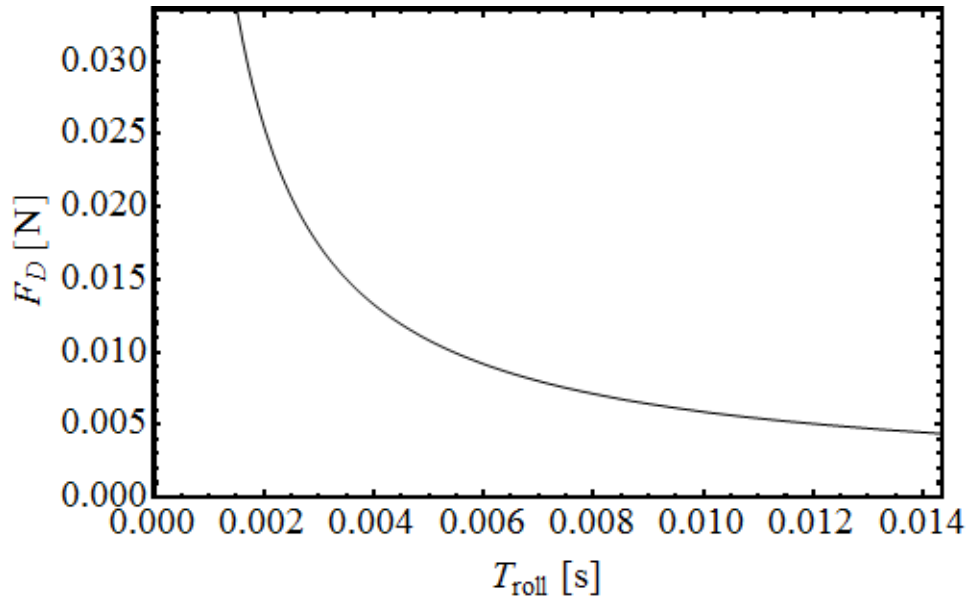


**Figure 6.** Threshold curve of critical drag and duration combinations, for the incipient entrainment of a quartz sphere in water ( $R_m=4 \text{ mm}$ ,  $R_b=4 \text{ mm}$ ,  $\alpha=0$ ,  $F_L=0$ ).

The accuracy of the analytical solution of the linearized equations of motion for rolling depends on the linearization approximation that the angular displacement,  $\Delta\theta$ , is relatively small during the application of the hydrodynamic forces. This assumption is correct for relatively short durations or high magnitudes of force, which is assessed by numerically solving the EoM (e.g. equation 10a). The critical impulse calculated from the theoretical linearized model, is slightly over-predicted compared to the numerical obtained solution. The ratio of excess impulse (due to positive grain velocity at the topmost position) over the imparted impulse can be used as an

indicator to quantitatively evaluate the magnitude of error, as shown in Figure 7. It is observed that for relatively high magnitudes of drag force (e.g. 3 times the particle submerged weight) the error is about 5% (with a maximum error of 12% for drag force of the order of the particle submerged weight). Considering that such extreme forces are expected when displacing a grain by saltation, the accuracy of the linearized solution is high.

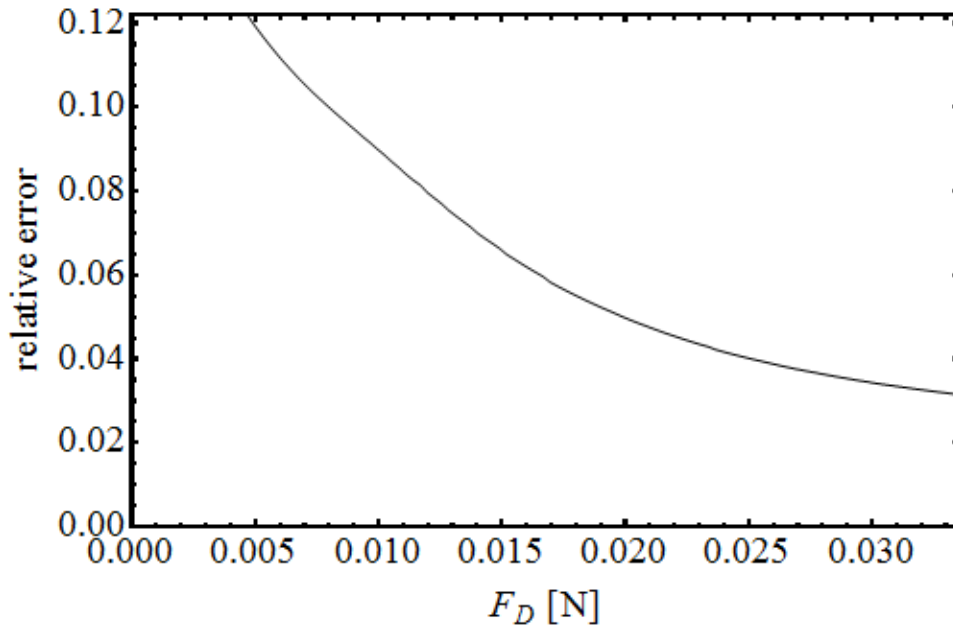


**Figure 7.** Relative error (expressed as the ratio of excess impulse over the imparted impulse) for a range of drag forces.

The required duration is almost inversely related to the applied drag force (not qualitatively different from the case of saltation). Thus as in the case of displacement by saltation, the magnitude of the force alone is insufficient to predict the complete removal of a spherical grain from its local position in the bed matrix. That is, given the short-lived nature of the applied hydrodynamic forces, information about the duration is relevant and necessary to fully capture the physics of the entrainment process. This conclusion is verified experimentally in the next section and the role of impulse is demonstrated to be the appropriate parameter to characterize the critical condition for entrainment.

## 4. Electromagnet experiments

To test the theoretical analysis, and demonstrate the relevance of impulse to grain dislodgment, a set of controlled bench-top experiments, modeling the incipient motion of a fully exposed spherical grain by rolling, were performed with the use of an electromagnet.

### 4.1. Description of setup and experimental process

The setup consisted of a mobile, steel sphere, located on top of a horizontal layer of fixed Teflon® spherical particles and an electromagnet through which forces of defined duration and magnitude could be applied in a controlled manner [Diplas *et al.*, 2008]. The triangular array of base particles was fixed on a horizontal plate of adjustable height and lateral position, permitting the precise positioning of the center of the mobile grain along the centerline of the electromagnet, with a known distance from its face ( $h$ ). The centers of the particles in the test fixture form a tetrahedron, which is the same local arrangement employed in the theoretical rolling analysis (Figure 4 inset). The experiments were performed in still air. The setup also included a data acquisition board (DAQ), a signal processor and a circuit used for voltage amplification. Appropriate software was used on a personal computer (PC), to generate user defined series of electromagnetic pulses of varying duration and magnitude. The circuit amplifies the signal sent by the DAQ system to the magnet, reads the voltage drop across the electromagnet as well as the current and then de-amplifies these signals to an appropriate range to be read back in by the DAQ. A total of 7 different local arrangements were tested (Table 1), either by changing the distance of the mobile grain from the face of the electromagnet ( $h_e$ ), or by varying the ratio of the radii of mobile to base particles ( $R_m/R_b$ ). Each of the runs is generally named after the combination of diameters of mobile and base particles. A high speed camera was used to accurately monitor the displacement of the steel particle. Careful observation of the videos verified the assumption that entrainment of the spherical particles occurred only by rolling (in the absence of sliding).

When current passes through the electromagnet coil, an electromagnetic field is generated, resulting in a force which, depending on its magnitude and duration, may mobilize the steel particle. Here, the electromagnetic force is considered to simulate, in a simplified way, the

drag force acting on a grain due to a peak in the local streamwise velocity component. However, rather than rapidly fluctuating hydrodynamic forces of unknown magnitude and durations, typically encountered in near boundary turbulent flow, these parameters are accurately controlled through suitable software and circuitry. Electromagnetic forces are applied in the form of square pulses characterized by certain values of force magnitude,  $F_e$ , and duration,  $T_e$ . For a given particle configuration, the magnitude of force is related to the voltage across the electromagnet,  $V_e(t)$ , via the following relation:

$$F_e(t) = \frac{N_e^2 \mu_e A_e}{2h_e^2 r_e^2} V_e(t)^2 \quad (19)$$

where  $N_e$ , is the number of turns of the wire in the coil of the electromagnet,  $A_e$ , is the characteristic area of the face of the electromagnet,  $\mu_e$ , is the magnetic permeability of the medium (here air) and  $r_e$ , the resistance of the electromagnet. The above equation is derived by considering the energy contained in the electromagnetic field, assuming that the magnetic flux induced by the electromagnet does not change when the particle is displaced from its initial location. Since for a given grain arrangement ( $i$ ) the values of the coefficients of the electromagnet as well as the parameters specific to the grain arrangement,  $A_e$  and  $h_e$ , are fixed, the combination of terms may be represented by a constant,  $c_i$ , and the applied force is directly proportional to the square of applied voltage ( $F_e = c_i V_e^2$ ). Thus it is possible to apply an electromagnetic pulse of specific duration and magnitude with this design, by controlling the voltage across the electromagnet.

For a particular grain arrangement a search for the critical  $F_e$ ,  $T_e$  combinations was performed, from which threshold curves could be obtained. The applied voltages ranged from 2.5 to 15 Volts, with a minimum voltage step size of 0.25 Volts, while the duration of their application varied from 3 to 75 ms with a time step of 2-4 ms. First, a series of electromagnetic pulses of sufficiently long duration (1.5 s), representing nearly steady state forcing conditions, were applied with increasing amplitude, until the particle is displaced. In this manner, the minimum voltage,  $V_{min}$ , required for particle removal was determined for each configuration. For a given particle configuration, two different strategies can be followed to find the minimum pulses that fully displace the particle; either the voltage ( $V_e > V_{min}$ ), is steadily increased for

constant duration (Figure 8a) or for constant voltage ( $V_e > V_{min}$ ) the duration is gradually increased (Figure 8b). For both cases the search is completed when the particle is entirely displaced from its initial location.

**Table 1.** Characteristics of different particle configurations and the best fit curves derived from the data points for which movement was observed.

set of runs	$2R_m$ (mm)	$2R_b$ (mm)	$h_e$ (mm)	number of runs	Best fit equation	$R^2$
4-4	4	4	3.15	224	$V_e^2 = 449.3T_e^{-1.03}$	0.96
6-6	6	6	4.73	184	$V_e^2 = 745.3T_e^{-1.00}$	0.98
8-8	8	8	6.31	286	$V_e^2 = 958.1T_e^{-0.95}$	0.98
6-8	6	8	6.31	273	$V_e^2 = 1714.5T_e^{-1.04}$	0.98
8-6	8	6	6.31	243	$V_e^2 = 892.4T_e^{-1.07}$	0.98
6-6b	6	6	6.31	260	$V_e^2 = 1048.0T_e^{-0.98}$	0.98
4-6	4	6	6.31	239	$V_e^2 = 1109.7T_e^{-0.89}$	0.98

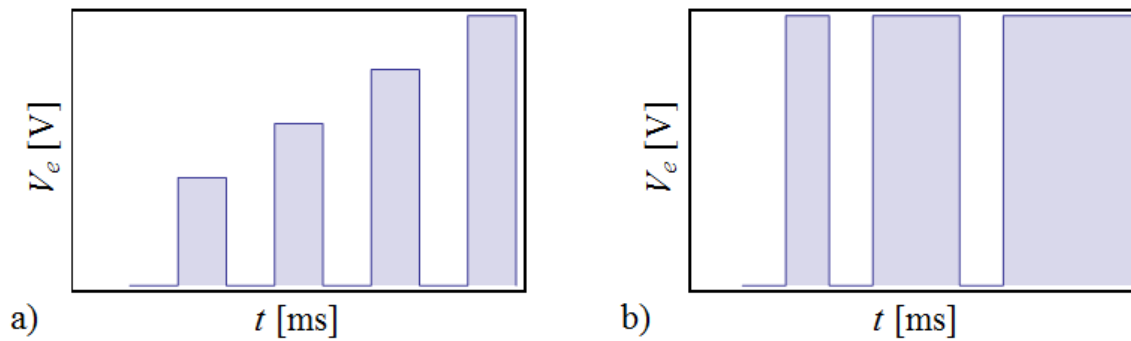


**Figure 8.** Representation of the programmable voltages for the generation of electromagnetic pulses a) by varying the voltage levels for fixed duration and b) by changing the duration for fixed magnitude.

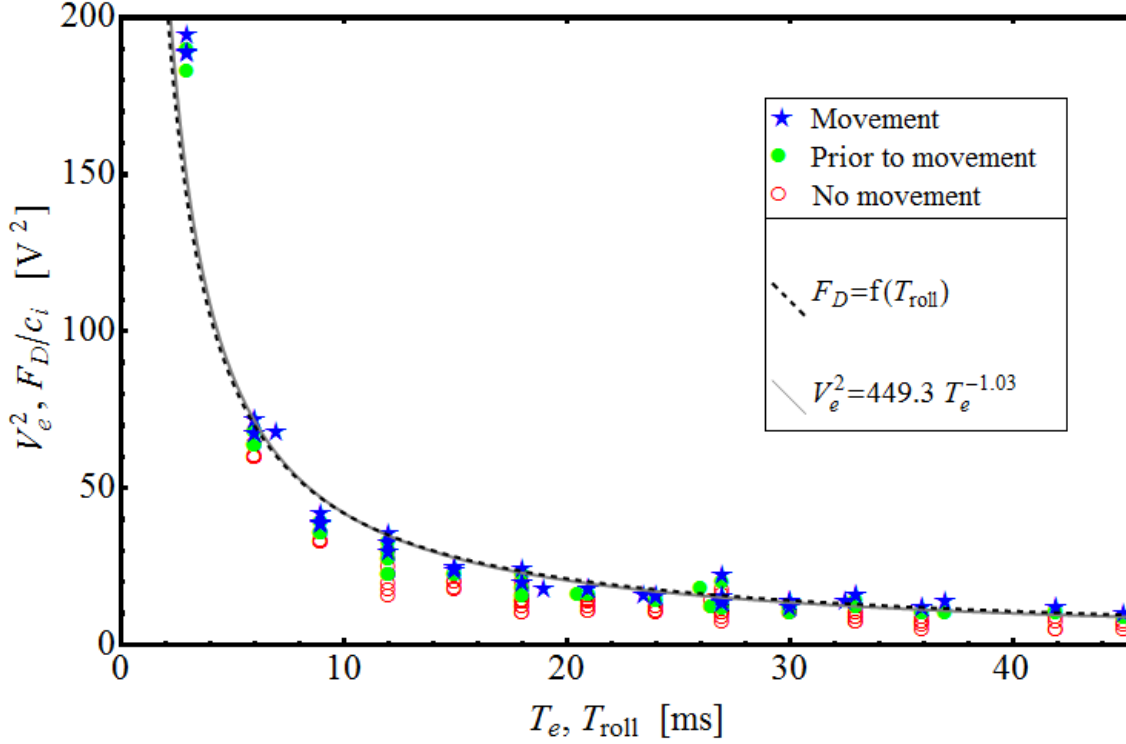


**Figure 9.** Plot of threshold curves and  $T_e$ ,  $V_e^2$  combinations, for run 4-4. Two critical curves are shown: the first obtained from the best fit of the data points for which entrainment was observed (continuous line) and the second predicted from equation 16 (dashed line, scaled appropriately to account for  $c_i$ ).

Figure 9, is typical of the results of the followed procedure. In this figure,  $(T_e, V_e^2)$  data pairs are presented for a 4 mm steel ball placed on a triangular arrangement of 4 mm base particles (run 4-4). For fixed pulse duration voltage was gradually increased until the sphere was barely dislodged from its initial arrangement. Then the duration was adjusted to a new fixed value and the above procedure was repeated. After a wide range of  $T_e$ - $F_e$  combinations have been explored, the threshold curve indicative of the necessary and sufficient impulsive force characteristics for complete grain dislodgment, should lie between the points signifying “movement” and those just “prior to movement” (Figure 9). Following the same procedure, the seven sets of runs corresponding to different particle arrangements with varying mobile and base particle diameters (from 4 to 8 mm), were completed. A total of 1709 data points were obtained (Table 1), which are used to derive the threshold curves for each particle configuration. Each experiment was performed up to three times to ensure repeatability and accuracy.

## 4.2. Results

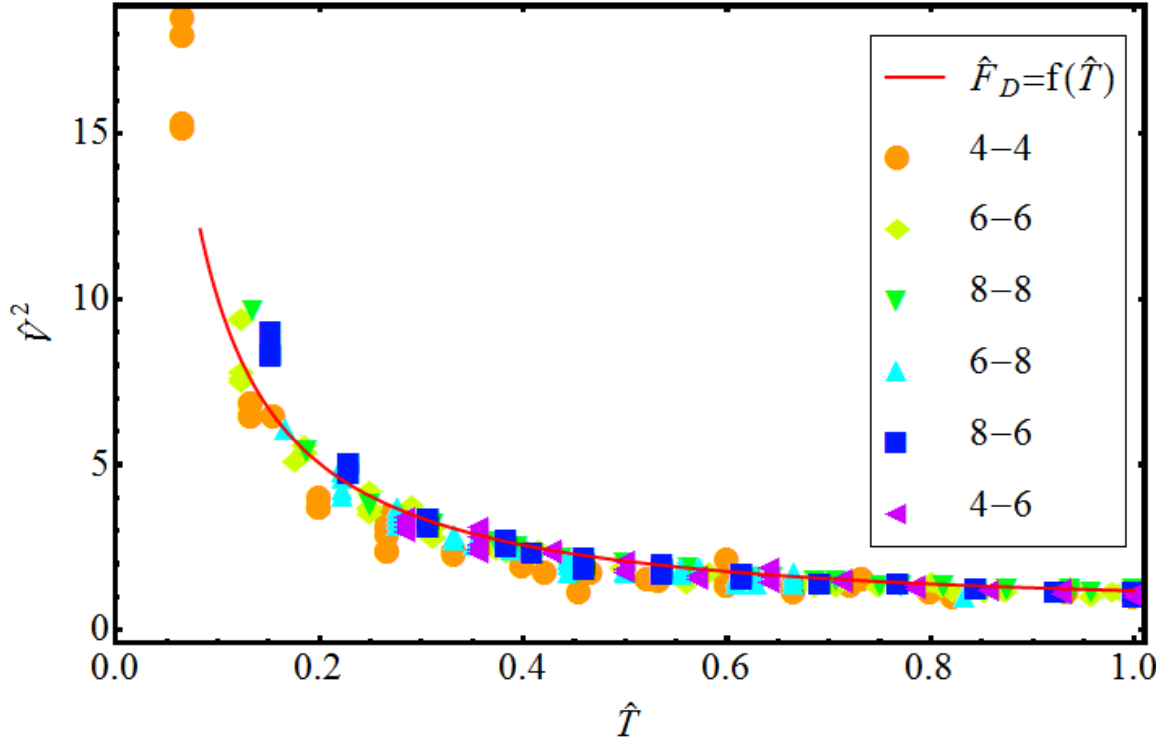
From the presentation of obtained data points as well as the threshold curves it is evident that a trend consistent with the theoretical results is observed (e.g. Figure 9, for run 4-4). Representative best fits for the group of data points for which movement was observed are obtained by matching a power equation of the form  $V_e^2 = kT_e^q$ , with  $k, q$  coefficients characteristic of each arrangement. For all sets of runs the coefficient of determination of the best fit curves is quite high ( $R^2 > 0.95$ , Table 1). For instance, the best fit equation for run 4-4 is given by equation  $V_e^2 = 449.3T_e^{-1.03}$  (continuous curve in Figure 9), with a coefficient of determination  $R^2 = 0.96$ . Comparison of the critical curves for entrainment obtained from a best fit to the observed data for each run, with the threshold curves predicted from rolling analysis, equation (16), reveals the accuracy of the analytical approach. As an example for the case of run 4-4, an almost perfect match between the two curves is seen. In agreement with the results of the theoretical analysis, while the range of critical electromagnetic force ( $F_e$  parameterized by  $V_e^2$ ), changes over an order of magnitude (e.g. from 13 to 195 volts<sup>2</sup> – Figure 9), the impulse computed as the product  $F_e T_e$ , remains almost invariable over the range of possible durations (e.g. for 4-4:  $I_e = 449.3T_e^{-0.03}$ , for  $T_e$  from 6-46 ms, the change in  $I_e$  is less than 6%).

Figure 10, shows the critical data points from all runs (367 in total), using normalized parameters [Diplas *et al.*, 2008]. For each set of experiments associated with a particular grain arrangement, the values of each ( $T_e, F_e$ ) data point are normalized by the corresponding measured values of  $T_e$  and  $F_e$  with the maximum duration and smallest force magnitude required for particle dislodgment ( $T_{e,max}, F_{e,min}$ ). Thus the normalized values of magnetic force and

duration are  $\hat{F}_e = \frac{F_e}{F_{e,min}} = \frac{c_i V_e^2}{c_i V_{min}^2} = \frac{V_e^2}{V_{min}^2} = \hat{V}^2$  and  $\hat{T}_e = \frac{T_e}{T_{e,max}}$  respectively, where  $V_{min}$  and  $T_{e,max}$  vary

for each combination of mobile and base grains. Diplas *et al.*, (2008) provide a best fit for these data ( $\hat{V}^2 = 0.96\hat{T}_e^{-0.99}$ , see dashed curve in Figure 10), with a coefficient of determination of  $R^2 = 0.96$ . The normalized threshold curve predicted from the rolling analysis (continuous line in Figure 10), from equation (18), provides a good fit to the normalized experimental data and almost overlaps with the best fit curve. In this context and in agreement with the analytical treatment of the phenomenon, a constant normalized impulse, defined as the product of

normalized force magnitude and normalized duration of its application ( $\hat{I}_e = \hat{F}_e \hat{T}_e = 0.96 \hat{T}_e^{0.01} \sim \text{constant}$ ), successfully describes the full entrainment of a particle.



**Figure 10.** Data points of normalized magnetic force (parameterized by  $\hat{V}^2$ ) and duration,  $\hat{T}_e$ , for which movement was observed, for all the runs. The best fit (dashed) curve and the threshold curve predicted from equation 18 (continuous line) are also shown.

## 5. Discussion

In the following, a comparison of the critical conditions for entrainment of a particle by saltation and rolling is explored, for a specific grain arrangement. Then, the critical conditions, for both modes, are expressed in terms of the normalized impulse, to generalize the results irrespective of the geometrical characteristics of particle configuration. Finally, the impulse concept is extended to describe different levels of motions.

## 5.1. Comparison of saltation and rolling thresholds: force-duration representation

The modes of grain movement are not only dependent on the local geometrical configuration, but also on the ratio of the relative magnitude of instantaneous drag and lift forces acting on it. This implies that even for the limiting case of a fully exposed particle, saltation could occur under particular flow conditions. Rolling occurs when the exposed particle retains contact with the downstream base particles, throughout its movement (e.g.  $O'A'$ , in Figure 2). This is true for ratios of drag to lift that satisfy equations 9a and 9b, or for simplicity considering static equilibrium of forces, equations (11a) and (11b);  $\Sigma F_\theta > 0$  and  $\Sigma F_\zeta < 0$ . Based on the same rationale, for greater lift forces movement will occur by saltation ( $\Sigma F_\theta > 0$  and  $\Sigma F_\zeta > 0$ ), while the case of no motion is described by  $\Sigma F_\theta < 0$ . Equation (11a) may be recast into a more meaningful form  $F_D / \left( F_L + B_f - W \frac{\cos \theta_0}{\cos(\theta_0 - \alpha)} \right) > \tan(\theta_0 - \alpha)$ , in which the term in the left hand side can be seen as the ratio of drag to a net lift force. Thus, the value of this ratio with respect to  $\tan(\theta_0 - \alpha)$ , or equivalently the sign of  $\Sigma F_\zeta$ , determines the initial mode of entrainment.

This can be illustrated by considering the example of an 8 mm particle, discussed in the results section of the rolling analysis (3.2.2). The different regimes of no motion and movement by rolling or saltation can be defined in the plane of lift and drag forces, normalized by the mobile particle's weight (Figure 11). The line  $\Sigma F_\zeta = 0$  (continuous line, Figure 11), separates the two modes of dislodgement, while the line  $\Sigma F_\theta = 0$  (dashed line, Figure 11), partitions the movement from the no-movement regimes.

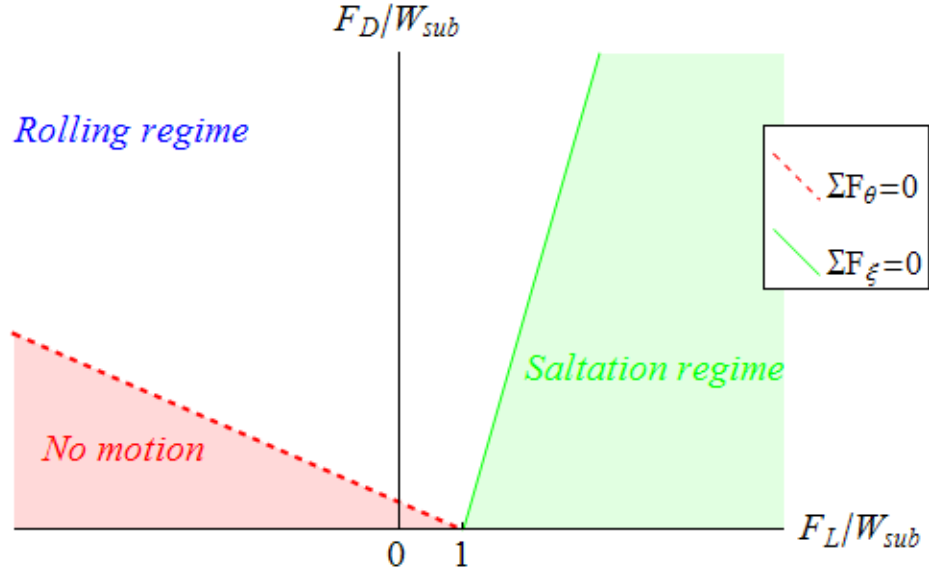


**Figure 11.** Classification of the representative modes of incipient motion, depending on the relative magnitude of drag to lift forces normalized by the mobile particle's weight (case of a completely exposed particle with  $R_m = 4$  mm,  $R_b = 4$  mm,  $\alpha = 0$ ). The dividing lines are obtained from the appropriate normalization of equations (11a) and (11b).

Even though the effect of the instantaneous magnitude of drag and lift on grain entrainment has been extensively investigated [Einstein and El-Samni, 1946; Sutherland, 1967; Nelson et al., 1995; Cheng and Chiew, 1998; Sechet and Guennec, 1999; Sumer et al., 2003; Schmeeckle and Nelson, 2003; Zanke, 2003; Hofland et al., 2005; Smart and Habersack, 2007, among others], here the role of duration of force is analytically and experimentally demonstrated to be of equal significance. Considering the analytical solutions for the two modes of entrainment (equations (7) and (16)), along with the constraint equations that delimit their boundaries, Figure 11 can be expanded to include duration as a third dimension (Figure 12), for the dimensional example of an exposed particle. In this figure, the surface plots representative of the critical ( $F_D$ ,  $F_L$ ,  $T$ ) combinations for saltation and rolling modes are illustrated (Figure 12a and 12b respectively).

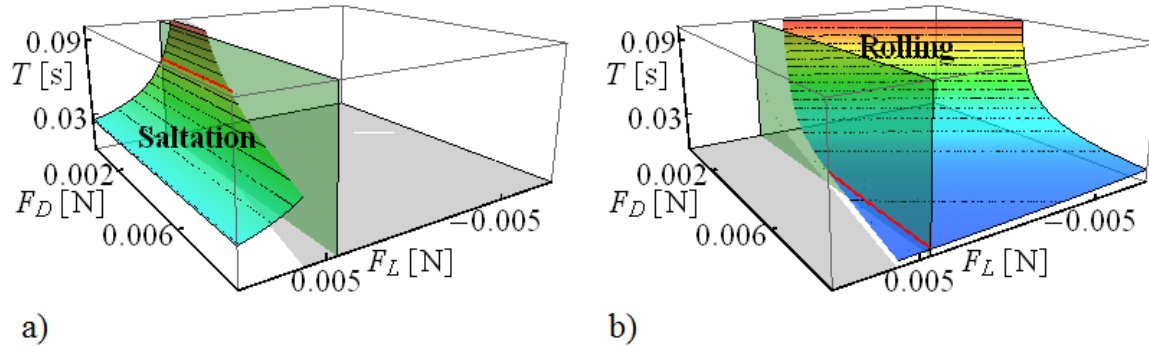


**Figure 12.** Threshold surfaces indicating the critical drag, lift and duration combinations, for the modes of entrainment by: a) saltation and b) rolling, for the case of an exposed particle ( $R_m = 4$  mm,  $R_m = 4$  mm,  $\alpha=0$ ). The intersection of the saltation and rolling critical surfaces with the vertical cut-plane,  $F_L = 1.5F_R = 0.0045$  N, is emphasized with a thick line, to illustrate the separation between the two modes.

A comparison of the thresholds of the two different modes for the case of a fully exposed grain reveals the need of higher magnitude of forces or duration for the case of saltation as opposed to the rolling mode (Figure 12a and 12b). For instance for the same drag and lift forces (e.g. along line  $\Sigma F_{\theta}=0$ ), saltation requires longer durations compared to rolling. Similarly for a constant level of force duration, the critical values of both lift and drag are higher if entrainment occurs by saltation (Figure 12a and 12b). Thus the saltation mode of entrainment requires greater impulses compared to the rolling mode, which is intuitively correct. This observation may be generalized to various degrees of exposure (here controlled by angle of repose, for a given particle size). Qualitatively, these results agree with the increase in magnitude of critical Shields' stress for saltation compared to incipient rolling [Ling, 1995; Wu and Chou, 2003].

The relation of critical force to duration is easier to examine by using vertical cut planes e.g. of constant lift force. For example the plane  $F_L=1.5F_R=0.0045$ N, is shown to intersect with both saltation and rolling threshold surfaces (thick continuous lines in Figures 12a and 12b, respectively). The resulting threshold curves, characteristic of each mode, are illustrated in Figure 13a. The saltation model does not account for drag force (equation 7), which is illustrated by the constancy of duration for different values of this parameter (Figure 13a). Beyond a certain

value of drag force (here for  $F_D > 1.5F_R$ ), entrainment occurs in rolling mode. It is worth noticing the relative difference in the magnitude of impulse duration ( $T$ ), between the saltation and rolling regimes. The duration required for entrainment by saltation mode, is almost seven times greater compared to the rolling mode (for the same magnitude of lift and drag forces), which renders displacement of the completely exposed particle by saltation under relatively low impulse values, significantly less probable. An increase of the lift force to a value of  $F_L = 1.7F_R$  (Figure 13b), reduces both required durations for saltation and rolling. As a result their ratio is retained almost the same (to a value of seven). The minimum drag force, separating saltation from rolling regimes, also increases (compare dashed vertical lines in Figures 13a and 13b), which is also supported from equation  $\Sigma F_\theta = 0$ . For negative values of  $\Sigma F_\xi$ , entrainment is possible only by rolling (Figure 12b) and saltation regime vanishes. For instance, for the cut plane  $F_L = -1.5F_R$ , the characteristic almost inverse relation of drag forces and duration is seen (Figure 13c). Relative to the previous cases of higher impulsive lift forces, relatively higher levels of drag forces are required for entrainment by rolling, which is in agreement with the stabilizing role of negative lift.

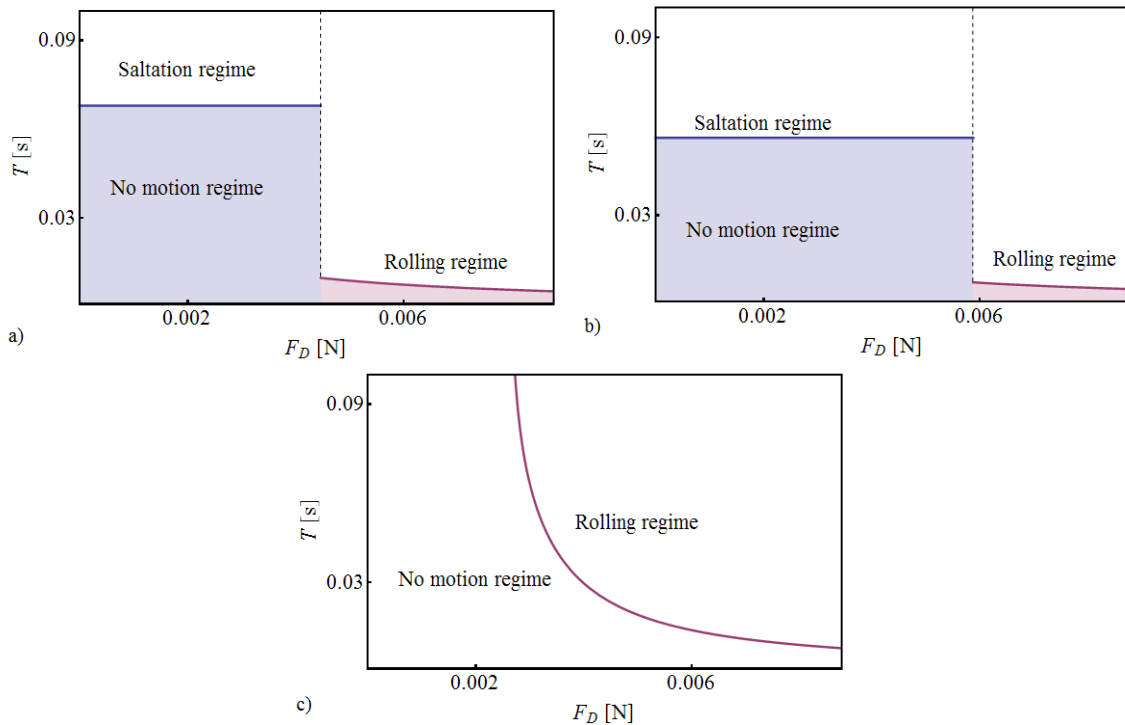


**Figure 13.** Threshold curves for movement by saltation or rolling, for the case of an exposed particle ( $R_m = 4$  mm,  $R_b = 4$  mm,  $\alpha = 0$ ) and different values of lift force: a)  $F_L = 1.5F_R$ , b)  $F_L = 1.7F_R$ , c)  $F_L = -1.5F_R$ .

## 5.2. Comparison of saltation and rolling thresholds: normalized impulse representation

The analytically derived normalized solutions of the equations of motion by saltation and rolling (equations 8 and 17) can be expressed in terms of the normalized critical impulse, as the product of magnitude of the appropriate driving force with the duration of its application. The normalized critical impulse for saltation,  $\hat{I}_{salt}$ , is the product of normalized lift force calculated from equation (8) and normalized duration is:

$$\hat{I}_{salt} = \hat{T}_{salt} \hat{F}_L = \frac{\hat{T}_{salt}}{2} \left( 1 + \sqrt{1 + \frac{4\hat{z}}{\hat{T}_{salt}^2}} \right) \quad (20)$$

According to equation (20), the critical level of impulse for saltation ( $\hat{z}=1$ ), depends on normalized duration (dashed line in Figure 14). For example, if the duration of impulse equals the free fall time of the particle ( $\hat{T}_{salt}=1$ ), an almost 50% increase of the impulse required for entrainment is necessary, compared to the case of infinitesimal durations. Estimations of the duration of forces above critical may be derived indirectly from observed values of characteristic trajectory parameters of saltating grains. *Nino and Garcia* (1994), provide data of mean streamwise grain velocities and saltation lengths for uniform grains of 15 and 31 mm. From these data mean durations for saltation are estimated to range between 0.16 and 0.29 seconds. In a later paper, *Nino and Garcia* (1998), report durations of saltation events for sand grains (0.9mm), in the range of 0.036 to 0.048 seconds. Differentiating equation (4), the duration required for the particle to reach the top of its trajectory ( $t_{salt}$ ) with zero upward velocity, is calculated:

$$t_{salt} = T_{salt} \frac{F_L}{F_R} \quad (21)$$

which implies that the greater the ratio of driving to resisting forces, the shorter the duration of force, compared to the saltation time. Equation (21) can be expressed in normalized variables if durations are normalized with the free fall time parameter ( $t_{ff}$ ):

$$\hat{t}_{salt} = \hat{T}_{salt} \hat{F}_L = \hat{I}_{salt} \quad (22)$$

The resulting variable  $\hat{t}_{salt}$ , is found to be equal to normalized impulse for saltation, with values that range from 1.37 to 2.3, for coarse particles and 1.83 to 2.45 for sand grains (considering the measurements in [Nino and Garcia, 1994] and [Nino and Garcia, 1998] respectively). These values should lie well above the predicted normalized threshold curve for saltation, given that the mean shear stress ranged from 1.33 to 2.33 times the critical Shields stress. Considering that the instantaneously fluctuating lift may obtain extreme values of e.g. up to six times the mean lift [Smccheekle et al., 2007], it becomes apparent (from equation (21)), that impulse durations are only a small fraction of the total saltation time. Thus the saltation impulse model predicts an almost constant value close to one for relatively short-lived impulses (Figure 14).

Using equation (17) the critical impulse for rolling,  $\hat{I}_{roll}$ , is obtained:

$$\hat{I}_{roll} = \hat{T}_{roll} \Sigma \hat{F}_\theta = \frac{\Sigma \hat{F}_\theta}{\sqrt{-\Sigma \hat{F}_\xi}} \text{Arcsinh} \left( \frac{\sqrt{-\Sigma \hat{F}_\xi}}{\Sigma \hat{F}_\theta} \right) \quad (23)$$

A nearly constant value of unity for the critical impulse is computed for different levels of  $\Sigma \hat{F}_\xi$  and  $\hat{T}_{roll}$ , that are of practical importance. For example for the case of  $\Sigma \hat{F}_\xi = -1$  the divergence from  $\hat{I}_{roll} = 1$  over the range of  $\hat{T}_{roll}$  from 0 to 1, is less than 12%. For the limiting case of  $\Sigma \hat{F}_\xi = 0$ , equations (18) and (23) predict a constant value of  $\hat{I}_{roll} = 1$ , independent of duration (solid line, in Figure 14). The constancy of impulse can be further illustrated from the experimental results contained in this study. Expressing the normalized data (Figure 10) of drag force magnitude (square of voltage) and duration, in terms of their product or impulse, provides the data points shown in Figure 14. A best fit is also given to illustrate the relative constancy of impulse (dashed-dotted line in Figure 14). Within experimental error, the analytically derived equation (23) for  $\Sigma \hat{F}_\xi = 0$ , predicts well the experimental results. For the previous comparison, the value of  $\Sigma \hat{F}_\xi = 0$  is used in the theoretical model, to best match the forcing conditions in the electromagnet experiments ( $F_L=0$  and  $\alpha=0$ ).

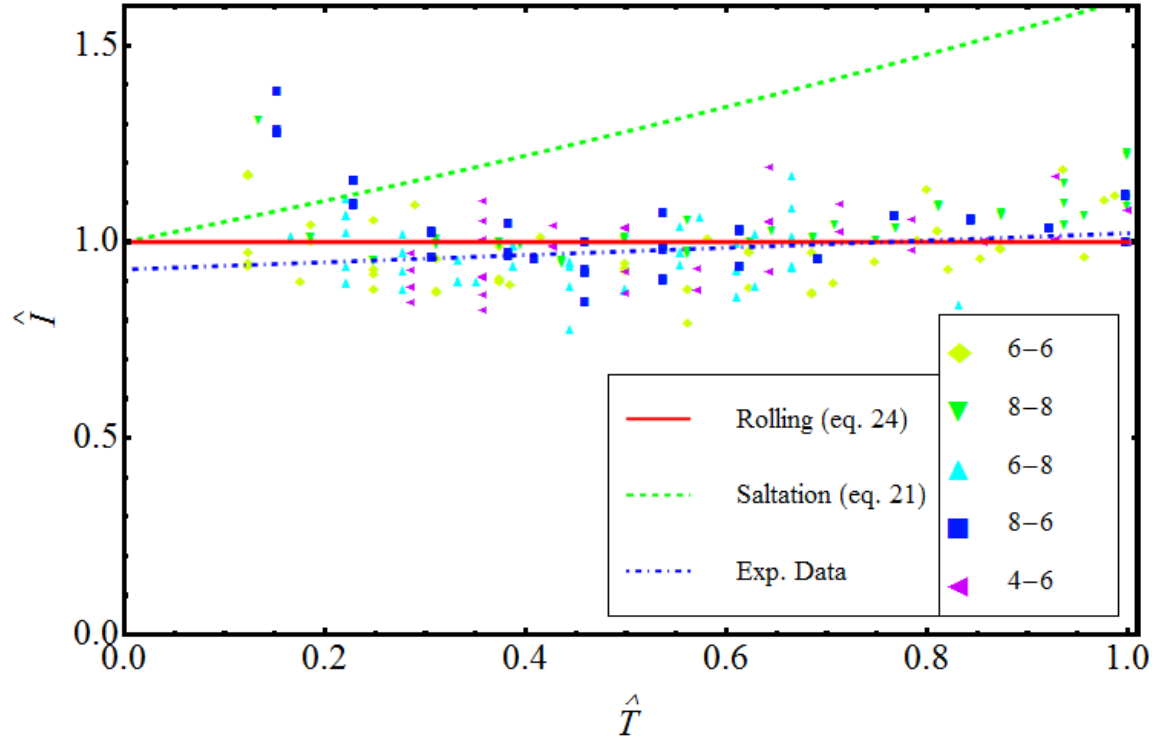


**Figure 14.** Critical normalized impulse for full dislodgement versus normalized duration: a) as predicted by saltation theory (dashed line), b) as predicted by rolling theory (continuous line) and c) as a linear best fit of the observed data from electromagnet experiments (dashed-dotted line).

### 5.3. Generalization of various degrees of movement

Consistent with lab and field observations the degree of movement of sediment grains depends on the intensity or strength of the flow. For flow conditions below threshold, the particle may vibrate or slightly hop within its pocket. For near threshold flow conditions these movements become stronger and at certain instances the critical level is reached or exceeded triggering a complete entrainment. Further increase of the flow intensity will result in more frequent and strong particle entrainments. Saltation or rolling impulse models can be utilized to describe this wide range of grain motions. For instance in accordance to equation (8), different saltation heights ( $\hat{z}$ ) are expected, depending on the value of the normalized force,  $\hat{F}_L$ , and duration,  $\hat{T}_{salt}$ , (or impulse  $\hat{I}_{salt}$ , considering Equation 20). Even though a definition of those phases of incipient motion is subjective, a classification may be attempted, in order of increasing  $\hat{z}$ , as follows (Figure 15):

$$\begin{aligned}
0 < \hat{z} < 0.3, \text{ vibration} \\
0.3 \leq \hat{z} < 1, \text{ hoping} \\
1 < \hat{z} \leq 2, \text{ weak entrainment} \\
2 < \hat{z}, \text{ strong entrainment}
\end{aligned} \tag{24}$$

Vibration is a term conventionally used to characterize weak movement that is difficult to be discerned with bare eyes, while hoping can be used to describe short hops which however do not result in full displacement. Similarly, higher than critical saltation impulses  $\hat{I}_{salt}$ , result to relatively greater values of  $\hat{z}$  ( $>1$ ). This observation is useful to extend the concept to entrainment of non-uniform bed material. If for instance the particles surrounding the mobile grain have  $n_s$  times its diameter ( $D_b=2n_sR_m$ ), complete entrainment by saltation requires that the saltation height will exceed  $D_b$  or  $\hat{z} > n_s$ .

Using the same rationale different impulse (or  $\hat{F}_D$ ,  $\hat{T}_{roll}$ ) levels, can be used to characterize different degrees of angular motion for the case of rolling. Equation (16) can be modified to describe partial grain motions:

$$T_{roll} = \sqrt{\frac{L_{arm} m_{mod}}{-\Sigma F_{\xi}}} \operatorname{arc\,sinh} \left( \sqrt{2W} \rho_{\theta} \lambda \frac{\sqrt{-\Sigma F_{\xi}}}{\Sigma F_{\theta}} \right) \tag{25}$$

with  $\lambda$ , the ratio of partial angular dislodgement to the angular displacement for complete entrainment:

$$\lambda = \frac{\sin(\theta_{fin}) - \sin(\theta_0)}{\sin(\frac{\pi}{2}) - \sin(\theta_0)} \tag{26}$$

where  $\theta_{fin} < \pi/2$ , signifies the final angular position of the particle. As in the case of saltation, curves predicting various levels of angular motion,  $\lambda$ , are illustrated in Figure 16, for run 8-8. The effect (angular displacement) of the offered impulses is recorded with a high speed camera, and the data points are classified with respect to  $\lambda$ , as shown in Figure 16. In general a satisfactory agreement is seen from both observed and predicted results.

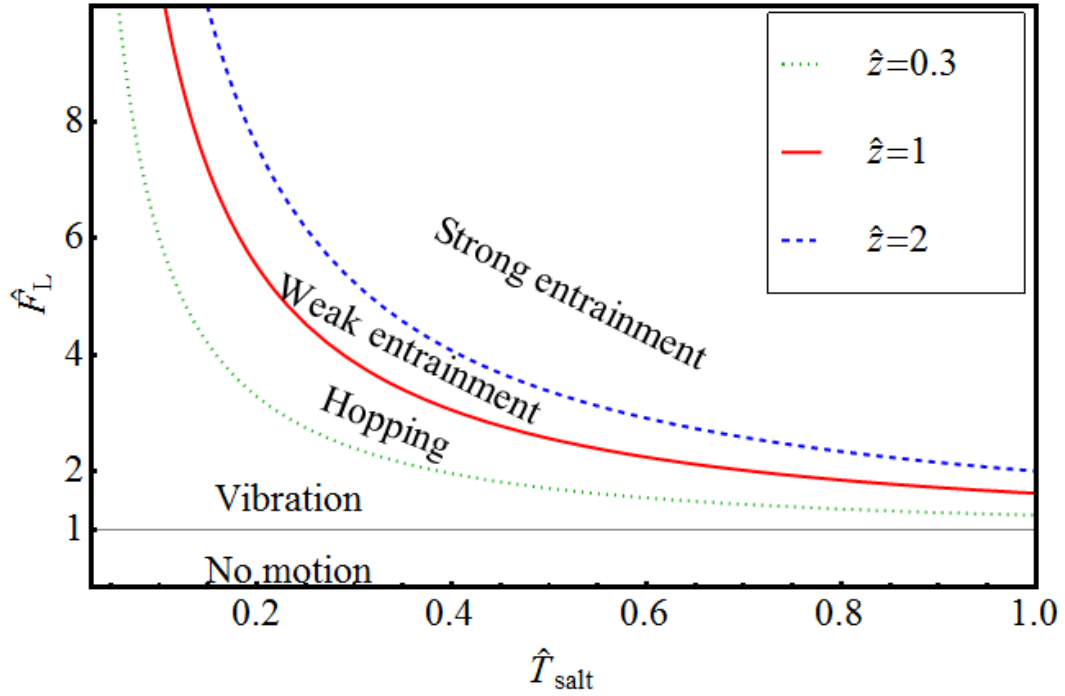


**Figure 15.** Generalized threshold curves for saltation, providing different levels of normalized linear grain displacement,  $\hat{z}$ , as a function of the offered impulse characteristics (normalized magnitude,  $\hat{F}_L$ , and duration,  $\hat{T}_{salt}$ ).

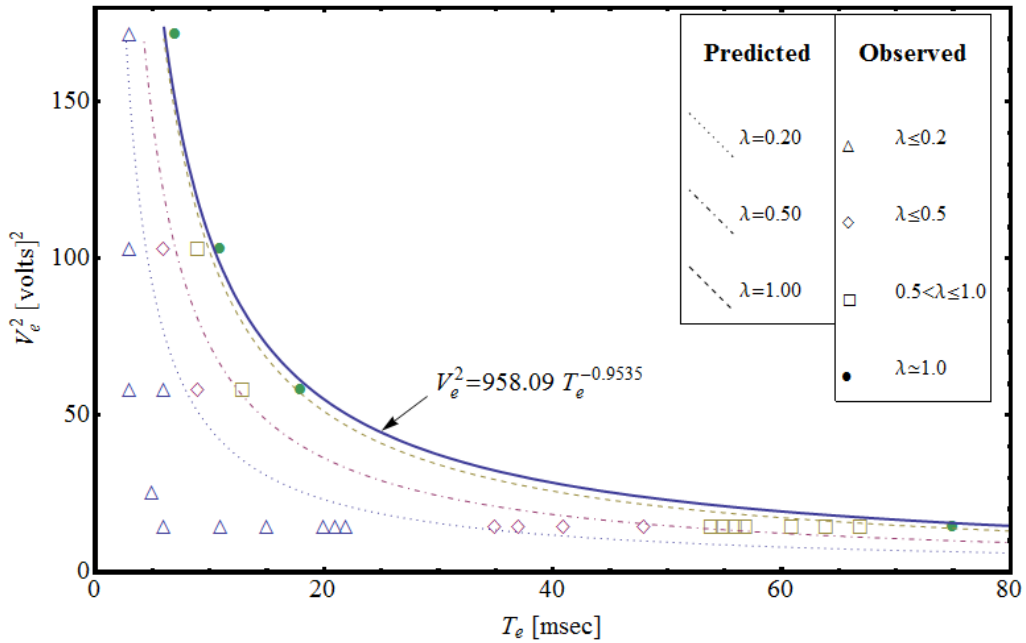


**Figure 16.** Generalized threshold curves for rolling, providing different levels of normalized angular grain displacement,  $\lambda$ , as a function of the offered impulse characteristics (normalized magnitude, parameterized by  $V_e^2$ , and duration,  $\hat{T}_e$ ).

In this manner, knowledge of the impulse content through the probability density function (PDF) of flow impulses or equivalently the joint PDF of the magnitude and duration of impulses, for a particular flow, will allow the estimation of the probability that a certain fraction of bed material will respond according to a defined mobility level ( $\hat{z}$ ).

#### **5.4. Generalization to other grain arrangements**

In the previous sections, the analytical formulation of the problem focused on the two limiting cases, completely exposed and fully hidden spherical grain, as shown in Figure 2. In both cases the mobile particle was resting on grains of the same size and shape. These two particle configurations were utilized because they are simpler to investigate the mechanics of particle entrainment, dominated by lift in the former case and drag in the latter. However, the electromagnet experiments further validated the impulse concept for particles of the same shape, spherical, but different size for the case representing drag-induced initiation of motion. The degree of particle exposure in these experiments ranged from 65% (for the 4mm on 6mm case) to 89% (for the 8mm on 6 mm case).

For a particle arrangement more representative of field conditions, the grain shape, size, exposure and packing density will vary significantly for both the mobile and its neighboring particles [e.g. *Kirchner et al.*, 1990]. In the more general case, particle dislodgement will be due to the combined effect of drag and lift forces. Because impulse is the relevant criterion for describing particle dislodgement for each of the two limiting cases, it is expected to remain valid for the more general case of variable local grain topography [*Diplas et al.*, 2008]. Nevertheless, additional work will be necessary to demonstrate this result conclusively.

#### **6. Conclusions**

A set of flume experiments have been performed wherein the magnitude and duration of hydrodynamic forcing events along with the incipient entrainment of coarse grains were recorded. These experiments demonstrated that peak values in the instantaneous drag force record are necessary but not sufficient to trigger particle entrainment. It was observed that the

duration of the peak values was a factor in particle entrainment. It is therefore conjectured that impulse rather than just the magnitude of hydrodynamic forcing, is relevant to the description of the incipient motion phenomenon.

This hypothesis was investigated by considering separately the analytical formulation of particle dislodgement for the two basic modes of entrainment, namely saltation and rolling. The problem was made more tractable by simplifying the grain parameters and micro-topography, assuming spherical, imbedded or fully exposed particles. For both modes of entrainment the significance of force duration has been demonstrated and the relevance of impulse has been established.

Novel experiments that employ an electromagnet to control the magnitude and duration of the mobilizing force are in agreement with the theoretical results for different degrees of particle exposure. The relevance of the impulse criterion is demonstrated further by applying this concept for the case of different levels of grain mobility.

The impulse criterion is physically sound since it appropriately accounts for the rapid fluctuations of the turbulent forces acting on grains. The developed equations can be used to characterize the mode of incipient motion of grains as well as signify the instances or frequency of their entrainment subject to applied hydrodynamic forces.

## Appendix

### Linearization of Equation (10a)

For short impulse durations the angular displacement,  $\Delta\theta$ , at any time instance  $t < T_{roll}$  is small.

Thus considering  $\theta = \theta_0 + \Delta\theta$  and assuming  $\Delta\theta \ll \theta_0$ :

$$\cos \theta = \cos(\theta_0 + \Delta\theta) = \cos \theta_0 \cos \Delta\theta - \sin \theta_0 \sin \Delta\theta = \cos \theta_0 - \Delta\theta \sin \theta_0 \quad (\text{A1.a})$$

$$\sin \theta = \sin(\theta_0 + \Delta\theta) = \sin \theta_0 \cos \Delta\theta + \cos \theta_0 \sin \Delta\theta = \sin \theta_0 + \Delta\theta \cos \theta_0 \quad (\text{A1.b})$$

Equation (10a), for  $t < T_{roll}$ , becomes:

$$L_{arm} \left( \frac{7}{5} \rho_s + \rho_f C_m \right) V \frac{d^2 \theta}{dt^2} = F_D \sin(\theta - \alpha) + (F_L + B_f) \cos(\theta - \alpha) - W \cos \theta \quad (\text{A2})$$

Considering equations (A1.a and A1.b), the linearized version of equation (A2) is::

$$L_{arm} \left( \frac{7}{5} \rho_s + \rho_f C_m \right) V \frac{d^2 \theta}{dt^2} = [F_D \sin(\theta_0 - \alpha) + (F_L + B_f) \cos(\theta_0 - \alpha) - W \cos \theta_0] - \Delta \theta [-F_D \cos(\theta_0 - \alpha) + (F_L + B_f) \sin(\theta_0 - \alpha) - W \cos \theta_0] \quad (A3)$$

Collecting the terms in equation (A3) and using equations (11a and 11b), the linearized form of equation of motion for rolling (equation 12) is obtained.

### Derivation of Equation (16)

Multiplication of all parts of equation (15) with the angular velocity,  $\Delta \theta'$  results in:

$$L_{arm} m_{mod} \Delta \theta' \frac{d^2 \Delta \theta}{dt^2} = \Delta \theta' [B_f \cos(\theta_0 + \Delta \theta - \alpha) - W \cos(\theta_0 + \Delta \theta)] \quad (A4)$$

Integrating equation (A4) from  $t = T_{roll}$  to  $t = t_{O'A'}$ , yields:

$$L_{arm} m_{mod} \frac{1}{2} (\Delta \theta_{T_{roll}}^2 - \Delta \theta_{t_{O'A'}}^2) = [W \cos(\theta_0 + \Delta \theta_{T_{roll}}) \sin \alpha + B_f \sin(\theta_0 + \Delta \theta_{T_{roll}}) - W \cos \alpha \sin(\theta_0 + \Delta \theta_{T_{roll}})] - [W \cos \theta_{t_{O'A'}} \sin \alpha + B_f \sin \theta_{t_{O'A'}} - W \cos \alpha \sin \theta_{t_{O'A'}}] \quad (A5)$$

Considering  $\theta(t = t_{O'A'}) = \pi/2$ ,  $\Delta \theta'(t = t_{O'A'}) = 0$  and  $\Delta \theta \ll \theta_0$ , equation (A5) is simplified as follows:

$$L_{arm} m_{mod} \frac{1}{2} \Delta \theta_{T_{roll}}^2 = [W \cos \theta_0 \sin \alpha + B_f \sin \theta_0 - W \cos \alpha \sin \theta_0] - [B_f - W \cos \alpha] \quad (A6)$$

Substituting in equation (A6) the angular velocity at time instance  $t = T_{roll}$  (from equation (14)), and solving for impulse duration,  $T_{roll}$ , the equation for entrainment of a particle by rolling is obtained (equation (16)).

### Notation

$A_e$	Area of the face of the electromagnet [ $L^2$ ]
$B_f$	Buoyancy force [ $M L t^{-2}$ ]
$c_i$	Coefficient of electromagnetic force (dimensionless)
$C_m$	Added mass coefficient (dimensionless)
$D_b$	Diameter of base particles [ $L$ ]
$D_{50}$	Bed material median size [ $L$ ]
$F$	Net hydrodynamic force acting on solid particle [ $M L t^{-2}$ ]
$F_D$	Hydrodynamic drag force [ $M L t^{-2}$ ]
$\hat{F}_D$	Normalized hydrodynamic drag force (dimensionless)
$F_e$	Electromagnetic force [ $M L t^{-2}$ ]

$F_L$	Hydrodynamic lift force [M L t <sup>-2</sup> ]
$\hat{F}_L$	Normalized hydrodynamic lift force (dimensionless)
$F_{Nz}$	Reaction force [M L t <sup>-2</sup> ]
$F_R$	Sum of resisting forces in z direction [M L t <sup>-2</sup> ]
$h_e$	Distance of the mobile particle from the face of the electromagnet [L]
$h_{max}$	Maximum elevation of particle [L]
$H$	Heaviside function
$I_i$	Impulse due to hydrodynamic force (generic definition) [M L t <sup>-1</sup> ]
$\hat{I}_{roll}$	Normalized impulse for rolling (dimensionless)
$\hat{I}_{salt}$	Normalized impulse for saltation (dimensionless)
$\hat{I}_e$	Normalized electromagnetic impulse (dimensionless)
$q$	Regression coefficient (dimensionless)
$L_{arm}$	Lever arm [L]
$m_{mod}$	Modified mass of particle (including added mass effects) [M]
$n_s$	Coefficient of relative magnitude of base to mobile particle size (dimensionless)
$N_e$	Number of turns of the wire in the coil of the electromagnet (dimensionless)
$k$	Regression coefficient (dimensionless)
$r_e$	Resistance of the electromagnet [ $\Omega$ ]
$R^2$	Coefficient of determination (dimensionless)
$R_b$	Radius of base particle [L]
$R_m$	Radius of the mobile particle [L]
$R^*$	Particle Reynolds number (dimensionless)
$t$	Time [t]
$t_{ff}$	Free fall time [t]
$t_{salt}$	Duration of upward movement of saltating particle [t]
$\hat{t}_{salt}$	Normalized duration of upward movement of saltating particle (dimensionless)
$T_e$	Duration of electromagnetic force [t]
$T_i$	Duration of hydrodynamic force [t]
$T_{roll}$	Duration of drag force [t]
$\hat{T}_{roll}$	Normalized duration of drag force (dimensionless)
$T_{salt}$	Duration of lift force [t]
$\hat{T}_{salt}$	Normalized duration of lift force (dimensionless)
$u^*$	Shear velocity [L t <sup>-1</sup> ]
$V$	Solid particle's volume [L <sup>3</sup> ]
$V_e$	Voltage across the electromagnet [V]
$V_{min}$	Minimum required voltage for particle removal [V]
$\hat{V}$	Normalized voltage across the electromagnet (dimensionless)
$W$	Solid particle's weight [M L t <sup>-2</sup> ]
$z$	Cartesian coordinate (normal to the bed) [L]
$z_{max}$	Maximum saltation height [L]
$\hat{z}$	Normalized saltation height (dimensionless)
$\alpha$	Bed slope [ $^\circ$ ]
$\Delta\theta$	Angular displacement [ $^\circ$ ]

$\theta, \zeta$	Polar coordinates [ $^{\circ}$ ]
$\theta_{fin}$	Final angular position of the particle (for incomplete motion) [ $^{\circ}$ ]
$\theta_0$	Pivoting angle [ $^{\circ}$ ]
$\lambda$	Ratio of partial to complete angular displacement (dimensionless)
$\nu$	Kinematic viscosity of water [ $M^2 t^{-1}$ ]
$\mu_e$	Magnetic permeability of the medium (here air) [ $M L t^{-2} A^{-2}$ ]
$\rho_f$	Density of fluid [ $M L^{-3}$ ]
$\rho_s$	Density of solid particles [ $M L^{-3}$ ]
$\rho_{\theta}$	Coefficient including effects of local geometry and relative density of solid-fluid phases (dimensionless)
$\Sigma F_{\zeta}$	Sum of forces in the radial direction [ $M L t^{-2}$ ]
$\Sigma \hat{F}_{\zeta}$	Normalized sum of forces in the radial direction (dimensionless)
$\Sigma F_{\theta}$	Sum of forces in the tangential direction [ $M L t^{-2}$ ]
$\Sigma \hat{F}_{\theta}$	Normalized sum of forces in the tangential direction (dimensionless)
$\tau^*$	Shields stress (dimensionless)

## Acknowledgement

The support of the National Science Foundation (EAR-0439663 and EAR-0738759) and Army Research Office is gratefully acknowledged. The presentation as well as the substance of this paper has been improved through the comments and insights of three reviewers and the associate editor.

## References

- Abbott, J. E., and J. R. D. Francis (1977), Saltation and suspension trajectories of solid grains in a water stream, *Philos. Trans. R. Soc. London A*, 284, 225-254.
- Apperley, L. W. and A.J. Raudkivi, (1989), The entrainment of sediments by the turbulent flow of water, *Hydrobiologia*, 176/177, 39-49.
- Auton, T. R., J. C. R. Hunt, and M. Prudhomme (1988), The force exerted on a body in inviscid unsteady non-uniform rotational flow, *J. Fluid Mech.*, 197, 241-257.
- Bagnold, R. A. (1973), The nature of saltation and of ‘bed-load’ transport in water, *Philos. Trans. R. Soc. London, A*, 332(1591), 473– 504, doi: 10.1098/rspa.1973.0038.

- Benedict, B. A., and B. A. Christensen (1972), Hydrodynamic lift on a stream bed, in *Sedimentation, Symp. to Honor Prof. H. A. Einstein*, edited by H. W. Shen, pp. 5.1-5.17, Water Resources Publication, Littleton, Colorado.
- Bettess, R. (1984), Initiation of sediment transport in gravel streams, *Proceedings - Institution of civil Engineers*, 77, 79-88.
- Buffington, J. M., and D. R. Montgomery (1997), A systematic analysis of eight decades of incipient motion studies, with special reference to gravel-bedded rivers, *Water Resour. Res.*, 33(8), 1993-2029.
- Cheng, E., and C. Clyde (1972), Instantaneous hydrodynamic lift and drag forces on large roughness elements in turbulent open channel flow, in *Sedimentation, Symp. to Honor Professor Hans A. Einstein*, edited by H. W. Shen, pp. 3.1-3.20, Water Resources Publication, Littleton, Colorado.
- Cheng, N.-S., and Y. M. Chiew (1998), Pickup Probability for Sediment Entrainment, *J. Hydraul. Eng.*, 124(2), 232-235.
- Chepil, W. (1958), The use of evenly spaced hemispheres to evaluate aerodynamic forces on soil surfaces. *Eos Trans. AGU*, 39, 397- 403.
- Chin, C. O., and Y. M. Chiew (1993), Effect of Bed Surface Structure on Spherical Particle Stability, *J. Waterway, Port, Coastal, Ocean Eng.*, 119(3), 231-242.
- Christensen, B. A. (1995). Incipient sediment motion on non horizontal slopes. Discussion. *J. Hydraul. Res.*, 33(5), 725-728.
- Coleman, S.E. and V. Nikora (2008), A unifying framework for particle entrainment. *Water Resour. Res.* 44, W04415, doi:10.1029/2007WR006363.
- Coleman, N. (1967), A theoretical and experimental study of drag and lift forces acting on a sphere resting on a hypothetical streambed, in *Proc.12th Congress Intern. Assoc. Hydr. Res.*, pp. 185-197, Fort Collins, Colorado.
- Dancey, C. L., P. Diplas, A. Papanicolaou, and M. Bala (2002), Probability of Individual Grain Movement and Threshold Condition, *J. Hydraul. Eng.*, 128(12), 1069-1175.
- Dey, S., and K. Debnath (2000), Influence of streamwise bed slope on sediment threshold under stream flow, *J. Irrigat. Drain. Eng.*, 126(4), 255-263.

- Diplas, P., C.L. Dancey, A. O. Celik, M. Valyrakis, K. Greer, and T. Akar (2008), The Role of Impulse on the Initiation of Particle Movement Under Turbulent Flow Conditions, *Science*, 322(5902), 717-720, doi:10.1126/science.1158954.
- Einstein, H. A., and E.-S. A. El-Samni (1949), Hydrodynamic forces on a rough wall, *Rev. Mod. Phys.*, 21(3), 520-527.
- Fenton, J. D., and J. E. Abbott (1977), Initial movement of grains on a stream bed: The effect of relative protrusion, *Proc. R. Soc. London, A*, 352(1671), 523–537.
- Garcia, C., H. Cohen, I. Reid, A. Rovira, X. Úbeda, and J. B. Laronne (2007), Processes of initiation of motion leading to bedload transport in gravel-bed rivers, *Geophys. Res. Lett.*, 34, L06403, doi:10.1029/2006GL028865.
- Gimenez-Curto L. A. and M.A. Corniero (2009), Entrainment threshold of cohesionless sediment grains under steady flow of air and water, *Sedimentology* 56, 493-509.
- Grass, A. J. (1970), Initial Instability of Fine Bed Sand, *J. Hydraul. Eng.*, 96(3), 619-632.
- Grass, A.J. (1971), Structural features of turbulent flow over smooth and rough surfaces, *J. Fluid Mech.*, 50(2): 233-255.
- Grass, A.J. (1983), The influence of boundary layer turbulence on the mechanics of sediment transport, in *Proc. Euromech 156: Mechanics of Sediment Transport*, edited by B.M. Sumer and A. Müller, pp. 3-17, Balkema, Rotterdam, The Netherlands.
- Gregoretti, C. (2001), Influence of streamwise bed slope on sediment threshold under stream flow Discussion, *J. Irrig. Drain. Eng.*, 127(6), 395-396.
- Gregoretti, C. (2008), Inception sediment transport relationship at high slopes, *J. Hydraul. Eng.*, 11(134), 1620-1629.
- Hofland, B., R. Booij, and J. Battjes (2005), Measurement of fluctuating pressures on coarse bed material, *J. Hydraul. Engrg.*, 131(9), 770–781.
- Hofland, B., and J. Battjes (2006), Probability Density Function of Instantaneous Drag Forces and Shear Stresses on a Bed, *J. Hydraul. Eng.*, 132(11), 1169–1175.
- James, C. S. (1990), Prediction of entrainment conditions for nonuniform, noncohesive sediments, *J. Hydraul. Res.*, 28(1), 25-41.
- Jeffreys, H. (1929), On the transportation of sediment by streams, *Proc. Cambridge Philos. Soc.*, 25, 272-276.
- Kirchner, J. W., Dietrich, W. E., Iseya, F., and Ikeda, H. (1990), The variability

- of critical shear stress, friction angle, and grain protrusion in water-worked sediments, *Sedimentology* 37(4), 647–672.
- Komar, P. D., and Li, Z. (1988), Application of grain-pivoting and sliding analyses to selective entrainment of gravel and to flow-competence evaluations, *Sedimentology*, 35, 681-695.
- Lam Lau, Y., and Engel, P. (1999), Inception of sediment transport on steep slopes." *J. Hydraul. Eng.*, 125(5), 544-547.
- Lavelle, J. W., and H. O. Mofjeld (1897), Do critical stresses for incipient motion and erosion really exist?, *J. Hydraul. Eng.* 113(3), 370-385.
- Leighly, J. B. (1934), Turbulence and the transportation of rock debris by streams, *The Geographical Rev.*, 24(3), 453-464.
- Ling, C.-H. (1995), Criteria for incipient motion of spherical sediment particles, *J. Hydraul. Eng.*, 121(6), 472-478.
- McEwan, I., and J. Heald (2001), Discrete particle modeling of entrainment from flat uniformly sized sediment beds, *J. Hydr. Eng.* 127(7), 588-597.
- McEwan, I., M. Sorensen, J. Heald, S. Tait, G. Cunningham, D. Goring, and B. Willets (2004), Probabilistic modeling of bed-load composition, *J. Hydraul. Eng.*, 130(2): 129-139.
- Mollinger, A. M., and F. T. M. Nieuwstadt (1996), Measurement of the lift force on a particle fixed to the wall in the viscous sublayer of a fully developed turbulent boundary layer, *J. Fluid Mech.*, 316, 285-306.
- Nelson, J. M., S. R. McLean, and S. R. Wolfe (1993), Mean flow and turbulence fields over two-dimensional bed forms, *Water Resour. Res.*, 29(12), 3935-3953.
- Nelson, J., R. L. Shreve, S. R. McLean, and T. G. Drake (1995), Role of near-bed turbulence structure in bed load transport and bed form mechanics, *Water Resour. Res.*, 31(8), 2071-2086.
- Nelson, J.M., M. W. Schmeeckle, and R. L. Shreve (2001), Turbulence and Particle Entrainment, in *Gravel-bed Rivers V*, edited by M. P. Mosley, pp. 221-248, NZ Hydrological Society, Wellington.
- Nino, Y., and M. Garcia (1994), Gravel saltation: 1. Experiments, *Water Resour. Res.*, 30(6), 1907–1914.

- Nino, Y., and M. H. Garcia (1996), Experiments on particle—turbulence interactions in the near-wall region of an open channel flow: implications for sediment transport, *J. Fluid Mech.*, 326, 285-319.
- Nino, Y., F. Lopez, and M. Garcia (2003), Threshold for particle entrainment into suspension, *Sedimentology*, 50, 247-263.
- Paiement-Paradis, G., T. Buffin-Belanger, and A. G. Roy (2003), Scaling for large turbulent flow structures in gravel-bed rivers, *Geophysical Res. Lett.*, 30(14), 1-4.
- Paintal, A. S. (1971a), Concept of Critical Shear Stress in Loose Boundary Open Channels, *J. Hydraul. Res.*, 9(1), 91-113.
- Paintal, A. S. (1971b), A stochastic model of bed load transport, *J. Hydraul. Res.*, 9(4), 527–554.
- Papanicolaou, A., P. Diplas, C. L. Dancey, and M. Balakrishnan (2001), Surface roughness effects in near-bed turbulence: Implications to sediment entrainment, *J. Eng. Mech.*, 127(3), 211-218.
- Papanicolaou, A. N., P. Diplas, N. Evaggelopoulos, and S. Fotopoulos (2002), Stochastic Incipient Motion Criterion for Spheres under Various Bed Packing Conditions, *J. Hydraul. Eng.*, 128(4), 369-380.
- Paphitis, D. (2001), Sediment movement under unidirectional flows: an assessment of empirical threshold curves, *Coastal Eng.*, 43, 227-245.
- Paphitis, D., M. B. Collins, L. A. Nash, and S. Wallbridge (2002), Settling velocities and entrainment thresholds of biogenic sands (shell fragments) under unidirectional flows, *Sedimentology*, 49, 211-225.
- Pigozzi D., C. Gregoretti and M. Pontin (2007), Limit rolling entrainment condition of sediment bed particles at high slopes, in *Proc. XXXII IAHR Congress*, Venice, Italy, 1-6 July.
- Raudkivi, A.J. (1966), Bed forms in alluvial channels, *J. Fluid Mech.*, 26(3), 507-514.
- Recking, A. (2009), Theoretical development on the effects of changing flow hydraulics on incipient bed load motion. *Water Resour. Res.* 45, W04401, doi:10.1029/2008WR006826.
- Schmeeckle, M. W., and J. M. Nelson (2003), Direct numerical simulation of bedload transport using a local, dynamic boundary condition, *Sedimentology*, 50(2), 279-301.
- Schmeeckle, M. W., J. M. Nelson, and R. L. Shreve (2007), Forces on stationary particles in near-bed turbulent flows, *J. Geophys. Res.*, 112, F02003, doi:10.1029/2006JF000536.

- Sechet, P., and B. Le Guennec (1999), Bursting phenomenon and incipient motion of solid particles in bed-load transport, *J. Hydraul. Res.*, 37(5), 683-696.
- Shields, A. (1936), Application of similarity principles and turbulence research to bed-load movement, Rep., No. 167, California Institute of Technology, Pasadena, CA.
- Shvidchenko, A. B., and G. Pender (2000), Flume study of the effect of relative depth on the incipient motion of coarse uniform sediments, *Water Resour. Res.*, 36(2), 619-628.
- Shvidchenko, A. B., and G. Pender (2001), Macroturbulent structure of open-channel flow over gravel beds, *Water Resour. Res.*, 37(3), 709-719.
- Smart, G. M., and H. M. Habersack (2007), Pressure fluctuations and gravel entrainment in rivers, *J. Hydraul. Res.*, 45(5), 661-673.
- Sumer, B. M., L. H. C. Chua, N.-S. Cheng, and J. Fredsoe (2003), Influence of Turbulence on Bed Load Sediment Transport, *J. Hydraul. Eng.*, 129(8), 585-596.
- Sutherland, A.J. (1967), Proposed mechanism for sediment entrainment by turbulent flows, *J. Geophysical Res.*, 72(24), 6183-6194.
- Valyrakis M., Diplas P., Celik A. O., Dancy C. L. (2008), Investigation of evolution of gravel river bed microforms using a simplified Discrete Particle Model, *Proc. River Flow 2008*, Ismir, Turkey, 03-05 September 2008.
- Varenus, Bemhardus (1664) *Geographia generalis, in qua affectiones generales telluris explicantur*, pp. 748, D. Amstelodami.
- Vollmer, S., and M. G. Kleinhans (2007), Predicting incipient motion, including the effect of turbulent pressure fluctuations in the bed, *Water Resour. Res.*, 43, W05410, doi:10.1029/2006WR004919.
- White, C. M. (1940), The Equilibrium of Grains on the Bed of a Stream, *Proc. R. Soc. London A*, 174(958), 322-338.
- Wu, F.-C., and Y.-C. Lin (2002), Pickup Probability of Sediment under Log-Normal Velocity Distribution, *J. Hydraul. Eng.*, 128(4), 438-442.
- Wu, F.-C., and Y.-J. Chou (2003), Rolling and Lifting Probabilities for Sediment Entrainment, *J. Hydraul. Eng.*, 129(2), 110-119.
- Wu, F.-C., and K.-H. Yang, (2004), Entrainment Probabilities of Mixed-Size Sediment Incorporating Near-Bed Coherent Flow Structures, *J. Hydraul. Eng.*, 130(12), 1187-1197.
- Zanke, U. C. E. (2003), On the influence of turbulence on the initiation of sediment motion, *Int. J. Sed. Res.*, 18(1), 17-31.

## **Chapter 3. Entrainment of coarse grains in turbulent flows: an Extreme Value Theory approach**

Manousos Valyrakis,<sup>1</sup> Panayiotis Diplas,<sup>1</sup> and Clint L. Dancey<sup>1</sup>

\*This chapter is a reprint of the article: Valyrakis, M., P. Diplas, and C. L. Dancey, (submitted), Entrainment of coarse grains in turbulent flows: an Extreme Value Theory approach, *Water Resour. Res.*, (submitted on 11-15-2010).

<sup>1</sup>Baker Environmental Hydraulics Laboratory, Department of Civil and Environmental Engineering, Virginia Polytechnic Institute and State University, Blacksburg, Virginia, USA.

### **Abstract**

The occurrence of sufficiently energetic flow events characterized by impulses of varying magnitude is treated as a point process. It is hypothesized that the rare but extreme magnitude impulses are responsible for the removal of coarse grains from the bed matrix. This conjecture is investigated utilizing distributions from Extreme Value Theory (EVT) and a series of incipient motion experiments. The application of extreme value distributions is demonstrated for both the entire sets of impulses as well as the maxima above a sufficiently high impulse quantile. In particular, the Frechet distribution is associated with a power law relationship between the frequency of occurrence and magnitude of impulses. It provides a good fit to the flow impulses, having comparable performance to other distributions. Next, a more accurate modeling of the tail

of the distribution of impulses is pursued, consistent with the observation that the majority of impulses above a critical value are directly linked to grain entrainments. The Peaks Over Threshold (POT) method is implemented to extract conditional impulses in excess of a sufficiently high impulse level. The Generalized Pareto Distribution is fitted to the excess impulses and parameters are estimated for various impulse thresholds and methods of estimation for all the experimental runs. Finally, the episodic character of individual grain mobilization is viewed as a survival process, interlinked to the extremal character of occurrence of impulses. The interarrival time of particle entrainment events is successfully modeled by the Weibull and exponential distributions, which belong to the family of extreme value distributions.

## 1. Introduction

One of the fundamental objectives in earth-surface dynamics and engineering is to obtain a better understanding of the underlying dynamics of the interaction of turbulent flows and the solid boundary that contains them, leading to transport of coarse particles in fluvial, coastal and aeolian environments. The precise identification of the critical flow conditions for the inception of sediment transport has many applications ranging from the protection of hydraulic structures against scour to the assessment and regulation of flow conditions downstream of reservoirs to ecologically friendly stream restoration designs.

The standard and widely employed method for the identification of incipient motion flow conditions is Shields' critical shear stress criterion. This is partly a reason why considerable effort has been spent to explain deviations from the *Shields* [1936] empirical diagram as well as to devise alternative plots for a variety of flow and sediment cases [*Miller et al.*, 1977; *Mantz*, 1977; *Yalin and Karahan*, 1979; *Bettess*, 1984; *Lavelle and Mofjeld*, 1987; *Buffington and Montgomery*, 1997; *Shividchenko and Pender*, 2000; *Paphitis*, 2001; *Paphitis et al.*, 2002]. Since then many researchers have adopted a deterministic perspective [*White*, 1940; *Coleman*, 1967; *Wilberg and Smith*, 1987; *Ling*, 1995; *Dey*, 1999; *Dey and Debnath*, 2000]. However, the comprehensive review of *Buffington and Montgomery*, [1997] shows a scatter of field and laboratory threshold of motion results in excess of an order of magnitude. This, in addition to the subjectivity inherent in precisely defining a threshold for mobilization of sediment grains [e.g. *Kramer*, 1935; *Papanicolaou et al.*, 2002], shows that a deterministic treatment of the turbulent

flow processes leading to particle entrainment, based on time and usually space averaged criteria, does not suffice to accurately describe the phenomenon.

In recognition of the variability of the hydrodynamic forces as well as of the local bed microtopography and grain heterogeneities, many researchers have supported a stochastic approach for the description of incipient movement [*Einstein and El-Samni*, 1949; *Paintal*, 1971; *Cheng and Chiew*, 1998; *Papanicolaou et al.*, 2002; *Wu and Yang*, 2004; *Hofland and Battjes*, 2006]. A statistical description of the critical flow conditions by means of probability distributions is necessary due to the wide temporal and spatial variability of the parameters that control it, such as relative grain exposure or protrusion [*Paintal*, 1971; *Fenton and Abbott*, 1977; *Hofland et al.*, 2005], friction angle [*Kirchner et al.*, 1990], local grain geometry [*Naden*, 1987] and bed surface packing conditions [*Dancey et al.*, 2002, *Papanicolaou et al.*, 2002]. Even for the simplified case of an individual particle resting on a fixed arrangement of similar grains, where the above parameters can be accurately specified, initiation of motion retains its probabilistic nature, due to the variability of the near bed turbulent stresses.

The relevance of high magnitude positive turbulence stress fluctuations in the vicinity of the boundary to the inception of particle entrainment was emphasized early in the literature [*Einstein and El Samni*, 1949; *Sutherland*, 1967; *Cheng and Clyde*, 1972]. Recent detailed experiments and analyses have provided strong evidence for the significance of peak hydrodynamic forces for grain entrainment particularly at low mobility flow conditions [*Hofland et al.*, 2005; *Schmeeckle et al.*, 2007; *Vollmer and Kleinhans*, 2007; *Gimenez-Curto and Corniero*, 2009]. However, *Diplas et al.* [2008] demonstrated via carefully performed experiments that a rather small portion of the peak values results in particle dislodgement, and instead proposed impulse, the product of force above a critical level and duration, as a more suitable criterion responsible for particle entrainment. *Valyrakis et al.* [2010] expanded and generalized the validity of the impulse criterion to a wide range of grain entrainment conditions by saltation and rolling. Analysis of experimental data indicates that turbulent force impulse values follow, to a good approximation, the log-normal probability density function [*Celik et al.*, 2010]. However their empirically derived critical impulse level, defined as the level above which the vast majority of impulses result in grain displacement, corresponds to the upper 3 to 7 percentile of the entire distribution of impulses, for which the performance of the log-normal distribution is observed to decrease.

Evidently of particular interest is the occurrence of relatively rare and extreme impulse events which are observed to dislodge a particle. In the following sections impulse theory is reviewed and the mobile particle flume experiments are described. The fundamental theorems and distributions of Extreme Value Theory (EVT) are employed to develop an appropriate probabilistic framework for the stochastic analysis of impulses. Here the impulse events extracted from a series of experiments are shown to closely follow the Frechet distribution, from the family of EVT distributions. This distribution is shown to be directly linked to a power law relation for the frequency and magnitude of occurrence of the impulses. The applicability of the Peaks Over Threshold method is demonstrated for extracting the conditional exceedances of impulse data. For a sufficiently high impulse level the Generalized Pareto Distributions (GPD) is fitted to the distribution of the excess impulses. Finally, the response of an individual particle under different flow conditions is analyzed stochastically by means of reliability theory. The Weibull and exponential distributions are utilized to model the time between consecutive particle entrainments.

### 1.1. Impulse theory

Impulse is one of the fundamental physical quantities used to describe transfer of momentum. *Bagnold* [1973] was among the first researchers who employed the concept of “mean tangential thrust” to define the mean flow conditions required to sustain suspension of solids in the water column. Incipient displacement of a particle by rolling has been traditionally treated using a moments or torques balance [*White*, 1940; *Coleman*, 1967; *Komar and Li*, 1988; *James* 1990; *Ling*, 1995], which also describes transfer of flow momentum to the particle. However, these static approaches refer to time averaged quantities, thus being unable to incorporate the fluctuating character of turbulence. Recently, *Diplas et al.* [2008], introduced impulse ( $I_i$ ) as the relevant criterion for the initiation of sediment motion. According to this concept, impulse is defined as the product of the hydrodynamic force ( $F(t)$ ), with the duration ( $T_i$ ) for which the critical resisting force ( $F_{cr}$ ) is exceeded (Figure 1):

$$I_i = \int_{t_i}^{t_i+T_i} F(t)dt, \text{ with } F(t) > F_{cr} \text{ for } t_i < t < t_i + T_i \quad (1)$$

The proposed criterion accounts for both duration as well as the magnitude of flow events, introducing a dynamical perspective for the incipient entrainment of coarse particles. *Valyrakis et al.* [2010] provided a theoretical framework for the incipient saltation and rolling of individual particles by impulses of varying magnitude and duration, validated by bench top mobile particle experiments in air. They derived iso-impulse curves corresponding to different particle responses ranging from incomplete movement (twitches) to energetic particle entrainment. In accordance to this theory, only impulses above a critical level ( $I_{cr}$ ), which is a function of particle properties and local pocket geometry, are capable for the complete removal of a particle out of its resting position.

An example illustrating the importance of duration in addition to the magnitude of a flow event is depicted in Figure 1 for the case of entrainment of a fully exposed grain by rolling (Figure 2). Two separate flow events with varying magnitude and duration and consequently different potential for momentum exchange impinge upon the particle under consideration. The instantaneous hydrodynamic force, parameterized with the square of the streamwise velocity, of the first flow event ( $i$ ), peaks higher than the second flow event ( $i+1$ ). However, the former is significantly more short-lived than the latter ( $T_{i+1} > T_i$ ). According to Equation (1), the integral of the hydrodynamic force over the duration of the flow event (highlighted regions in Figure 1) is greater for the later impulse ( $I_{i+1} > I_i$ ), leading to a more pronounced response of the particle [*Valyrakis et al.*, 2010]. If this impulse exceeds the critical impulse level ( $I_{i+1} > I_{cr}$ ), then the particle will be fully entrained (noted by the vertical dotted line). Thus, before the probabilistic framework of impulse and grain entrainment is attempted, the definition of  $u_{cr}$ , used in extracting impulse events, as well as the theoretical impulse level for complete entrainment,  $I_{cr}$ , has to be provided.

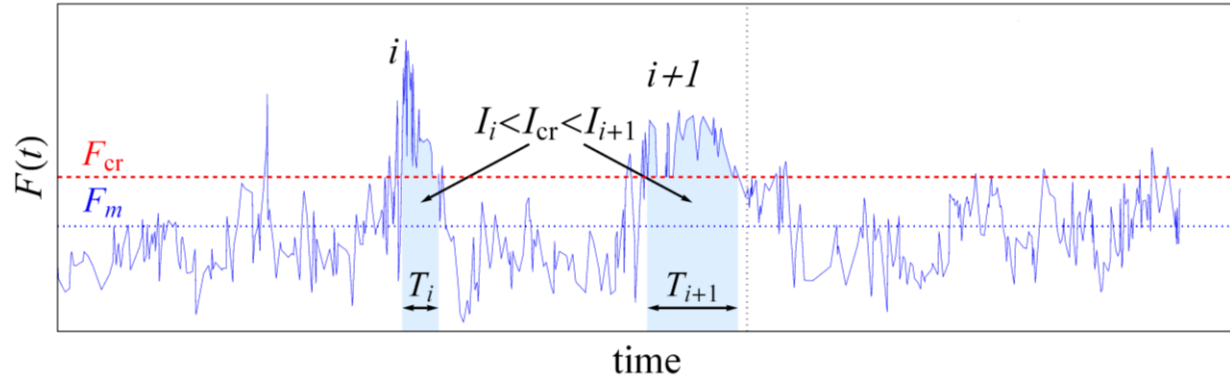


**Figure 1.** Sketch of the temporal history of hydrodynamic force ( $F(t)$ ) acting on a grain (the mean,  $F_m$ , and critical,  $F_{cr}$ , force levels are shown with the dotted and dashed horizontal lines). Impulse events (shaded areas) with magnitude above a critical level ( $I_{cr}$ ) result in complete particle entrainment (vertical dotted line).

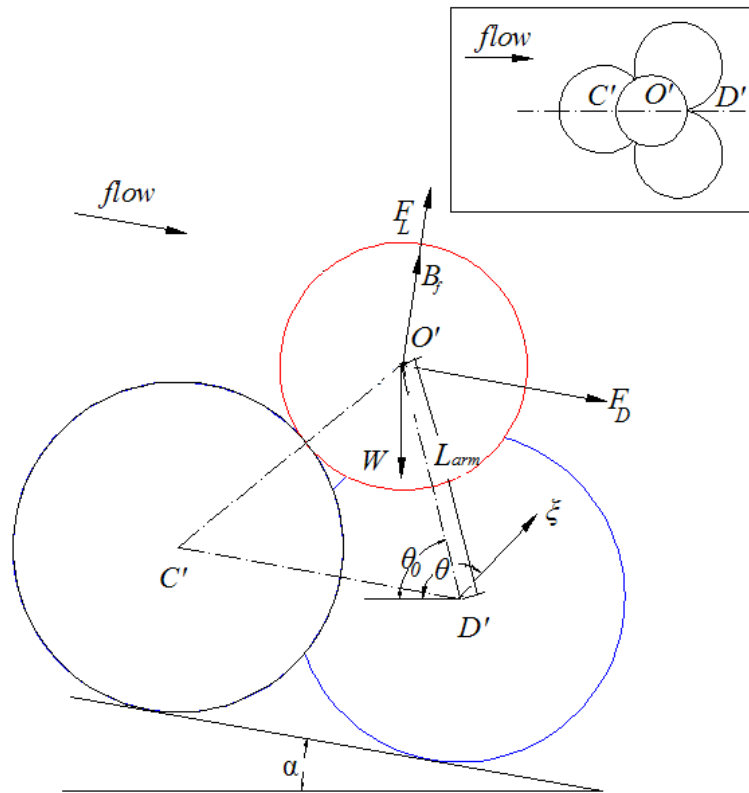


**Figure 2.** Definition sketch for the local arrangement and forces exerted on a fully exposed mobile particle Inset: Top view of particle configuration illustrating the cut plane (dot-dashed line).

## 1.2. Detection of impulse events and determination of $I_{cr}$

As opposed to the traditional incipient motion identification techniques, the impulse concept provides an event based approach, accounting for the dynamical characteristics of flow

turbulence. In order to examine the statistical properties and distributions of impulse events and their effects on entrainment of coarse grains, the method employed for their identification must first be described. In the following, the applicability of the scheme proposed to extract impulse events and implementation of the theoretically derived critical impulse level for incipient rolling, are critically reviewed.

Typically, a simplified tetrahedral arrangement of well packed spherical particles (Figure 2) is considered. Of interest is the response of the exposed particle which is a function of the hydrodynamic and resisting forces, assumed to act through its center of gravity. Loss of initial stability may occur as a result of an impulse event imparting sufficient momentum to the particle. Over the duration of this event the sum of drag ( $F_D$ ), lift ( $F_L$ ) and buoyancy ( $B_f$ ) force components along the direction of particle displacement, exceed the corresponding component of particle's weight ( $W$ ):

$$F_D \sin(\theta_0 - \alpha) + (F_L + B_f) \cos(\theta_0 - \alpha) \geq W \cos \theta_0 \quad (2)$$

where  $\theta_0$ , is the pivoting angle, formed between the horizontal and the lever arm ( $L_{arm}$ , in Figure 2) and  $\alpha$  is the bed slope [Valyrakis *et al.*, 2010]. Equation (2) describes the static equilibrium of forces or equivalently torques about the axis of rotation located at the origin of the polar coordinate system ( $D'$ , in Figure 2). Usually the effect of lift force for entrainment of completely exposed particles has been neglected without significant error [Schmeeckle *et al.*, 2003]. Inclusion of the hydrodynamic mass coefficient,  $f_h = [\rho_s - \rho_f (1 - C_m)] / (\rho_s - \rho_f)$ , with  $C_m$  the added mass coefficient (equal to 0.5, for water [Auton, 1988]),  $\rho_f$ , the density of fluid and  $\rho_s$ , the particle's density, increases the effect of the submerged particle's weight and equation (2) becomes:

$$F_D \sin(\theta_0 - \alpha) \geq f_h W_s \cos \theta_0 \quad (3)$$

where  $W_s = (\rho_s - \rho_f) V g$ , is the submerged particle's weight (assuming uniform flow),  $V$  is the particle's volume and  $g$  is the gravitational acceleration. Equations (2) and (3) may be solved for the critical drag force, considering the equal sign, to define the minimum level above which impulse events capable of dislodging a particle occur ( $F_{cr}$ , in Figure 1). For steady flows it is

customary to parameterize the instantaneous drag force with the square of the streamwise local velocity component upstream the exposed particle [e.g. *Hofland and Battjes, 2006*]. Then it is convenient to define the critical flow conditions directly in terms of the square of the local flow velocity:

$$u_{cr}^2 = \frac{2}{\rho_f C_D A} f_h W_s \frac{\cos \theta_0}{\sin(\theta_0 - \alpha)} \quad (4)$$

with  $A$  the particle's projected area perpendicular to the flow direction and  $C_D$  the drag coefficient assumed here to be equal to 0.9. It can be shown that equation (4) is similar to the stability criterion suggested by *Valyrakis et al. [2010]* (if  $f_h=1$ , by neglecting  $C_m$  at this stage) and identical to the critical level proposed by *Celik et al. [2010]* (after the appropriate algebraic/trigonometric manipulations are performed).

All of the detected flow impulses have the potential to initiate particle displacement. However, *Valyrakis et al. [2010]* predict complete removal of the exposed particle from its local configuration by rolling only when impulses exceed a theoretical critical impulse level, defined as the product of impulse duration ( $T_{roll}$ ) with the characteristic drag force ( $F_D$ ) assumed constant over the duration of the flow event:

$$I_{cr} = F_D T_{roll} = F_D \sqrt{\frac{L_{arm} \left( \frac{7}{5} \rho_s + \rho_f C_m \right) V}{F_D \cos(\theta_0 - \alpha) + W_s \sin \theta_0}} \operatorname{arc} \sinh \left( \frac{\sqrt{2W} \rho_\theta \sqrt{F_D \cos(\theta_0 - \alpha) + W_s \sin \theta_0}}{F_D \sin(\theta_0 - \alpha) - W_s \cos \theta_0} \right) \quad (5)$$

with  $\rho_\theta = (1 - \sin \theta_0) \left( \frac{\cos \theta_0}{1 - \sin \theta_0} \sin \alpha + \left( \cos \alpha - \frac{\rho_f}{\rho_s} \right) \right)$ , a coefficient incorporating the effects of initial geometrical arrangement and the relative density of fluid and solid grain. This theoretical level corresponds to impulse events extracted using equation (2), neglecting hydrodynamic lift.

Application of equation (5) allows for the *a priori* determination of physically based impulse levels ( $I_{cr}$ ), as opposed to their empirical estimation [*Celik et al., 2010*], which requires experimental identification of the impulses leading to entrainment. The two methods return equivalent results if the impulse values obtained by means of the former method are multiplied

with an appropriate impulse coefficient ( $C_I$ ). For the typically encountered cases of water flows transporting grains of specific density ranging from 2.1 to 2.6,  $f_h$  is close to 1.4 and  $C_I$  is determined to have a value of approximately 0.5 (by matching the theoretical and experimentally defined critical impulse levels).

Even though for an individual particle and local bed surface arrangement, the critical conditions for entrainment can be deterministically defined, the randomness of turbulent flow forcing renders a statistical description of the critical flow conditions more meaningful. Development of a complete and reliable probabilistic theory for inception of grain entrainment requires consideration of the impulse theory together with appropriate statistical distributions which account for the intermittent character of the modeled phenomenon. In the following section a stochastic framework for the accurate identification of the probability of entrainment of coarse grains for low mobility flow conditions is considered.

## 2. Stochastic modeling of Impulses

Many researchers have recently implemented and stressed the need for a stochastic approach to the initiation of sediment entrainment due to the action of near bed turbulence [e.g. *Dancey et al.*, 2002; *Papanicolaou et al.*, 2002]. Central to such models is the assumption that the episodic removal of an individual particle from the bed surface is strongly linked to the occurrence of turbulent stresses exceeding a critical level (e.g. Figure 3a). Here, contrary to the past stochastic approaches, turbulence is treated as a discrete point process, where separate flow structures of varying magnitude and duration, are modeled as impulse events ( $I_i$ ) occurring at random instances in time (Figure 3b). Similarly the sequence of conditional impulse exceedances ( $\xi_i = I_i - I_{thr}$ ) above a certain threshold ( $I_{thr}$ ), describes the point process of peak impulses. Here  $I_{thr}$  (not to be confused with  $I_{cr}$ , which depends on the grain and local micro-topography parameters), refers to the impulse level above which the tail of the distribution of impulses is defined.

The probability of particle entrainment,  $P$ , may be approximated by the probability of occurrence of impulses in excess of the theoretically defined (e.g. equation (5)) critical level ( $P_E = P(I_i > I_{cr})$ ). This concept is shown in Figure 4, where the very infrequent occurrence of such events, especially near threshold conditions, is evident. Since of interest are largely the extreme values of the distribution, its tail (region  $I_i > I_{thr}$ ) may be modeled separately. Then the probability

of particle entrainment may be found from the conditional probability that the critical impulse level is surpassed,  $P((\zeta_i > I_{cr} - I_{thr}) | I_i > I_{thr})$ . Thus, it is important to find statistical distributions that accurately model the magnitude and extremal character of impulses and their conditional exceedances, for low mobility flow conditions. For this purpose distributions from Extreme Value Theory (EVT) are considered to provide an appropriate statistical tool.

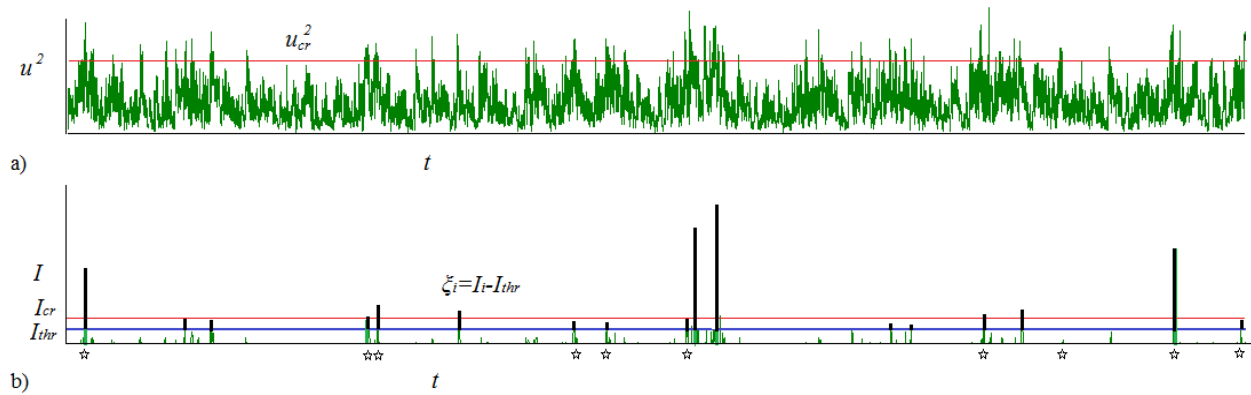


**Figure 3.** Representation of hydrodynamic forcing history on a coarse particle: a) as a continuous time series of the drag force,  $F_D \sim u^2$  and b) as a discrete point process of corresponding impulse events and impulse exceedances ( $\zeta_i$ , denoted by the thick vertical lines above  $I_{thr}$ ) randomly occurring in time. The threshold impulse level  $I_{thr} (< I_{cr})$  and impulse events associated with particle displacement (stars) are also shown.

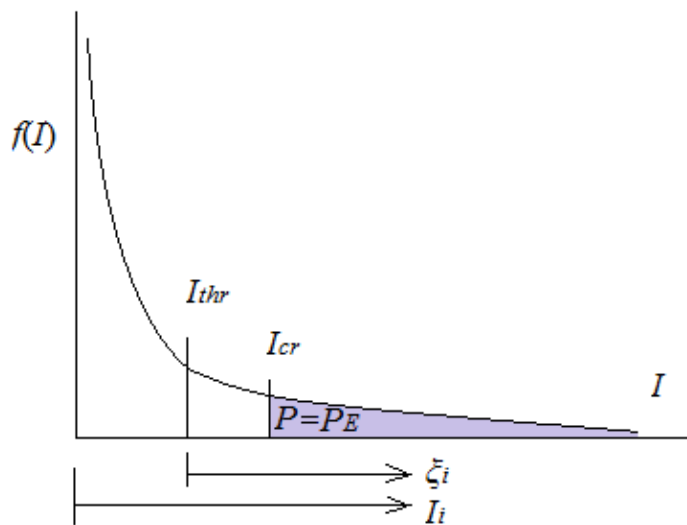


**Figure 4.** The probability of particle entrainment ( $P_E$ ) is approximated by the probability of occurrence of extreme impulse events above critical, defined from the probability distribution of impulses, ( $P(I_i > I_{cr})$ ), or from the conditional probability of impulse exceedances ( $P(\xi_i > I_{cr} - I_{thr} | I_{cr} > I_{thr})$ ), using equation (19)).

## 2.1. Extreme Value Modeling

Mobile particle flume experiments discussed in [Diplas *et al.*, 2008] revealed the significance of high magnitude impulses for grain entrainment. In their work it was first observed that only a few of the most extreme impulses, those that exceed an empirically defined critical level, result in particle entrainment. These peak impulses represented a small portion, about 4.4% of the entire sample and belong to the upper tail of the distribution of impulses. Celik *et al.* [2010] proposed that impulses follow the log-normal distribution. A good fit is visually observed for the core of the distribution, in the 1 to 2.5 range of normalized impulses ( $\hat{I} = I/I_{mean}$ , with  $I_{mean}$  the sample's mean, viz. Fig. 9 in [Celik *et al.*, 2010]). However, particularly for  $\hat{I} > 3$ , the tail of the log-normal distribution falls quite faster than the distribution of the sample. The relatively high values of reported parameters such as the skewness and flatness, support the observation that the impulse distribution has a heavy tail. It is also noted that the vast majority of impulses leading to particle displacement, have values above an empirically defined critical level. Careful examination shows that for most experiments this level corresponds to  $\hat{I} = I_{cr} / I_{mean} > 2.5$  (e.g. using  $I_{cr} = 0.0063$  and  $I_{mean}$  values from Table 1). This implies that the log-normal may not be the most suitable distribution in the range of interest, which may also affect the accuracy of the probability of particle entrainment estimations. EVT provides a flexible stochastic framework with the potential to model more accurately impulse events, having the ability to capture the extremal character of turbulence-particle interactions for near threshold flow conditions.

### 2.1.1. Generalized Extreme Value distribution (GEV)

EVT provides representative distributions which model the stochastic character of extreme values from the sequence of impulses,  $I_i$ , assumed to be independent and identically distributed (iid) [Gumbel, 1958]. The Generalized Extreme Value distribution unites the three types of

extreme value distributions into a single family, allowing for a continuous range of possible shapes with cumulative distribution function [e.g. *Kotz and Nadarajah, 2000*]:

$$F_{GEV}(x) = \begin{cases} \exp\left\{-\left[1 + \gamma(x - \mu)/\sigma\right]^{-\frac{1}{\gamma}}\right\}, & \text{for } \gamma \neq 0 \\ \exp\left\{-e^{-(x-\mu)/\sigma}\right\}, & \text{for } \gamma=0 \end{cases} \quad (6)$$

with  $\gamma$  the shape parameter (determines the type of the extreme value distributions),  $\sigma$  the scale parameter and  $\mu$  the location parameter. For  $\gamma=0$ , it corresponds to the Gumbel (Type I) distribution, for  $\gamma>0$ , to the Frechet (Type II) unbounded distribution, while for  $\gamma<0$  it is the Weibull (Type III) distribution with an upper bound. Application examples are given in the following sections to illustrate the utility of these distributions.

### 2.1.2. Generalized Pareto Distribution (GPD)

Another family of distributions from the arsenal of EVT is the GPD. It is used to model the distribution of exceedances above a threshold and has been widely applied to a broad range of fields ranging from finance to environmental engineering and engineering reliability [*Gumbel, 1954; Ashkar et al., 1991*]. For the case of flow impulses, modeling the distribution of extreme values (maxima) separately is of particular interest, considering that common models may be biased in the right tail due to the relatively lower density of data.

According to the limit probability theory, the Generalized Pareto Distribution (GPD) is the appropriate distribution for exceedances ( $I_i - I_{thr}$ ), as it always fits asymptotically the tails of conditional distributions in excess of a sufficiently large threshold ( $I_i > I_{thr}$ ) [*Pickands, 1975*]. The GPD is a right skewed distribution parameterized by a shape ( $\gamma_{GPD}$ ) and a scale ( $\sigma_{GPD}$ ) parameter, with probability density function:

$$f_{GPD}(I_i > x | I_i > I_{thr}) = (1/\sigma_{GPD}) \left[1 + \gamma_{GPD}(x - I_{thr})/\sigma_{GPD}\right]^{-1 - \frac{1}{\gamma_{GPD}}}, \gamma_{GPD} \neq 0 \quad (7)$$

Equation (7) provides an accurate representation of the tail of the distribution provided that the exceedances are statistically independent and the selected threshold sufficiently high. Similarly

to the GEV, GPD is classified to the Frechet (Type II) and the Weibull (Type III) distributions based on the shape or tail index, for  $\gamma_{GPD} > 0$  and  $\gamma_{GPD} < 0$  respectively. For  $\gamma_{GPD} = 0$ , GPD becomes the two parameter exponential distribution:

$$f_{GPD}(I_i > x | I_i > I_{thr}) = \exp[-(x - I_{thr}) / \sigma_{GPD}] \quad (8)$$

While the shape parameter for the GEV and GPD has identical meaning and value, the scale parameters are interlinked with the threshold according to:  $\sigma_{GPD} = \sigma + \gamma x_{thr}$  [Coles, 2001]. The relation between the cumulative distribution functions of the two distributions is  $F_{GPD} = 1 + \ln(F_{GEV})$ . GPD provides an adequate model, assuming that the threshold as well as the number of exceedances is sufficiently high, so that the asymptotic approximation of the distribution is not biased and accurately estimated. The peaks over threshold (POT) method proposed by Davison and Smith [1990], is utilized to extract excess impulses above an appropriate threshold and fit the GPD model to the tail of impulses distribution.

Extreme impulses extracted using the block maxima (or the epochal method) could be also modeled by attempting to fit them to the GEV distribution. However, such modeling is not directly applicable for the phenomenon under investigation, because extreme impulses do not occur at regular or physically meaningful, easy to identify intervals. To the contrary, GPD utilizes only the peak impulses in excess of a high, but below critical, impulse threshold ( $I_{thr} < I_{cr}$ ). This renders GPD ideal for modeling the tail of distribution of impulses for low mobility conditions, since for such flow conditions,  $I_{cr}$  is relatively large, allowing for a sufficiently high choice of  $I_{thr}$  without biasing the distribution. The utility of GPD is demonstrated through application of threshold-excess method after the description of the experimental method and setup employed to obtain a series of sample impulse distributions.

### 3. Description of setup and experimental process

Incipient motion experiments were performed to obtain coupled data for the entrainment of a fully exposed Teflon® (specific gravity = 2.3) spherical particle in addition to the local flow field upstream of it. The test section is located about 14.0 m downstream from the inlet of the 20.5 m long and 0.6 m wide flume to guarantee fully developed turbulent flow conditions. The sphere (12.7mm diameter) rests on top of two layers of fully packed glass beads of the same size,

forming a tetrahedral arrangement (Figure 5). The bed slope ( $\alpha$ ) remains fixed to 0.25% for all of the conducted experiments. The series of conducted experiments refer to uniform and near threshold to low mobility conditions. For those flow conditions the use of data acquisition techniques that do not interfere with the flow, renders possible the identification of the impulse events as well as entrainment instances, with greater accuracy [Diplas *et al.*, 2010].

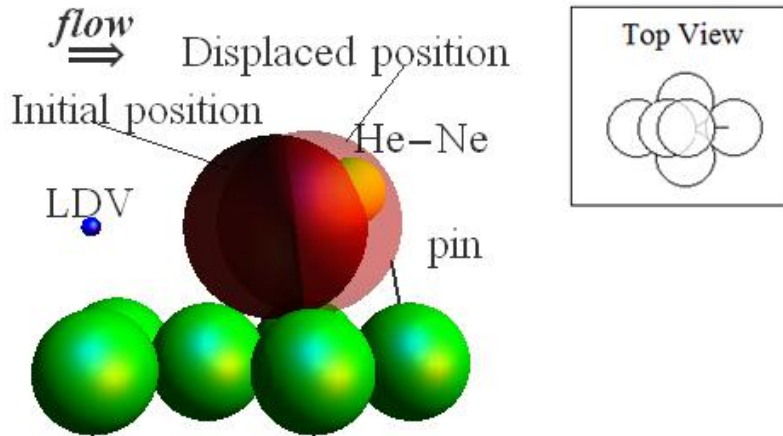


**Figure 5.** Sketch (side view) of the experimental setup (top view shown in the inset), illustrating the possible locations of the mobile particle and its local configuration with a retaining pin.

The motion of the mobile sphere is recorded via a particle tracking system composed of a photomultiplier tube (PMT) and a low power (25-30mW) He-Ne laser source. As seen in Figure 5, the He-Ne laser beam is aligned to partially target the test particle. Calibration of the setup showed that the angular dislodgement of the targeted particle is a linear function of the signal intensity of the PMT, which changes proportionally to the light received. A continuous series of entrainments is made possible due to a restraining pin located 1.5 mm downstream of the mobile sphere (Figure 5), which limits the maximum dislodgement of the grain to the displaced position. The grain will not be able to sustain its new location for long and will eventually fall back to its initial position after the flow impulses are reduced below a certain level, without a need to interrupt the experiment to manually place the sphere back to its resting configuration.

The time history of the streamwise velocity component one diameter upstream of the particle and along its centerline ( $u(t)$ ) is obtained by means of laser Doppler velocimetry (4W Argon ion LDV) at an average sampling frequency of about 350Hz (Figure 5). These measurements are obtained simultaneously with the displacement signal, employing a multichannel signal

processor. Utilizing equations (1) and (4), impulse events of instantaneous hydrodynamic forces exceeding a critical value can be extracted from the time series of  $F_D=f(u^2)$ .

A series of experiments (*E1-E6*) were carried out, during which coupled measurements of flow intensity and particle response were recorded for different low mobility flow conditions. For each of the experimental runs the flow conditions were stabilized to achieve a constant rate of particle entrainment,  $f_E$ , over long durations (about 2 hours). Impulses are extracted from the about 15 min long time series of the local flow, to allow for their statistical representation. The main flow and grain response characteristics are shown in Table 1, for each experimental run. All of these experiments refer to near incipient motion conditions of about the same mean local velocity,  $u_{mean}$ , dimensionless bed shear stress,  $\tau^*$ , and turbulent intensity (equal to 0.27). Contrary to the aforementioned flow parameters which remain relatively invariant, the rate of occurrence of impulses,  $f_I$ , and  $f_E$ , change more than an order of magnitude (Table 1). Thus estimation of the mean rate of particle mobilization is less sensitive if based on  $f_I$ , compared to using any of the above traditional flow parameters. In the following sections the relationship between the flow impulses and grain response is further explored under a probabilistic context.

**Table 1.** Summary of flow characteristics for mobile particle flume experiments.

	$u_{mean}$	$\tau^*$	$Re_p$	$I_{mean}$	$f_I$	$f_E$
	(m/s)	-	-	(m <sup>2</sup> /s <sup>2</sup> )	(events/s)	(entr./s)
<b><i>E1</i></b>	0.248	0.007	424.18	0.0024	2.20	0.147
<b><i>E2</i></b>	0.243	0.007	412.75	0.0023	1.73	0.114
<b><i>E3</i></b>	0.238	0.006	397.51	0.0021	1.31	0.051
<b><i>E4</i></b>	0.230	0.006	384.81	0.0021	0.80	0.031
<b><i>E5</i></b>	0.228	0.005	377.19	0.0022	0.33	0.012
<b><i>E6</i></b>	0.218	0.005	364.49	0.0019	0.47	0.002

## 4. Analysis and results

### 4.1. Frequency-magnitude relationship

Preliminary analysis of the impulse data obtained experimentally for near threshold flow conditions showed that extreme events of both high magnitude and relatively low frequency of occurrence are linked to the instances of particle dislodgement. Thus it is of interest to establish a relationship between the frequency of occurrence of extreme impulse events and their magnitude. To this purpose, the mean number of impulses per second ( $f_j(I_i)$ ), above a certain level ( $I_i$ ) is found for practically the whole range of magnitude of impulses, for all experimental runs (*E1-E6* corresponding to  $j=1$  to 6). If the obtained pairs ( $I_i, f_i$ ), are plotted on a double-logarithmic scale, they are observed to closely follow an almost straight line (Figure 6). This behavior is strongly indicative of power law dependence between the two variables:

$$f_j(I_i) = b_j I_i^{-a_j} \quad (9)$$

with  $a_j (>0)$  the power law exponent and  $b_j$  the base coefficient for a certain flow condition defined by index  $j$ .

Equation (9) is fitted to the sample pairs, for each experiment, to acquire the values ( $a_j, b_j$ ) that parameterize it (Table 2). For the range of flow conditions examined here the frequency of occurrence and magnitude of impulse events obey a power-law relationship to a very good approximation as confirmed by the high values of the coefficient of determination ( $R^2 \sim 0.92$  to 0.98, Table 2). Here the scaling region, defining the range of applicability of power law, spans virtually the whole distribution of impulses. The value of the exponent remains almost constant ( $a=1.82 \pm 0.10$ ) for the different experiments. The value of the coefficient ( $b_j$ ) obtains higher values with increasing flow strength ( $j$  from 1 to 6), implying that the peak impulses become more frequent. Comparison between the various flow conditions is facilitated by normalizing the impulse values with the critical impulse level,  $I_{cr} = 0.0063$ . Use of the normalized impulses, changes the value of base coefficient to  $b_{n,j} = b_j I_{cr}^{-a_j}$ , while the exponent remains the same (Table 2). The effect of decreasing flow conditions (from *E1* to *E6*) on the relation between frequency and magnitude of normalized impulses is clearly demonstrated in Figure 7. Such a representation is of practical importance and predictive value since it directly provides the expected frequency of occurrence of impulses at the critical ( $I_i/I_{cr}$ ) or multiples of it levels, which are of interest for particle entrainment.

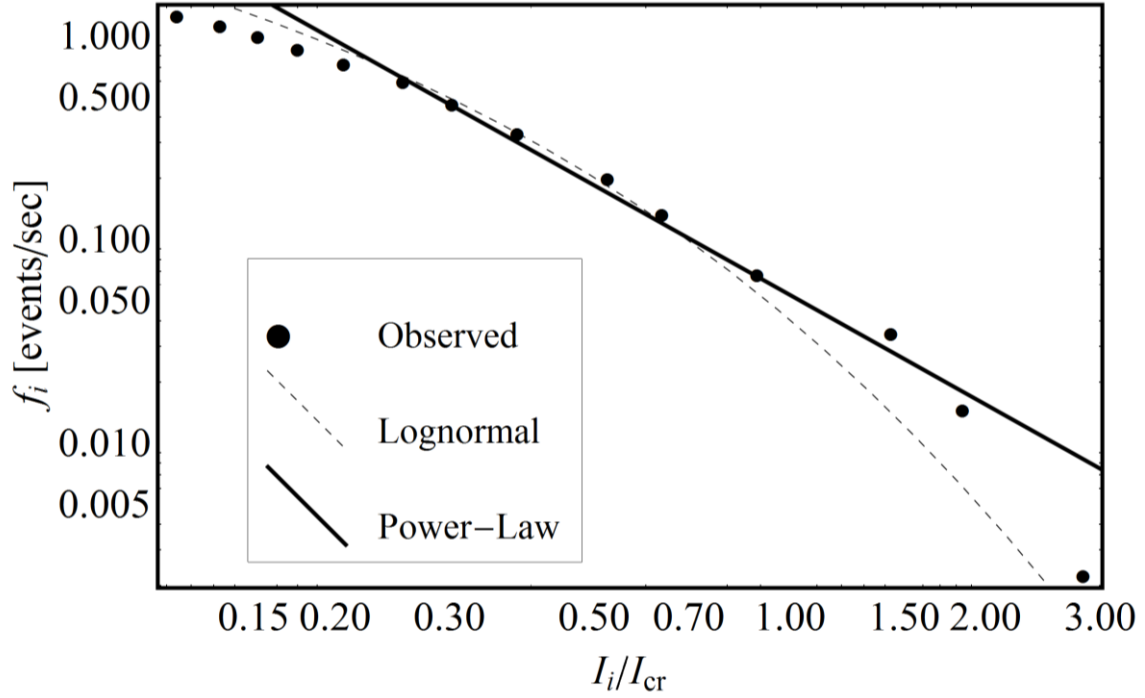


**Figure 6.** Variation of magnitude of impulses normalized with the critical impulse level ( $I_i/I_{cr}$ ) with the mean frequency of their occurrence ( $f_i$ , for run  $E3$ ) and fitted power-law relationship (the lognormal fit is also shown for comparison).

**Table 2.** Summary of power-law and Fréchet parameters characterizing the magnitude-frequency relation and distribution of impulses, respectively.

<b>Run</b>	$\alpha=\gamma$	$b$	$b_n$	$\sigma_n$	$R^2$
<i>E1</i>	1.73	0.000014	0.094	0.26	0.93
<i>E2</i>	1.75	0.000010	0.070	0.22	0.94
<i>E3</i>	1.79	0.000006	0.053	0.19	0.95
<i>E4</i>	1.69	0.000007	0.036	0.14	0.98
<i>E5</i>	1.92	0.000001	0.013	0.10	0.95
<i>E6</i>	1.83	0.000005	0.020	0.12	0.92

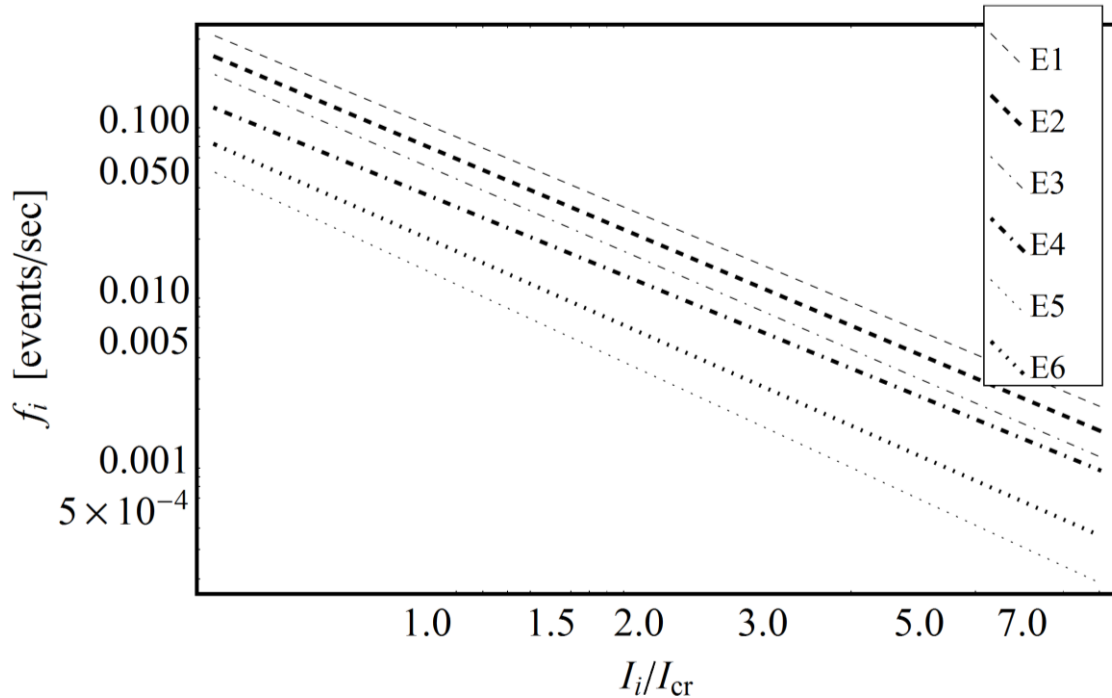


**Figure 7.** Illustration of the dependence of the frequency-magnitude power law relationship (equation 9) of the normalized impulse values on the different flow conditions (E1-E6).

Power law models are attractive since they have the ability to describe a wide range of scale invariant phenomena in Earth sciences [Schroeder, 1991; Turcotte, 1997], from the occurrence of rare natural hazards such as earthquakes [Bak and Tang, 1989; Rundle et al., 1996] to the self-similarity of channel networks and corresponding energy and mass distribution [Rodriguez-Iturbe et al., 1992; Rogriguez-Iturbe and Rinaldo, 1997]. Their superiority compared to more sophisticated models has been also demonstrated for the prediction of bedload transport rates [Barry et al., 2004]. Here the power law characterizes the momentum and energy contributed by flow structures towards particle entrainment.

#### 4.2. Impulse distribution

In addition to their simplicity and effectiveness in expressing the frequency of high magnitude impulses resulting in particle dislodgement, it may be shown that the proposed power law relation is statistically associated to the Frechet distribution [Leadbetter, 1983]. Assuming that the iid impulse events arrive according to a Poisson process with a mean frequency  $f_j$ , then the

probability that no impulses of magnitude greater than  $I_i$ , occur in the unit time (sec) is  $F_j(I_i)=\exp(-f_j(I_i))$ , or using equation (9):

$$F_j(I_i) = e^{-b_j I_i^{-a_j}}, \text{ for } I_i > 0 \quad (10)$$

which is the cumulative density function of the Frechet distribution as a special case of the GEV, equation (6), with shape parameter  $\gamma=a_j$  and scale parameter  $\sigma=b_j^{1/a_j}$  (or  $\sigma_n=b_{nj}^{1/a_j}$ , if  $I_i$  is normalized with  $I_{cr}$ , Table 2).

Equation (10) together with the lognormal distribution are plotted against the data sample for one of the experimental runs, for comparison purposes (Figure 8). Generally both distributions are seen to have a good overall fit to the sample impulses. However, the Frechet distribution has a relatively heavier tail behavior compared to other distributions such as the lognormal [Mitzenmacher, 2003]. This may easily be observed in the double logarithmic representation of normalized magnitude and frequency of impulses (Figure 6), where the region of extreme impulses (normalized with  $I_{cr}$ ) is emphasized. It is shown that the logarithmic distribution generally underestimates the frequency of occurrence of extreme impulses (Figure 6) or their probability (Figure 8) as opposed to the power law and corresponding Frechet distribution, respectively.

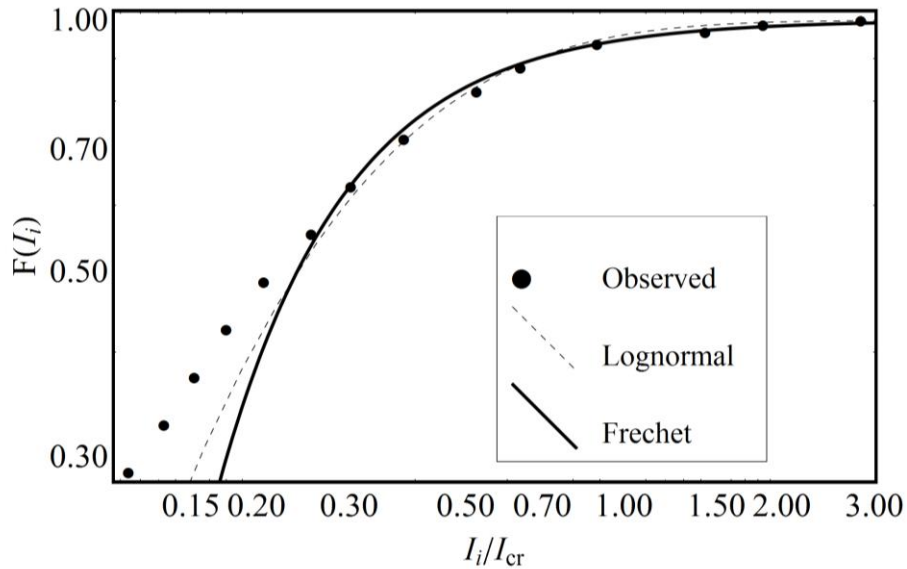


**Figure 8.** Cumulative distribution function of impulse data ( $F(I_i)$ , for run *E3*) and corresponding fitted models (equation 10).

### 4.3. Distribution of conditional excess impulses

In the previous sections the extremal character of distribution of impulses has been demonstrated. Since out of the whole distribution it is rather the peak impulses which are linked to grain mobilization, separate modeling of the tail of the distribution is appropriate. Here due to the heaviness of the tail the POT method is employed to extract the conditional impulses ( $\xi_i$ ) in excess of a threshold level ( $I_{thr}$ ) and fit the GPD. Since POT is threshold dependent, guidelines justifying the choice of  $I_{thr}$  are provided. The GPD parameters are evaluated for the range of examined flow conditions, using different methods of estimation and the model's performance is accessed.

#### 4.3.1. Application of POT

For design applications, it is of interest to define the near critical flow conditions for certain gravel properties and bed surface arrangement. The proximity to the critical flow conditions may be measured by the probability of grain entrainment ( $P_E$ ) which can be estimated through the conditional probability of impulse exceedances,  $P(\xi_i > I_{cr} - I_{thr} | I_i > I_{thr})$ .

Evidently the goodness of fit as well as appropriateness of the GPD model depends on the choice of threshold value. A very low threshold may utilize more data but it may violate the assumption of the asymptotic nature of the model, biasing the distribution. On the contrary, a very high threshold will increase statistical noise due to high variability of the extreme values affecting the accuracy of estimated parameters. In the case when the sample size of conditional excess impulses is large (e.g. several hundreds of data points) for high impulse quantiles, the sensitivity of the method to the threshold selection is not high. However, for flow conditions very close to critical, the sample of  $\xi_i$ 's becomes relatively small and the selection of an optimal threshold with which both statistical certainty and accurate parameter estimation are achieved, requires further investigation.

In practice, graphical diagnostic tools such as the mean excess over threshold plot are commonly employed in estimating a suitable  $I_{thr}$  [e.g. *Davison and Smith, 1990*]. This graph depicts the pairs of the threshold impulse and corresponding mean excess over threshold function,  $\{I_{thr}, e_n(I_{thr})\}$ , for a range of threshold values. The mean excess over threshold function,

$e_n(I_{thr})$ , is defined as the ratio of the sum of impulses in excess of the threshold  $I_{thr}$ , over the number of those exceedances  $n_{thr}$ :

$$e_n(I_{thr}) = \frac{1}{n_{thr}} \sum_{i=1}^{n_{thr}} (I_i - I_{thr}) \quad (11)$$

with  $I_i > I_{thr}$ . Equation (11) provides an empirical estimation of the mean excess function  $E(I_i - I_{thr} | I_i > I_{thr})$  of impulses. The mean excess over threshold function is plotted for a range of thresholds for run *EL* (Figure 9a). The distribution of excess impulses follows a GPD above a threshold impulse, when the mean residual excess plot shows a line with approximately constant gradient [Davison and Smith, 1990; Embrechts et al., 1997; Beirlant et al., 2004]. As an example, for experiment *EL*, this region corresponds to the range of 87.5% to 97.5% quantiles of the impulse distribution. Based on the above observation and considering utilizing a relatively high number of data points (Figure 9b) for improved accuracy, a relatively low  $I_{thr}$ , such as the 90% quantile of the distribution, may be chosen ( $I_{thr}=0.005$ , vertical dashed line in Figures 9a, b). This impulse level provides an acceptable threshold for all the uniform flow conditions examined here. Alternatively, a practical, physically sound threshold may be predefined considering a value for the ratio  $I_{thr}/I_{cr} (<1)$ . Here for the selected threshold this ratio varied from about 0.6 to 0.8. For a lower threshold e.g. corresponding to the 85% quantile, it may range from 0.53 to 0.7.

#### 4.3.2. Estimation of GPD parameters and model performance

For the previously defined  $I_{thr}$  the basic properties of the GPD model are satisfied. Thus the shape ( $\gamma_{GPD}$ ) and scale ( $\sigma_{GPD}$ ) model parameters are estimated for various choices of the threshold (corresponding to the 87.5% and 90% quantiles) and different methods of estimation.

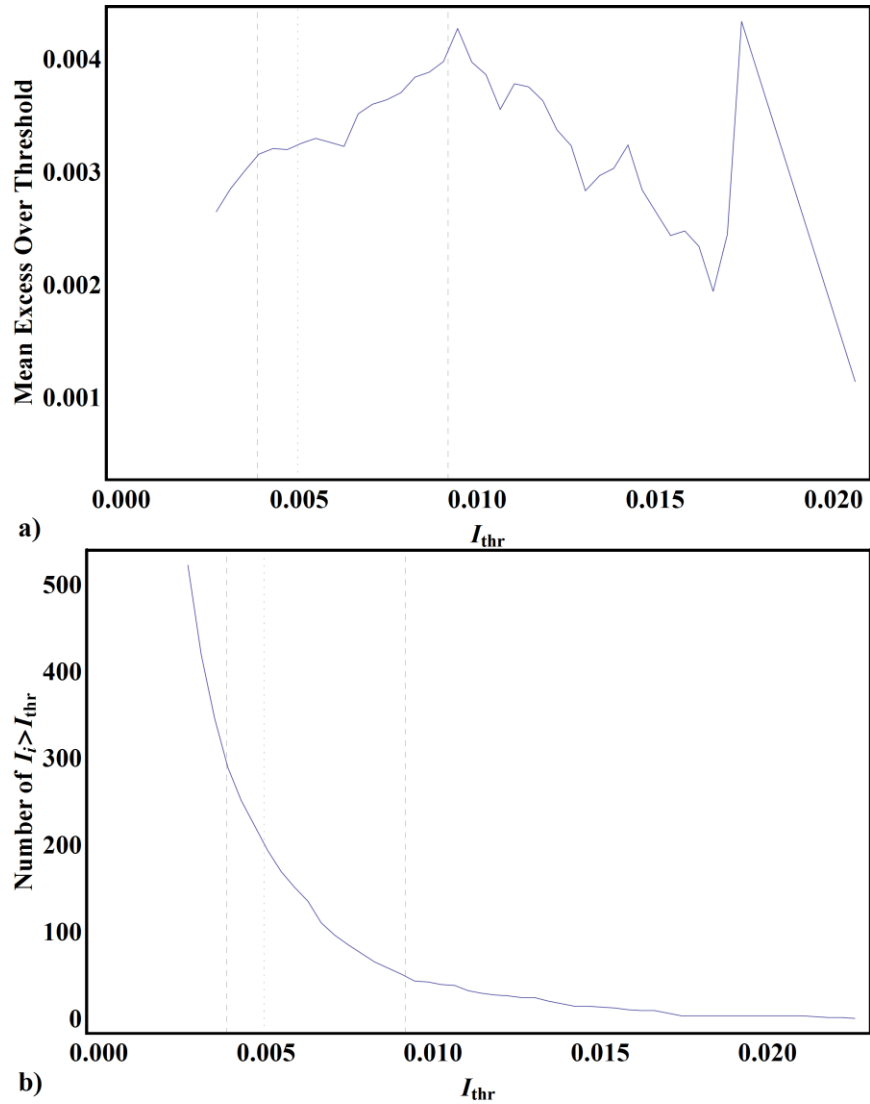


**Figure 9.** Graphical method for selection of optimal  $I_{thr}$ , for run *EI*: a) plot of mean excess over threshold and b) plot of number of exceedances for a range of threshold impulses (dashed lines correspond to the limits of 85% and 97.5% quantiles, defining the range of possible thresholds). The dotted vertical line corresponds to the chosen threshold  $I_{thr}=0.005$  ( $m^2/s^2$ ), corresponding to the 90% quantile.

The estimation of GPD parameters may be performed using a variety of methods such as the maximum likelihood method (MLE) and the method of moments (MOM). The maximum likelihood method, as discussed in *Embrechts et al.* [1997], is employed to obtain parameter estimations and their standard errors (with 95% confidence interval), for the distribution of conditional excess impulses normalized with the mean of the distribution. Normalizing the impulse exceedances in this manner essentially removes the effect of increasing magnitude of excess impulses for increasing flow conditions, allowing evaluation of whether changes occur in

the shape of the tail of the distribution. The method of moments [Hosking and Wallis, 1987] employs the mean ( $E(\xi_i)$ ) and standard deviation ( $std(\xi_i)$ ) of impulse exceedances,  $\xi_i$ , to obtain the empirical estimates of  $\gamma_{GPD}$  and  $\sigma_{GPD}$ , respectively:

$$\gamma_{GPD} = \frac{1}{2} \left\{ 1 - \left[ \frac{E(\xi_i)}{std(\xi_i)^2} \right] \right\} \quad (12a)$$

$$\sigma_{GPD} = \frac{1}{2} E(\xi_i) \left\{ 1 + \left[ \frac{E(\xi_i)}{std(\xi_i)^2} \right] \right\} \quad (12b)$$

The summary of the estimated parameters is shown in Table 3. In particular, the variation of the parameters computed for different thresholds and method of estimation is shown, to enable their comparison. The relative precision of the estimates, indicated by the standard errors, decreases as the sample size of normalized  $\xi_i$  is reduced (*E1* to *E6*). Both the tail and scale parameters remain positive and relatively constant with a mean of  $\gamma_{GPD}=0.14(\pm 0.12)$  and  $\sigma_{GPD}=1.08(\pm 0.16)$ , for experiments *E1-E5* (Table 3). For the experiment closest to the critical flow conditions (*E6*) the shape estimate becomes negative, indicating a possible change in the form of the distribution (from unbounded to a distribution with an upper bound). However, the uncertainty for such an observation is relatively high, considering that the standard error is greater than the estimated value and the confidence intervals span above zero. This probably occurs because of the relatively small sample of impulse exceedances (only 29, for  $I_{thr} = 90\%$  quantile). The within sampling error invariance of the model parameters with threshold selection, further justifies the appropriateness of the GPD for modeling impulses above the chosen threshold.

The probability density function (equation 7) and cumulative density function predicted by the GPD model are plotted against the empirical observations, in Figures 10a and 10b, for run *E1*. Despite the relative uncertainty in the estimation of the tail parameter, the GPD model provides an excellent fit to the tail of impulse events distribution, as assessed visually. The fitted distributions for all of the experiments are shown collectively in Figure 11, represented in a double logarithmic scale, to emphasize the region of greater normalized  $\xi_i$ . In agreement with the previous observations and within statistical uncertainty the shape of the distributions remains invariant for the different examined flows. This implies lack of any significant trend for the

shape parameter for uniform flow conditions, of about the same turbulence intensity levels but different Reynolds numbers.

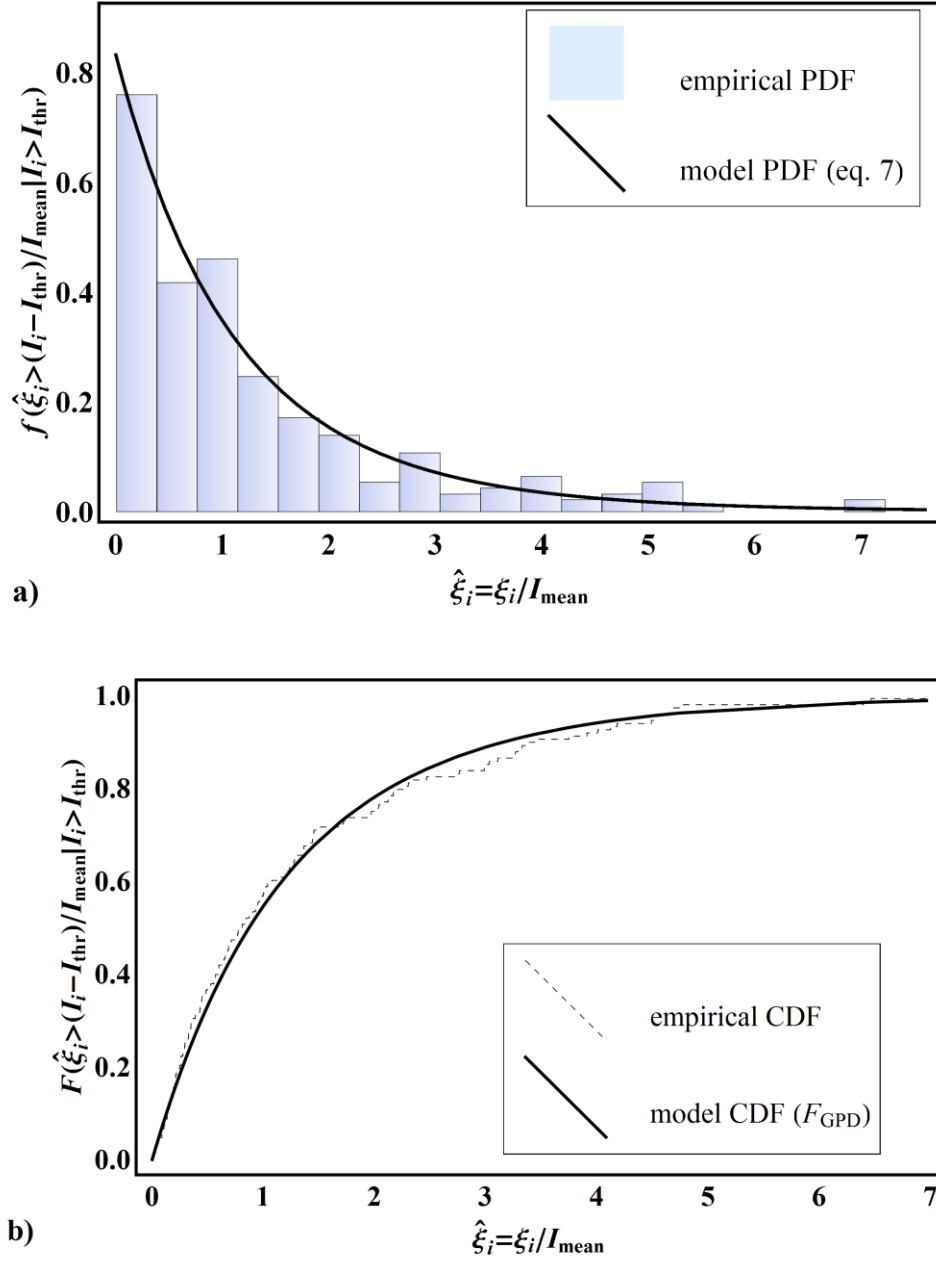


**Figure 10.** Distribution of the tail of impulses for run *EI* and threshold corresponding to the 90% quantile ( $I_{thr}=0.005 \text{ (m}^2/\text{s}^2)$ ): a) probability of conditional excess impulses and best fit of the GPD model and b) empirical cumulative distribution function (CDF) of conditional excess impulses and the corresponding model fit (equation 7).

**Table 3.** Summary of the GPD shape ( $\gamma_{GPD}$ ) and scale ( $\sigma_{GPD}$ ) parameters, estimated using maximum likelihood method (MLE -standard errors are shown in parenthesis) and method of moments (MOM), for all experimental runs.

Run	MLE (87.5%)		MLE (90%)		MOM (90%)	
	$\gamma_{GPD}$	$\sigma_{GPD}$	$\gamma_{GPD}$	$\sigma_{GPD}$	$\gamma_{GPD}$	$\sigma_{GPD}$
<i>E1</i>	0.09 (0.07)	1.20 (0.12)	0.05 (0.08)	1.30 (0.14)	0.04	1.31
<i>E2</i>	0.18 (0.08)	0.94 (0.10)	0.22 (0.10)	0.91 (0.11)	0.23	0.90
<i>E3</i>	0.23 (0.13)	1.02 (0.15)	0.10 (0.12)	1.29 (0.20)	0.07	1.33
<i>E4</i>	0.18 (0.14)	1.12 (0.19)	0.15 (0.15)	1.22 (0.23)	0.11	1.28
<i>E5</i>	0.13 (0.15)	0.86 (0.17)	0.15 (0.18)	0.86 (0.20)	0.10	0.89
<i>E6</i>	-0.03 (0.23)	1.11 (0.31)	-0.18 (0.22)	1.35 (0.39)	-0.08	1.24

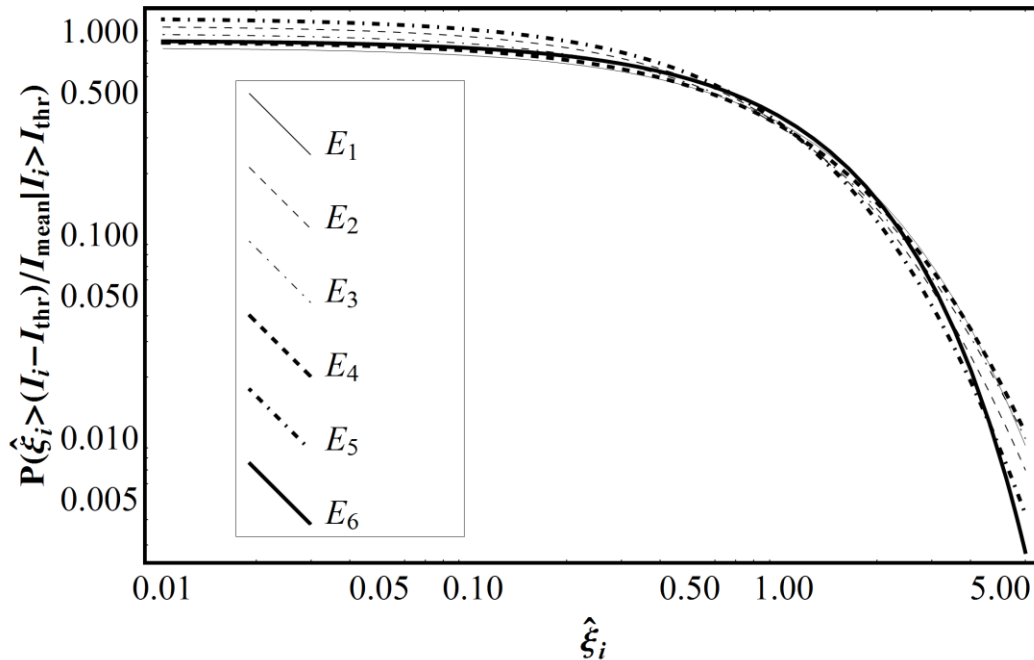


**Figure 11.** Probability density functions predicted by the GPD model, for all flow conditions.

#### 4.4. Reliability of grain dislodgement

In addition to the rate of occurrence of impulses in a flow, the interarrival times between the instances of entrainment may be further statistically studied under an EVT context. Specifically, considering the episodic nature of the phenomenon, the time to grain entrainment for low mobility flow conditions, is analyzed here utilizing reliability (or survival) theory. Under this framework, the complete entrainment of individual coarse particles may be viewed as a stochastic process, with a certain reliability or probability of survival of entrainment events, for a specific time interval and flow conditions. Similar concepts have been employed from *Ancey et al.*, [2008], who considered the flux of coarse grains as a birth-death process, as well as *Tucker and Bradley* [2010], who investigated the probability of grain entrapment while moving along a transport path.

##### 4.4.1. Empirical estimation

Consider a surface particle resting in its local configuration. Survival of the particle past time  $t_i$ , is defined as the probability that the particle remains in its position after time  $t_i$ , without being entrained:  $S(t_i) = P(T_e > t_i)$ , with  $T_e > 0$  the random variable representing the time to entrainment. According to the multiplication rule for joint events, this probability may also be expressed as:  $S(t_i) = P(T_e > t_i | T_e \geq t_i) P(T_e \geq t_i)$ , where the probability of entrainment occurring at least after  $t_i$ , equals the probability of surviving past the time  $t_{i-1}$ :  $P(T_e \geq t_i) = P(T_e > t_{i-1}) = S(t_{i-1})$ . By recursive application of the above formulas, it is possible to express the survival from entrainment past time  $t_i$ , in terms of all the conditional probabilities for entrainment in times before  $t_i$ , leading to the product-limit formula:

$$S(t_i) = \prod_{j=1}^i P(T_e > t_j | T_e \geq t_j) \quad (13)$$

For a particular flow condition, equation (13) implies that the survival function is a decreasing function of the time for grain entrainment.

Equivalent to equation (13) is the Kaplan-Meier estimator [Kaplan and Meier, 1958] which is widely used for the nonparametric empirical estimation of the survival function. Utilizing the time series of particle dislodgement, obtained from the He-Ne laser for different flow conditions, the inter-arrival times for each entrainment event can be defined as the time intervals between the instances of deposition and entrainment of the mobile grain. The order statistics for the interarrival times ( $t_i, i=1, \dots, m$ ) for a total of  $m$  complete entrainment events may be obtained, for each experiment. This is equivalent to having a population of  $m$  different particles, which get entrained at time  $t_i$ , when a particular low mobility flow condition is imposed. For such flows it is safe to assume statistical independence between different grain mobilization events. Defining  $n_i$  as the number of particles that have “survived” entrainment just before time  $t_i$  and  $k_i$  as the number of dislodgements (or “deaths”) occurring at time  $t_i$ , the Kaplan-Meier estimation of the survival function is expressed as:

$$S(t) = \prod_{j=1}^i \frac{n_j - k_j}{n_j}, \text{ for } i = 1, 2, \dots, m \quad (14)$$

where  $t$  belongs to the duration interval over which the particle is expected to dislodge ( $t_i < t < t_{i+1}$ ). Then the survival function,  $S(t)$ , indicates the percentage of grains that have “survived” entrainment by time  $t$ . As expected, for a fixed level of  $S$ , the higher the flow conditions the lower the estimated time to displacement is (e.g. compare  $S(t)=0.5$ , decreasing from  $E4$  to  $E1$ , Figure 12).

Estimates of the survivability of a grain to entrainment or of its reliability that it does not get entrained until past a certain time instance,  $t$ , are provided by equation (14) and plotted for various flow conditions in Figure 12. Usually the right-hand tail of the survival function becomes unreliable when the number of grains remaining at risk for entrainment becomes small (e.g. less than 10 may be used as a rule of thumb). Consequently, it is not statistically meaningful to evaluate the survivability for experiments with very low number of entrainments ( $E5$ - $E6$ ). Similarly, it may be observed that longer sampling times may be required for accurate assessment of  $S(t)$ , at very low mobility conditions. A useful parameter signifying the reliability of grain entrainment is the mean time between entrainments (MTBE), which is the inverse of the mean frequency of complete grain entrainments (Table 4).

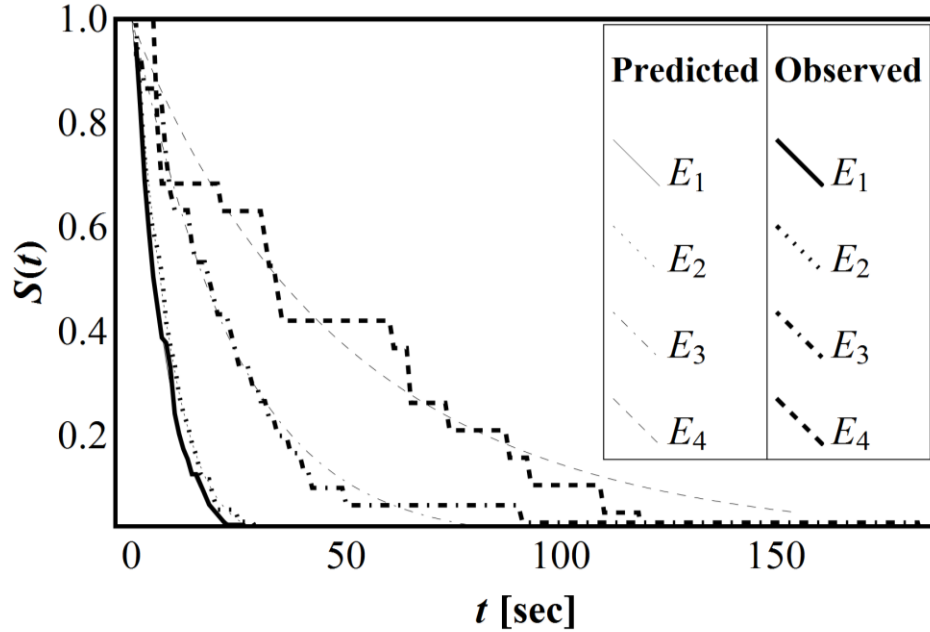


**Figure 12.** Plot of the empirical survival function,  $S(t)$ , estimated employing the nonparametric Kaplan-Meier estimator (equation 14) and best fit curves predicted using the Weibull model (equation 15).

**Table 4.** Summary of empirical model estimators and Weibull and exponential model parameters and mean time to displacement ( $E_w, E_e$ ), characterizing the survival function for various flow conditions ( $E1-E4$ ).

	$MTBE$	$\lambda_w$	$\gamma_w$	$E_w$	$R^2$	$\lambda_{exp}$	$E_e$	$R^2$
<b><i>E1</i></b>	8.7	0.103	1.124	9.3	1.00	0.136	7.4	0.99
<b><i>E2</i></b>	10.5	0.075	1.175	12.6	1.00	0.114	8.8	0.99
<b><i>E3</i></b>	29.1	0.035	1.060	28.1	0.99	0.042	23.6	0.99
<b><i>E4</i></b>	45.1	0.023	0.960	43.8	0.98	0.020	50.6	0.98

#### 4.4.2. Parametric modeling

A number of parametric models for survival times have been proposed in the literature. Typically, distributions such as the exponential have been used to characterize the inter-arrival of rainfall events in hydrology [e.g. *Adams and Papa, 2000*]. Herein, the application of Weibull and exponential distributions is demonstrated in modeling the extremal character of inter-event times of particle entrainment.

First, the two parameter Weibull survivor function is defined as:

$$S(t) = P(T_e \geq t) = \exp[-(\lambda_w t)^{\gamma_w}] \quad (15)$$

where the positive parameters  $\lambda_w$  and  $\gamma_w$ , denote the scale and shape parameters of the Weibull model, respectively. The mean time to full grain dislodgement as predicted by the Weibull model may be analytically estimated as:

$$E_w = \lambda_w^{-1} \Gamma\left(1 + \frac{1}{\gamma_w}\right) \quad (16)$$

with  $\Gamma(\cdot)$  the Euler Gamma function defined as  $\Gamma(x) = \int_0^{\infty} v^{x-1} e^{-v} dv$ . In addition to the survival function, the hazard rate function may be of practical utility. Here the hazard rate may be defined as a measure of the probability per unit time that a particle does not get entrained by time  $t$ . It may be calculated as the number of entrainments per unit time until time  $t$ , divided by the number of particles that have survived entrainment:

$$h(t) = \frac{\frac{d}{dt} S(t)}{S(t)} = \lambda_w \gamma_w (\lambda_w t)^{\gamma_w - 1} \quad (17)$$

The shape parameter defines the behavior of the hazard function, which is predicted to be monotonically increasing for  $\gamma_w > 1$ , decreasing for  $\gamma_w < 1$  and constant otherwise. Best fit values for the Weibull model parameters are provided in Table 4. The coefficients of determination ( $R^2 \sim 0.99$ ) indicate an excellent model fit. The mean estimated time to entrainment compares well to the empirical estimation. It is observed that the shape parameter for the different flow conditions is very close to 1, which within statistical uncertainty implies a constant hazard rate. This, in turn, confirms that entrainment of individual grains in low flow rates is a Poissonian-like process without memory, contrary to the case of higher flows when grains are entrained collectively [Ancy et al., 2008].

Even though the Weibull model exhibits flexibility, which may be useful for higher flow conditions as well, for near threshold conditions it is more realistic and physically sound to assume that the survival times are sampled from a population with a constant hazard rate. To this

purpose the one parameter exponential distribution, a special case of the Weibull model with  $\gamma_W=1$ , may be used. The survivor function and density function of the exponential distribution are:

$$S(t) = P(T_e \geq t) = e^{-\lambda_{exp}t} \quad (18a)$$

$$f(t) = \lambda_{exp} e^{-\lambda_{exp}t} \quad (18b)$$

with  $\lambda_{exp}$ , the time independent hazard rate of the exponential model. The simplicity of the model is further showcased considering that the expected time to entrainment ( $E_e$ ) is the reciprocal of the hazard rate. The performance of the exponential distribution is very good as assessed by the high values of the coefficient of determination ( $R^2 \sim 1$ ). Practically the curves predicted by the two models almost collapse on the same curve providing a good fit to the empirical estimation as may be assessed visually (Figure 12). Overall the mean time to entrainment and hazard rate of the exponential model provide easily to calculate and efficient tools for characterizing the frequency of grain response to uniform and relatively low mobility flow conditions.

## 5. Discussion

### 5.1. Probability of entrainment for an individual particle

In the previous sections EVT models were fitted to the distribution of impulses and their tail. It was observed that any change in the Reynolds number, is reflected mainly in the alteration of the scale parameter (in the case the fit is performed for  $I_i$  or  $\xi_i$ ) or equivalently of the  $I_{mean}$  (when impulses or their exceedances are normalized with  $I_{mean}$ ). Herein the ability of the suggested models to predict the probability of entrainment for individual particles is evaluated, assuming that impulses above the defined critical level are responsible for their mobilization.

For the case of impulses which closely follow the Frechet distribution this probability is straightforwardly obtained from the probability of exceeding the theoretically derived critical level ( $P=P(I_i>I_{cr})$ ). Considering that the GPD model provides the conditional impulse

exceedances above impulse threshold the probability of grain entrainment is given by  $P=P(\xi_i>I_{cr}-I_{thr})$ , with:

$$P(\xi_i > I_{cr} - I_{thr}) = P(I_i > I_{thr})P(\xi_i > I_{cr} - I_{thr} | I_i > I_{thr}) \quad (19)$$

where the probability of exceedance at the threshold value ( $P(I_i>I_{thr})$ ), is estimated as the ratio of the number of impulses exceeding the threshold impulse over the impulses of the entire data set (for instance  $P(I_i>I_{thr})=0.10$ , for  $I_{thr}$  corresponding to the 90% quantile).

The probability of particle entrainment ( $P_E$ ) may be approximated employing various methods. For instance, *Ancey et al.*, (2008) used for  $P_E$  the ratio  $\tau_e/(\tau_e+\tau_w)$ , where  $\tau_e$  is the mean duration of entrainment and  $\tau_w$  is the average waiting time for entrainment to occur. This definition works well for the case when grains may freely dislodge downstream. For the case when the downstream motion of the particle is restrained (Figure 5), the same rationale may be implemented, by approximating  $\tau_e$  as the average time the particle remains displaced. Then  $P_E$  may be plotted against each model distribution,  $P$ , as shown in Figure 13a.

In addition to the previous method,  $P_E$ , may be estimated by the relative frequency of impulses resulting in grain mobilization or equivalently the ratio of mean frequency of impulse events ( $f_I$ ) to the average rate of particle displacement ( $f_E$ ) [*Celik et al.*, 2010]. The results obtained via this method are plotted in Figure 13b. This definition of  $P_E$  accounts for all impulse events or equivalently the flow events for which  $u^2>u_{cr}^2$ , along with their observed impact on mobilizing the particle (from twitches to complete dislodgements). However, there exists some uncertainty associated with estimating the above frequencies ( $f_E, f_I$ ). First, it is assumed that all particle mobilization events (even small displacements) are accounted for, while many of them may not be discernable due to being hidden by the small scale high frequency fluctuations inherent in the displacement signal. Second, the estimation of  $f_I$  or mean number of impulses per unit time is quite sensitive to the selection of  $u_{cr}$  [*Celik et al.*, 2010], implying that the estimation of  $P_E$  will vary depending on whether very small (and possibly ineffective) impulses are accounted for or not.

Based on the previous observations the exceedance probability  $P(I_i>I_{cr})$ , may be more appropriately estimated as the ratio  $f(I_{cr})/f_C$ , with  $f_C$  the rate of occurrence of complete particle entrainments and  $f(I_{cr})$  the mean frequency of impulses above critical ( $I_{cr}$ ). Using the theoretical

prediction of  $u_{cr}$  (derived from equation 2), the resulting  $P_E$  is plotted against the various model predictions ( $P$ ) in Figure 13c. Essentially, the latter estimation method of  $P_E$ , considers the effectiveness of the extreme impulse events (above a critical level  $I_{cr}$ ), avoiding some of the uncertainties associated to the previous method.

Careful observation of Figures 13a, b and c, reveals the same trend for each model distribution, independent of the various methods of estimation of  $P_E$  presented above. The overall performance of the Frechet and GPD distributions is very satisfactory and at least comparable to the lognormal distribution. Particularly, it is seen that the GPD has high predictive ability when the model assumptions are satisfied (e.g. *E1-E4*). For the case of relatively small data samples of impulse exceedances (*E5-E6*) the uncertainty of statistical estimation increases, implying that the closer to threshold the flow conditions are the longer the required flow sampling time needs to be.

On the contrary, the Frechet distribution has a consistent and superior performance throughout the range of examined flow conditions. The predictions from this distribution fall very close to the line of perfect agreement ( $P=P_E$ ) returning a smaller error compared to the other models (Figure 13c). As opposed to the GPD, it can model the whole distribution of impulses.

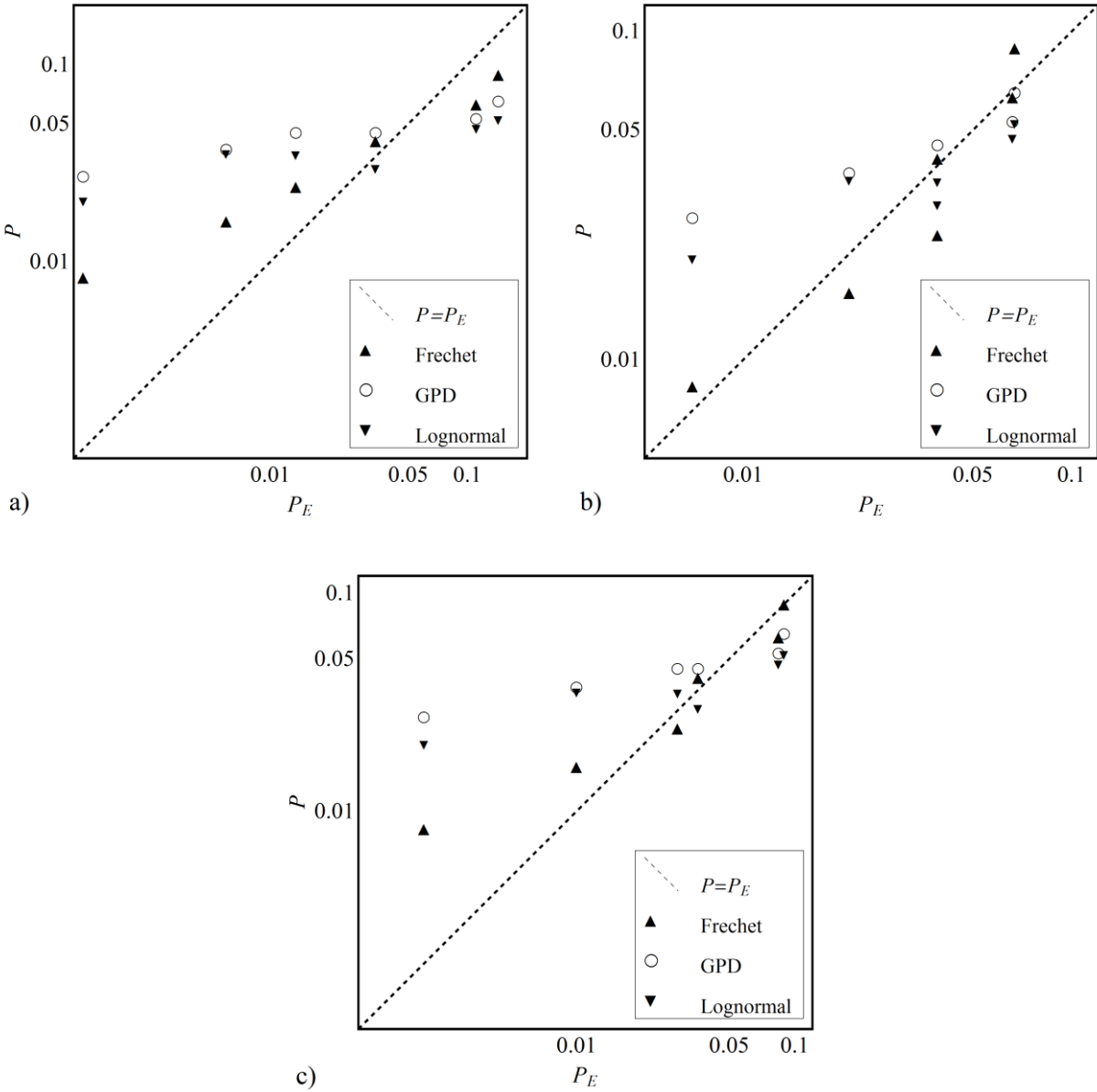


**Figure 13.** Comparison of the exceedance probability of impulses,  $P=P(I_i>I_{cr})$ , predicted using different model distributions with the probability of entrainment of a single particle  $P_E$ , using various methods of estimation: a)  $P_E=\tau_e/(\tau_e+\tau_w)$ , b)  $P_E=f_l/f_E$ , and c)  $P_E=f(I_i)/f_c$ .

## 5.2. Extension of the utility of the power law relation to variable grain and flow characteristics

The connection of the proposed extreme value distributions to a power law relation for the magnitude and frequency of impulses renders it a tool of great utility in characterizing the impact of a particular flow on individual particles. Specifically, two particle arrangements may have

varying critical impulse levels ( $I_1, I_2$ , with ratio  $m=I_2/I_1$ ), due to a number of factors such as different geometrical characteristics of the local bed configuration and/or the grains composing it (see equation (5)). By application of equation (9) a relation between the power law coefficients ( $b_1, b_2$ ) describing the two critical flow conditions and the ratio of the critical levels may be derived. For approximately constant exponent  $a$  (which is demonstrated to be valid here for a relatively small range of flow conditions), the ratio of rate of occurrence of two different impulses is:

$$\frac{f_1(I_1)}{f_2(I_2)} = \frac{b_1}{b_2 m^{-a}} \quad (20)$$

Different threshold conditions are defined in terms of the same probability of entrainment ( $P_{E,1}/P_{E,2}=1$  which is reduced to  $f_1(I_1)/f_2(I_2)=1$ , if the efficiency of transfer of flow momentum to the particle is assumed constant). Based on the above assumptions and using equation (20), the relationship between the two threshold flow conditions becomes:  $b_2=b_1 m^a$ .

Similarly, for a given flow condition (or equivalently fixed values of the power law parameters), flow events of  $m$ -times the magnitude of a reference impulse ( $I_{ref}$ ) appear  $m^{aj}$  times less frequently:

$$\frac{f_j(I_{ref})}{f_j(mI_{ref})} = \frac{1}{m^{-aj}} \quad (21)$$

For example, considering that the range of flow conditions for the performed experiments is characterized by a relatively invariant negative exponent,  $a$  ( $=1.82$ ), flow events of magnitude  $2I_{ref}$ , have a rate of occurrence decreased by 3.5 times (for the same flow condition). This means that grains of same diameter and about 52% greater density, or equivalently same density and 2.1-fold greater diameter are entrained downstream at a rate, 3.5 times smaller compared to the case of the reference grain arrangement at the flow conditions examined here. In addition, when the bed surface is characterized by a range of particle sizes, the relative contribution of each size fraction to the total bed load transport may be estimated by measuring the average distance over

which each particle will dislodge when an impulse above  $I_{cr}$ , is applied to it (e.g. using particle tracking and synchronized flow measurement techniques).

*Grass* [1970], viewed incipient motion as a stochastic process and used the distributions of the applied hydrodynamic as well as resisting critical stresses to account for their variability. He suggested that the threshold conditions and generally any level of grain movement could be modeled by the overlap between the distributions of instantaneous bed shear stresses and the critical shear stresses required for the inception of motion of the bed surface grains. Following the same reasoning, the frequency distributions of flow impulses ( $I_i$ ) and critical impulses ( $I_{cr}$ ) may be employed to characterize the flow forcing and motion resisting conditions (due to heterogeneities in grain and local micro-topography parameters). Then the overlap between the two distributions of impulse (Figure 14a and b) may provide an alternative means of accurately accessing marginal bed load transport rates. The above approach demonstrates conceptually how the utility of impulse model may be extended to characterize threshold conditions for a general bed configuration and variable grain parameters.

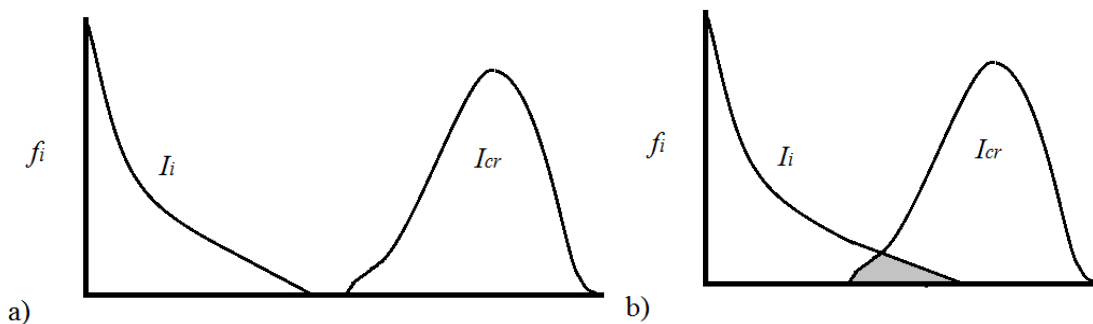


**Figure 14.** Conceptual illustration of the utility of impulse concept in defining different levels of grain mobilization: a) no entrainment –the distributions ( $f$ ) of  $I_i$ ,  $I_{cr}$  are apart, and b) threshold of motion characterized by a small but finite probability of grain mobilization or a certain degree of the distributions’ overlap (higher degree of overlap will result in higher transport rates).

### 5.3. Implications for bed load transport

At near threshold flow conditions and relatively low transport rates, grain entrainment becomes a highly intermittent process. The wide spatial and temporal fluctuations of bed load transport rates that have been observed in both laboratory experiments [e.g. *Kuhnle and Southard*, 1988; *Ancey et al.*, 2008] and field studies [e.g. *Drake et al.*, 1988], demonstrate the appropriateness of

treating bed load movement as a probabilistic process. *Einstein* [1937] was among the first to recognize the stochastic nature of grain entrainment and develop distribution functions for the number of grains passing through a cross section. Recent probabilistic bed load transport studies, model the intermittently occurring grain entrainment and detrainment as a Markov process [e.g. *Lisle et al.*, 1998; *Papanicolaou et al.*, 2002; *Ancey et al.*, 2008; *Turowski*, 2009]. Particle instability may be triggered when the instantaneous hydrodynamic forces exerted to it exceed the resisting frictional and gravitational forces ( $u > u_c$ ).

Here under a similar context, flow events or impulses of sufficient magnitude,  $I > I_{cr}$ , may impart enough momentum for particle removal to a downstream location. As shown in the previous section (5.1), the distribution of impulse exceedances modeled by means of extreme value distributions,  $P(I > I_{cr})$ , are directly linked to  $P_E$  and consequently to the time average frequency of particle entrainment ( $1/n_c$ ). In addition, the frequency of impulse exceedances above critical (as predicted by equation (9)) exhibits an almost linear relation ( $R^2=0.93$ ), to the average frequency of entrainment (modeled by the exponential distribution of time to entrainment, equation (18b)). Those observations strengthen the significance of impulse on particle entrainment.

Herein, for low mobility flow conditions the inter-arrival times between entrainments is modeled by an exponential distribution. This result offers an experimental validation of *Einstein's* [1937] assumption of exponentially distributed rest durations, when no collective transport occurs. Furthermore, assuming an exponential distribution for the waiting time between entrainments, the rate of transport may be shown to follow a Poisson distribution [*Ancey et al.*, 2008; *Turowski*, 2010]. The Poisson distribution for bed load is found to provide a good fit to high resolution field data, when the transport is not dominated by bed form motion [*Turowski*, 2010].

In agreement to the above studies, it is shown that at relatively low transport rates particle entrainment (with  $T_e$  following the exponential distribution) is a process without memory, implying that  $P_E$  should remain constant over time (for the same flow conditions and bed geometry). As the transport rate increases, particles may be set into motion from bed material already entrained which is not captured from a Poissonian representation of bed load [*Ancey et al.*, 2008]. For such cases, it may be more appropriate to implement the Weibull distribution

(equation 15) to model the distribution of  $T_e$ , due to its flexibility to account for time dependence.

## 6. Conclusions

The extremal character and episodic nature of the occurrence of high magnitude impulse events and associated time to entrainments is considered here employing stochastic measures and distributions from the Extreme Value Theory, for low mobility flow conditions. The probability of particle entrainment is approximated by the probability of impulse exceedances above a theoretically defined critical level. Impulses and conditional impulse exceedances are treated as random occurrences of flow events of different magnitude and duration.

It is demonstrated that the distribution of impulses closely follows a Frechet distribution which is associated with a power law relation for the frequency and magnitude of impulses. The exponent of this relation did not show any significant trend for the range of examined flow conditions. The increase in flow rates was mainly demonstrated by an increase of the base coefficient. Such a description offers a useful tool for the prediction of particle entrainment for particular flow conditions.

Additionally, the Generalized Extreme Value distribution is shown to be an acceptable model for the tail of the distribution of impulses. The Peaks Over Threshold method is implemented to extract the conditional excess impulses above a certain threshold. Guidelines for appropriate selection of the impulse threshold are provided and the methods' sensitivity to this threshold is also assessed. Different methods are employed for the estimation of the model parameters. The robustness of the method is indicated by the satisfactory fit of the Generalized Pareto Distribution to the sample of conditional excess impulse data.

The overall performance of the distributions is at least comparable or better than the lognormal distribution, as assessed by direct comparison of the predicted and observed probabilities of entrainment for different flow conditions. In direct analogy to the statistical concept of *Grass* [1971], an extension of the utility of the proposed power law relation is offered, by expressing the distribution of forces driving and resisting grain mobilization in terms of impulses rather than shear stresses.

Further, the grain response is statistically described employing concepts from reliability theory to model the time to full grain entrainment. The exponential distribution is a useful model providing mean time to entrainment and hazard rates for dislodgement, which efficiently characterize the intermittent nature of the phenomenon for low flow rates. The goodness of fit of the exponential model to the empirical distribution provides an experimental validation of the assumption employed by a number of bedload transport models.

In addition to providing good statistical approximations to impulses and time to occurrence of grain entrainment, EVT models provide enhanced understanding and simulation abilities, which are required for development of predictive equations for sediment entrainment.

## Notation

$\alpha$	bed slope.
$\Gamma(\cdot)$	Euler Gamma function.
$\gamma$	shape parameter of the GEV distribution (equation 6).
$\gamma_{GPD}$	shape parameter of the GPD (equations 7, 8).
$\gamma_W$	shape parameter of the Weibul model (equation 15).
$\theta_0$	pivoting angle.
$\lambda_W$	scale parameter of the Weibul model (equation 15).
$\lambda_{exp}$	hazard rate of the exponential model (equation 17).
$\mu$	location parameter of the GEV distribution (equation 6).
$\xi_i$	conditional exceedance of impulse $I_i$ above a threshold level.
$\rho_f$	density of the fluid.
$\rho_s$	density of the particle.
$\rho_\theta$	coefficient including effects of local grain arrangement and relative density of fluid and solid grain.
$\sigma$	the scale parameter of the GEV distribution (equation 6).
$\sigma_{GPD}$	the scale parameter of the GPD (equations 7, 8).
$\tau^*$	dimensionless bed shear stress.
$a_j$	power law exponent (equation 9), for flow conditions defined by index $j$ .
$b_j$	base coefficient (equation 9), for flow conditions defined by index $j$ .
$B_f$	buoyancy force.
$C_D$	drag coefficient.
$C_I$	impulse coefficient.
$C_m$	added mass coefficient.
$E_W$	Weibul mean time to particle entrainment, equation (16).
$E_e$	exponential mean time to particle entrainment ( $=1/\lambda_{exp}$ ).
$e_n(I_{thr})$	function of mean excess impulses over a threshold ( $I_{thr}$ ).
$F(t)$	total hydrodynamic force.
$F_{GEV}$	cumulative distribution function of the GEV distribution (equation 6).
$F_{GPD}$	cumulative distribution function of the GPD.

$F_{cr}$	critical force level.
$F_D$	hydrodynamic drag force.
$F_L$	hydrodynamic lift force.
$F_m$	mean force level.
$f_C$	mean rate of complete particle entrainments.
$f_E$	mean rate of particle entrainments.
$f_{GPD}$	probability density function of the GPD (equations 7, 8).
$f_i$	mean rate of occurrence of impulses.
$f_h$	hydrodynamic mass coefficient.
$f_j(I_i)$	frequency of impulses in excess of $I_i$ , for flow conditions defined by index $j$ .
$g$	gravitational acceleration.
$h(t)$	hazard rate function (equation 17).
$\hat{i}$	impulse normalized with mean of distribution sample ( $I_{mean}$ ).
$I_i$	impulse event $i$ (equation 1).
$I_{cr}$	critical impulse level (equation 5).
$I_{thr}$	threshold impulse level (defining the tail of distribution of impulses).
$L_{arm}$	lever arm.
$n_{thr}$	number of exceedances over a threshold ( $I_{thr}$ ).
$P$	theoretical probability of exceeding the critical impulse level, $P(I_i > I_{cr})$ .
$P_E$	empirical estimation of probability of entrainment.
$R^2$	coefficient of determination.
$S(t)$	Survival function past time $t$ .
$T_e$	time to particle entrainment.
$T_i$	duration of event $i$ .
$T_{roll}$	impulse duration (for entrainment by rolling).
$t_i$	time instance when event $i$ occurs.
$u(t)$	streamwise velocity component.
$u_{cr}$	critical flow velocity.
$u_{mean}$	local time averaged flow velocity.
$V$	volume of the particle.
$W$	weight of the particle.
$W_s$	submerged weight of the particle.

## Acknowledgement

The support of the National Science Foundation (EAR-0439663, EAR-0738759 and CBET-1033196) and Army Research Office is gratefully acknowledged.

## References

Adams, B., and Papa, F. (2000). *Urban stormwater management planning with analytical probabilistic models*, J. Wiley and Sons, New York.

- Ancey, C., A. C. Davison, T. Bohm, M. Jodeau, and P. Frey (2008), Entrainment and motion of coarse particles in a shallow water stream down a steep slope. *J. Fluid Mech.*, 595, 83-114.
- Ashkar, F., N. El-Jabi, and S. Semaan (1991), Study of hydrological phenomena by extreme value theory, *Natural Hazards*, 4(4), 373-388.
- Auton, T. R., J. C. R. Hunt, and M. Prudhomme (1988), The force exerted on a body in inviscid unsteady non-uniform rotational flow, *J. Fluid Mech.*, 197, 241-257.
- Bak, P., and C. Tang (1989), Earthquakes as a self-organized critical phenomena, *J. Geophys. Res.*, 94(B11), 15,635–15,637.
- Barry, J.J., J.M. Buffington, and J.G. King (2004), A general power equation for predicting bed load transport rates in gravel bed rivers, *Water Resour. Res.*, 40: W10401, doi:10.1029/2004WR003190.
- Beirlant, J., Goeghebeur, Y., Teugels, J. and Segers, J. (2004), *Statistics of Extremes: Theory and Applications*. Wiley, Chichester, U.K.
- Bettess, R. (1984), Initiation of sediment transport in gravel streams, *Proc. Inst. Civ. Eng.*, 77, 79-88.
- Buffington, J. M., and D. R. Montgomery (1997), A systematic analysis of eight decades of incipient motion studies, with special reference to gravel-bedded rivers, *Water Resour. Res.*, 33(8), 1993-2029.
- Celik, A. O., P. Diplas, C. L. Dancy, and M. Valyrakis (2010), Impulse and particle dislodgement under turbulent flow conditions, *Physics of Fluids*, 22(4), 046601.
- Cheng, E., and C. Clyde (1972), Instantaneous hydrodynamic lift and drag forces on large roughness elements in turbulent open channel flow, in *Sedimentation, Symp. to Honor Professor Hans A. Einstein*, edited by H. W. Shen, pp. 3.1-3.20, Water Resources Publication, Littleton, Colorado.
- Coleman, S.E., and V. Nikora (2008), A unifying framework for particle entrainment. *Water Resour. Res.*, 44, W04415, doi:10.1029/2007WR006363.
- Coles, S. (2001), *An Introduction to Statistical Modeling of Extreme Values*, Springer-Verlag, London.
- Dancy, C. L., P. Diplas, A. Papanicolaou, and M. Bala (2002), Probability of Individual Grain Movement and Threshold Condition, *J. Hydraul. Eng.*, 128(12), 1069-1175.

- Davison, A., and Smith, R. (1990), Models for exceedances over high thresholds, *J. Royal Stat. Soc. Series B*, 52, 393-442.
- Dey, S. (1999), Sediment threshold, *Appl. Math. Mod.*, 23(5), 399-417.
- Dey, S., and K. Debnath (2000), Influence of streamwise bed slope on sediment threshold under stream flow, *J. Irrigat. Drain. Eng.*, 126(4), 255-263.
- Diplas, P., C.L. Dancey, A. O. Celik, M. Valyrakis, K. Greer, and T. Akar (2008), The role of impulse on the initiation of particle movement under turbulent flow conditions, *Science*, 322(5902), 717-720.
- Diplas, P., A. O. Celik, C. L. Dancey and M. Valyrakis (2010), Non-intrusive method for Detecting Particle Movement Characteristics near Threshold Flow Conditions, *J. Irrig. Drain. Eng.*, 136(11), 774-780.
- Drake, T. G., R. L. Shreve, W. E. Dietrich, P. J. Whiting, and L. B. Leopold (1988), Bedload transport of fine gravel observed by motion picture photography, *J. Fluid Mech.*, 1(192), 193-217.
- Embrechts, P., C. Klüppelberg, and T. Mikosch (1997), *Modelling Extremal Events for Insurance and Finance*. Springer, New York.
- Einstein, H. A., and E.-S. A. El-Samni (1949), Hydrodynamic forces on a rough wall, *Rev. Mod. Phys.*, 21(3), 520-527.
- Einstein, H. A. (1937), Bedload transport as a probability problem, PhD thesis, Zurich (English translation by Sayre, W.W. In: Shen, H.W. (1972), *Sedimentation*. Fort Collins Colorado).
- Einstein, H.A. (1950), The bed-load function for sediment transportation in open channel flows. *Tech. Rep. 1026*. United States Department of Agriculture.
- Fenton, J. D., and J. E. Abbott (1977), Initial movement of grains on a stream bed: The effect of relative protrusion, *Proc. Royal Soc. London, Series A*, 352(1671), 523–537.
- Gimenez-Curto, L. A. and M.A. Corniero (2009), Entrainment threshold of cohesionless sediment grains under steady flow of air and water, *Sedimentology*, 56, 493-509.
- Gumbel, E. J. (1954), Statistical theory of extreme values and some practical applications, *Applied Math Series*, 33, National Bureau of Standards, Washington, D.C.
- Gumbel, E. J. (1958), *Statistics of Extremes*, Columbia University Press, New York.
- Grass, A. J. (1970), Initial Instability of Fine Bed Sand, *J. Hydraul. Eng.*, 96(3), 619-632.

- Hofland, B., J. A. Battjes, and R. Booij (2005), Measurement of Fluctuating Pressures on Coarse Bed Material, *J. Hydraul. Eng.*, 131(9), 770-781.
- Hofland, B., and J. Battjes (2006), Probability Density Function of Instantaneous Drag Forces and Shear Stresses on a Bed, *J. Hydraul. Eng.*, 132(11), 1169–1175.
- Hosking, J. R. M., and J. R. Wallis (1987), Parameter and quantile estimation for the generalized pareto distribution, *Technometrics*, 29, 339-349.
- Kaplan, E. L. and P. Meier (1958), Nonparametric Estimation from Incomplete Observations, *J. Am. Stat. Assoc.*, 53(282), 457-481.
- Kirchner, J. W., W. E. Dietrich, F. Iseya, and H. Ikeda (1990), The variability of critical shear stress, friction angle, and grain protrusion in water-worked sediments, *Sedimentology*, 37(4): 647–672.
- Kotz, S., and S. Nadarajah (2000), *Extreme Value Distributions: Theory and Applications*, Imperial College Press, London.
- Kramer, H. (1935), Sand mixtures and sand movement in fluvial models, *Trans., ASCE*, 100(1909), 798–838.
- Kuhnle, R. A, and J. B. Southard (1988), Bed-load transport fluctuations in a gravel bed laboratory channel, *Water Resour. Res.*, 24(2), 247-260.
- Lavelle, J. W., and H. O. Mofjeld (1897), Do critical stresses for incipient motion and erosion really exist?, *J. Hydraul. Eng.*, 113(3), 370-385.
- Leadbetter, M. R., G. Lindgren, and H. Rootzen (1983), *Extremes and Related Properties of Random Sequences and Processes*, Springer, New York
- Ling, C.-H. (1995), Criteria for incipient motion of spherical sediment particles, *J. Hydraul. Eng.*, 121(6), 472-478.
- Lisle, I. G., C. W. Rose, W. L. Hogarth, P. B. Hairsine, G. C. Sander, and J. Y. Parlange (1998), Stochastic sediment transport in soil erosion, *J. Hydrol.*, 204(1-4), 217-230.
- Mantz, P. A. (1977), Incipient transport of fine grains and flanks by fluids-extended Shields diagram, *J. Hydraul. Div.*, 103, 601-615.
- McEwan, I., M. Sørensen, J. Heald, S. Tait, G. Cunningham, D. Goring, and B. Willetts (2004), Probabilistic Modeling of Bed-Load Composition, *J. Hydraul. Eng.*, 130, 129-139.

- Miller, M. C., I.N. McCave, and P. D. Komar (1977), Threshold of sediment motion under unidirectional currents, *Sedimentology*, 24, 507-527.
- Mitzenmacher, M. (2003), A brief history of generative models for power law and lognormal distributions, *Internet Mathematics*, 1, 226-51.
- Nelson, J. M., R. L. Shreve, S. R. McLean, and T. G. Drake (1995), Role of near bed turbulence structure in bed load transport and bed form mechanics, *Water Resour. Res.*, 31(8), 2071-2086.
- Paintal, A. S. (1971), Concept of Critical Shear Stress in Loose Boundary Open Channels. *J. Hydraul. Res.*, 9(1), 91-113.
- Papanicolaou A. N., P. Diplas, N. Evaggelopoulos, and S. Fotopoulos (2002), Stochastic Incipient Motion Criterion for Spheres under Various Bed Packing Conditions, *J. Hydraul. Eng.*, 128(4), 369-380.
- Paphitis, D. (2001), Sediment movement under unidirectional flows: an assessment of empirical threshold curves, *Coastal Eng.*, 43, 227-245.
- Paphitis, D., M. B. Collins, L. A. Nash, and S. Wallbridge (2002), Settling velocities and entrainment thresholds of biogenic sands (shell fragments) under unidirectional flows, *Sedimentology*, 49, 211-225.
- Pickands, J. (1975), Statistical inference using extreme order statistics, *Annals of Statistics*, 3, 119-131.
- Rodriguez-Iturbe, I., E. J., Ijjasz-Vasquez, R. L. Bras, and D. G. Tarboton (1992), Power law distributions of discharge mass and energy in river basins, *Water Resour. Res.*, 28, 1089-1093.
- Rodriguez-Iturbe, I., and A. Rinaldo (1997), *Fractal River Basins*, Cambridge University Press, Cambridge, 564 p.
- Rundle, J., W. Klein, and D. L. Turcotte (1996), *Reduction and predictability of natural hazards*, Westview Press.
- Schroeder, M. (1991), *Fractals, Chaos, and Power Laws*, W.H. Freeman and Com., New York.
- Schmeeckle, M. W., and J. M. Nelson (2003), Direct numerical simulation of bedload transport using a local, dynamic boundary condition, *Sedimentology*, 50(2), 279-301.

- Schmeeckle, M. W., J. M. Nelson and R. L. Shreve (2007), Forces on Stationary Particles in Near-Bed Turbulent Flows, *J. Geophys. Res.*, *112*, F02003.
- Shvidchenko, A. B., and G. Pender (2000), Flume study of the effect of relative depth on the incipient motion of coarse uniform sediments, *Water Resour. Res.*, *36*(2), 619-628.
- Sumer, B. M., Chua, L. H. C., Cheng, N.-S and J. Fredsoe (2003), Influence of Turbulence on Bed Load Sediment Transport, *J. Hydraul. Eng.*, *129*(8), 585-596.
- Sutherland, A. J. (1967), Proposed mechanism for sediment entrainment by turbulent flows, *J. Geophysical Res.*, *72*(24), 6183-6194.
- Tucker, G. E., and D. N. Bradley (2010), Trouble with diffusion: Reassessing hillslope erosion laws with a particle-based model, *J. Geophys. Res.*, *115*, F00A10, doi:10.1029/2009JF001264.
- Turcotte, D.L. (1997), *Fractals and chaos in geology and geophysics*, Cambridge Univ. Press, Cambridge.
- Turowski, J. M. (2009), Stochastic modeling of the cover effect and bedrock erosion, *Water Resour. Res.*, *45*, W03422, doi:10.1029/2008WR007262
- Turowski, J. M. (2010), Probability distributions of bed load transport rates: A new derivation and comparison with field data, *Water Resour. Res.*, *46*, W08501, doi:10.1029/2009WR008488.
- Valyrakis M., P. Diplas, C. L. Dancy, K. Greer, and A. O. Celik (2010), The role of instantaneous force magnitude and duration on particle entrainment, *J. Geophysical Res.*, *115*, F02006, doi:10.1029/2008JF001247.
- Vollmer, S., and M. G. Kleinhans (2007), Predicting incipient motion, including the effect of turbulent pressure fluctuations in the bed, *Water Resour. Res.*, *43*, W05410, doi:10.1029/2006WR004919.
- White, C. M. (1940), The Equilibrium of Grains on the Bed of a Stream, *Proc. R. Soc. London A*, *174*(958), 322-338.
- Wiberg, P. L., and J. D. Smith (1989), Model for Calculating Bed Load Transport of Sediment, *J. Hydraul. Eng.*, *115*(1), 101-123.
- Yalin, M. S., and E. Karahan (1979), Inception of sediment transport, *J. Hydraul. Eng.*, *105*(11), 1433-1443.

## **Chapter 4. Prediction of coarse particle movement with adaptive neuro-fuzzy inference systems\***

Manousos Valyrakis,<sup>1</sup> Panayiotis Diplas,<sup>1</sup> and Clint L. Dancey<sup>1</sup>

\*This chapter is a reprint of the article: Valyrakis, M., P. Diplas, and C. L. Dancey, (submitted), Prediction of coarse particle movement with adaptive neuro-fuzzy inference systems, *Hydrologic Processes*, (submitted on 1-28-2011).

<sup>1</sup>Baker Environmental Hydraulics Laboratory, Department of Civil and Environmental Engineering, Virginia Polytechnic Institute and State University, Blacksburg, Virginia, USA.

### **Abstract**

The use of a neuro-fuzzy approach is proposed to model the dynamics of entrainment of a coarse particle by rolling. It is hypothesized that near bed turbulent flow structures of different magnitude and duration or frequency and energy content are responsible for the particle displacement. A number of Adaptive Neuro-Fuzzy Inference System (ANFIS) architectures are proposed and developed to link the hydrodynamic forcing exerted on a solid particle to its response and model the underlying nonlinear dynamics of the system. ANFIS combines the advantages of fuzzy inference (If-Then) rules with the power of learning and adaptation of the neural networks. The model components and forecasting procedure are discussed in detail. To demonstrate the model's applicability for near threshold flow conditions an example is provided, where, flow velocity and particle displacement data from flume experiments are used as input and output for the training and testing of the ANFIS models. In particular, a Laser Doppler velocimeter (LDV) is employed to obtain long records of local streamwise velocity component upstream of a mobile exposed particle. These measurements are acquired synchronously with the time history of particle's position detected by a setup including a He-Ne laser and a photodetector. The representation of the input signal in the time and frequency domain is implemented and the best performing models are found capable of reproducing the complex dynamics of particle response. Following a trial and error approach the different models are compared in terms of their efficiency and forecast accuracy using a number of performance indices.

**Key Words:** forecasting, grain entrainment, ANFIS, wavelet transform

## 1. Introduction

The determination of the exact conditions under which incipient motion of bed material occurs, constitutes a central problem in engineering and earth surface dynamics. Obtaining better understanding of the fundamental process and dynamics of grain mobilization is essential for a variety of applications ranging from fluvial hydraulics and environmental engineering to stream ecology. Common examples range from the design of stable channel bed and banks and the protection of hydraulic structures against scouring processes, to the estimation of flushing flow conditions downstream of a reservoir.

Since the seminal work of *Shields* [1936], many researchers have adopted a deterministic approach [e.g. *White*, 1940; *Coleman*, 1967; *Ling*, 1995], suggesting that grain entrainment is initiated when a spatially and temporally averaged bed shear stress exceeds a critical value. However, such a perspective has been challenged by many researchers proposing a stochastic approach due to the nature of turbulent flow and the role of instantaneous stresses. In particular, *Lavelle and Mofjeld* [1987] and *Buffington and Montgomery* [1997] showed that particle motion may occur for thresholds well below the defined critical Shields' stress values. As opposed to the traditional deterministic criterion of mean shear stress, a probabilistic framework is motivated by the fluctuations of the hydrodynamic forces [*Einstein and El-Samni*, 1949; *Cheng and Chiew*, 1998; *Papanicolaou et al.*, 2002; *Wu and Yang*, 2004; *Hofland and Battjes*, 2006], the variability of the local bed microtopography and grain heterogeneities (*Paintal*, 1971; *Fenton and Abbott*, 1977; *Kirchner et al.*, 1990). In addition, a number of different methods have been used to define critical levels for the onset of transport of sediment grains, unavoidably leading to variability in the proposed thresholds or even methodological bias [*Lavelle and Mofjeld*, 1987; *Buffington and Montgomery*, 1997].

Recently the neuro-fuzzy paradigm has been successfully implemented in a number of disciplines, having a wide range of applications in nonlinear modelling and prediction [*Jang*, 1997]. A comprehensive review demonstrating a plethora of applications of data driven networks in hydrology is given in [*ASCE Task Committee*, 2000]. More recently such models have been applied in river flow forecasting [*Sivakumar et al.*, 2002], prediction of sediment transport [*Kisi*,

2003; *Tayfur et al.*, 2003] and estimation of the impact of scouring processes downstream of hydraulic structures [*Azmathullah*, 2006]. The utility of those networks in addressing the problem of onset of particle entrainment is apparent, considering that the stochastic phenomenon of bedload transport becomes more intermittent and episodic at low mobility flow conditions [*Diplas et al.*, 2010]. In addition, the use of fuzzy inference systems appropriately accounts for the subjectivity and vagueness inherent in precisely defining threshold values for the inception of particle movement as well as for the sensitivity and bias due to the method of determination.

Here the neuro-fuzzy approach is employed as a predictive tool in an attempt to model the dynamics of individual entrainment of coarse particles at near threshold flow conditions. The proposed adaptive neuro-fuzzy inference system (ANFIS) combines the features of neural networks such as the data driven process of learning, with fuzzy inference systems which account for imprecision and uncertainties regarding the definition and the quantitative data. In the following section, the framework under which this data-driven modeling technique may be implemented to predict the initiation of a particle sediment motion is provided. The architecture of the ANFIS networks is discussed. As a case study, the technique is demonstrated using a number of different ANFIS architectures trained with high frequency near bed flow velocity data related to the history of hydrodynamic forces exerted on a particle. The setup and method used for the acquisition of the experimental data are reported. Representations of the input in time and frequency domain are employed to train and test the model and the results of the better performing architectures are compared via different statistical indices. The validated ANFIS models generally perform well, effectively modeling the dynamics of particle entrainment at low mobility flow conditions.

## **2. Framework for the prediction of the onset of particle entrainment**

In this section, the context under which ANFIS may be implemented to model the dynamics of particle entrainment as well as the associated physical mechanisms thought to govern this process are provided, first in time and then in frequency domain. As every data driven method, the model performance greatly depends on the ability of the input to relate to the desired output. The rationale, under which the representation of the velocity signal in the time and frequency domain may be used as input for the ANFIS model, is developed next.

## 2.1. Time domain forecasting

In accordance with the stochastic view introduced earlier, the role of instantaneous, fluctuating rather than the mean stresses is outlined. In particular, recent experiments [Hofland *et al.*, 2005; Schmeeckle *et al.*, 2007; Vollmer and Kleinhans, 2007; Gimenez-Curto and Corniero, 2009] emphasize the significance of the peak hydrodynamic forces in the vicinity of the boundary for particle entrainment particularly at low mobility flow conditions. Typically, the forces acting on an exposed particle forming a tetrahedral arrangement is considered (Figure 1). Of interest is the response of the particle, which depends on the ratio of the hydrodynamic and resisting forces, assumed to act through its center of gravity as illustrated in Figure 1. Whenever the ratio is greater than one, the total force applied on the particle is positive and its mobilization is possible. In this case, the sum of drag ( $F_D$ ), lift ( $F_L$ ) and buoyancy ( $B_f$ ) force components along the direction of particle displacement, exceed the corresponding component of particle's weight ( $W$ ):

$$F_D \sin(\theta_0 - \alpha) + F_L \cos(\theta_0 - \alpha) \geq f_h W_s \cos \theta_0 \quad (1)$$

where  $\theta_0$ , is the pivoting angle, formed between the horizontal and the lever arm ( $L_{arm}$ , in Figure 1),  $W_s = W - B_f$ , is the submerged particle weight (assuming steady, uniform flow),  $\alpha$  is the bed slope,  $f_h = [\rho_s - \rho_f (1 - C_m)] / (\rho_s - \rho_f)$ , is the hydrodynamic mass coefficient with  $C_m$  the added mass coefficient which for water is equal to 0.5 [Auton, 1988],  $\rho_f$ , the density of fluid and  $\rho_s$ , the particle's density [Valyrakis *et al.*, 2010a]. Equation (1) describes the equilibrium of torques about the axis of rotation located at the origin of the polar coordinate system ( $D'$ , in Figure 1).

Due to the absence of detailed information regarding the nature and relative magnitude of the components of the instantaneous hydrodynamic force, it is convenient to attempt a parameterization based on the square of the local streamwise flow velocity ( $u$ ), in a manner similar to the classical drag force parameterization. If for example a constant value is assumed for the drag coefficient ( $C_D$ ) and the lift force is neglected, equation (1) may be expressed as:

$$u^2 \geq u_{cr}^2 = \frac{2}{\rho_f C_D A} f_h W_s \frac{\cos \theta_0}{\sin(\theta_0 - \alpha)} \quad (2)$$

with  $A$  the particle's projected area perpendicular to the flow direction. Equation (2) defines an approximate condition for the onset of particle entrainment, requiring only the record of the instantaneous velocity upstream the particle.

Furthermore, the theoretical and experimental work of *Diplas et al.* [2008], *Valyrakis et al.* [2010a] and *Celik et al.* [2010] showed that, in addition to the magnitude, the duration of the peak turbulent events satisfying the above condition (equation 2), is also of equal significance. Considering the above physically based theories, data driven models are developed here to simulate the dynamics of particle entrainment. It is hypothesized that turbulent flow events of high magnitude ( $u \geq u_{cr}$ ) and sufficient duration are responsible for the transport of a particle. This is implemented in the ANFIS network for the prediction of the displacement of the particle,  $\Delta x(t+\Delta t)$ , by using as input  $u(t)$  and an appropriate number of shifted inputs,  $u(t-i\Delta t)$ , each lagging over a duration  $i\Delta t$ , to account for the variability of magnitude and duration of the flow events. This can be represented by the following input-output relation:

$$\Delta x(t + \Delta t) = \Phi_1(u(t), u(t - \Delta t), \dots, u(t - i\Delta t), \dots, u(t - n\Delta t)), \text{ for } i = 1, \dots, n \quad (3)$$

where,  $\Phi_1$  is the ANFIS model that maps the vector of  $n+1$  streamwise velocity inputs lagging by  $\Delta t$ , to the predicted output  $\Delta x(t+\Delta t)$ . The lag ( $\Delta t$ ) should be of the same order as the characteristic timescale of a flow event leading to entrainment, commonly ranging from 10 to 100 ms depending on the size of the particle.

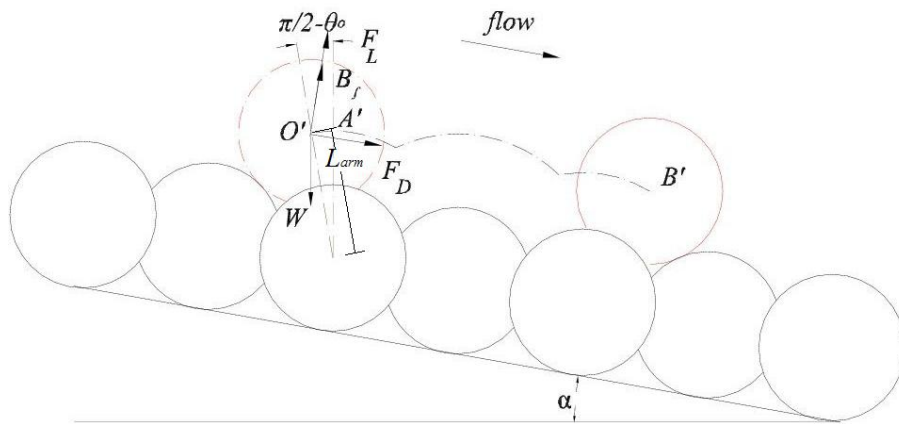


**Figure 1.** Illustration of forces acting on a fully exposed particle (dashed circle), leading to its entrainment by rolling (following the trajectory  $O'B'$ ).

## 2.2. Frequency domain representation

Distinct from the above force-duration approach for the prediction of particle entrainment, is the energy-frequency concept developed here. While the former is concerned with the force and duration of a flow event, the latter focuses on its energy content and corresponding frequency. Preliminary analysis of mobile particle flume experiments reveals the possibility that dislodgement may be caused from a sequence of energetic flow pulses, rather than a single one [Valyrakis *et al.*, 2010b]. In the frequency domain those flow pulses may appear as a group of sub-events of different energy content over a range of characteristic frequencies. Thus it is postulated that the frequencies and energy content of the flow signal is a useful representation for the model input.

Traditional tools for the analysis of turbulent flows are techniques based on Fourier transform such as the power spectral density, providing the distribution of energy among a range of flow frequencies. However, these methods have the disadvantage that they are temporally averaged, thus not preserving any information with regard to when an event occurred in time. Wavelet analysis overcomes this limitation by providing information both on the energy content of the signal, as well as the energetic frequencies of the signal at a specific instant. In this manner, it allows for time localization of the distribution of flow energy over a range of relevant frequencies of interest. Wavelet analysis has a plethora of applications ranging from geophysics [Kumar and Foufoula-Georgiou, 1997] to turbulence [Farge, 1992]. Singh *et al.* [2009], demonstrated its utility for the study of the entrainment of coarse grains which especially at low solid discharges is highly nonlinear and intermittent. Since the temporal context of the signal is preserved, time histories of input-output pairs can be formed and used in the ANFIS models to predict the response of the particle. Two basic methods, namely the continuous wavelet transform and the wavelet multiresolution analysis, are employed here to provide appropriate input representations that enable ANFIS to detect the energy containing frequencies that contribute to inception of motion.

### 2.2.1. Continuous wavelet transform

The continuous wavelet transform of the local streamwise velocity signal,  $u(t)$ , at a scale  $\phi > 0$  and translation parameter,  $x$ , is defined as the convolution of  $u(t)$  with  $\psi^*$ :

$$W_u(\phi, x) = \frac{1}{\sqrt{\phi}} \int_{-\infty}^{\infty} u(t) \psi^* \left( \frac{t-x}{\phi} \right) dt \quad (4)$$

where,  $W_u(\phi, x)$  corresponds to the value (or coefficient) of the wavelet transform and  $\psi^*$  denotes the complex conjugate of the basis (mother) wavelet function  $\psi$ , which has been scaled and shifted by  $\phi$  and  $x$ , respectively. The square of the continuous wavelet transform ( $|W_u(\phi, x)|^2$ ) corresponds to the power of the signal. Thus,  $W_u(\phi, x)$  offers a representation of the energy content of the signal localized in time and frequency.

For example, a fraction of the time series of  $u(t)$ , shown in Figure 2a, is analyzed using equation 4 and Daubechies D3 as the mother wavelet. The corresponding plot of the continuous wavelet transform coefficients, for a range of smoothly varying scale and translation parameters, is illustrated in Figure 2b. The lower scales correspond to the high frequencies of the signal, while the higher scales refer to the slowly fluctuating components of the signal. Careful observation of the displacement signal (Figure 2a) with the wavelet map (Figure 2b), reveals the existence of certain patterns with regard to when entrainment and deposition are initiated, corresponding to positive versus negative peaks (Figure 2b). While it is difficult to derive a physically based formulation for the onset of movement, models such as ANFIS are employed to learn from these trends and provide empirical rules. Here, the hypothesis that prediction of particle displacement depends on knowledge of the energy content of different flow frequencies, is described by the following equation:

$$\Delta x(t + \Delta t) = \Phi_2(W_u(\phi_1, 0), \dots, W_u(\phi_1, 0), \dots, W_u(\phi_n, 0)), \text{ for } i = 1, \dots, n \quad (5)$$

with  $\Phi_2$ , the ANFIS model that performs nonlinear mapping of the input vector of  $n$  wavelet coefficients at various scales,  $\phi_i$ , to the output  $\Delta x(t + \Delta t)$  at a time step  $\Delta t$  in the future.

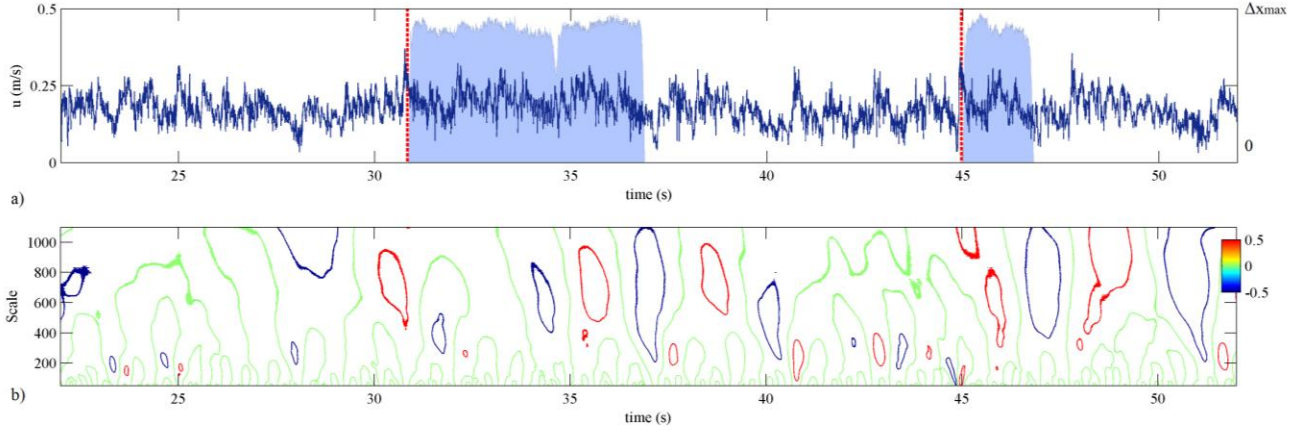


**Figure 2.** Illustration of the continuous wavelet transform of the streamwise velocity  $u$ : a) time history of  $u$  and of the displacement signal  $\Delta x$  (vertical dashed lines show instants of onset of entrainment), b) wavelet coefficient maps of the corresponding signal over a wide range of scales of interest.

### 2.2.2. Wavelet multiresolution analysis

A less computationally intensive method to the continuous wavelet transform which computes values for practically all scales in a given range is the discrete wavelet transform. The discrete wavelet transform, can be implemented using scale and translation parameters that change in discrete steps [Mallat, 1989]:

$$W_u(m, n) = \frac{1}{\lambda_0^{m/2}} \sum_{i=0}^{N-1} u(t_i) \psi\left(\frac{t_i - nt_0 \lambda_0^m}{\lambda_0^m}\right) \quad (6)$$

where  $m$  and  $n$  are integers which define the scale (dilation),  $\lambda_0^m$ , and translation,  $nt_0 \lambda_0^m$ , parameters. Commonly the dyadic representation with  $\lambda_0=2$  is preferred, where the used scale and translation parameters are powers of two. According to the multiresolution formulation of the discrete wavelet transform, the signal  $u(t)$  may be decomposed into a low frequency coarse component (approximation,  $A_I$ ) and a high frequency component (detail,  $D_I$ ). At the next level of decomposition the approximation is split into the next level approximation and detail (e.g. Figure 3). Recursive application of the above algorithm over  $\kappa$  levels results in signal components of successively decreasing resolution. According to Mallat [1989], the original signal can be

reconstructed by progressively adding the approximation of the  $\kappa$  level with the details of all levels. For instance, for the two level decomposition shown in Figure 3, the original signal is obtained by adding the second level approximation and detail to the first level detail ( $S=D_1+A_2+D_2$ ).

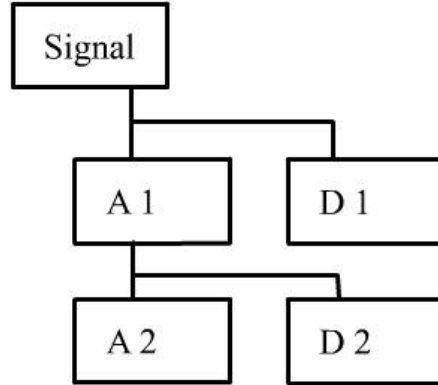


**Figure 3.** Schematic diagram illustrating the two-level wavelet decomposition of a signal,  $S$ , into approximations ( $A_i$ ) and details ( $D_i$ ), where  $i$ , refers to the level of decomposition of  $S$  or  $A_{i-1}$ .

As an example, the wavelet multiresolution method is applied to a segment of the time series of  $u(t)$  (Figure 4a, showing also the entrainment events,  $\Delta x$ ). The streamwise velocity signal is analyzed using the Haar wavelet, up to level two,  $\kappa=2$ , showing the second level approximation and the first and second level details (Figure 4b, c and d, respectively). Similar to the above formulation (equation 5), the output is now a function of the various flow velocity signal components:

$$\Delta x(t + \Delta t) = \Phi_3(A_n(t), D_1(t), \dots, D_i(t), \dots, D_n(t)), \text{ for } i = 1, \dots, n \quad (7)$$

where,  $\Phi_3$  is the ANFIS architecture using as input vector the  $n$  details and the  $n$  level approximation obtained from the  $n$  level decomposition of the signal.

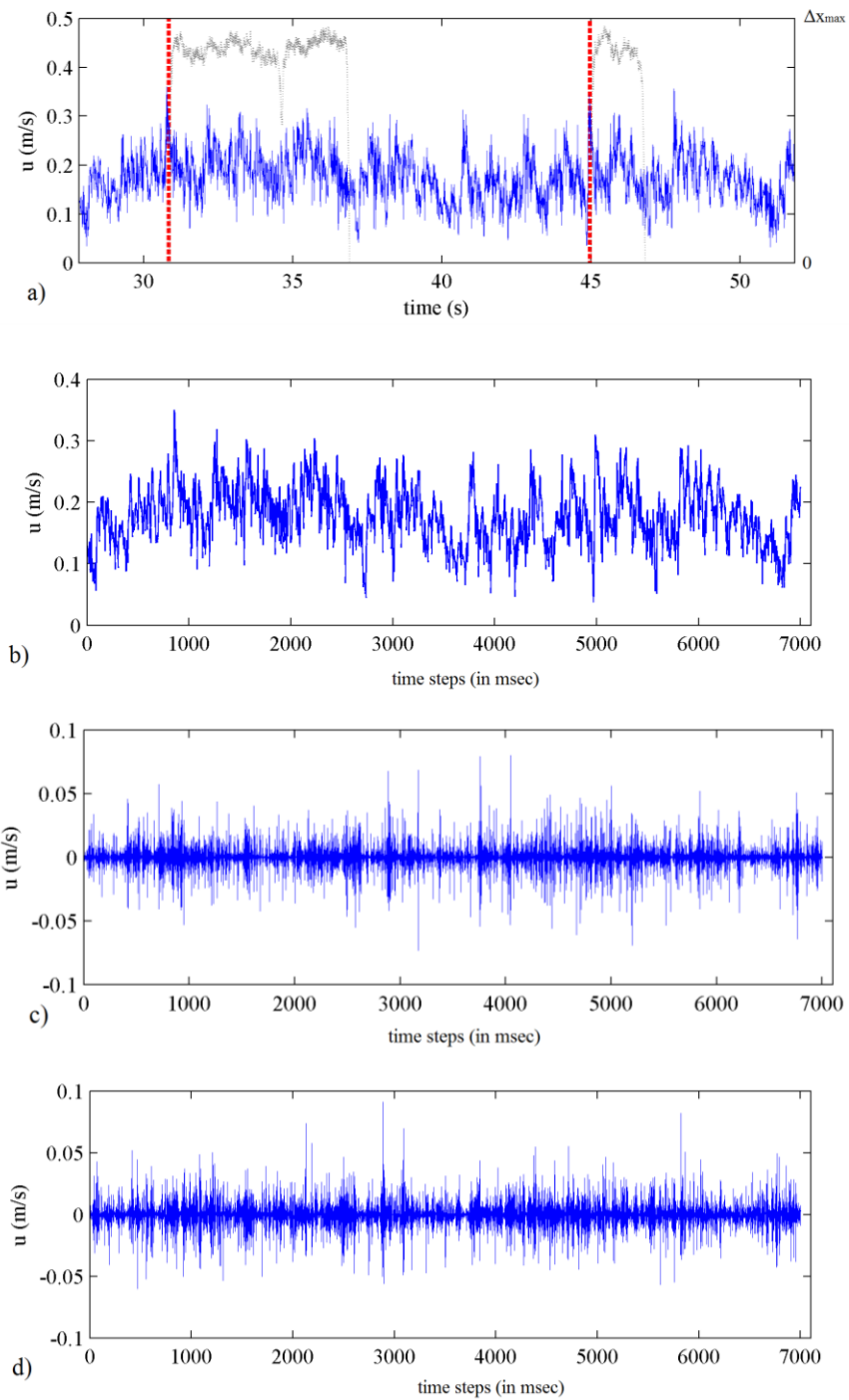


**Figure 4.** Demonstration of the wavelet multiresolution analysis (two-level decomposition) of a fraction of the streamwise velocity signal: a) original signal ( $u$ ) and displacement signal (vertical dashed lines show instants of onset of entrainment), b) level-2 approximation of  $u$ , c) level-1 detail of  $u$ , and d) level-2 detail of  $u$ .

### 3. ANFIS Methodology

#### 3.1. ANFIS overview

Adaptive Neuro-Fuzzy Inference Systems (ANFIS) combine the advantages of both Artificial Neural Networks (ANN) and Fuzzy Inference Systems (FIS). They demonstrate inherent learning abilities due to the neural network training algorithm incorporated for the tuning of the nonlinear parameters, while they also have a rule based structure to perform fuzzy reasoning and extract the dynamics of the studied phenomenon.

ANN are data driven algorithmic structures which are able to accurately predict the evolution of a nonlinear system by adapting to it. In contrast to the conventional physics oriented numerical, empirical or analytical approaches they do not require *a priori* knowledge of the system or construction of rigorous approximating relationships. They are data driven models able to perform well if their structure has the required complexity to nonlinearly associate the input-output pairs. However, the exact relationship between input and output remains hidden in the network structure, thus they work as “black boxes” since they are unable to reveal the way the variables interact with each other. On the other hand fuzzy logic is able to provide rules for the underlying dynamics of the studied system dealing also effectively with impreciseness of the utilized data [Zadeh, 1973]. For this reason ANFIS is thought to integrate the mentioned virtues of both ANN and FL into a powerful computational hybrid model [Jang, 1993].

Over the last decades soft-computing methods have been extensively utilized and are successfully employed for the prediction of sediment load [Nagy *et al.*, 2002; Yitian and Gu, 2003; Ariffin *et al.*, 2004]. In a previous study [Valyrakis *et al.*, 2006], the authors constructed several ANFIS structures and compared them with ANN models of about the same structural complexity, for the prediction of dislodgement events of a particle. Generally the ANFIS models demonstrated superior performance compared to the ANN.

#### 3.2. Algorithm architecture

As an example, a first order Takagi and Sugeno fuzzy inference system with two if-then rules, two inputs ( $x, y$ ), an output  $f_k(x,y)$ , may be expressed as follows [Sugeno, 1985]:

Rule 1: If  $x$  is  $A_1$  and  $y$  is  $B_1$ , Then  $f_1=p_{1,1}x+p_{2,1}y+r_1$

Rule 2: If  $x$  is  $A_2$  and  $y$  is  $B_2$ , Then  $f_2=p_{2,1}x+p_{2,2}y+r_2$

where  $A_i, B_i$  are values of membership functions for  $x, y$  respectively, in the premise part and  $p_{i,k}$  and  $r_k$  are the linear parameters of the consequent part, for each input parameter  $i$  and rule  $k$ .

The ANFIS is essentially a Takagi and Sugeno type fuzzy inference system using rule based thinking and employs a multilayer feed-forward ANN, to enable learning and optimize the input-output mapping process [Jang, 1993]. As shown in Figure 5, each layer of ANFIS has adaptive or fixed nodes,  $n$  number of inputs ( $x_i, i=1, \dots, n$ ),  $n_m$  membership functions (or linguistic labels  $A_{i,j}, i=1, \dots, n$  and  $j=1, \dots, n_m$ ) for each input  $x_i$  and a total of  $n_R$  number of rules. Typically the ANFIS model consists of five layers and a synoptic description of each of the layers is given as follows.

The first layer consists of a total of  $N$  adaptive nodes ( $N=nn_m$ , one for every linguistic label  $A_{i,j}$ ) with a membership function ( $\mu_{i,j}$ ), which maps the input  $x_i$ , to a certain output value:

$$O_{i,j}^1 = \mu_{i,j}(x_i) \quad (8)$$

where,  $O_{i,j}^h$  is the output of the  $h$  layer. Widely used are bell shaped functions bounded from zero to one from which the most popular is the Gaussian:

$$\mu_{i,j}(x) = \exp \left[ - \left( \frac{x - c_{i,j}}{2\sigma_{i,j}} \right)^2 \right] \quad (9)$$

defined by  $c_{i,j}, \sigma_{i,j}$  named as premise parameters. The second layer consists of the rule nodes, each of which combines the transmitted signals by using membership functions of different input variables. Thus the output of each node is analogous to the firing strength (or degree of fulfillment) of the rule it represents. The operator used to combine the signals is the multiplication (AND) T-norm fuzzy operator [Tanaka, 1996]:

$$O_k^2 = w_k = \prod \mu_{i,j}(x) \quad (10)$$

meaning that the antecedent part of  $k^{th}$  rule which involves one membership function  $\mu_A(x)$  for each input, is satisfied proportionally to the weight  $w_k$ . In the third layer, the firing strength of each rule is normalized with their sum. This normalization is performed calculating the ratio:

$$O_3^k = \overline{w}_k = \frac{w_k}{\sum_{i=1}^{n_R} w_i} \quad (11)$$

where,  $\overline{w}_k$  is the normalized firing strength for  $k^{th}$  rule. The consequent part of fuzzy reasoning is performed in the fourth layer where the contribution of each of the rules ( $k=1, \dots, n_R$ ) in the final output is given by:

$$O_k^4 = \overline{w}_k f_k = \overline{w}_k \left( \sum_{i=1}^{n_R} p_{i,k} x_i + r_k \right) \quad (12)$$

with  $p_{i,k}$ ,  $r_k$  the consequent parameters. In the final layer the total output is calculated as the sum of the normalized weighted output of each rule, by adding the signals transferred from the previous layer:

$$O^5 = \sum_{i=1}^{n_R} \overline{w}_i f_i \quad (13)$$

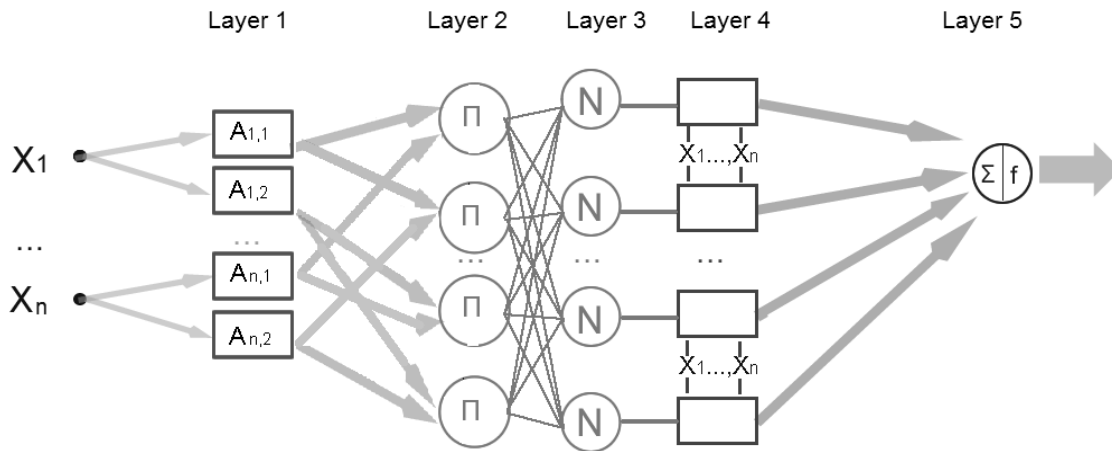


**Figure 5.** ANFIS architecture for an  $n$ -input Sugeno model with 2 membership functions per input ( $A_{i,j}$ ,  $j=1,2$ ) and  $N_R$  number of rules (rectangular boxes represent adaptive nodes, circles represent fixed nodes).

The above equations describe the forward pass of the input signal and computations through each layer of the network towards the calculation of the output. The hybrid learning procedure proposed by *Jang* [1993], involves tuning of the linear adaptive parameters  $p_{i,k}$ , and  $r_k$  of the consequent part, by means of a linear optimization procedure such as the least square method, so that the error in the output layer is minimized. The difference of calculated output from the observed output is defined as error of the output layer. While the above parameter tuning occurs in a forward pass of the transmitted signal, ANFIS is also trained with supervised learning, which involves a backward propagation of the output error. During this backward pass, the model adjusts its premise part adaptive parameters ( $c_{i,j}$ ,  $\sigma_{i,j}$ ), with a nonlinear optimization method such as gradient descent. In this manner the network learns the underlying dynamics of the modeled process by adjusting the weights between its nodes.

There exists no guiding rule in defining a priori an optimal architecture for ANFIS since it is highly dependent on the nature and dynamic complexity of the studied phenomenon. In general a complex structure with many nodes attains high accuracy (small training error) but poor generalization ability (higher testing error). In contrast a simple, relatively to the size of the training data set, architecture exhibits the worse approximation and good generalization. Thus optimization of the ANFIS parameters is performed following a trial and error method.

#### 4. Description of setup and experimental method

A series of incipient motion experiments were performed to obtain synchronous time series of the local flow velocity and particle position indicating the time of entrainment and deposition. The Viton<sup>®</sup> spherical particle (8mm diameter and specific gravity of 18.3), rests on top of four layers of fully packed glass beads of the same size, forming a tetrahedral arrangement (Figure 6). This arrangement renders it completely exposed to the incident flow, so that entrainment is possible in rolling mode. The test section is located about 15 m downstream from the inlet of the 20.5 m long and 0.6 m wide flume to guarantee fully developed flow conditions. The bed slope ( $\alpha$ ) remains fixed to 0.25% and equals the surface slope ensuring that the flow is uniform. The use of non-interference techniques for the data acquisition guarantees more precise identification of the flow events as well as entrainment instances, are employed to achieve higher accuracy [Diplas *et al.*, 2010].

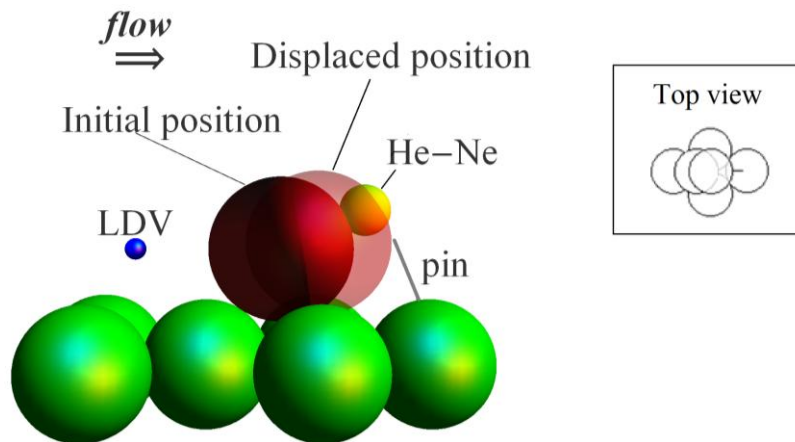


**Figure 6.** Sketch (side view) of the experimental setup (top view shown in the inset), illustrating the range of possible locations of the mobile particle and the local base particle arrangement with a retaining pin to constrain further entrainment downstream. The targeting locations of the LDV and He-Ne laser are also depicted in relation to the mobile sphere.

The time history of the streamwise and perpendicular to the channel bed velocity components ( $u(t)$ ,  $v(t)$ ) are obtained by means of laser Doppler velocimetry (4W Argon ion LDV) at an average sampling frequency of about 350Hz. Their targeting location with respect to the mobile particle is shown in Figure 6. The LDV measurement volume is located one diameter upstream

of the particle and along its centerline. A multichannel signal processor enables simultaneous recording of the flow measurements with the displacement signal of the spherical particle.

The motion of the mobile sphere is recorded via a particle tracking system composed of a photomultiplier tube (PMT) and a low power (25-30mW) He-Ne laser source. As seen in Figure 6, the He-Ne laser beam is aligned to partially target the test particle. Calibration of the setup showed that the angular dislodgement of the targeted particle is a linear function of the signal intensity of the PMT. The obtained signal is transformed to the dislodgement events history, so that the resting and displaced position correspond to dislodgements of 0 and  $\Delta x_{max}=1\text{mm}$ . Such an “electric eye” arrangement has many advantages compared to previously employed methods [Valyrakis *et al.*, 2006]. In particular, the signal is obtained at high frequency (about 350Hz, with a capacity of up to 1000Hz) and resolution as well as synchronously to the velocity measurements in contrast to the more commonly employed motion photography technique where data acquisition rate is limited to 60fps (for a commercial camcorder), and particle movement is detected visually.

A continuous series of entrainments is made possible due to a restraining pin located about 1 mm downstream of the mobile sphere (see Figure 6), which limits the maximum dislodgement of the grain to the displaced position. The particle will remain dislodged and attached to the pin as long as the hydrodynamic forces exerted on it exceed the resisting gravitational component. When this condition ceases the particle cannot sustain its position and will eventually fall back to its initial position. This technique, as opposed to traditional approaches, allows acquisition of relatively longer measurements, since there is no need of interrupting the experiment in order to manually place the particle back to its resting configuration, once it has been removed from the test section.

As a case study, experimental data corresponding to one of the nearly incipient motion flow conditions are analyzed to demonstrate the applicability and performance of the proposed approach. The models are also implemented to another two flume experiments, also referring to uniform low mobility flow conditions, which were carried out separately to ensure reproducibility of the results and consistent performance. For each of the experimental runs the flow conditions were stabilized to achieve a constant rate of particle entrainment,  $f_E$ , over long durations (about 1 hour). The 4 minutes long, synchronized time series of flow signal are employed to train and test the models. The mean quantities of main flow and grain response are

shown in Table 1. All of the performed experiments refer to near incipient motion conditions (nearly 3 entrainments per minute) of about the same mean local velocity,  $u_m$ , dimensionless bed shear stress,  $\tau^*$ , and turbulent intensity (equal to 0.348).

**Table 1.** Summary of time averaged local flow characteristics and mean particle entrainment rate for incipient entrainment experiments.

$u_m$ (m/sec)	$u_{st}$ (m/sec)	Turbulent intensity	$f_e$ (entrainments/sec)
0.115	0.040	0.348	0.055

## 5. ANFIS simulations

To demonstrate the validity of the proposed framework as well as the utility of ANFIS in modelling the dynamics of particle mobilization at low mobility flow conditions, an application example is provided as a case study.

### 5.1. Data preparation

For the training and validation of the constructed ANFIS architectures, the data sets are split into two equally sized sets, namely the training and testing (or validation) subsets. The two subsets are of the same size in order to sufficiently train the model without compromising the validation procedure. The role of the training set is to compute the model weights by tuning the adaptive nodes in the consequent and premise part of each fuzzy rule. The validation subset is utilized to simulate the network and provide a model with good generalization ability. These data sets must not have any overlapping data points, so that the validation procedure is not biased and ensure that the performance of the models is representative of their forecasting ability. In addition, the statistical properties of the subsets remain constant (Table 2), which indicates that they represent about the same region of the solution domain.

## 5.2. Input selection

For this study, a number of ANFIS architectures of different complexity are developed, using the above input structures, by varying the size of the input vector ( $n$ ) and the number of membership functions per input ( $n_m$ ). Their input space is divided into  $n_R = n \cdot n_m$  fuzzy subspaces, each of which is characterized/defined-governed by a Takagi and Sugeno fuzzy if-then rule. The number of utilized membership functions determines the granularity (or level of detail) of the model [Zadeh, 1997], while the size of the input vector relates to the number of parameters that contain sufficient information for the prediction of the output. If too many are used there exists a possibility of contamination of the input vector with information irrelevant to the modeled dynamics, deteriorating the predictability of the model forecast.

There exists no methodical approach in estimating the type and number of parameters that provide the best architecture performance. Thus a trial and error approach is followed testing for the performance of a wide range of network combinations, with parameters ranging from 3 to 4 inputs and 2 or 3 membership functions per input. After the input vector and model parameters are appropriately defined, the training and testing process follows, to evaluate its performance. A number of ANFIS models that employed a smaller number of fuzzy inference rules, showed poor performance, implying that such low complexity models have poor ability in describing the dynamics of particle response. On the other hand some of the examined models with number of inputs or membership functions greater than 4 and 3 respectively, improved the performance for the already seen data from the training subset but reduced the prediction ability for unseen data (e.g. from the testing subset). This is commonly referred to as overtraining of the network, and is undesired since it reduces the overall model performance. Based on this observation model structures of higher complexity were not further investigated.

The particle response forecasting algorithms use one of the three input structures presented in equations (3), (5) and (7), where the input signal is represented in either the time domain or the frequency domain. In particular, the best performing models for each input structure and their corresponding characteristics, are shown in Table 2. For example,  $\Phi_I$  uses a time delay structure of the velocity signal (equation 3). The best performing network (Table 2) has 3 inputs (time delay velocity signal), 1 output (displacement signal), 2 membership functions per input and 9 fuzzy inference rules. It follows the same structure presented in Figure 5, with a total of 42

fitting parameters, 6 of which belong to the premise part of the model while 36 to the consequent part. Cross-correlation between the time series of flow velocity and particle dislodgement may be utilized to acquire information regarding the temporal lag of flow velocity events that mostly influence the particle displacement at a certain time instant. Such a time lag is of the order of 100 ms for the conducted incipient motion experiments and may be used as a rough guide for the  $n$  and  $\Delta t$  to be applied.

The other two input structures employ time series of continuous wavelet coefficients using the Symlet of 4<sup>th</sup> order as mother wavelet ( $\Phi_2$ ) and a wide range of scales (from 100 to 1000) or time series of wavelet coefficients obtained from the two level decomposition of the multiresolution discrete wavelet transform ( $\Phi_3$ ), using Daubechies third order (D3) as mother wavelet. As shown in Table 2, the number of parameters for the best performing  $\Phi_2$  and  $\Phi_3$  models is slightly above those of the corresponding  $\Phi_1$  model. In the following the proposed models are compared and the criteria to evaluate their performance are presented.

**Table 2.** Characteristics of selected ANFIS models for each input representation.

ANFIS name	Input domain representation	Number of input ( $n$ )	Number of MF ( $n_m$ )	Number of rules ( $n_R$ )
$\Phi_1$	Time	3	2	9
$\Phi_2$	Continuous wavelet	4	3	64
$\Phi_3$	Discrete wavelet	3	3	27

## 6. Discussion

### 6.1. ANFIS evaluation

To assess the overall predictive efficiency of each of the developed models and allow their comparison, the following commonly employed accuracy criteria and error metrics are adopted [e.g. *Twomey and Smith, 1996*]. The performance of the different ANFIS architectures is evaluated using certain criteria based on the residual between observed and predicted values

( $e_{(i)}=o_{(i)}-t_{(i)}$ ), such as the root mean square error (*RMSE*), the mean average error (*MAE*) and the normalized coefficient of efficiency (*CE*):

$$RMSE = \sqrt{\frac{\sum_{i=1}^N (o_i - t_i)^2}{N}} \quad (14a)$$

$$MAE = \frac{\sum_{i=1}^N |o_i - t_i|}{N} \quad (14b)$$

$$CE = 1 - \frac{\sum_{i=1}^N (o_i - t_i)^2}{\sum_{i=1}^N (t_i - t_{mean})^2} \quad (14c)$$

where  $o_i, t_i$  are the computed and the observed (target) output the for each ( $i$ ) of the  $N$  data points, while  $t_{mean}$  is the mean of the observed values. The *MAE* is a weighted average of the absolute errors and the lower it is the better a model performs. The lower the values of *RMSE* and *MAE* are and closer to zero, the more precise the model is. The *CE* measures the model's ability to detect the occurrence of particle entrainment and varies from minus infinity to one for poor and perfect forecasting ability, respectively. The correlation coefficient (*CC*) is a measure of the strength of the interrelation between the observed and predicted values:

$$CC = \frac{Cov(o_i, t_i)}{\rho_{o_i} \rho_{t_i}} \quad (15a)$$

$$Cov(o_i, t_i) = \sum_{i=1}^N [(o_i - o_{mean})(t_i - t_{mean})] / N \quad (15b)$$

where  $\rho_{o_i}, \rho_{t_i}$  are the standard deviations of the model's output and the target respectively and  $Cov(\cdot)$  is their covariance. The *CC*, ranges from 0 to 1, with a value closer to 1 indicating better performance.

## 6.2. ANFIS simulation results

In order to assess the models' sensitivity to the size of shifted input vectors and number of membership functions per input, a number of ANFIS architectures are examined. The prediction efficiencies of the models are compared on the basis of the presented performance metrics, their computational robustness and generalization ability.

The above error indices are computed for both training and testing (or validation) subsets in order to assess the accuracy as well as the generalization ability of the model. Specifically, the training and validation errors refer to the measure of the difference between the observed and predicted output from the training and testing subsets respectively. When those errors do not improve significantly over a number of training cycles, namely epochs, then the learning process is considered practically completed. Commonly 50 epochs would suffice for model training. Additionally the change in the position and shape of the fuzzy membership functions indicates that the training process has occurred. A model is able to generalize well when the training and testing errors have the same order of magnitude (Table 3). In contrast, a higher complexity model may lead to overtraining, as mentioned earlier. For example using  $n=4$  instead of 3 for  $\Phi_3$ , resulted in about the same testing error ( $NMSE=0.82$ ), but relatively lower training error ( $NMSE=0.40$ ), which was indicative of overtraining and that employing structures of such complexity essentially does not improve the model's performance.

**Table 3.** Evaluation of the selected ANFIS models according to computational time and error indices.

ANFIS models	CPU time (s)	RMSE		NMSE		CC		MAE	
		Train	Test	Train	Test	Train	Test	Test	Test
$\Phi_1$	916.47	0.111	0.128	0.677	0.615	0.823	0.799	0.0123	0.0162
$\Phi_2$	2241.8	0.183	0.265	0.117	-0.68	0.341	0.084	0.0335	0.0704
$\Phi_3$	685.44	0.188	0.208	0.228	0.142	0.477	0.378	0.0352	0.0432

Generally, the accuracy of the networks depends on the ability of the input to model the dynamics of particle entrainment. The error indices for the networks with the best performance for each structure of the input vector,  $\Phi_i$ , with  $i=1$  to 3, are shown in Table 3. Overall, the performance of those models is satisfactory. The relatively low error metrics (e.g.  $RMSE$ ) and

high  $CC$ , implies good matching of the measured and predicted output. Whereas all of the presented models have an acceptable level of accuracy, the  $\Phi_1$  architecture, employing the time domain representation of the input signal, demonstrated superior predictive accuracy ( $RMSE=0.128$ ), compared to the  $\Phi_2$  and  $\Phi_3$  models ( $RMSE=0.265$  and  $0.208$  respectively), using the wavelet transform for the representation of the velocity signal. However, it is possible that the performance of the latter improves if a mother wavelet, different than the ones used in this study, that better matches the general morphology of the signal is implemented. Also the correlation coefficient for the selected  $\Phi_1$  model is quite close to 1 ( $CC=0.8$ ). A graphical representation of the model performance is provided in Figure 7, showing the predicted and observed values of the normalized particle displacement,  $\Delta x/\Delta x_{max}$  ranging from 0 to 1. The first half of the time series corresponds to the training subset while the other half to the testing subset, allowing for comparison between the two cases and evaluation of the model's predictive ability when new (unseen) data are given as input.

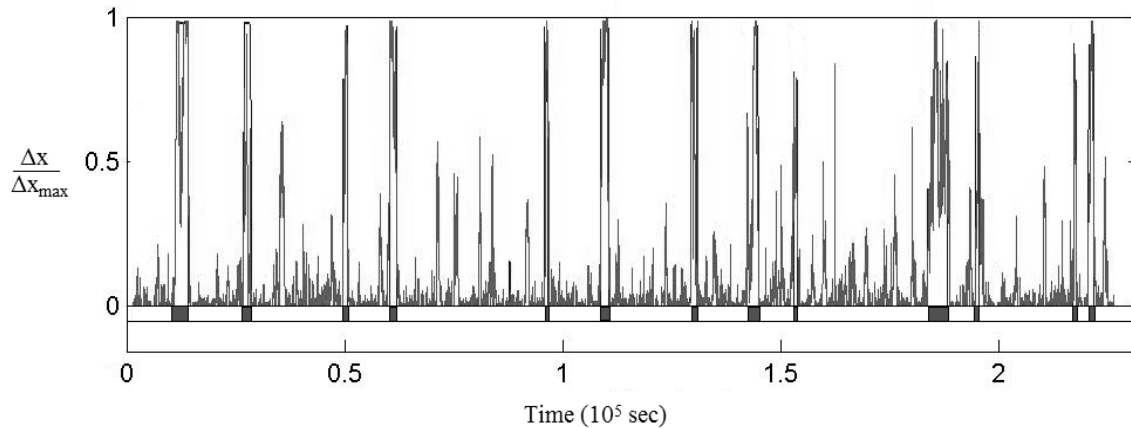


**Figure 7.** Illustration of the history of predicted normalized particle displacements ( $\Delta x/\Delta x_{max}$ ), for the model with the best performance (U3In). The filled boxes in the timeline below the horizontal axis, correspond to the events when the particle is completely dislodged.

Furthermore, another metric to assess the performance of the models is the computational efficiency measured in terms of processing ( $CPU$ ) time as shown in Table 3. The training and testing of the models was carried out on a personal computer (Pentium® 4 processor, 3.20 GHz with 1.25 GB of RAM). Generally, there exists a tradeoff between accuracy and computational

robustness. As the size of the input data and network complexity become greater, the computational time required to complete the learning process, increases dramatically. Comparing the processing time for the  $\Phi_2$  and  $\Phi_3$  models (Table 3), it is seen that the latter is more efficient than the former.

### 6.3. Knowledge representation and general applicability

Expert knowledge about the dynamics the ANFIS simulates may be extracted in terms of fuzzy if-then rules. For instance, for the 3 input  $\Phi_1$  model, Takagi and Sugeno type fuzzy rules of the following form may be given:

If  $u_f(t)$  is *high* and  $u_f(t-\Delta t)$  is *high* and  $u_f(t-2\Delta t)$  is *high*,

$$\text{Then } \Delta x(t+\Delta t) = p_{1,1} u_f(t) + p_{2,1} u_f(t-\Delta t) + p_{3,1} u_f(t-2\Delta t) + r_1$$

where the output in the antecedent part is expressed as a linear function of the learning parameters,  $p_{i,k}$ , adjusted in the process of learning (or model training). The knowledge such a rule represents may become more transparent if the antecedent part is expressed in terms of a fuzzy variable e.g. *high*, for the case of a full dislodgement. In this case, the above rule implies that if the magnitude of  $u_f$  is relatively high for a sufficient duration (from  $t-2\Delta t$  to  $t$ ), then the particle is expected to be entrained. Same result may be predicted by a shorter duration but higher magnitude flow event, given in the premise part by e.g.  $u_f(t)$  is *very high*. Similarly, for low values of the temporally lagged velocity signal, no displacement or weak dislodgement (twitches) is expected, corresponding to low values of the predicted output. The above observation may be extended to the  $\Phi_2$  and  $\Phi_3$  models, implying that if the energy content of the velocity signal is relatively high for the characteristic frequencies, then the predicted particle response is expected to be high as well. This clearly demonstrates the ability of ANFIS to model the nonlinear dynamics of the phenomenon, based on a wide range of flow event characteristics (magnitude-duration or frequency-energy content). Thus the rules governing the model dynamics are observed to be consistent with the hypothetical framework introduced in this study, in agreement to the intuition for the response of the physical system.

The generalization ability of ANFIS or equivalently their capacity to perform well for different uniform flow conditions is of utmost importance. In particular, the error metrics were practically invariant and the performance of the examined models was found to be consistent for

the experimental flow conditions and specific particle arrangement. However, their application to different local bed micro-topographies has not been assessed. A possible way to extend the models' applicability to a general case of low mobility flow conditions characterized by the time series of  $u_f$ , and variable particle properties and setup defined by variable levels of  $u_{cr}$  (equation 2), is to train the network with the normalized time series  $(u_f - u_{cr}) / u_{cr}$ , instead of  $u_f$ . In this manner, the model incorporates the effect of the available relative to the required level of flow forcing, removing the need to obtain synchronous flow and particle response data to repeat the training process for the new particle configuration. This network might provide acceptable results for a wider range of conditions than the one with which it is trained. Such an extension could find potential applications in the field, requiring only the time series describing the near bed flow conditions and assuming a  $u_{cr}$  level representative of the bed surface grains and local arrangement. However, the potential of ANFIS for flows with varying physical effects (e.g. other than uniform), has not been evaluated and there may be a need to train the model again, to learn the new dynamics of the system.

## 7. Conclusion

In this study the effectiveness of ANFIS in predicting the incipient entrainment of a coarse particle at low mobility uniform flow conditions, is investigated. It is hypothesized that incorporating as model input flow characteristics, such as the magnitude and energy content of the local instantaneous flow, at past time instants and different frequencies respectively, suffices for the prediction of the particle response. A case study, employing a series of incipient mobilization experiments is demonstrated, to test this conjecture. The experimental setup consists of a system of lasers (LDV and He-Ne), allowing for the acquisition of synchronous velocity and particle displacement measurements. The time and frequency representation of the velocity time series is used as input for the model. ANFIS architectures of increasing complexity are trained and tested using the obtained input-output pairs. A variety of indices are utilized to evaluate the models' performance. For each input structure the best models are selected and compared based on their forecast accuracy, computational efficiency and generalization ability. The chosen ANFIS models are shown to have the capacity to model the underlying dynamics of the phenomenon and generalize well by retaining their predictive capacity for a range of near

incipient flow conditions. Even though the output of the Takagi and Sugeno fuzzy rules is not directly represented in terms of linguistic fuzzy variables, their heuristic interpretation and extracted knowledge is in agreement with the introduced hypothesis. The context under which these models may be applied for a wider range of flow conditions and particle configurations, while offering acceptable results, is discussed. This demonstrates their potential use in a broader array of phenomena in geomorphology.

## Notation

$\alpha$ ,	bed slope
$\Delta x_{max}$ ,	maximum particle displacement (constrained by the pin)
$\Delta t$ ,	temporal lag
$\theta_0$ ,	pivoting angle
$\nu$ ,	kinematic viscosity of medium (water)
$\rho_f$ ,	density of the fluid
$\rho_s$ ,	density of the particle
$\rho\theta$ ,	coefficient including effects of local grain arrangement and relative density of fluid and solid grain
$\tau^*$ ,	dimensionless bed shear stress
$\Phi$ ,	representation of general ANFIS structure
$B_f$ ,	buoyancy force
$C_D$ ,	drag coefficient
$f_e$ ,	mean rate of complete particle entrainments
$n$ ,	number of inputs
$n_m$ ,	number of membership functions
$n_R$ ,	number of rules
$N$ ,	number of data points
$o_i$ ,	computed output for the data point $i$
$R^2$ ,	coefficient of determination
$t_i$ ,	observed output for the data point $i$
$u_{cr}$ ,	critical flow velocity
$u(t)$ ,	instantaneous local streamwise component of the flow velocity
$u_m$ ,	time averaged streamwise flow velocity
$V$ ,	volume of the particle
$W$ ,	weight of the particle
$W_s$ ,	submerged particle's weight

## Acknowledgement

The support of the National Science Foundation (EAR-0439663, EAR-0738759 and CBET-1033196) and Army Research Office is gratefully acknowledged.

## References

- Ariffin J, Ghani AA, Zakaria NA, Yahya AS. 2004. Sediment prediction using an ANN and regression approach. In *Rivers 04, Proceedings of the 1st International Conference on Managing Rivers in the 21st Century: Issues and Challenges*, Ghani AA, Zakaria NA, Abdullah R, Ahama MSS (eds); 168-174.
- ASCE Task Committee. 2000. Artificial neural networks in hydrology. II: hydrologic applications. *Journal of Hydrologic Engineering*, ASCE 5(2): 124-137.
- Auton TR, Hunt JCR, Prudhomme M. 1988. The force exerted on a body in inviscid unsteady non-uniform rotational flow. *Journal of Fluid Mechanics* 197: 241-257.
- Buffington JM, Montgomery DR. 1997. A systematic analysis of eight decades of incipient motion studies, with special reference to gravel-bedded rivers. *Water Resources Research* 33(8): 1993-2029.
- Celik AO, Diplas P, Dancey CL, Valyrakis M. 2010. Impulse and particle dislodgement under turbulent flow conditions. *Physics of Fluids* 22(4): 046601-13.
- Cheng NS, Chiew YM. 1998. Pickup Probability for Sediment Entrainment. *Journal of Hydraulic Engineering* 124(2): 232-235.
- Coleman SE, Nikora V. 2008. A unifying framework for particle entrainment. *Water Resources Research* 44, W04415, doi:10.1029/2007WR006363.
- Diplas P, Dancey CL, Celik AO, Valyrakis M, Greer K, Akar T. 2008. The role of impulse on the initiation of particle movement under turbulent flow conditions. *Science* 322: 717-720.
- Diplas P, Celik AO, Dancey CL, Valyrakis M. 2010. Non-intrusive method for Detecting Particle Movement Characteristics near Threshold Flow Conditions. *Journal of Irrigation and Drainage Engineering* 136(11): 774-780.

- Einstein HA, El-Samni ESA. 1949, Hydrodynamic forces on a rough wall, *Review of Modern Physics* 21(3): 520-527.
- Farge M. 1992. Wavelet transforms and their applications to turbulence, *Annual Review of Fluid Mechanics* 24: 395-457.
- Fenton JD, Abbott JE. 1977. Initial movement of grains on a stream bed: The effect of relative protrusion. *Proceedings of the Royal Society, London, A* 352(1671): 523–537.
- Gimenez-Curto LA, Corniero MA. 2009. Entrainment threshold of cohesionless sediment grains under steady flow of air and water. *Sedimentology* 56: 493-509.
- Jang J-SR. 1993. ANFIS: Adaptive Network-Based Fuzzy Inference System, *IEEE Transactions on Systems, Man and Cybernetics Society* 23(3): 665-685.
- Jang J-SR, Sun C-T, Mizutani E. 1997. *Neuro-Fuzzy and Soft Computing: A Computational Approach to Learning and Machine Intelligence*, Prentice Hall: New Jersey, 614.
- Hofland B, Booij R, Battjes J. 2005. Measurement of fluctuating pressures on coarse bed material. *Journal of Hydraulic Engineering* 131(9): 770–781.
- Hofland B, Battjes J. 2006. Probability Density Function of Instantaneous Drag Forces and Shear Stresses on a Bed. *Journal of Hydraulic Engineering* 132(11): 1169–1175.
- Kasabov NK. 1996. *Foundations of Neural Networks, Fuzzy Systems, and Knowledge Engineering*, MIT Press: Massachusetts, 568.
- Kisi Ö. 2004. Multi-layer perceptions with Levenberg–Marquardt training algorithm for suspended sediment concentration prediction and estimation. *Hydrological Sciences Journal* 49: 1025-1040.
- Kumar P, Fouroula-Georgiou E. 1997. Wavelet analysis for geophysical application. *Review of Geophysics* 35: 385-412.
- Lavelle JW, Mofjeld HO. 1897. Do critical stresses for incipient motion and erosion really exist? *Journal of Hydraulic Engineering* 113(3): 370-385.
- Ling C-H. 1995, Criteria for incipient motion of spherical sediment particles, *Journal of Hydraulic Engineering* 121(6): 472-478.
- Mallat SG. 1989. A theory for multi resolution signal decomposition: the wavelet representation. *IEEE Transactions on Pattern Analysis and Machine Intelligence* 11(7): 674–693.
- Mallat S. 1999. *A wavelet tour of signal processing*. Academic Press: San Diego; 805.

- Nagy HM, Watanabe K, Hirano M. 2002. Prediction of Sediment Load Concentration in Rivers using Artificial Neural Network Model. *Journal of Hydraulic Engineering* 128(6): 588-595.
- Papanicolaou AN, Diplas P, Evaggelopoulos N, Fotopoulos S. 2002. Stochastic Incipient Motion Criterion for Spheres under Various Bed Packing Conditions. *Journal of Hydraulic Engineering* 128(4): 369-380.
- Schmeeckle MW, Nelson JM, Shreve RL. 2007. Forces on stationary particles in near-bed turbulent flows. *Journal of Geophysical Research* 112: F02003-21, DOI:10.1029/2006JF000536,.
- Shields A. 1936. Application of similarity principles and turbulence research to bed-load movement. Report No. 167, California Institute of Technology: Pasadena, California; 47.
- Singh A, Fienberg K, Jerolmack DJ, Marr J, Foufoula-Georgiou E. 2009. Experimental evidence for statistical scaling and intermittency in sediment transport rates. *Journal of Geophysical Research* 114: F01025, DOI:10.1029/2007JF000963.
- Sivakumar B, Jayawardena AW, Fernando TMKJ. 2002. River flow forecasting: use of phase-space reconstruction and artificial neural networks approaches. *Journal of Hydrology* 265: 225–245.
- Sugeno M. 1985. *Industrial applications of fuzzy control*. Elsevier Science: New York; 278.
- Tanaka K. 1996. *An introduction to fuzzy logic for practical applications*. Springer; 148.
- Tayfur G. 2002. Artificial neural networks for sheet sediment transport. *Hydrological Sciences Journal* 47: 879-892.
- Tayfur G, Ozdemir S, Singh VP. 2003. Fuzzy logic algorithm for runoff-induced sediment transport from bare soil surfaces. *Advances in Water Resources* 26: 1249-1256.
- Twomey JM, Smith AE. 1996. Validation and verification. In *Artificial Neural Networks for Civil Engineers: Fundamentals and Applications*, Kartam N, Flood I, Garrett J (eds) ASCE Press: New York; 44-64.
- Yitian L, Gu R. 2003. Modeling flow and sediment transport in a river system using an artificial neural network. *Environmental Management* 31(1): 122-134.
- Valyrakis M, Diplas P, Dancey CL, Akar T, Celik AO. 2006. Development of a hybrid adaptive Neuro-Fuzzy system for the prediction of sediment transport. In *River Flow 2006: Proceedings of the International Conference on Fluvial Hydraulics, Lisbon, Portugal*, 6-

- 8 September, Ferreira RML, Alves ECTL, Leal JGAB, Cardoso AH (eds), Taylor and Francis; 2304.
- Valyrakis M, Diplas P, Dancey CL, Greer K, Celik AO. 2010a. The role of instantaneous force magnitude and duration on particle entrainment. *Journal of Geophysical Research-Earth Surface* 115:1-18 DOI:10.1029/2008JF001247.
- Valyrakis M, Diplas P, Dancey CL, Celik AO. 2010b. Incipient rolling of coarse particles in water flows: a dynamical perspective. In *River Flow 2010: Proceedings of the International Conference on Fluvial Hydraulics Braunschweig, Germany, 08-10 September*, Dittrich, Koll, Aberle, Geisenhainer (eds), Taylor and Francis; 769-776.
- Vollmer S, Kleinhans MG. 2007. Predicting incipient motion, including the effect of turbulent pressure fluctuations in the bed. *Water Resources Research* 43: W05410, DOI:10.1029/2006WR004919.
- White CM. 1940. The Equilibrium of Grains on the Bed of a Stream. *Proceedings Royal Society London A* 174(958): 322-338.
- Wu FC, Yang KH. 2004. Entrainment Probabilities of Mixed-Size Sediment Incorporating Near-Bed Coherent Flow Structures. *Journal of Hydraulic Engineering* 130(12): 1187-1197.
- Zadeh LA. 1973. Outline of a new approach to the analysis of complex systems and decision processes. *IEEE Transactions on Systems, Man, and Cybernetics* 3(1): 28-44.
- Zadeh, LA. 1997. Toward a theory of fuzzy information granulation and its centrality in human reasoning and fuzzy logic. *Fuzzy Sets and Systems* 90(2): 111-127, DOI:10.1016/S0165-0114(97)00077-8.

## Chapter 5. Entrainment of coarse particles in turbulent flows: an energy approach

Manousos Valyrakis,<sup>1</sup> Panayiotis Diplas,<sup>1</sup> and Clint L. Dancey<sup>1</sup>

\*This chapter is a reprint of the article: Valyrakis, M., P. Diplas, and C. L. Dancey, (under submission), Entrainment of coarse particles in turbulent flows: an energy approach, *Physical Rev. E*.

<sup>1</sup>Baker Environmental Hydraulics Laboratory, Department of Civil and Environmental Engineering, Virginia Polytechnic Institute and State University, Blacksburg, Virginia, USA.

### Abstract

The entrainment of coarse sediment particles under the action of fluctuating hydrodynamic forces is investigated from an energy perspective. It is demonstrated that the mobilization of a grain resting on the channel boundary is possible when the instantaneous flow power transferred to it exceeds a critical level. Its complete removal from the bed matrix occurs only if the impinging flow events supply sufficient mechanical energy. The energy based criterion is formulated theoretically for entrainment of individual spherical particles in both saltation and rolling modes. Out of the wide range of flow events that can perform mechanical work on a coarse grain, only those with sufficient power and duration or equivalently energy density and characteristic length scale, may accomplish its complete dislodgement. Using data from flume experiments, the energy transfer coefficient defined as the ratio of the mechanical work performed on the particle to the mean energy of the flow event responsible for its dislodgement, is found to range from 0.04 to 0.10. At the examined low mobility flow conditions the majority (about 80%) of the energetic structures leading to complete particle entrainment have a characteristic length of about two to four particle diameters.

## 1. Introduction

Soil erosion in rivers, estuaries and aeolian environments, represents one of the major challenges to engineers and researchers in the field of earth surface dynamics. Of specific interest is the accurate identification of the flow conditions near the threshold of movement, having a wide range of applications from stable channel design to establishing acceptable flushing flow rates downstream reservoirs.

A number of diverse theories have been proposed in an attempt to relate flow strength, expressed by means of a certain flow parameter or derivatives of it, to the resulting rates of sediment transport. These theories can be classified into two basic categories, depending on the fundamental laws of physics they rely upon.

The first approach, based on Newton's laws of motion utilizes vectorial quantities such as mean stream velocity ( $U$ ) [Hjulstrom, 1939; Sundborg, 1956] or Shields [1936] parameter,  $\tau^* = \tau/[g(\rho_s - \rho_f)D_{50}]$  (where  $\tau$  is the boundary shear stress,  $g$  the acceleration of gravity,  $D_{50}$  the bed material median size,  $\rho_f$  and  $\rho_s$  the density of fluid and sediment, respectively). The latter criterion is widely employed for identifying flow conditions near incipient movement despite the criticism it has received in the literature [Miller et al., 1977; Bettess, 1984; Buffington and Montgomery, 1997; Shvidchenko and Pender, 2000; Paphitis et al., 2002].

The second approach is linked to the laws of thermodynamics, trying to correlate the scalar variables of energy or its derivative quantities to the rate of entrainment of sediment. One of the first attempts to emphasize the role of "stream energy" on sediment discharge can be found in the classical work of Gilbert [1914]. Gilbert specified that the rate of expenditure of available potential energy between two stations of different elevation equals the product  $QSg$ , with  $Q$  the water discharge and  $S$  the bed slope. Since then power theories have been related to the rate of expenditure of kinetic energy of the stream or of available potential energy (gravitational power) to transport sediment by a number of researchers [Rubey, 1933; Knapp, 1938; Velinakov, 1955; Bagnold, 1956]. However it was not until the work of Bagnold [1966] that this concept was extended to develop quantitative equations for the prediction of total sediment concentration. Bagnold [1966] introduced the concept of specific streampower,  $\omega = QSg/b$ , with  $b$  the width or hydraulic perimeter of the stream, as the rate of the stream's energy supply per unit area or simply as the product  $U\tau$  [Bagnold, 1977; Bagnold, 1980; Bagnold, 1986]. Yang, hypothesized

that unit streampower, defined as the rate of expenditure of potential energy per unit weight of water and given by the product of mean flow velocity and energy slope,  $U S$ , is the pertinent quantity controlling the concentration of suspended sediment, bedload or total sediment discharge as verified from statistical analysis of experimental data [Yang, 1972; Yang and Stall, 1976; Yang, 1979; Yang and Molinas, 1982].

Both traction and power approaches usually employ temporally and sometimes spatially averaged quantities such as mean velocity, bed shear stress or their product. Such mean quantities fail to capture the effect of rapidly fluctuating hydrodynamic forces on the entrainment of bed material. Particularly for the rough turbulent flow regime (e.g. boundary Reynolds number,  $R_* (=u_* D_{50}/\nu) > 100$ , with  $u_*$  the shear velocity, and  $\nu$  the kinematic viscosity of water), Shields' criterion for inception of motion of coarse particles shows scatter of more than an order of magnitude [Buffington and Montgomery, 1997; Lavelle and Mofjeld, 1987, among others]. Many researchers acknowledging the limitations of the above criteria, particularly for near critical flow conditions, have emphasized the significance of the magnitude of peaks in the instantaneous hydrodynamic forces in the vicinity of the boundary [Einstein and El-Samni, 1949; Sutherland, 1967; Paintal, 1971; Apperley and Raudkivi, 1989; Papanicolaou et al., 2001; Sumer et al., 2003; Zanke, 2003; Hofland et al., 2005; Schmeeckle et al., 2007; Vollmer and Kleinhans, 2007]. Recently, Diplas et al. [2008] demonstrated the importance of duration of flow events above a critical level of the instantaneous stress tensor and suggested their product, impulse, as the criterion to characterize incipient motion conditions. Valyrakis et al. [2010] extended the proposed impulse criterion over a wide range of grain mobility levels for both saltating and rolling particles. The validity of the impulse concept and the results of the theoretical formulation were demonstrated through a series of appropriately designed experiments [Diplas et al., 2008; Valyrakis et al., 2010; Celik et al., 2010].

In the present study a new criterion for particle entrainment linking the available energy of turbulent flow events to the mechanical work required for grain entrainment, is proposed for both pure saltation and rolling. The energy approach to grain dislodgement, while directly linked to the impulse criterion, is demonstrated to be more versatile and intuitive. The validity of the proposed criterion is examined through the detailed analysis of mobile particle flume data corresponding to low mobility conditions.

## 2. Role of energetic events to grain mobilization

Customarily theoretical deterministic or stochastic studies of inception of motion of grains from the bed matrix have implemented a force and moments balance approach for both saltation [Cheng and Chiew, 1998; Wu and Lin, 2002] and rolling entrainment modes [Papanicolaou et al., 2002], respectively. Specifically, such traditional approaches define that entrainment occurs when the drag and lift forces, commonly parameterized by the square of the instantaneous local flow velocity ( $u_f(t)^2$ ) in the vicinity of the particle [e.g. Einstein and El-Samni, 1949; White, 1940], exceed a critical level ( $u_c^2$ ) which may be determined from the particle properties and the local grain configuration [e.g. Valyrakis et al., 2010].

From an energy viewpoint the temporal history of the instantaneous flow power defined as a linear function of the cube of local flow velocity,  $P_f=f(u_f(t)^3)$ , is of interest rather than the instantaneous hydrodynamic forces or stresses. Then the condition  $u_f(t)>u_c$ , describes when the transfer of flow energy to the particle is positive. For such cases, the available flow power is linked to the rate of energy transfer from the flow to the particle via the relationship  $C_{eff}P_f = u_p \frac{d(u_f^2)}{dt} = \Delta W_p / \Delta t$ , where  $u_p$  and  $u_f$  are the particle and flow velocities (averaged over the time interval  $\Delta t$ ),  $C_{eff} = u_p/u_f$  is the mean energy transfer coefficient and  $\Delta W_p$ , the mechanical work done on the particle over  $\Delta t$ . Thus, peaks in the temporal history of the instantaneous  $P_f$ , have a potential to perform work on the particle by setting it into motion.

However, the above condition does not suffice to guarantee complete entrainment, as demonstrated by the following example obtained from laboratory experiments. A portion of the temporal history of  $u_f(t)^3$  measured in the vicinity of an exposed particle along with the instance of its complete entrainment (dotted vertical line) are shown in Figure 1. Based on the condition  $u_f(t)>u_c$ , two flow events have the potential to entrain the particle (events A and B, in Figure 1). It is observed that complete dislodgement does not occur with the flow event having the greater instantaneous peak of  $P_f$ . On the contrary, the later flow event (B), lasting significantly longer ( $T_B>T_A$ ), is capable of completely dislodging the particle out of its pocket. It is concluded that the rate of flow energy transfer is an important indicator signifying the local strength of flow towards grain mobilization, but alone it does not suffice to determine which of the flow events may trigger a complete grain entrainment.

A quantity, that accounts for both the local power of flow,  $P_f(t)$  and the duration ( $T_i$ ) of a flow event  $i$  over which mechanical work is performed towards particle entrainment, is the available energy of the flow event, defined as the following integral:

$$E_{f,i} = \int_{t_0}^{t_0+T_i} P_f(t) dt, \text{ with } u_f(t) > u_c \text{ for } t_0 < t < t_0 + T_i \quad (1)$$

where  $t_0$  refers to the time instant when the flow event commences transferring energy to the grain. A suitable criterion for specifying the threshold level for grain entrainment should link the amount of energy transferred by energetic flow events,  $C_{eff} E_{f,i}$ , with the minimum amount of work required for particle entrainment,  $W_{p,cr}$ :

$$C_{eff} E_{f,i} > W_{p,cr} \quad (2)$$

According to the event based energy balance framework presented in equation (2), if the duration of the energetic event or the length-scale of the flow structure is long enough to transfer sufficient mechanical energy to the grain then full grain entrainment is possible. In this manner the dynamical significance of the fluctuating near boundary velocity and pressure fields in transferring energy to mobilize sediment grains is accounted for by considering the short but finite duration of energetic flow events. For the example of Figure 1, the applicability of the energy criterion may be demonstrated by comparing the shaded areas  $E_{f,A}$  and  $E_{f,B}$ , which represent the portion of flow energy made available for mobilizing the grain (assuming constant  $C_{eff}$ ). The amount of flow energy required for full grain entrainment,  $W_{p,cr}$ , should lie between the energy values of the events resulting in full dislodgement and those which do not ( $E_{f,A} < W_{p,cr}/C_{eff} < E_{f,B}$ ).

In the following, the above conjecture is investigated by providing the theoretical framework for two modes of entrainment, namely saltation and rolling. Data from a series of flume experiments near incipient motion conditions are analyzed to further demonstrate the validity and utility of the energy concept.

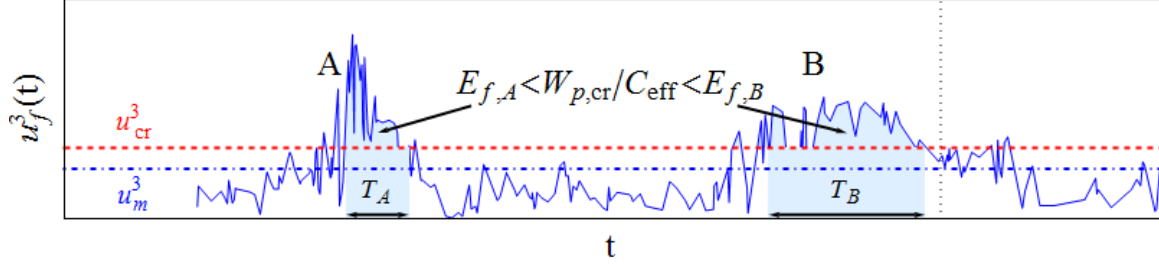


**Figure 1.** Time history of instantaneous flow power ( $P_f \sim u_f^3$ ) exerted on a completely exposed particle. Energetic flow events ( $E_i$  –shaded areas) have instantaneous flow power in excess of the threshold level ( $u_{cr}^3$  –dashed line) lasting for duration ( $T_i$ ). The instant of full entrainment denoted by the dotted vertical line.

### 3. Energy criterion formulation

Two modes of grain dislodgement are considered in this study: saltation and rolling. The frequency of occurrence of each entrainment mode strongly relates to different dynamic processes and specific bed micro-topographies. For instance, a completely hidden grain resting on the bed surface layer experiences lift forces,  $F_L$ , that may cause its saltation (Figure 2a). On the contrary, a grain with maximum exposure to the approaching flow, experiences hydrodynamic drag forces,  $F_D$ , which usually trigger its movement (Figure 2b). Consistent with the dynamic definition of grain entrainment [Valyrakis *et al.*, 2010], a particle is considered to have enough energy to perform a complete entrainment when it can reach a new location of higher elevation or greater exposure from where its further dislodgement downstream is guaranteed. Thus the work that needs to be performed ( $W_{p,cr}$ ) for complete grain removal should equal the change in potential energy between the location it has to be raised and its resting position. This critical level depends only on particle properties and local grain arrangement characteristics, being proportional to the elevation difference between the two positions.

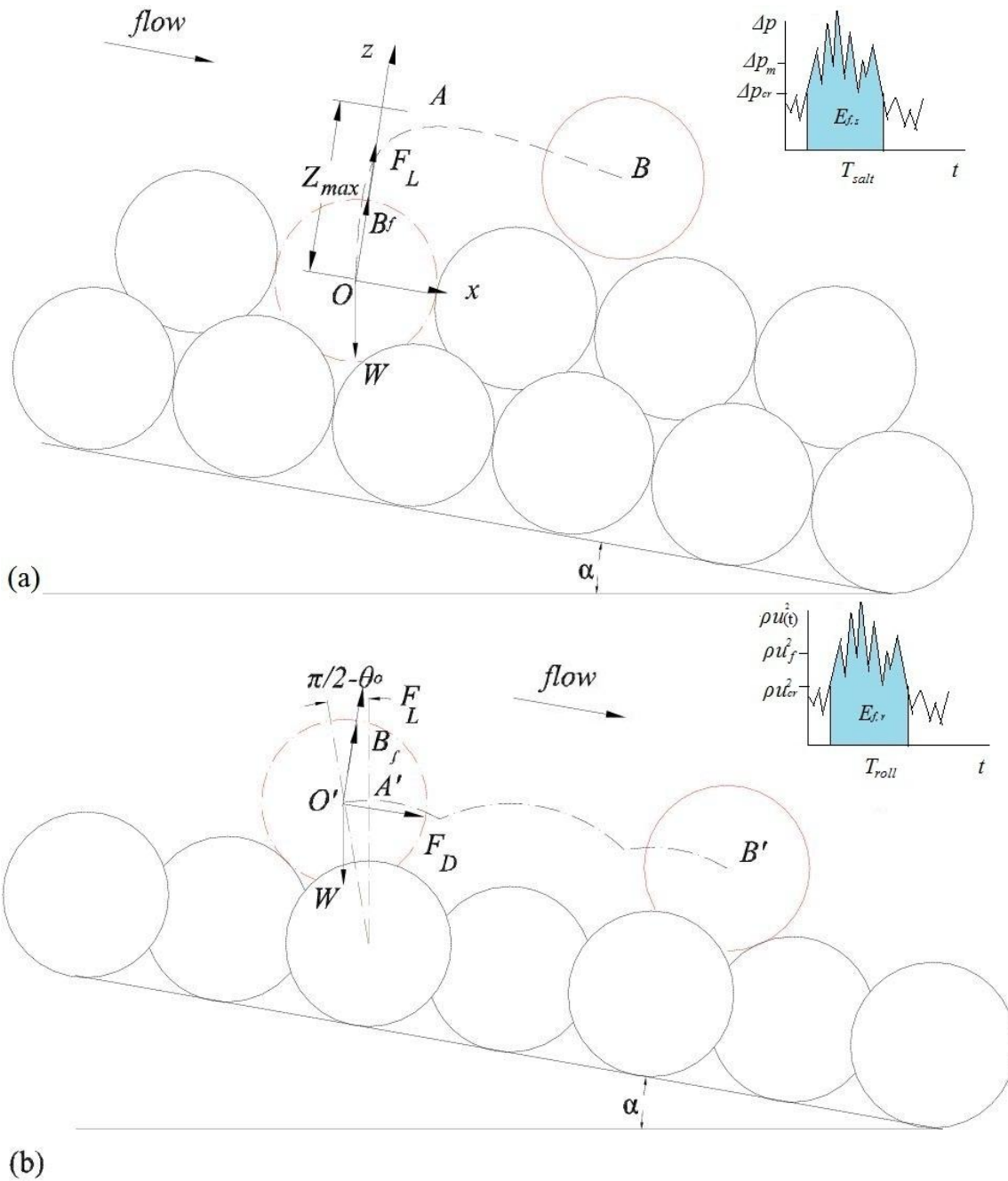


**Figure 2.** Entrainment of particle by: a) saltation; mobile particle (dashed circle) is initially surrounded by neighboring particles, and b) rolling; mobile particle (dashed circle) is completely exposed to the flow. For both cases the position of the downstream entrained particle, due to mean flow forcing, is depicted with a continuous thick circle, while the path followed is shown with a dot-dashed curve. Complete entrainment is initiated by energetic events above critical,  $E_{fi}$ , shown in the inset.

### 3.1. Incipient Saltation

The entrainment of coarse grains by saltation, due to the action of hydrodynamic lift forces has been the focus of many theoretical and experimental studies [Jeffreys, 1929; Chepil, 1958; Benedict and Christensen, 1972; Cheng and Chiew, 1998; Wu and Lin, 2002; Nino et al., 2003]. The representative case of hexagonal arrangement of spherical particles comprising a fully packed bed surface is shown in Figure 2a. For such a local configuration a particle may be initially suspended, when the pressure difference between its top and bottom surfaces ( $\Delta p$ ) is significant (resulting in a mean lift force greater than the submerged particle weight) and then follow a projectile-like motion (similar to trajectory  $OAB$ , Figure 2a) due to the mean flow forcing. Typically, the theoretical development of a criterion for inception of saltation is based on balance of the hydrodynamic lift force ( $F_L$ ), the buoyancy,  $B_f = \rho_f V g \cos \alpha$ , with  $\alpha$  the bed slope,  $V = 4\pi R_m^3/3$  the grain volume and  $R_m$  its radius, and the particle weight,  $W = \rho_s V g$ . However here, an energy (rather than a force) balance equation is employed (equation 2).

According to the above equation, energy is supplied to a solid particle from an impinging energetic flow event ( $E_{fi}$ ) of characteristic size and energy density. The maximum area over which the flow structure transfers energy to a particle is effectively limited by the cross-sectional area of the latter perpendicular to the flow direction,  $A = \pi R_m^2$ . This flow structure has a characteristic streamwise lengthscale that may be defined as the product of its mean advection velocity ( $u_f$ ) and its duration ( $T_{salt}$ ). The pressure difference between the top and bottom of the particle,  $\Delta p_m$ , averaged over the duration of the event may be considered as a representation of the mean energy density of the flow structure due to the rapidly fluctuating pressure field. Einstein and El Samni [1949] performed a series of experiments to directly relate the pressure difference between the upper and lower surface of hemispheres fixed to the wall with the velocity measured 0.35 diameters from the theoretical bed level. Based on their findings the mean value of energy density can be related to the average velocity of the flow event:

$$\Delta p_m = C_p \rho_f u_f^2 \quad (3)$$

with  $C_p$  a mean pressure coefficient. Equation (3) may be thought as an expression for the energy density ( $C_p \rho_f u_f^2$ ) of the flow event. The overall impact of the flow event with regard to particle

entrainment, depends on the characteristic dimensions of this flow event, namely its streamwise length ( $u_f T_{salt}$ ) and the effective area of its interaction with the solid particle ( $C_A A$ , with  $C_A (<1)$  an effectiveness coefficient denoting the percentage of the particle's cross-sectional area over which the flow forcing is applied). Then the required flow energy for saltation,  $E_{f,s}$ , may be defined as the product:

$$E_{f,s} = (u_f T_{salt})(C_A A)(C_p \rho_f u_f^2) \quad (4)$$

The particle should be able to reach the topmost position ( $z_{max}$ ) with the energy supplied from the flow event. Then the work performed on the particle during the advection of the flow structure should match the minimum mechanical energy at this location or equally the stored potential energy:

$$W_{p,s} = (\rho_s - \rho_f) \cos \alpha V g z_{max} \quad (5)$$

For threshold conditions the required particle displacement may be considered of the order of its diameter ( $z_{max} = 2R_m$ ). Consequently, the energy equation (equation (2)) becomes for the case of a saltating grain:

$$(C_{salt} u_f T_{salt})(C_A C_p u_f^2) \geq \frac{8}{3} \cos \alpha \frac{\rho_s - \rho_f}{\rho_f} g R_m^2 \quad (6)$$

with  $C_{salt} (=u_p/u_f)$ , denoting the efficiency of flow energy transfer to the saltating grain. Equation (6) suggests that the required amount of flow energy per unit area of the particle expended towards its entrainment remains constant. It also demonstrates the dependence of the proposed criterion on particle and bed properties, while identifying the characteristics of the energetic flow events relevant to grain mobilization, which may be expressed in terms of the threshold curves. In particular, threshold energy levels may be expressed as a combination of average effective power of the flow event ( $P_f$ ) and its duration ( $T_{salt}$ ), or equivalently its specific energy ( $\Delta p_m / \rho_f$ ) and characteristic advection length scale ( $u_f T_{salt}$ ), varying in an inversely proportional manner.

An illustrative example is provided in Figures 3a and b, where the threshold curve is expressed in terms of the above quantities. The threshold curve is predicted from the energy equation for saltation, for the case of a 12.7mm spherical particle resting on a horizontal layer of a closely packed arrangement of the same particles with density  $\rho_f=2300\text{kg/m}^3$ , in water (similar to Figure 2a). Flow events defining points that fall above the hyperbolic shaped curve (Figure 3a, b) will result in particle removal from its resting configuration, while those below the curve will not suffice for complete particle dislodgement.

Extreme pressure events are short-lived and depending on the flow conditions and bed configuration may reach even more than 6 times the time mean value [Hofland *et al.*, 2005; Schmeeckle *et al.*, 2007]. Despite their variability, the energy criterion captures the essential characteristics of energetic flow structures leading to entrainment. For instance, a pressure event of magnitude  $6\Delta p$  and duration  $\Delta T$ , results in the same particle response as the pressure event with smaller peak ( $3.8\Delta p$ ) and twice as long the duration ( $2\Delta T$ ), based on equation (6). These results are consistent to those derived from the impulse concept [Diplas *et al.*, 2008; Valyrakis *et al.*, 2010] for saltating particles and short  $T$ , as shown in [Valyrakis *et al.*, 2011b].

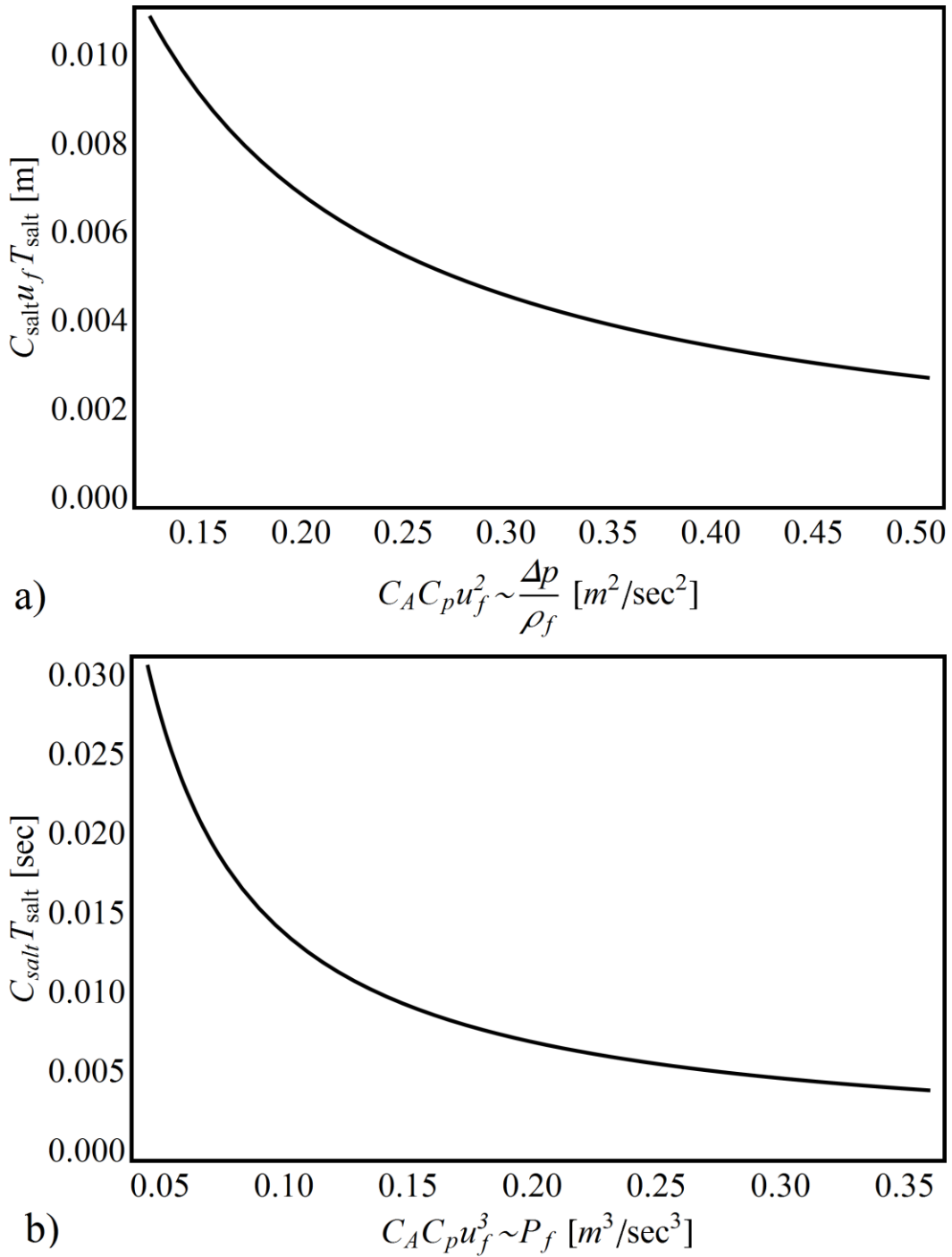


**Figure 3.** Representation of energy threshold for entrainment of a 12.6 mm particle in saltation mode by: a) mean specific energy and advection length scale, and b) mean flow power ( $P_f$ ) and duration ( $C_{salt}T_{salt}$ ) combinations.

### 3.2. Incipient Rolling

The development of an energy based criterion for the entrainment of coarse grains by rolling mode follows the same rationale used for the derivation of the energy threshold for saltation. While a grain hidden in the surface layer is mobilized by lift forces, in the limiting case of a fully exposed particle, entrainment is the outcome of mechanical work performed by the action of hydrodynamic drag ( $F_D$ ). Usually, for unobstructed uniform flows, the rapidly fluctuating lift forces ( $F_L$ ) have a rather secondary role in facilitating grain removal [Zanke, 2003; Hofland *et al.*, 2005; Schmeeckle *et al.*, 2007]. Depending on the flow conditions and particle arrangement, the effect of  $F_L$  may be taken into account by appropriately adjusting the particle weight (and effectively  $W_{p,cr}$ ) or simply be neglected. In contrast to past theoretical approaches employing balance of moments of forces and applied torques about an axis of rotation or a pivot point [White, 1940; Komar and Li, 1988; James, 1990; Wu and Yang, 2004], an event based energy balance framework is employed in this study.

A spherical particle resting on top of similar bed grains fully dislodges when it reaches the topmost position of the local bed arrangement (location  $A'$ , in Figure 2b). From this location of maximum exposure the particle may further be transported downstream by the action of the mean flow (e.g. follow the path  $O'A'B'$ , Figure 2b). The work performed on the particle for rolling ( $W_{p,r}$ ), will depend on the required angular displacement  $\theta = \pi/2 - \theta_0$ , with  $\theta_0$ , the pivoting angle, formed between the horizontal and the lever arm ( $L_{arm}$ ):

$$W_{p,r} = (\rho_s - \rho_f) \cos \alpha V g (1 - \sin \theta_0) L_{arm} \quad (7)$$

The flow energy transferred during the passage of a sufficiently energetic flow structure should equal or exceed the mechanical work,  $W_{p,r}$ . Such flow events apply high normal and shear stresses to the particle transferring flow energy at a rate proportional to the cube of the instantaneous approaching flow velocity, for duration ( $T_{roll}$ ). Similar to the case of entrainment by saltation, the energy of the flow event for rolling,  $E_{f,r}$ , may be given as the product of the energy density of the flow structure ( $(C_D/2)\rho_f u_f^2$ ), its streamwise length ( $u_f T_{roll}$ ) and the portion of the exposed area of the solid particle ( $C_{AA}$ ):

$$E_{f,r} = (C_A A) \left( \frac{C_D}{2} \rho_f u_f^2 \right) (u_f T_{roll}) \quad (8)$$

Incorporating the efficiency of flow energy supply to the rolling grain with the energy transport coefficient for rolling mode ( $C_{roll}=u_p/u_f$ ), equations (2), (7) and (8) yield:

$$(C_{roll} u_f T_{roll}) \left( \frac{C_D}{2} C_A u_f^2 \right) \geq \frac{4}{3} \cos \alpha (1 - \sin \theta_0) \frac{\rho_s - \rho_f}{\rho_f} g L_{arm} R_m \quad (9)$$

In addition to the particle's properties such as its radius ( $R_m$ ) and density ( $\rho_s$ ) equation (9) indicates the dependence of the threshold on the local microtopography parameters such as the lever arm ( $L_{arm}=(2R_m^2+8R_mR_b)^{1/2}$ , with  $R_b$  the radius of particles forming the surface layer) and pivot angle ( $\theta_0=\alpha+\text{arccot}(R_b/(3R_m^2+6R_mR_b-R_b^2))$ ). With regard to the features of the flow events mobilizing the particle it is noticed that the mean magnitude of their energy density is linked to its length-scale in an inverse fashion. Similarly, the longer the flow structure transfers energy to the particle, the less the magnitude of required power and likewise the greater the rate of energy supply is, the shorter the minimum duration required for particle dislodgement will be.

For instance, a quantitative example may be offered, considering the spherical particle ( $R_m=6.35$  mm,  $\rho_s=2300\text{kg/m}^3$ ), shown in Figure 2b, entrained in water by rolling. The critical energy level predicted from the energy equation for rolling (equation 9, using the equal sign) is illustrated (thick curve in Figures 4a and b). The qualitative dependence of the magnitude of the event in terms of energy density or power and its scale expressed in streamwise length size or duration, shown in Figure 4a and b respectively, is similar to the case of saltation. Only the events represented by points above the predicted threshold curve may transfer enough flow energy for full entrainment.

The wide distribution of hydrodynamic forcing on a grain [Hofland and Battjes, 2006; Schmeeckle et al., 2007] added to the variability of effects of its local configuration [Fenton and Abbott, 1977; Chin and Chiew, 1993; Kirchner et al., 1990; Dey and Debnath, 2000; Gregoretti, 2008; Recking, 2009] complicate the exact identification of a rolling threshold by traditional

methods. However, the constancy of the proposed criterion along with its ability to account for all those diverse but physically relevant effects in a simple and yet intuitive manner, demonstrate its versatility and appropriateness for predictive purposes.

#### 4. Incipient entrainment experiments

The experimental data used for this analysis was obtained from a set of flume experiments reported and analyzed in *Celik et al.*, [2010] and *Valyrakis et al.*, [2010]. In those experiments the precise motion of a Teflon sphere, near incipient conditions, was measured simultaneously with the local flow velocity upstream of the sphere. A small retaining pin is used to prevent the dislodged target grain from moving downstream, so that many events are measured without manual intervention. All of the experiments refer to near incipient motion conditions of about the same mean local velocity,  $u_{mean}$ , and dimensionless Shields bed shear stress,  $\tau^*$ , while the rate of occurrence of energetic events,  $f_P$ , and rate of particle entrainment,  $f_E$ , changes more than an order of magnitude. For convenience and completeness the key parameters of these experiments are repeated in Table 1.

The 15 minute long, synchronized, time series of flow power as a function of the cube of the recorded instantaneous streamwise velocity component ( $u_f(t)$ ) and grain angular displacement ( $\theta(t)$ ) are analyzed to examine the validity of the energy concept.

**Table 1.** Summary of flow characteristics for incipient entrainment experiments.

	$u_{mean}$	$\tau^*$	$P_{mean}$	$f_P$	$f_E$
	(m/s)	-	(m/s)	(events/s)	(entr./s)
<b>E1</b>	0.248	0.007	0.0027	2.23	0.147
<b>E2</b>	0.243	0.007	0.0024	1.75	0.114
<b>E3</b>	0.238	0.006	0.0024	1.33	0.051
<b>E4</b>	0.230	0.006	0.0021	0.81	0.031
<b>E5</b>	0.218	0.005	0.0018	0.33	0.002
<b>E6</b>	0.228	0.005	0.0021	0.58	0.012
<b>E7</b>	0.227	0.005	0.0018	0.48	0.008

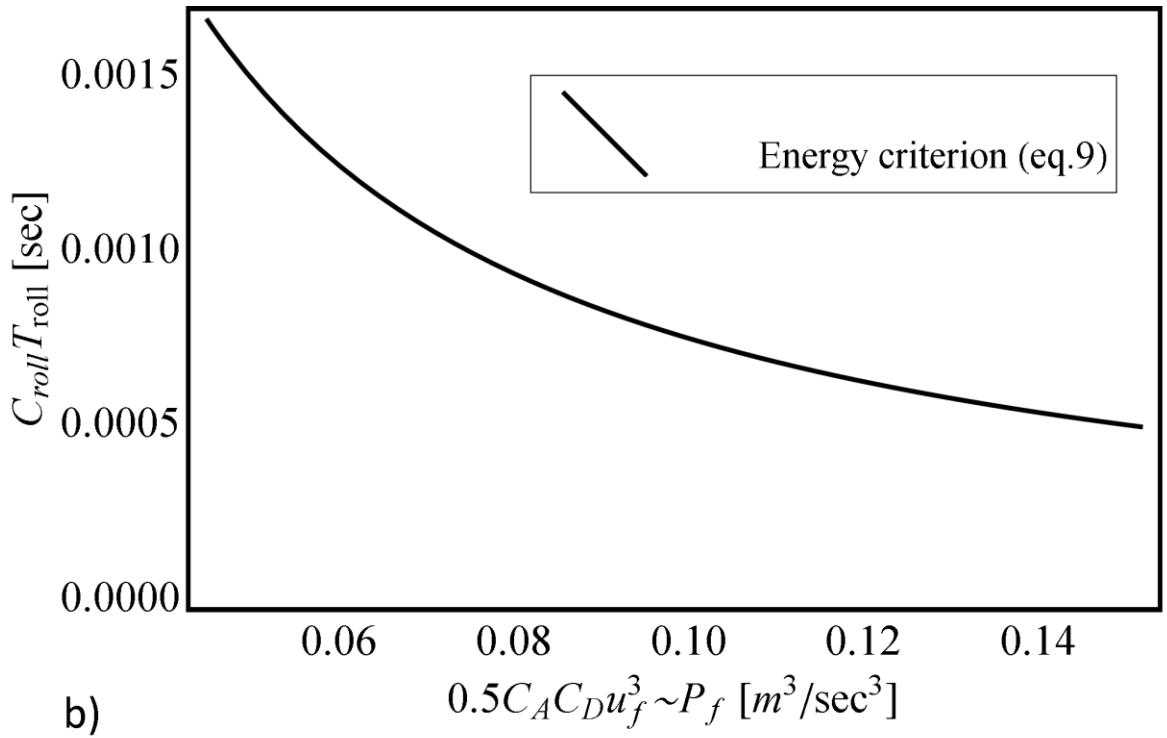
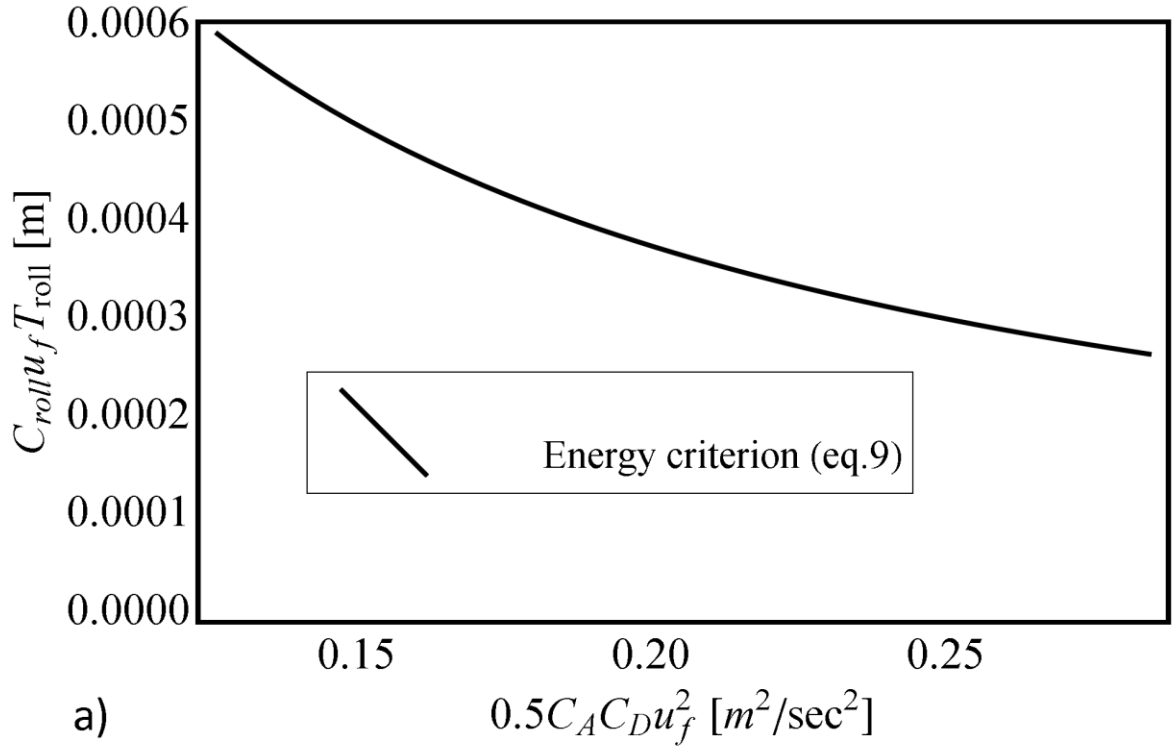


**Figure 4.** Illustration of the energy threshold for entrainment of a 12.6 mm particle in rolling mode by: a) characteristic specific energy ( $\sim u_f^2$ ) and lengthscale combinations, and b) mean flow power ( $P_f$ ) and duration ( $C_{roll}T_{roll}$ ) combinations.

## 5. Results and discussion

### 5.1. Trajectory analysis of rolling particle

In an effort to demonstrate the utility of the proposed criterion and its versatility in characterizing threshold conditions for a variety of flow event features, the dynamics of grain entrainment are analyzed for three representative cases of different duration, energy content and energy transfer coefficient. Flow energy is transferred to the grain when the condition  $u_f(t) > u_c(t)$ , is satisfied, with  $u_c(t)$ , representing the history of the gravitational force component resisting the grain's displacement at any time instant,  $t$ :

$$u_c(t) = \sqrt{\frac{2(\rho_s - \rho_f)}{\rho_f C_D A} f_h mg \frac{\cos \theta(t)}{\sin(\theta(t) - \alpha)}} \quad (10)$$

where the hydrodynamic mass coefficient is given by  $f_h = [\rho_s - \rho_f (1 - C_m)] / (\rho_s - \rho_f)$ . Equation (10) is similar to the condition  $u_f(t) > u_c$ , (cf. equation (4), in [Valyrakis *et al.*, 2011a]), but with  $u_c(t)$ , changing as a function of the angular displacement ( $\cos \theta(t)$ ). This essentially lowers the down-crossing level, rendering the flow events detection scheme less sensitive to the fluctuation of  $u_f(t)$ . In a different case, a single flow event might be shown as a number of different trailing flow pulses, due to consecutive upcrossings and downcrossings from a constant  $u_c$ . Thus the above condition may better represent the energetic events that perform work on the particle. The magnitude of particle response (from twitches to energetic entrainment) as well as the total time required to achieve it ( $t_{tot}$ ), depends on the rate and effectiveness of energy transfer and the duration of the flow event. Thus it is expected that the dynamics of grain entrainment show a wide range of attributes, which are captured by the following examples.

Several quantities of interest, such as the representation of the power of the resisting forces,  $u_c^3(t)$ , and the flow power ( $u_f^3(t)$ , Figure 5), the net power transferred to the grain (Figure 6) and the work performed on it (Figure 7), are provided for three distinctive entrainment events. In particular, the power function,  $P_f$ , plotted in Figure 5, is the product of  $u_c^3(t)$  or  $u_f^3(t)$  with  $0.5\rho_f C_D \pi R_m^2$ . The net power function (Figure 6) is the product  $\Sigma F u_p = [F_D \sin(\theta(t)) - (W - B_f) \cos(\theta(t))] \dot{u}_p$ , while the mechanical work (Figure 7) is the sum of kinetic and potential energies of the particle,  $W_{p,r} = (7/10)m_{tot} u_p^2 + (W - B_f) \cos(\theta(t)) R_m$ . The first part is obtained after calculation of the

velocity of the particle using a central difference scheme on the linear displacement signal ( $\Delta x(t)$ ) while the latter is computed by directly finding the angular displacements:  $\theta(t) = \Delta\theta(t) + \theta_0 = \text{ArcCos}(\text{Cos}\theta_0(1 - \Delta x/\Delta x_{max}) + \text{Cos}(\theta_0 + \Delta\theta_{max})\Delta x/\Delta x_{max})$ .

The first is a short-lived but of significantly high magnitude flow event (Figure 5a). On the other extreme, the second flow event has longer duration but lower magnitude (Figure 5b). The third case lies in between, but compared to the former has greater value of  $C_{eff}$  (Figure 5c). The figures include a short history of the above variables ranging from about 0.55 s before the instant of inception of motion (shown with the dashed vertical line) until the time the entrainment ceases when the retaining pin is reached. Beyond this location ( $\theta(t_{tot})$ ) grain entrainment is certain since the mean flow velocity becomes greater than the reduced critical level ( $u_m > u_c(t_{tot})$ ).

It is observed that due to the reducing resistance during the grain's displacement, the duration over which the net effective power on the grain is positive may increase (e.g. dotted line in Figure 5b and c). In most of the cases the detected flow events on their own offer sufficient energy for complete grain entrainment. For those events successive pulses offer an energy surplus rendering grain's response stronger and faster. Otherwise, when the detected flow events fall below the critical level, either because of low efficiency or due to the low rate or duration of energy transfer, a small displacement is possible (vibrations to twitches). However for a few of those cases, the particle is brought to a location of reduced resistance and before it manages to fall back in its resting pocket, a new flow event displaces it further downstream (Figure 5b).

The instantaneous rate of transferred flow energy,  $\Sigma F u_p$ , is also proportional to the difference of the power functions of  $u_f(t)$  and  $u_c(t)$ , with  $C_{roll}$  as a proportionality constant. This may be readily seen by comparing the events of Figure 6 with the corresponding events of Figure 5. Even though the magnitude of flow events following a peak event is relatively lower, the reduced resistance and increased particle velocity towards the end of movement may result in energy transfer rates between the flow events of comparable magnitude (Figure 6c).

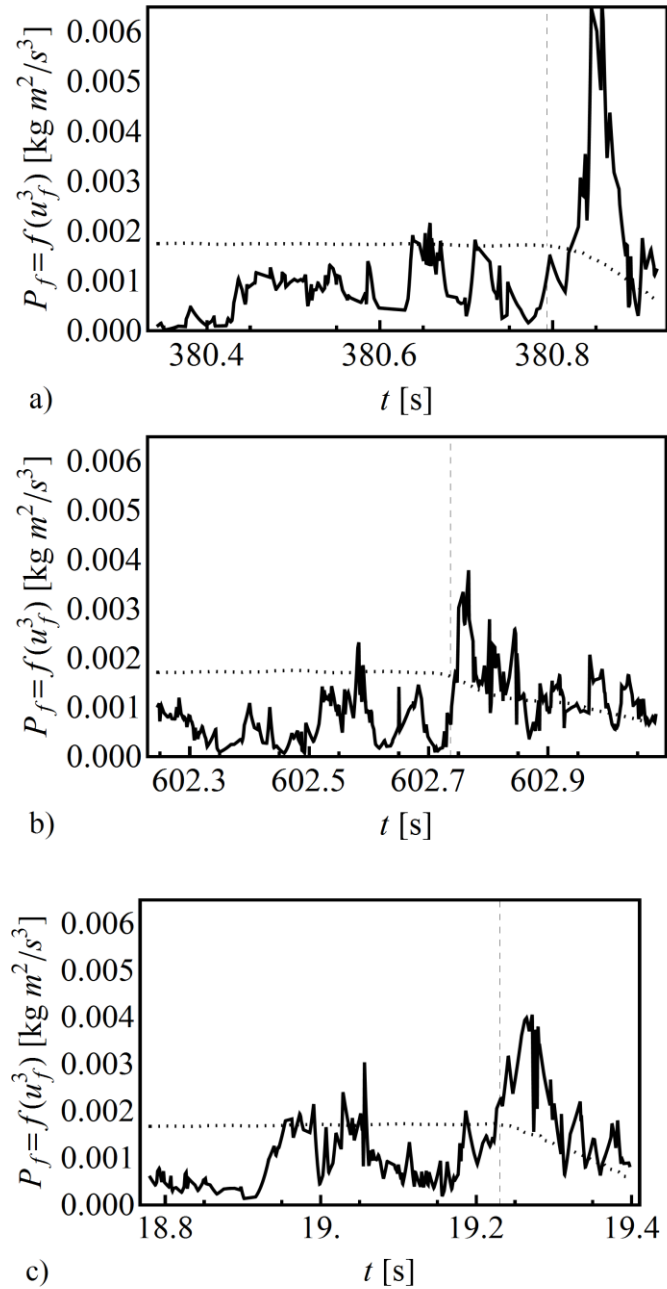


**Figure 5.** Representation of the available flow power and corresponding resistance level (dotted curve) for representative cases of particle entrainment: a) relatively short flow event of high energy content, b) long duration of flow event and low energy content, and c) representative case of relatively high  $C_{eff}$ . The vertical dashed line shows the instant of initiation of entrainment.

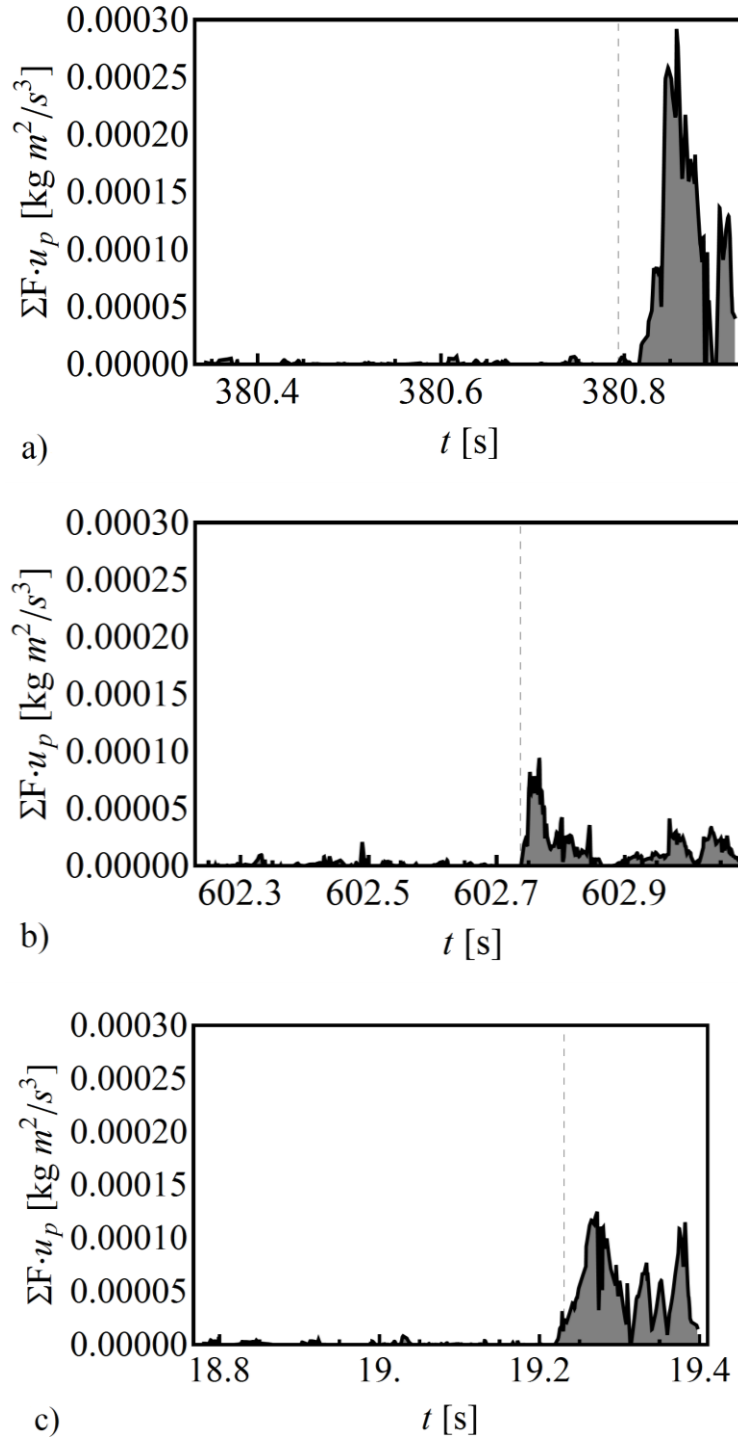
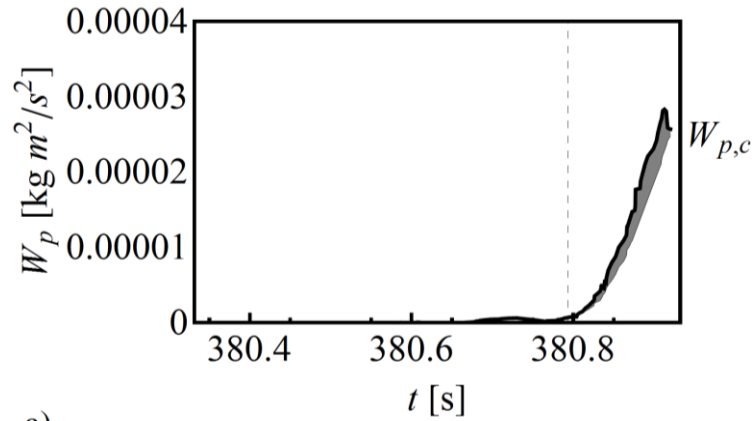
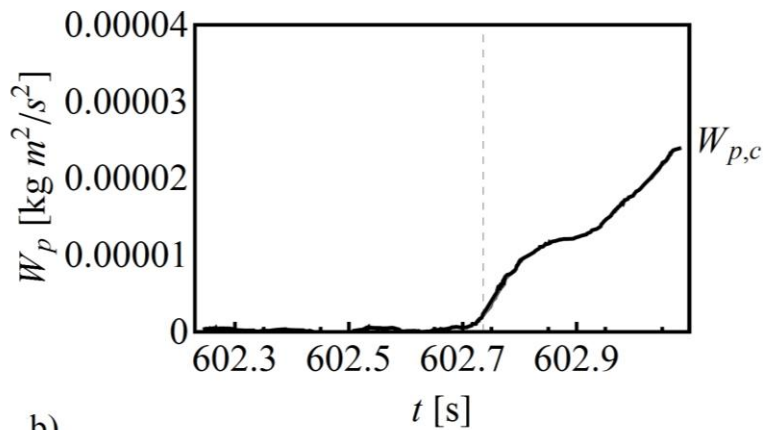


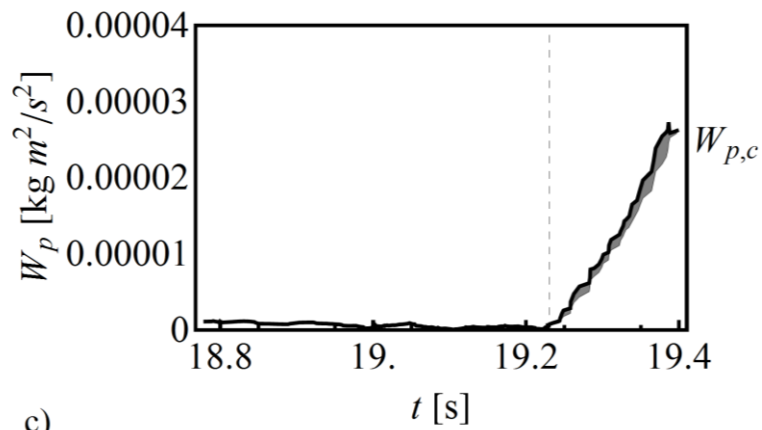
**Figure 6.** Representation of the net power transferred towards the grain's dislodgement (shaded area corresponds to the total offered energy) for representative cases of particle entrainment: a) relatively short flow event of high energy content, b) long duration of flow event and low energy content, and c) representative case of relatively high  $C_{eff}$ . The vertical dashed line shows the instant of initiation of entrainment.



a)



b)



c)

**Figure 7.** Representation of the history of the mechanical work performed on the particle until the critical level is reached for representative cases of particle entrainment: a) relatively short duration of flow event and high specific energy, b) long duration of flow event and low specific energy, and c) representative case of relatively high  $C_{eff}$ . The vertical dashed line shows the instant of initiation of entrainment.

The integral of the rate of energy transfer from the instant of onset of movement until time  $t < t_{tot}$ , indicates the mechanical work performed on the particle. In the first case, the highly energetic flow event transfers additional energy above the critical level and at a high rate. As a result the particle reaches the fully exposed position relatively fast, with an excess amount of kinetic energy ( $W_p(t_{tot}) > W_{p,c}$ ), which in the absence of the pin would possibly allow it to get transported several diameters downstream (Figure 7a). Quite the reverse holds for the second case, where the weak flow events barely manage to displace the grain until the final position (Figure 7b). Because of the low rate of energy transfer (Figure 6b) the critical energy level is reached at a relatively high  $t_{tot}$  (more than twice the mean).

## 5.2. Comparison of experimental data to theoretical predictions

Based on equation (1) and using the cube of the streamwise velocity signal to parameterize the instantaneous flow power, the energetic events are detected. Analysis of the synchronously obtained entrainment signal reveals whether each of the extracted flow events manage to completely dislodge the particle or not. The data points that manage to perform mechanical work and entrain the particle are shown in Figure 8 (solid circles). As shown in Figure 8 most of the detected energetic flow events that manage to fully entrain the particle fall above the energy threshold. For example only 6% or 6 out of 104 events, for run E1, fall below the threshold level defined by equation 9.

The critical energy level should remain the same since the particle and its local arrangement are fixed for all of the performed experiments. The energy transfer coefficient may be defined considering that its product with the available energy content of each flow event should at least equal or exceed the minimum required work done on the particle for its dislodgement. As illustrated in Figure 8, as well as predicted from equation (9), the higher the value of the energy transport efficiency the lower the required flow energy is. Most of the flow events resulting in entrainment have a  $C_{eff}$ , ranging from 0.04 to 0.10 (Figure 9 and 10).

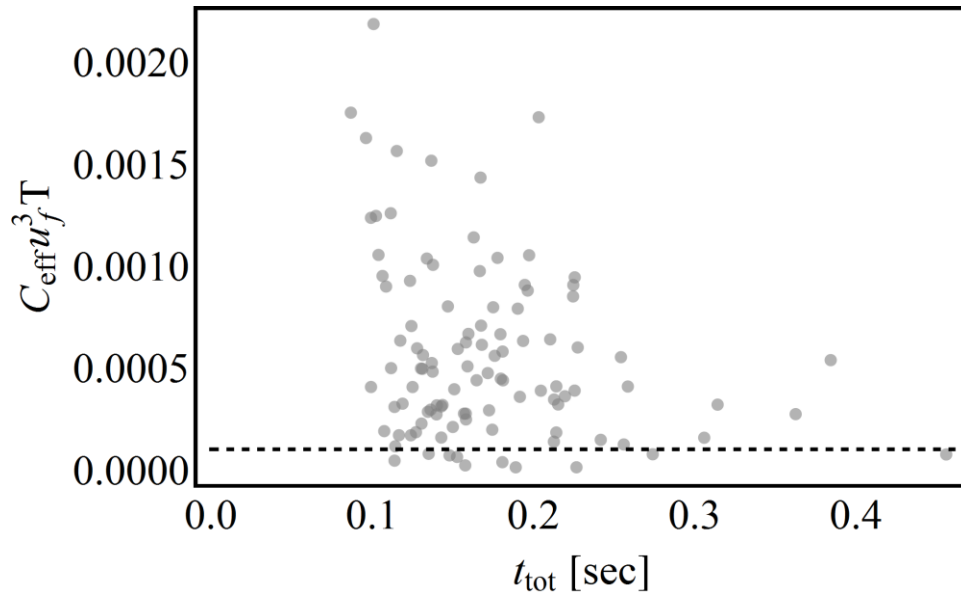


**Figure 8.** Plot of energy content of flow events ( $C_{\text{roll}} u_f^3 T_{\text{roll}}$ ) against the total duration for entrainment ( $t_{\text{tot}}$ ), for experimental run E1, showing also the threshold energy level (dashed line) as predicted from equation (9).

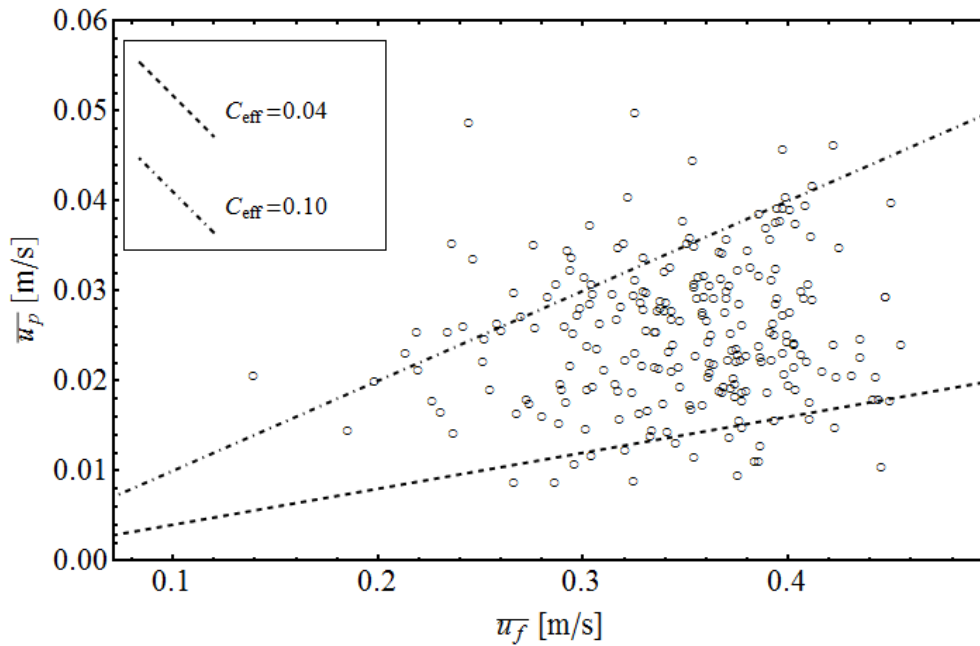


**Figure 9.** Relation between the mean velocity of the flow event and the resulting particle velocity (averaged over the duration of dislodgement).

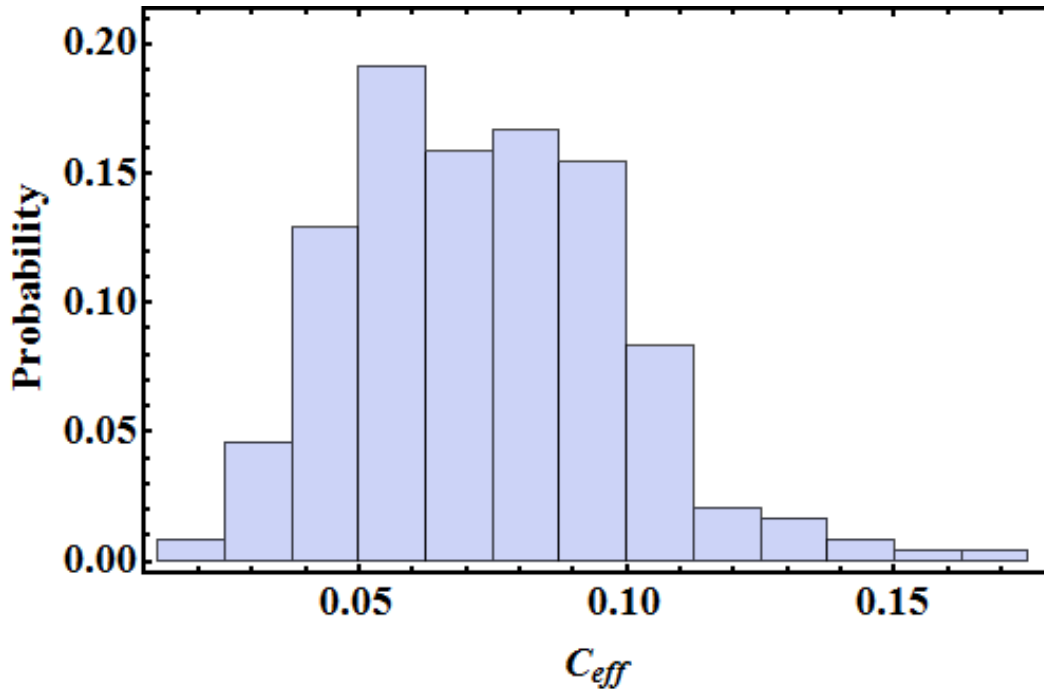


**Figure 10.** Distribution of the coefficient of energy transfer,  $C_{eff}$  (values from all experiments).

### 5.3. Characteristic features of energetic events resulting in particle entrainment

As already discussed the basis of the proposed energy concept, is that the rate of occurrence, as well as the characteristics of energetic events are associated with the rate of work done on sediment particles. The magnitude of the energetic flow events relative to the particle and local micro-topography characteristics, define its stability or resistance to entrainment. For a particle saltating due to the action of extreme magnitude and short-lived hydrodynamic lift [Smart and Habersack, 2007], it is more intuitive to describe the supply of flow energy in terms of duration and mean flow power above a critical level (equation 1). Regarding the case of a grain rolling out of its resting pocket due to an impinging flow structure, it is physically sound to consider the flow energy density and its characteristic lengthscale as the relevant parameters.

The distributions of these features characterizing the overall energy content of the flow events are shown in Figures 11 and 12. It is important to observe that the majority of flow events (more than 50%) resulting in dislodging the particle have a characteristic length scale of the same order as the particle diameter,  $2R_m = 12.7$  mm (Figure 11). About a quarter of the data points belonging in the entrainment region have a size from 2 to 3 diameters, while less than 3%

of those events span from 4 to about 5 diameters. Concerning the distribution of energy density it may be readily observed that it varies over a relatively narrower range (about 50% compared to 5-fold increase of the length scale). The synergetic action of those features may explain why a significant amount of work performed in transporting bed material or equivalently an increase in bedload, may be observed in cases where an increase in organized coherent flow structures is present in the flow field even for about the same shear stress [Shvidchenko and Pender, 2001; Sumer et al., 2003]. This finding is consistent with the experimental results of Hofland et al. [2005], reporting sizes of sweeps structures ranging from 2-4 grain diameters in the streamwise direction and 0.5-1 D in the stream normal direction.

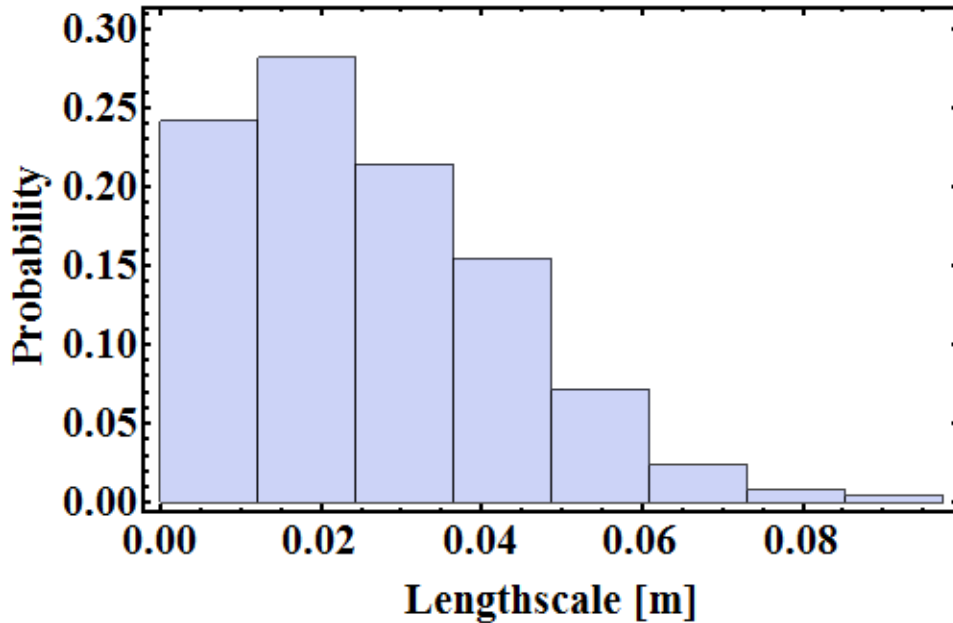


**Figure 11.** Probability distribution of the characteristic lengthscale of the flow events (for all experiments).

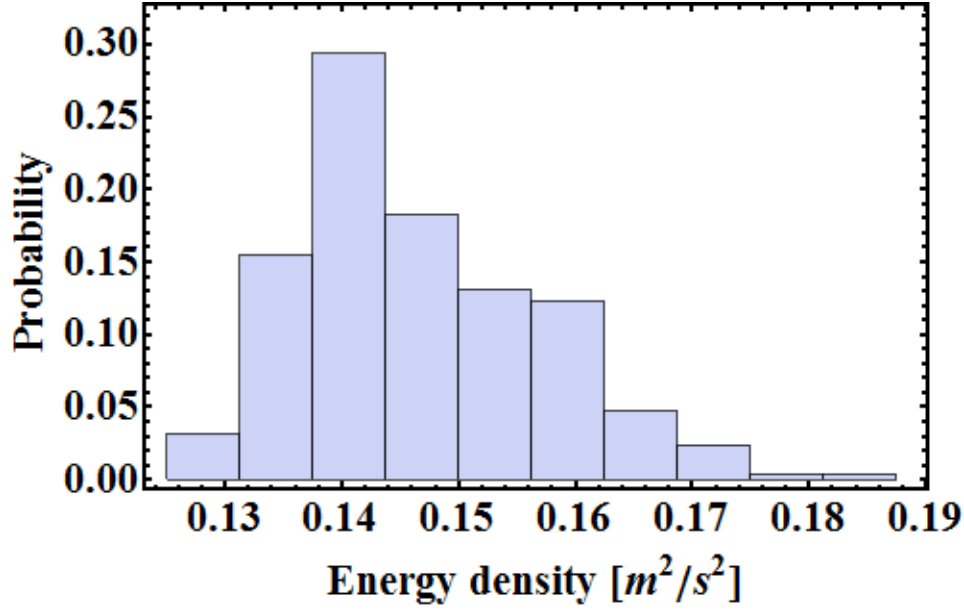


**Figure 12.** Probability distribution of the energy density of the flow events (for all experiments).

#### 5.4. Comparison of saltation and rolling thresholds

Based on equation (2), a comparison of the minimum flow energy supplied for entrainment by saltation and rolling assuming the same order of magnitude of energy transport coefficients reveals that a greater amount of mechanical work is required for saltating grains. This may be readily illustrated by estimating the ratio of the two thresholds:

$$\frac{W_{p,roll}}{W_{p,salt}} = \frac{(1 - \sin \theta_0)L_{arm}}{2R_m} \quad (11)$$

which for moderate slopes and ratio of mobile to base particles greater than 0.2, is always less than unity. Then according to equation (11) the saltation threshold is greater than the critical value for rolling. For the case of the incipient motion experiments this ratio is 0.1. This implies that in order to observe particles being entrained by saltation, the magnitude of energy of the flow events has to exceed ten times the critical level for rolling. However the maximum flow energy observed for all experiments is close to fivefold the rolling threshold, which explains why rolling, is the sole expected entrainment mode for the examined flow conditions. This remark is

in qualitative agreement with the results reported in the literature [*Bagnold, 1973; Ling, 1995; Wu and Chou, 2003*].

### 5.5. Comparison of energy criterion to traditional energetic approaches

Usually the dynamical behavior of the flow energy may be considered via the turbulent kinetic energy (TKE) budget equation [*Pope, 2001; Davidson, 2004*]:

$$\frac{Dk'}{Dt} = P - \bar{\varepsilon} + D \quad (12)$$

with  $k'$  the mean turbulent kinetic energy,  $P$  the mean production of TKE,  $\bar{\varepsilon}$  the pseudo-dissipation or difference between the dissipation and diffusion of Reynolds stress tensor and  $D$  the diffusion term, including the turbulent diffusion, the pressure diffusion and viscous diffusion. For near boundary turbulent flows the production of TKE dominates mainly due to the contribution from the high streamnormal flow gradients:

$$P = -\overline{u_i' u_j'} \frac{\partial u_j}{\partial x_i} = \frac{\tau}{\rho_f} \frac{\partial u}{\partial y} \quad (13)$$

Equation (13) shows that TKE production, which is responsible for intensifying the turbulent energy, occurs primarily as a result of the action of the shear stress,  $\tau$  (neglecting viscous shear stresses), on the velocity gradient. Velocity profiles one diameter upstream the location of the target particle (with the target particle removed from the bed surface), are constructed from a series of LDV measurements along the flow depth (Figure 13). Those profiles may provide information (e.g. velocity gradients) relevant to the estimation of the flow energy budget. A part of this flow energy should be inevitably linked to the work done for bed material entrainment, which should appear as a sink term in the TKE budget equation. *Yang and Song [1982]* integrated TKE production over the flow depth to relate it to unit stream power for transport of suspended sediment.

In a similar fashion, the rate of work done by the boundary shear stresses ( $P_{mean} \sim u\tau^*$ ), should be associated to the frequency of grain removal ( $f_E$ ). However, a minute change in the values of  $P_{mean}$ , results in a change of about two orders of magnitude for  $f_E$  (see corresponding values from Table 1). On the contrary, the rate of events offered above a critical power level has a wider variation (about an order of magnitude change as shown in Figure 15, compared to less than 50% increase for mean stream power), being a good indicator of the rate of work performed on the particle. This clearly demonstrates the appropriateness of the proposed event based energy approach, as opposed to traditional power methods based on mean flow characteristics.

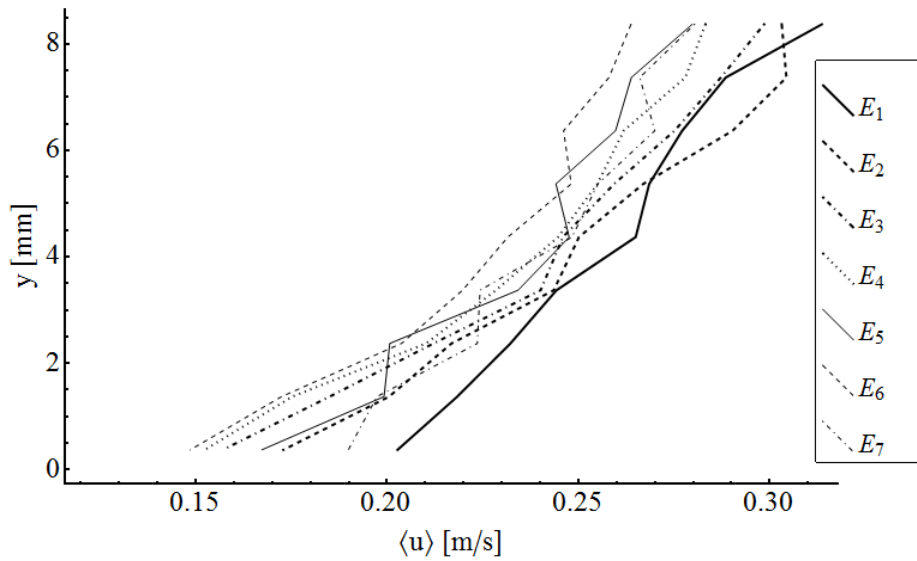


**Figure 13.** Mean streamwise velocity profile for the various experimental runs,  $E1$  to  $E7$  (only the near bed portion is shown for clarity).

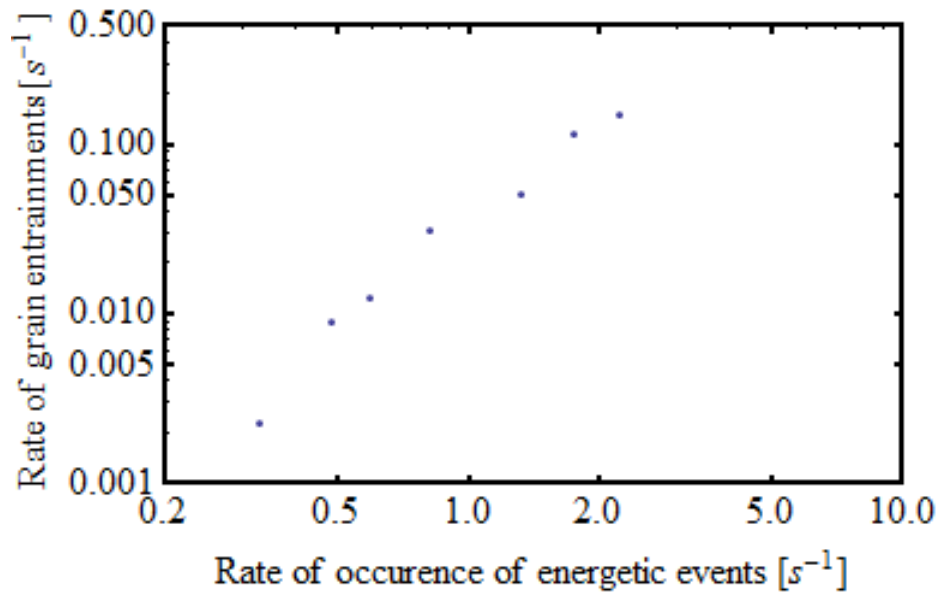


**Figure 14.** Plot of rate of occurrence of energetic events showing an almost linear dependence with the frequency of grain entrainments.

## 6. Conclusions

Herein a new criterion for identification of the incipient flow conditions is proposed, following an energy approach. The basis for its development relies on the concept that a portion of the available energy of sufficiently energetic flow events is expended in performing mechanical work on solid grains by mobilizing and transporting them downstream. It is hypothesized that only high energy events lasting for a sufficiently long duration may mobilize coarse grains from the bed matrix. Equivalently the product of energy content of flow events with their characteristic length scale has to exceed a critical energy level, which equals the work of the forces resisting movement.

A theoretical framework for entrainment of spherical particles in saltation or rolling mode is developed utilizing the energy balance equation, incorporating a coefficient to account for the efficiency of energy transfer. Equations defining the threshold energy curves are provided for both entrainment modes. In agreement to results reported in the literature, the limit for saltation is greater than for rolling.

The validity of the concept is elucidated using experimental data from mobile particle flume experiments. The energetic flow structures are extracted based on a detection algorithm and they

are subsequently distinguished according to their impact on grain displacement. For appropriate values of the energy transport coefficient the theoretically predicted threshold curves perform satisfactory in determining whether a flow event will dislodge the mobile particle or not.

It is found that even though the energetic flow events exhibit a wide range of characteristic magnitude, the ability of the majority of the events to perform sufficient mechanical work on the coarse grain for entrainment is limited only to a small percentage of those having relatively high energy content.

## Notation

$\alpha,$	bed slope
$\Delta p_m,$	mean pressure difference between the top and bottom of the particle for a flow event
$\theta_0,$	pivoting angle
$\nu,$	kinematic viscosity of medium (water)
$\rho_f,$	density of the fluid
$\rho_s,$	density of the particle
$\rho\theta,$	coefficient including effects of local grain arrangement and relative density of fluid and solid grain
$\tau^*$ ,	dimensionless bed shear stress
$B_f,$	buoyancy force
$C_D,$	drag coefficient
$C_{eff}$	energy transfer coefficient
$C_{salt},$	coefficient for the energy transfer for a saltating particle
$C_{salt},$	coefficient for the energy transfer for a rolling particle
$C_p,$	mean pressure coefficient
$E_{f,i},$	available energy of flow event $i$
$E_{f,r},$	energy of flow event resulting in particle entrainment by rolling
$E_{f,s},$	energy of flow event resulting in particle entrainment by saltation
$F(t),$	total hydrodynamic force
$F_{cr},$	critical force level
$F_D,$	hydrodynamic drag force
$F_L,$	hydrodynamic lift force
$F_m,$	mean force level
$f_E,$	mean rate of particle entrainment
$f_I,$	mean rate of occurrence of impulses
$f_h,$	hydrodynamic mass coefficient
$g,$	gravitational acceleration
$\hat{i}$	impulse normalized with mean of distribution sample ( $I_{mean}$ )
$I_i,$	impulse event $i$ (equation 1)
$I_{cr},$	critical impulse level
$L_{arm},$	lever arm
$n_c,$	number of complete particle entrainments

$P_f$ ,	instantaneous local power of the flow
$P_R$ ,	instantaneous power of resisting forces
$R_*$ ,	boundary Reynolds number
$R^2$ ,	coefficient of determination
$T_{salt}$ ,	duration of flow event (for entrainment by saltation)
$T_{roll}$ ,	duration of flow event (for entrainment by rolling)
$t_i$ ,	time instance when event $i$ occurs
$u_*$ ,	shear velocity
$u_{cr}$ ,	critical flow velocity
$u_f$ ,	local flow velocity averaged over the duration of the flow event
$u_f(t)$ ,	instantaneous local flow velocity
$u_m$ ,	time averaged flow velocity
$V$ ,	volume of the particle
$W$ ,	weight of the particle
$W_p$ ,	work done on the particle
$W_{p,cr}$	mechanical energy required for complete particle entrainment
$W_{p,r}$ ,	mechanical energy required for complete particle entrainment by rolling
$W_{p,s}$ ,	mechanical energy required for complete particle entrainment by saltation

## Acknowledgement

The support of the National Science Foundation (EAR-0439663, EAR-0738759 and CBET-1033196) and Army Research Office is gratefully acknowledged.

## References

- Apperley, L. W., and A.J. Raudkivi (1989), The entrainment of sediments by the turbulent flow of water, *Hydrobiologia*, 176/177, 39-49.
- Ancey, C., A. C. Davison, T. Bohm, M. Jodeau, and P. Frey (2007), Entrainment and motion of coarse particles in a shallow water stream down a steep slope, *J. Fluid Mech.*, 595, 83-114.
- Auton, T. R., J. C. R. Hunt, and M. Prudhomme (1988), The force exerted on a body in inviscid unsteady non-uniform rotational flow, *J. Fluid Mech.*, 197, 241-257.
- Bagnold, R. A. (1956), The Flow of Cohesionless Grains in Fluids, *Philos. Trans. R. Soc. of London, A*, 249(964), 235-297.

- Bagnold, R. A. (1966), An approach of sediment transport model from general physics, *US Geol. Survey Prof. Paper 422-I*.
- Bagnold, R. A. (1973), The nature of saltation and of 'bed-load' transport in water, *Philos. Trans. R. Soc. London, A*, 332(1591), 473– 504, doi: 10.1098/rspa.1973.0038.
- Bagnold, R. A. (1977), Bed load transport by natural rivers, *Water Resour. Res.*, 13, 303-312.
- Bagnold, R. A. (1980), An Empirical Correlation of Bedload Transport Rates in Flumes and Natural Rivers, *Philos. Trans. R. Soc. London, A*, 372(1751), 453-473.
- Bagnold, R. A. (1986), Transport of Solids by Natural Water Flow: Evidence for a Worldwide Correlation, *Philos. Trans. R. Soc. London, A*, 405(1829), 369-374.
- Benedict, B. A., and B. A. Christensen (1972), Hydrodynamic lift on a stream bed, in *Sedimentation, Symp. to Honor Prof. H. A. Einstein*, edited by H. W. Shen, pp. 5.1-5.17, Water Resources Publication, Littleton, Colorado.
- Bettess, R. (1984), Initiation of sediment transport in gravel streams, *Proceedings - Institution of civil Engineers*, 77, 79-88.
- Buffington, J. M., and D. R. Montgomery (1997), A systematic analysis of eight decades of incipient motion studies, with special reference to gravel-bedded rivers, *Water Resour. Res.*, 33(8), 1993-2029.
- Celik, A. O., P. Diplas, C. L. Dancey, and M. Valyrakis (2010), Impulse and particle dislodgement under turbulent flow conditions, *Physics of Fluids*, 22(4), 046601.
- Cheng, N.-S., and Y. M. Chiew (1998), Pickup Probability for Sediment Entrainment, *J. Hydraul. Eng.*, 124(2), 232-235.
- Chepil, W. (1958), The use of evenly spaced hemispheres to evaluate aerodynamic forces on soil surfaces. *Eos Trans. AGU*, 39, 397- 403.
- Chin, C. O., and Y. M. Chiew (1993), Effect of Bed Surface Structure on Spherical Particle Stability, *J. Waterway, Port, Coastal, Ocean Eng.*, 119(3), 231-242.
- Davidson, P. A. (2004), *Turbulence: An introduction for scientists and engineers*, Oxford University Press.
- Dey, S., and K. Debnath (2000), Influence of streamwise bed slope on sediment threshold under stream flow, *J. Irrigat. Drain. Eng.*, 126(4), 255-263.

- Diplas, P., C.L. Dancey, A. O. Celik, M. Valyrakis, K. Greer, and T. Akar (2008), The Role of Impulse on the Initiation of Particle Movement Under Turbulent Flow Conditions, *Science*, 322(5902), 717-720, doi:10.1126/science.1158954.
- Diplas, P., A.O., Celik, C.L., Dancey, and M., Valyrakis (2010), Non-intrusive method for Detecting Particle Movement Characteristics near Threshold Flow Conditions, *J. Irrig. Drain. Eng.*, in press
- Einstein, H. A., and E.-S. A. El-Samni (1949), Hydrodynamic forces on a rough wall, *Rev. Mod. Phys.*, 21(3), 520-527.
- Fenton, J. D., and J. E. Abbott (1977), Initial movement of grains on a stream bed: The effect of relative protrusion, *Proc. R. Soc. London, A*, 352(1671), 523–537.
- Gimenez-Curto L. A. and M.A. Corniero (2009), Entrainment threshold of cohesionless sediment grains under steady flow of air and water, *Sedimentology* 56, 493-509.
- Gilbert, G. K. (1914), The transportation of debris by running water, *U.S. Geological Survey Professional Paper*, 86, 263.
- Gregoretti, C. (2008), Inception sediment transport relationship at high slopes, *J. Hydraul. Eng.*, 11(134), 1620-1629.
- Hjulström, F. (1939), Transportation of Debris by Moving Water, in *Recent Marine Sediments*, edited by P. D. Trask, pp. 5-31, American Association of Petroleum Geologists, Tulsa, Oklahoma.
- Hofland, B., R. Booij, and J. Battjes (2005), Measurement of fluctuating pressures on coarse bed material, *J. Hydraul. Engrg.*, 131(9), 770–781.
- Hofland, B., and J. Battjes (2006), Probability Density Function of Instantaneous Drag Forces and Shear Stresses on a Bed, *J. Hydraul. Eng.*, 132(11), 1169–1175.
- James, C. S. (1990), Prediction of entrainment conditions for nonuniform, noncohesive sediments, *J. Hydraul. Res.*, 28(1), 25-41.
- Jeffreys, H. (1929), On the transportation of sediment by streams, *Proc. Cambridge Philos. Soc.*, 25, 272-276.
- Kirchner, J. W., W. E. Dietrich, F. Iseya, and H. Ikeda (1990), The variability of critical shear stress, friction angle, and grain protrusion in water-worked sediments, *Sedimentology* 37(4), 647–672.

- Knapp, R. T. (1938), Energy balance in stream flows carrying suspended load, *Am. Geophys. Union Trans.*, 501-505.
- Lane, E. W. (1955), The importance of fluvial morphology in hydraulic engineering, *Proc. ASCE* 81, paper no. 745.
- Lavelle, J. W. and H. O. Mofjeld (1897), Do critical stresses for incipient motion and erosion really exist?, *J. Hydraul. Eng.* 113(3), 370-385.
- Leighly, J. B. (1934), Turbulence and the transportation of rock debris by streams, *The Geographical Rev.*, 24(3), 453-464.
- Ling, C.-H. (1995), Criteria for incipient motion of spherical sediment particles, *J. Hydraul. Eng.*, 121(6), 472-478.
- McEwan, I., M. Sorensen, J. Heald, S. Tait, G. Cunningham, D. Goring, and B. Willets (2004), Probabilistic modeling of bed-load composition, *J. Hydraul. Eng.*, 130(2): 129-139.
- Middleton, G. V. and J. B. Southard (1984), *Mechanics of sediment movement*, Society of Economic Paleontologists and Mineralogists.
- Miller, M.C., I.N. McCave, and P.D. Komar (1977), Threshold of sediment motion under unidirectional currents, *Sedimentology*, 24, 507-527.
- Nino, Y., F. Lopez, and M. Garcia (2003), Threshold for particle entrainment into suspension, *Sedimentology*, 50, 247-263.
- Paintal, A. S. (1971), Concept of Critical Shear Stress in Loose Boundary Open Channels, *J. Hydraul. Res.*, 9(1), 91-113.
- Paintal, A. S. (1971), A stochastic model of bed load transport, *J. Hydraul. Res.*, 9(4), 527-554.
- Papanicolaou, A., P. Diplas, C. L. Dancy, and M. Balakrishnan (2001), Surface roughness effects in near-bed turbulence: Implications to sediment entrainment, *J. Eng. Mech.*, 127(3), 211-218.
- Papanicolaou, A. N., P. Diplas, N. Evaggelopoulos, and S. Fotopoulos (2002), Stochastic Incipient Motion Criterion for Spheres under Various Bed Packing Conditions, *J. Hydraul. Eng.*, 128(4), 369-380.
- Paphitis, D., M. B. Collins, L. A. Nash, and S. Wallbridge (2002), Settling velocities and entrainment thresholds of biogenic sands (shell fragments) under unidirectional flows, *Sedimentology*, 49, 211-225.
- Pope, S. B. (2000), *Turbulent Flows*, Cambridge University Press.

- Recking, A. (2009), Theoretical development on the effects of changing flow hydraulics on incipient bed load motion. *Water Resour. Res.* 45, W04401, doi:10.1029/2008WR006826.
- Rhoads, B. (1993), Streampower: a unifying theme for urban fluvial geomorphology, in Herricks, E.E. (Ed.), *Urban Runoff and Receiving Systems: an Interdisciplinary Analysis of Impact, Monitoring and Management. Proceedings Engineering Foundation Conference*, Mt Crested Butte CO, pp. 91–101.
- Rubey, W. W. (1933), Equilibrium conditions in debris-laden streams, *Am. Geophys. Union Trans., 14th Ann. Meeting*.
- Schmeeckle, M. W., J. M. Nelson, and R. L. Shreve (2007), Forces on stationary particles in near-bed turbulent flows, *J. Geophys. Res.*, 112, F02003, doi:10.1029/2006JF000536.
- Sechet, P., and B. Le Guennec (1999), Bursting phenomenon and incipient motion of solid particles in bed-load transport, *J. Hydraul. Res.*, 37(5), 683-696.
- Shields, A. (1936), Application of similarity principles and turbulence research to bed-load movement, Rep., No. 167, California Institute of Technology, Pasadena, CA.
- Shvidchenko, A. B., and G. Pender (2000), Flume study of the effect of relative depth on the incipient motion of coarse uniform sediments, *Water Resour. Res.*, 36(2), 619-628.
- Shvidchenko, A. B., and G. Pender (2001), Macroturbulent structure of open-channel flow over gravel beds, *Water Resour. Res.*, 37(3), 709-719.
- Smart, G. M., and H. M. Habersack (2007), Pressure fluctuations and gravel entrainment in rivers, *J. Hydraul. Res.*, 45(5), 661-673.
- Sundborg, Å. (1956), The river Klarälven. A study of fluvial processes. *Geogr. Ann.*, 38
- Sumer, B. M., L. H. C. Chua, N.-S. Cheng, and J. Fredsoe (2003), Influence of Turbulence on Bed Load Sediment Transport, *J. Hydraul. Eng.*, 129(8), 585-596.
- Sutherland, A.J. (1967), Proposed mechanism for sediment entrainment by turbulent flows, *J. Geophysical Res.*, 72(24), 6183-6194.
- Valyrakis, M., P., Diplas, C.L., Dancey, K., Greer, and A.O. Celik (2010), The role of instantaneous force magnitude and duration on particle entrainment, *J. Geophysical Res.*, 115:1-18 DOI:10.1029/2008JF001247.
- Valyrakis, M., P., Diplas, C.L., and Dancey (2011a), Entrainment of coarse grains in turbulent flows: an Extreme Value Theory approach, *Water Resour. Res.*, (submitted).

- Valyrakis, M., P., Diplas, C.L., and Dancey (2011b), Comparison of event based criteria for the entrainment of coarse particles in turbulent flows, *Geoph. Res. Let.* (under submission).
- Vollmer, S., and M. G. Kleinhans (2007), Predicting incipient motion, including the effect of turbulent pressure fluctuations in the bed, *Water Resour. Res.*, 43, W05410, doi:10.1029/2006WR004919.
- White, C. M. (1940), The Equilibrium of Grains on the Bed of a Stream, *Proc. R. Soc. London A*, 174(958), 322-338.
- Wu, F.-C., and Y.-C. Lin (2002), Pickup Probability of Sediment under Log-Normal Velocity Distribution, *J. Hydraul. Eng.*, 128(4), 438-442.
- Wu, F.-C., and Y.-J. Chou (2003), Rolling and Lifting Probabilities for Sediment Entrainment, *J. Hydraul. Eng.*, 129(2), 110-119.
- Wu, F.-C., and K.-H. Yang (2004), Entrainment Probabilities of Mixed-Size Sediment Incorporating Near-Bed Coherent Flow Structures, *J. Hydraul. Eng.*, 130(12), 1187-1197.
- Yang, C. T. (1972), Unit Stream power and sediment transport, *J. Hydraul. Div.*, 98, 1804-1826.
- Yang, C.T. and Stall, J.B., (1976), Applicability of Unit Stream Power equation, *J. Hydraul. Div.*, 102(HY5), 559-568.
- Yang, C.T. (1979), Unit Stream Power Equations for Total Load, *Jourrzal of Hydrology*, 40, 123-138.
- Yang, C. T. and A. Molinas (1982), Sediment Transport and Unit Stream Power Function, *J. Hydraul. Div.*, 108(HY6), 774-793.
- Zanke, U. C. E. (2003), On the influence of turbulence on the initiation of sediment motion, *Int. J. Sed. Res.*, 18(1), 17-31.

## **Chapter 6. Comparison of event based impulse and energy criteria for the entrainment of coarse particles in turbulent flow**

Manousos Valyrakis,<sup>1</sup> Panayiotis Diplas,<sup>1</sup> and Clint L. Dancey<sup>1</sup>

\*This chapter is a reprint of the manuscript: Valyrakis, M., P. Diplas, and C. L. Dancey, (2011), Comparison of event based impulse and energy criteria for the entrainment of coarse particles in turbulent flow, *Geophysical Research Letters*, (under submission).

<sup>1</sup>Baker Environmental Hydraulics Laboratory, Department of Civil and Environmental Engineering, Virginia Polytechnic Institute and State University, Blacksburg, Virginia, USA.

### **Abstract**

Two new criteria namely impulse and energy have been proposed to incorporate the dynamically significant flow characteristics required for prediction of the onset of particle motion. These criteria have been theoretically formulated as well as experimentally validated for a range of turbulent flow conditions. This paper focuses on the interconnection between the two concepts and establishes their relationship on a theoretical basis as derived from fundamental principles of mechanics and laws of physics. Particular emphasis is given to the accuracy and utility of the energy criterion. The applicability of this concept is extended with the analysis of highly energetic flow events responsible for the entrainment of sediment particles and their characterization in terms of coherent flow structures, by means of quadrant analysis. For this purpose a series of mobile particle flume experiments corresponding to low mobility conditions are employed. Time series of instantaneous stream-wise and stream-normal velocity components before and during entrainment are presented along with the associated trajectories of the dislodging particle. The role of high magnitude stream-wise velocity sustained for a period of time on particle entrainment –either as long sweep events or sequence of sweep events with outward interactions and ejections, is outlined. Detailed trends between the occurrence of specific flow structures and their impact on particle response are provided, with specific emphasis on the characteristic magnitude and scales of the associated energetic flow events.

## 1. Introduction

Understanding the underlying mechanism of the processes leading to transport of sediment particles in fluvial, coastal and aeolian environments, is one of the fundamental problems in earth-surface dynamics. The dynamic interplay of the rapidly fluctuating turbulent flow near the hydraulically rough boundary with the bed surface particles has been a topic of active research for several decades. Knowledge of the flow conditions near the threshold of entrainment is important for a variety of applications ranging from hydraulic engineering (e.g. river bed and bank protection and armoring against bridge scour), to environmental engineering and stream ecology (transport of contaminated sediments and fish biota).

Temporally and spatially averaged criteria such as the Shields [1936] critical stress are widely employed to accurately identify the flow conditions leading to sediment transport notwithstanding the criticism expressed with regard to their accuracy [Miller *et al.*, 1977; Bettess, 1984; Buffington and Montgomery, 1997; Shvidchenko and Pender, 2000; Paphitis *et al.*, 2002]. Acknowledging the limitations of such mean parameters, a number of researchers have outlined the role of the peaks of the instantaneous hydrodynamic forces exerted on a particle, that result on its entrainment downstream [Einstein and El-Samni, 1949; Sutherland, 1967; Paintal, 1971; Apperley and Raudkivi, 1989; Papanicolaou *et al.*, 2001; Sumer *et al.*, 2003; Zanke, 2003; Hoffland *et al.*, 2005; Schmeeckle *et al.*, 2007; Vollmer and Kleinhans, 2007].

In addition to the role of the magnitude of the instantaneous stress tensor, Diplas *et al.* [2008], incorporated the duration of the peak events proposing their product or impulse as the criterion for the onset of entrainment of coarse grains. Under this framework, the impulse criterion has been theoretically extended for different modes of entrainment, as well as experimentally investigated and probabilistically modeled [Valyrakis *et al.*, 2010; Valyrakis *et al.*, 2011a].

Considering the energy of the flow events transferred towards the grain entrainment rather than the imparted momentum, Valyrakis *et al.* [2011b], proposed an energy based criterion to describe the entrainment of coarse sediment particles at near threshold flows. Both impulse and energy criteria are event based approaches that capture the dynamically important flow features required for prediction of the onset of particle movement and as such bare many similarities. The

purpose of this work is to examine the similarities as well as the utility of the above concepts. Particular emphasis is given to the derivation of the energy criterion and its interconnection to impulse via the energy-impulse equation, as well as the versatility and advantages of the energy criterion. Its application is further extended to the analysis of mobile particle experiments, with specific focus on the role and characteristic features of turbulent coherent flow structures –more specifically sweeps, that are shown to carry single or multiple highly energetic events triggering various levels of grain mobilization in rolling mode, from small twitching motions to rapid full dislodgements.

## **2. Derivation of impulse and energy criteria from first principles**

The fundamental physical laws of classical mechanics have set the basis for the theoretical development of the applied science of engineering hydraulics. In particular, the equations of classical mechanics that describe the transport of sediment particles due to the action of turbulent flows are the equations of motion. There exist two major formulations of the equations of motion, namely the Newtonian and the Lagrangian. The first approach, also called vectorial, is based on the magnitude and direction of all of the forces acting on a body, while the latter is a scalar approach incorporating energy and its variants. In the following sections, the relationship between the above formulations and the criteria used to describe particle entrainment at near threshold flow conditions is outlined.

### **2.1. Newtonian formulation**

Newton's laws of motion are three equations central to classical mechanics which are typically used to describe the effect of forces on the motion of the body upon which they act. These physical laws employ the parameters of force and acceleration or momentum. Traditionally researchers investigating the inception of motion of coarse particles due to the action of turbulent flows have employed a static balance of forces [Jeffreys, 1929; Benedict and Christensen, 1972; Ling, 1995; Nino *et al.*, 2003] and/or moments [e.g. White, 1940; Coleman, 1967; Komar and Li, 1988; James 1990; Kirchner *et al.*, 1990; Papanicolaou *et al.*, 2002] for grains entrained in saltation and rolling mode respectively. This literature has typically embraced a static definition

of incipient motion based on the first of Newton's laws of motion, stating that a particle initially at rest starts moving due to the action of external unbalanced forces ( $F > F_{cr}$ , with the threshold force being dependent on the particle and local arrangement parameters).

However, close observation of the entrainment process revealed that a significant portion of the high magnitude instantaneous forces do not last long enough to fully dislodge a particle out of its resting pocket [Diplas *et al.*, 2008]. Such cases where the particle was observed to twitch unable to be further entrained downstream have been observed both in the lab as well as on the field [Garcia *et al.*, 2007]. To enable a more complete and accurate description for the entrainment process of sedimentary particles a dynamic event based definition is required. The second law of motion allows for this by considering that the external force and torque applied to a particle equals the time derivative of its linear and angular momentum. In this manner, dynamic criteria for saltating and rolling particles have been formulated [Diplas *et al.*, 2008; Valyrakis *et al.*, 2010], based on impulse ( $I$ ) defined as:

$$I = \int_t^{t+T} F dt, \text{ with } F > F_{cr} \text{ for } t < t < t+T \quad (1)$$

This framework proposes impulse, the product of hydrodynamic force above a certain threshold, ( $F > F_{cr}$ ) with the duration ( $T$ ) over which it is applied as the central parameter describing particle entrainment. In both of the above approaches Newton's third law, also called the action-reaction law, serves to provide kinematic constraints and determine whether the mode of entrainment is by saltation or rolling [Yalin, 1972].

## 2.2. Lagrangian formulation

The Lagrangian formulation, introduced by Lagrange in 1788 –about a century after Newton's formulation of classical mechanics, is an analytical variational approach, which instead of the forces acting on the particle focuses on its mechanical energy. It is assumed that the system is characterized by two energy functions: kinetic ( $E_{kin}$ ) and potential ( $E_{pot}$ ). The difference between kinetic and potential energies is called the Lagrangian ( $L$ ), and this approach targets at minimizing its time integral called action ( $S$ ):

$$\delta[S] = \delta[\int L dt] \quad (2)$$

where  $\delta[\ ]$  denotes the operator of variation. The principle of least action, equation (2), is equivalent to Lagrange's and Hamilton's principle [Lanczos, 1949], and may be used to show that a grain rolling out of its pocket will always follow the minimum resistance (or minimum energy) path.

Starting from D'Alembert's principle of virtual work the interrelation between Newtonian and Lagrangian formulations may be shown [Torby, 1984; Yang, 1992]. The Lagrange equations can be solved to find the critical conditions for grain entrainment due to energetic events:

$$\frac{d}{dt} \frac{\partial L}{\partial \dot{q}_i} - \frac{\partial L}{\partial q_i} = Q_i \quad (3)$$

with  $Q_i$  the generalized external forces,  $q_i$  the generalized displacements for  $i=1, \dots, n$ , where  $n$  is the number of degrees of freedom. The energy criterion relates the amount of energy transferred from a highly energetic flow event ( $E_f$ ) to the solid particle ( $W_{p,cr}$ ):  $C_{eff} E_f > W_{p,cr}$ . Equation (3) may be employed to derive the threshold energy level required or minimum work performed on the particle ( $W_{p,cr}$ ) for entrainment by saltation or rolling, as illustrated in the following examples.

For the case of a saltating particle using a Cartesian coordinate system (see Fig. 2, in [Valyrakis et al., 2011b]), the Lagrangian is defined as the difference between the kinetic and potential energy at an elevation ( $z$ ):

$$L = \frac{1}{2} (\rho_s + \rho_f C_m) V_p \dot{z}^2 - (\rho_s - \rho_f) V_p g z \cos \alpha \quad (4)$$

with  $\alpha$  the bed slope,  $V_p = 4\pi R_m^3 / 3$  the particle's volume and  $R_m$  its radius,  $\rho_f$  the fluid density,  $\rho_s$  the particle's density and  $C_m$  is the added mass coefficient, which equals 0.5 for spheres in water [Auton, 1988]. Then replacing  $L$  from equation (4) into the Lagrange equation (equation 3) with  $q_i = z$ , yields:

$$\ddot{z} = -g \cos a \left( \frac{\rho_s - \rho_f}{\rho_s + \rho_f C_m} \right) \quad (5)$$

which using the appropriate initial and final conditions ( $z(t=0)=0$ ,  $u_p(t=0)=0$  and  $z(t=t_{tot})=z_{max}=2R_m$  and  $u_p(t=t_{tot})=0$ ) the energy criterion for saltation is obtained:

$$(C_{salt} u_f T_{salt}) (C_A C_p u_f^2) \geq \frac{8}{3} \cos \alpha \frac{\rho_s - \rho_f}{\rho_f} g R_m^2 \quad (6)$$

with  $C_{salt}$ , the efficiency of flow energy transfer to the saltating grain,  $C_A$ , denoting the effective area of flow event and solid particle interaction and  $C_p$ , an empirical pressure coefficient.

Similarly, for the case of a particle entrained by rolling, the Lagrangian is defined in polar coordinates as follows:

$$L = \frac{1}{2} (\rho_s + \rho_f C_m) V_p (R_m^2 \dot{\theta}^2) - (\rho_s - \rho_f) V_p g R_m \sin \theta \cos a \quad (7)$$

where  $\theta$  is the angular displacement of the particle. Then again using the appropriate initial and final conditions ( $\theta(t=0)=\theta_0$ ,  $u_p(t=0)=0$  and  $\theta(t=t_{tot})=\pi/2$  and  $u_p(t=t_{tot})=0$ ) the energy criterion for rolling is obtained:

$$(C_{roll} u_f T_{roll}) \left( \frac{C_D}{2} C_A u_f^2 \right) \geq \frac{4}{3} \cos \alpha (1 - \sin \theta_0) \frac{\rho_s - \rho_f}{\rho_f} g L_{arm} R_m \quad (8)$$

with  $C_{roll}$ , the energy transport coefficient for the rolling particle,  $C_D$  the drag coefficient,  $\theta_0 = \alpha + \text{arccot}(R_b / (3R_m^2 + 6R_m R_b - R_b^2))$  the pivot angle,  $R_b$  the radius of particles forming the surface layer and  $L_{arm} = (2R_m^2 + 8R_m R_b)^{1/2}$  the lever arm.

### 3. Comparison between the impulse and energy criteria

#### 3.1. Similarities

As shown earlier, the impulse and energy criteria may be derived from the two fundamental formulations of equations of motion of classical mechanics, the Newtonian and Lagrangian which are interconnected [e.g. *Torby*, 1984; *Yang*, 1992]. In practice, a direct link between the two concepts may be established assuming infinitesimally small displacements,  $\Delta x$ , over the duration ( $T$ ) of application of the hydrodynamic force  $F$  (with  $F$  representing a mean force magnitude over  $T$ ). Then the required mechanical work performed on the particle,  $W_{p,cr}=F\Delta x$ , where  $\Delta x=Tu_p$  and  $u_p$  is the mean velocity of the particle over the duration  $T$ . Then equation 1 becomes:  $I=FT= W_{p,cr}/u_p$ , or  $W_{p,cr} = I \cdot u_p$ , which is the energy-impulse equation.

Beyond their direct interconnection and linkage with respect to their derivation from first laws and principles, the impulse and energy concepts are physically sound and more appropriate compared to past traditional approaches. They are compatible to the dynamic character of particle transport, by including for the temporal dimension of high magnitude turbulent events. In accordance to many observations in the literature arguing for the intermittent and episodic nature of particle entrainment at near threshold flow conditions, the impulse and energy criteria are threshold based theories where only the randomly occurring high magnitude events (in excess of a momentum,  $I_{cr}$ , or energy threshold,  $W_{cr}$ , respectively), may trigger particle entrainment. Thus both approaches may be implemented using an appropriate stochastic modeling framework such as extreme value theory [e.g. *Valyrakis et al.*, 2010].

#### 3.2. Advantages of energy criterion

Traditionally engineers have been reluctant to use concepts they have not been familiar with, which may also seem to be cumbersome to define because of their somewhat abstract nature. Energy methods belong to this category, as opposed to force approaches to which engineers are more accustomed. Despite this, the utilization and application of the energy criterion may be at least as intuitive and physically meaningful as the impulse criterion. Both criteria can be expressed as the product of duration and hydrodynamic force for the former or effective flow

power for the latter. However, the energy threshold may also be expressed in terms of the specific energy ( $\sim u_f^2$ ) of the flow event and its lengthscale ( $u_f T_{roll}$ ), which directly relate to the intensity and dimension of the event.

In terms of predictive ability the energy criterion performs slightly better compared to the impulse criterion for the common case of a rolling particle. This happens because for the linearization of the solution of the Newtonian formulation of equations of motion, the impulse criterion assumes small angular displacements for the particle during the occurrence of the flow event. This assumption generally holds true, but renders this formulation less accurate for relatively long durations. Furthermore, with regard to their application, the implementation of the Newtonian approach as for example in discrete particle methods requires recursive computation of the forces exerted on each mobile and bed surface particle [Valyrakis *et al.*, 2008], rendering this formulation computationally intensive. As opposed to the previous method the energy criterion could be employed under less computationally intensive and more physically intuitive, thermodynamic or statistical mechanics modeling framework.

Energy is one of the most significant concepts in many branches of science and engineering, capable of describing a plethora of nonlinear phenomena and complex processes across a wide range of spatial and temporal scales, from the small scales of individual particle to the larger scales of geomorphic systems [e.g. Thorn, 1994]. In this manner, an energy criterion may provide a simple and universal measure towards a unified theory, which bridges a variety of the already existing theories.

### 3.3. Application examples

For instance, a quantitative example may be offered, considering the local particle configuration parameters described in [Valyrakis *et al.*, 2011b]. Assume a spherical particle of radius  $R_m= 6.3$  mm, and density  $\rho_s=2300\text{kg/m}^3$  in water flow. In the case it is hidden in the bed surface layer, entrainment is assumed to occur by saltation, due to the passage of an energetic flow event of specific energy  $u_f^2 \sim \Delta p/\rho_f$  and effective lengthscale  $C_{salt} u_f T_{salt}$  or  $u_p T_{salt}$ . The two formulations of equation of motion return exactly the same solution as shown in Figure 1a.

In the case of a completely exposed particle entrained by rolling the critical energy level is predicted from equation 8 as illustrated in Figure 1b (thick curve). The qualitative dependence of

the magnitude of the event in terms of energy density and its streamwise length scale, is similar to the case of saltation. Only the events represented by points above the predicted threshold curve may transfer enough flow energy for full entrainment.

The energy criterion for rolling is directly related to the corresponding impulse criterion via the energy-impulse equation, where the critical impulse required may be computed e.g. from equation (5), in [Valyrakis *et al.*, 2011a]. A direct comparison of the two criteria may be performed, by plotting the threshold curves from the energy and impulse criteria, given by  $C_{roll} T_{roll} \cdot u_f$  and  $T_{roll} \cdot u_p$ , respectively (Figures 1b). Compared to the energy criterion (dashed line, Figure 1b), the prediction of the impulse criterion overestimates the threshold for relatively low values of specific energy ( $\sim u_f^2$ ), due to the linearization of the equations of motion. This is in agreement with the findings of [Valyrakis *et al.*, 2010], who observed increasing error for decreasing magnitude of the flow event ( $F \sim u_f^2$ ). Thus the energy criterion provides a more accurate representation of the threshold of entrainment by rolling. Employing the experimental data obtained from relevant mobile particle experiments (e.g. run *E1* in presented in the aforementioned publication), a direct comparison of the two concepts may be pursued (assuming a mean representative value for  $C_{roll} \sim 0.08$ ). The impulse theory was successful at predicting 72% of the complete particle entrainment events, while the energy criterion performed somewhat more satisfactorily (predicted about 78% of them).

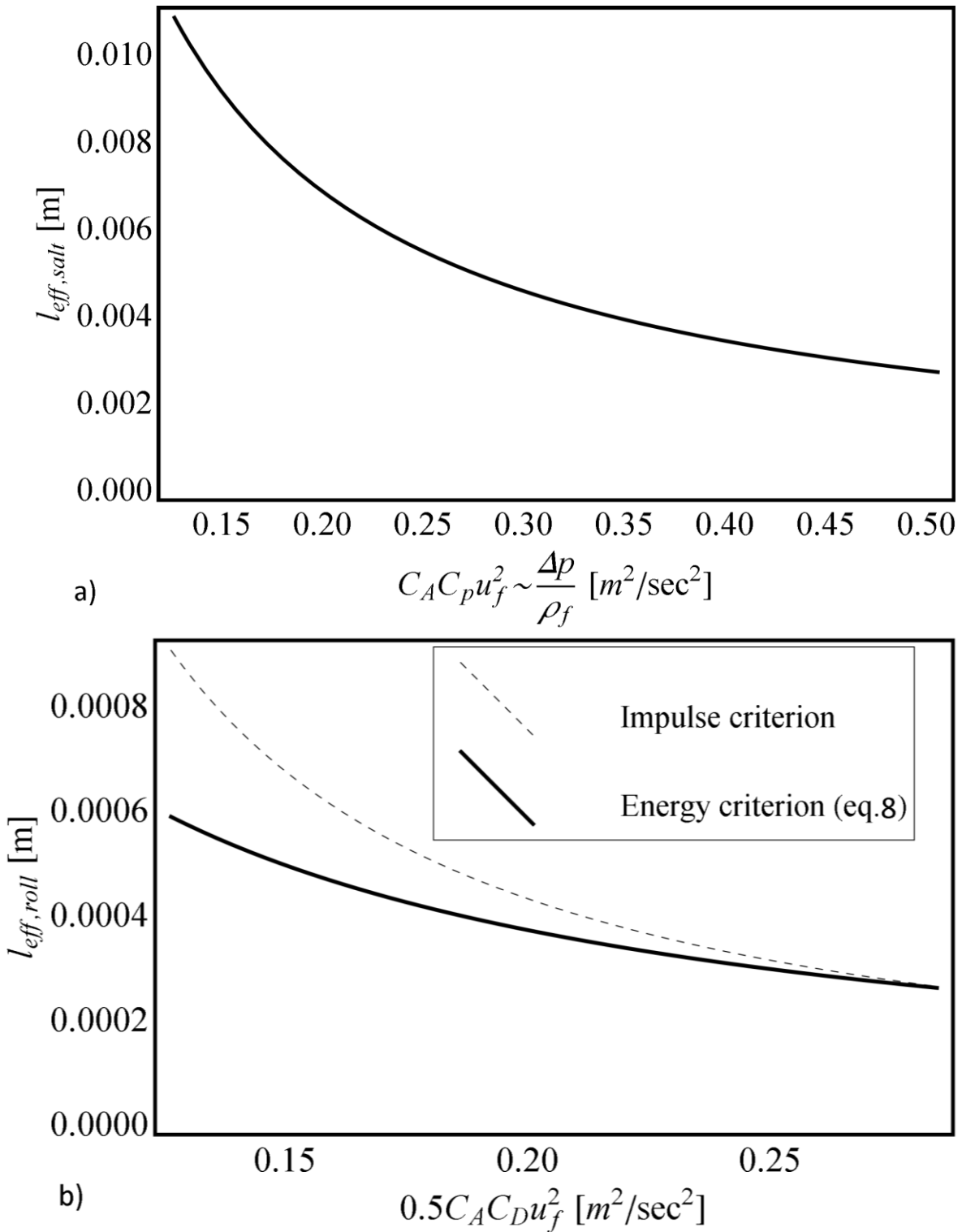


**Figure 1.** Representation of energy threshold for entrainment (equation 6) of a 12.6 mm particle by a) saltation, and b) rolling, as a function of the average specific energy ( $\sim u_f^2$ ) and lengthscale of the flow event.

#### 4. Classification of high energy events with regard to entrainment duration and the coherent flow structures

In this section the application of energy criterion is extended to characterize and find potential patterns describing the flow structures carrying the highly energetic flow events that lead to particle entrainment. To this purpose, available synchronous records of particle displacement and the local flow field upstream of it, are employed from appropriate mobile particle flume experiments (e.g. *E1*). This analysis is offered to complement the trajectory analysis of energetic events [Valyrakis *et al.*, 2011b], by providing additional information regarding the sequence of flow structures (employing the stream-normal component of the flow velocity), flow velocity signatures and possible trends that help group these flow events with regard to their effectiveness.

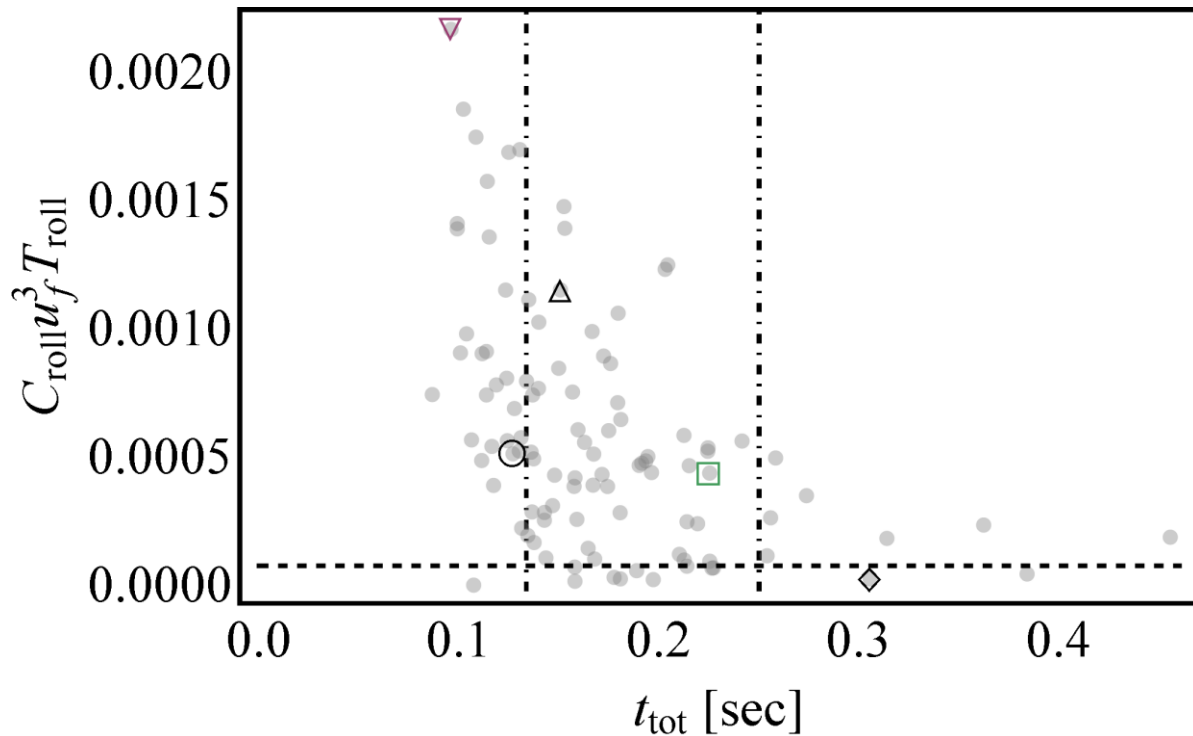


**Figure 2.** Classification of the energetic flow events (shown with grey, filled circles) based on the duration required for the particle to complete its entrainment ( $t_{tot}$ ). The events depicted with open symbols (del, circle, triangle, square and diamond) correspond to the typical events analyzed in the figure pairs 3a-b, c-d, e-f, g-h, and i-k respectively.

The time to full particle displacement,  $t_{tot}$ , is a direct measure of the total mechanical work performed on the particle or equivalently the effectiveness of energy transfer from the flow. Thus the duration required for the particle to complete its displacement may be used to group the flow events into three main regions, as shown on Figure 2. Thus, the energetic events are separated into the region of rapid entrainments ( $t_{tot} < 0.134\text{s}$ ), long entrainments ( $0.134\text{s} < t_{tot} < 0.225\text{s}$ ) and very long entrainments ( $t_{tot} > 0.225\text{s}$ ), denoted by the dot-dashed vertical lines in Figure 2. The above limits are determined after inspecting the sequence of flow structures before and during entrainment and are only given to facilitate clustering the events with relatively common features. The full range of durations of particle entrainment (for run *EI*) spans from 0.086 to more than 5 times the shortest duration (0.455s).

In the following sections, the traditional quadrant analysis proposed by [Lu and Willmarth, 1973] is employed to extract information relevant to the coherent flow structures. This is attained by decomposing the stream-wise and stream-normal velocity components into their mean ( $u_{f,m}$ ,  $v_{f,m}$ ) and fluctuating parts ( $u_f'$ ,  $v_f'$ ). Then the flow structures are classified into four quadrants, namely outward interactions (Q<sub>1</sub>, with  $u_f' > 0$ ,  $v_f' > 0$ ), ejections (Q<sub>2</sub>, with  $u_f' < 0$ ,  $v_f' > 0$ ), inward interactions (Q<sub>3</sub>, with  $u_f' < 0$ ,  $v_f' < 0$ ) and sweeps (Q<sub>4</sub>, with  $u_f' > 0$ ,  $v_f' < 0$ ). For the near bed region, sweeps and ejections are the most commonly occurring structures, contributing significantly to the production of Reynolds shear stresses,  $-\rho_f u'v'$  [Nezu and Nakagawa, 1993]. Based on their definition, sweeps are high speed flow structures that move downwards, while ejections correspond to upward moving low speed fluid.

Since particle entrainment is a dynamic process of finite duration, it is significant, in addition to characterizing the flow structures which occur at the instant of entrainment, to investigate whether certain velocity signatures or sequence of coherent flow patterns can be discerned. Typical examples representative of these flow structures are provided in Figure 3. To facilitate the visual identification of the sequence of flow structures before and during entrainment the curves' shading is appropriately color-coded. In addition, to enable linking those structures to the energetic flow events associated with particle entrainment, the corresponding threshold level is shown (horizontal dot-dashed line in Figures 3a, c, e, g and i), defined as the events where  $u_f' > u_{cr} - u_{f,m}$ . In accordance with the energy criterion, whenever the above inequality holds true mechanical work is performed towards particle entrainment. The trajectory of the particle (Figures 3b, d, f, h and k) is also analyzed employing the normalized time series of its

streamwise displacement ( $\Delta x/\Delta x_{max}$ ), which are highly accurate (background noise level of about 1.4%), as well as of high temporal resolution (about 3.5ms on average). This further allows the accurate coupling of the characteristic features and relevant scales of the advected flow structures and energetic events they carry, with the degree of particle response (from twitches to full entrainment).

#### 4.1. Rapid particle entrainments

The region of relatively short duration of particle entrainments contains about 29% of the energetic events leading to complete entrainment. These may be further separated into the relatively high energy transfer events (points in the upper left region in Figure 2, such as the event denoted with the del symbol) and the low energy transfer events (found in the lower left part of Figure 2, such as the event marked with the open circle). Generally, these events are characterized by high magnitude of instantaneous flow power (adopting the parameterization of power as a function of the triple correlation of  $u_f$ ) as illustrated in Figures 3a and c. The more sustained the peaking energy events are (e.g. Figure 3a) or the greater the streamwise scale of the event (e.g. larger than 2 or 3 particle diameters), the greater the amount of performed work on the particle. This means that the particle obtains greater kinetic energy and dislodges much faster compared to the other cases (Figure 3b).

Regarding the flow structures, the dominant role of sweeps [e.g. *Nezu and Nakagawa, 1993*] is emphasized. The sweep events occurring at or during the time of particle displacement have temporal scales ranging from about 10 to 60ms. Most (about 73%) of these structures include sustained and/or high peaking energy events. In certain cases (20% of these events), these structures are interrupted by shortlived outward interactions (Figure 3a), or more scarcely (7%) by abrupt ejections (Figure 3c) at the instant of entrainment. This succession of sweep events may include several high energy events, peaking above the theoretical threshold (e.g. Figure 3a).

#### 4.2. Slow particle entrainments

The rest of the entrainment events (74 out of 104) are classified as long events, 15% of which last very long (here with  $t_{tot} > 0.225s$ ). Similar to the previous observations, the greater the scale

and magnitude of the energy events is, the faster the particle will dislodge (e.g. compare Figure 3e and g). At certain cases, a sequence of initially weak but of gradually increasing magnitude (or duration) energy events is observed (Figure 3e). In these occasions the particle initially dislodges out of its pocket very slowly, a process which accelerates, as may be observed in Figure 3f. This may be seen as a result of the increasing rate of energy transfer due to the passage of a succession of more energetic flow events. Again, the role of sweep structures is very significant. However, in contrast to the well sustained sweeps discussed before, these structures are not as strong, while being interrupted by ejection events of about the same intensity. Thus in several instances, these events cannot provide sufficient energy on their own to completely dislodge the particle.

For many of these cases a subsequent event performing additional work on the particle follows at a relatively small temporal separation after the first high energy event (Figure 3i). For such conditions, the particle is seen to dislodge more slowly compared to the aforementioned cases until the impact of a successive event above threshold occurs (Figure 3i). If the temporal separation of the sequence of energy events is more pronounced (in this case from 10-20ms as shown in Figure 3k), it will take longer for the particle to complete its dislodgement. Initially a first energetic flow event, transfers enough energy only to bring the particle to a new location from which a subsequent flow event can further complete the entrainment. The particle accelerates during the passage of the event that triggers its dislodgement and then it decelerates until the follow-up events that provide the rest of the required energy take place. This is regularly demonstrated with an inflection point in the trace of the trajectory plot (Figure 3k), indicating that a second accelerating phase has initiated. As expected, this pattern occurs for all of the events for which entrainment lasts very long (e.g. for  $t_{tot} > 0.225s$ , for the current experimental arrangement and flow conditions).

### **4.3. Incomplete particle entrainments**

The aforementioned cases correspond to the cases where the particle fully dislodged downstream. There are also many cases (about 1/3 of the complete entrainment events) where the energy transferred did not suffice for full entrainment, but only produced a weak response or twitch. This may be seen as an extension of the previous pattern of particle entrainment

dynamics, where a sequence of  $Q_4$  and  $Q_2$  flow structures takes place. In particular, during the former energy is transferred towards particle displacement, while during the latter the particle is seen to be pushed back into its pocket (e.g. see flow events about 602.0s in Figure 3i and). The energetic  $Q_4$  events are relatively short-lived and their impact with regard to the particle response is disrupted by the effect of other structures. It is interesting to note that about one out of the four cases of incomplete grain movement (twitches), are directly followed by a complete particle entrainment.

## 5. Discussion: Generalization of the energy criterion

Based on the previous observations, it is concluded that a wide range of different degrees of particle response and entrainment dynamics patterns may be triggered by the passage of a single or multiple energetic flow events carried by certain coherent flow structures. Depending on the characteristic scales and magnitude of the high energy flow events, as well as the sequence of the flow structures before and during particle entrainment, various particle mobility levels are discerned, ranging from incomplete to strong entrainments.

These levels of particle mobility may be incorporated in the energy criterion by including the ratio of potential energy stored in the final particle location to the reference critical level ( $W_{p,cr}$ ),  $\gamma$ . In this manner, the energy criterion can be adjusted to account for a range of objectively described incipient motion thresholds found in the literature [e.g. *Lavelle and Mofjeld, 1987; Buffington and Montgomery, 1997*]. In addition, the energy criterion can be modified to include all the energy events carried by a single or successive small scale coherent flow structures that perform mechanical work on the particle:

$$\sum_{i=1}^n (C_{eff,i} E_{f,i}) \geq \gamma W_{p,cr}, \text{ for } i=1,2,\dots,n \quad (9)$$

where the index  $i$ , corresponds to the  $i^{th}$  energetic flow event from a group of  $n$  events that contribute towards the incomplete ( $\gamma < 1$ ), full ( $\gamma = 1$ ) or energetic ( $\gamma > 1$ ) particle entrainment. The above extension (equation 9), offers a generalized approach to the energy criterion, which enhances its descriptive ability and renders it more versatile.

## 6. Conclusions

The event based impulse and energy incipient motion criteria are derived from fundamental laws of classical mechanics and compared with regard to their performance, applicability and extensibility. Specifically, their derivation from the interconnected Newtonian and Lagrangian formulations of the equations of motion of a particle is demonstrated for entrainment by saltation and rolling. It is also shown that the performance of two criteria is comparable with the energy equations having slightly better predictive ability, for the flow conditions examined.

Trends between certain velocity signatures and particle entrainment dynamics are further investigated employing classical quadrant analysis of the turbulent velocity signal along with trajectory analysis of the entrained particle. Emphasis is given on the characterization of the turbulent flow structures and the identification of the features of high energy flow events they carry, just before and during particle entrainment. In this manner, particle entrainment events are classified with regard to the duration required for completing its full displacement, into rapid and slow events, while the role of strong sweep structures is delineated. It is illustrated that the former class of (rapid) displacement events is associated mainly with single, high magnitude and duration flow events, while the latter (slow) corresponds to a sequence of short-lived but energetic flow pulses. In light of the above observations, the energy criterion is extended to incorporate the case of multiple high energy flow events that are grouped together to have a cumulative effect on particle's response.

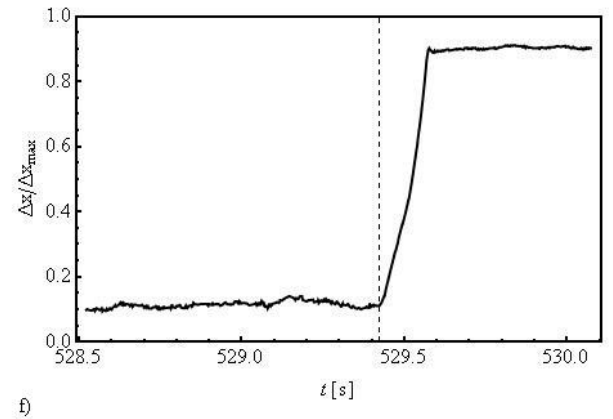
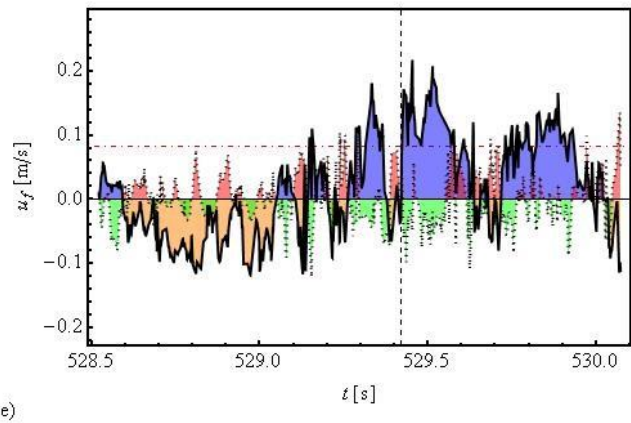
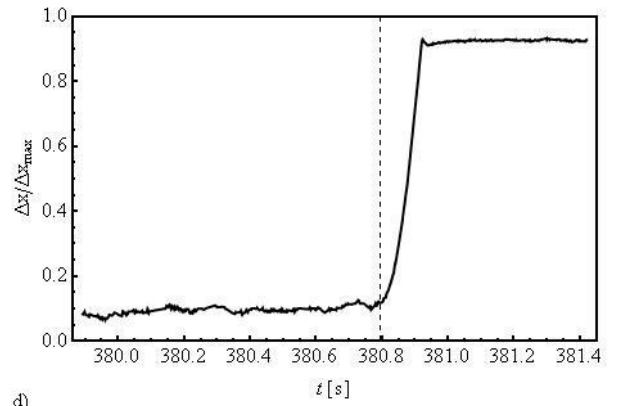
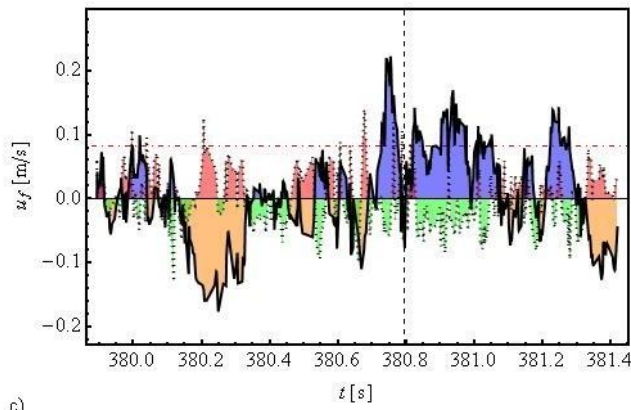
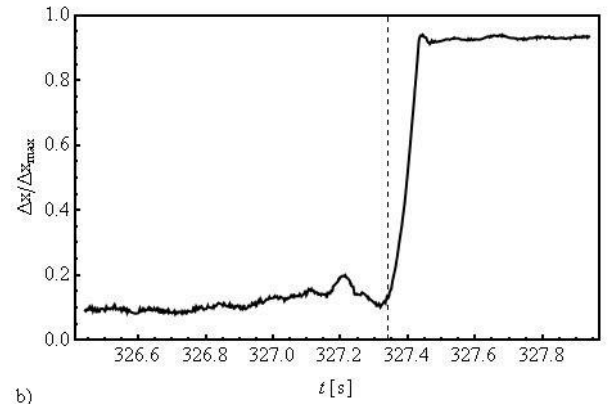
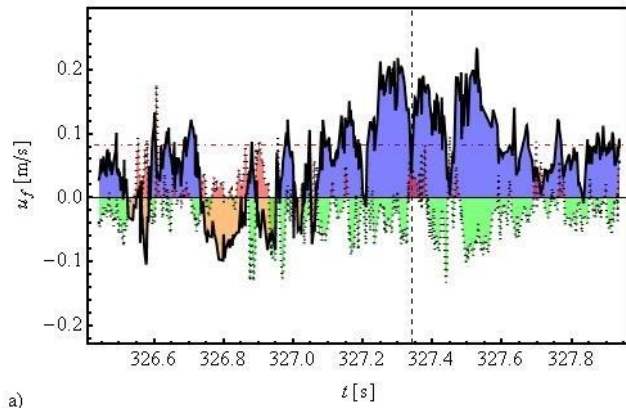
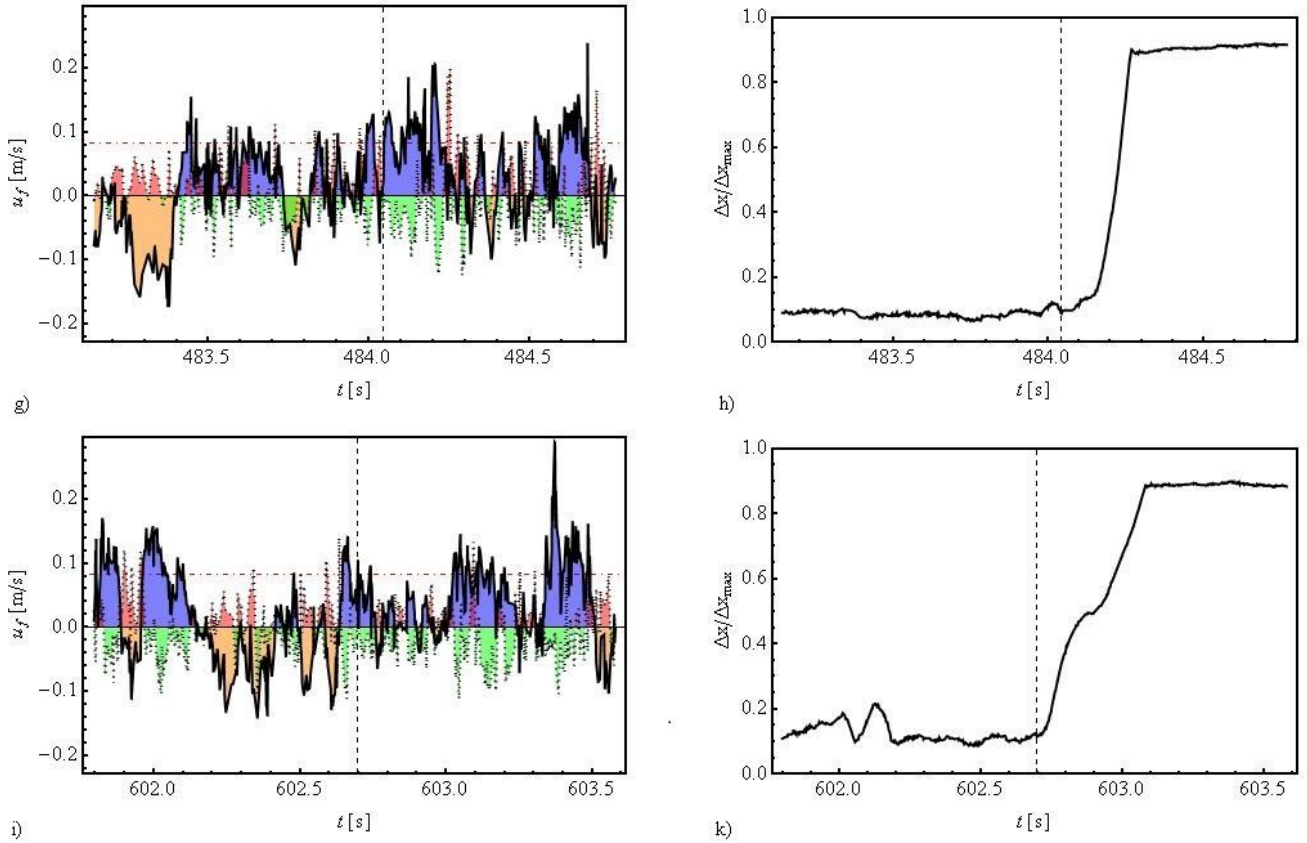


Figure 3 caption provided in the following page.



**Figure 3. a, c, e, g, i):** Fluctuating velocity components ( $u_f'$ ,  $v_f'$  shown as thick continuous and dotted lines, respectively) and corresponding critical streamwise velocity level ( $u_{cr}-u_{f,m}$ , indicated as the horizontal dot-dashed line) for typical entrainment events. Segments of the velocity record with positive  $u_f'$  and  $v_f'$  are shaded with blue and red color, while the regions of down-crossings of  $u_f'$  and  $v_f'$  are shaded with orange and green color respectively. **b, d, f, h, k):** Characteristic particle trajectories corresponding to the typical cases shown in (a, c, e, g, i). The instant of initiation of particle entrainment is depicted with the dotted vertical line.

## Acknowledgement

The support of the National Science Foundation (EAR-0439663, EAR-0738759 and CBET-1033196) and Army Research Office is gratefully acknowledged.

## References

- Apperley, L. W. and Raudkivi, A.J. (1989), The entrainment of sediments by the turbulent flow of water, *Hydrobiologia*, 176/177, 39-49.
- Auton, T. R., J. C. R. Hunt, and M. Prudhomme (1988), The force exerted on a body in inviscid unsteady non-uniform rotational flow, *J. Fluid Mech.*, 197, 241-257.
- Benedict, B. A., and B. A. Christensen (1972), Hydrodynamic lift on a stream bed, in *Sedimentation, Symp. to Honor Prof. H. A. Einstein*, edited by H. W. Shen, pp. 5.1-5.17, Water Resources Publication, Littleton, Colorado.
- Bettess, R. (1984), Initiation of sediment transport in gravel streams, *Proceedings - Institution of civil Engineers*, 77, 79-88.
- Buffington, J. M., and D. R. Montgomery (1997), A systematic analysis of eight decades of incipient motion studies, with special reference to gravel-bedded rivers, *Water Resour. Res.*, 33(8), 1993-2029.
- Coleman, N. (1967), A theoretical and experimental study of drag and lift forces acting on a sphere resting on a hypothetical streambed, in *Proc. 12th Congress Intern. Assoc. Hydr. Res.*, pp. 185-197, Fort Collins, Colorado.
- Diplas, P., C.L. Dancey, A. O. Celik, M. Valyrakis, K. Greer, and T. Akar (2008), The role of impulse on the initiation of particle movement under turbulent flow conditions, *Science*, 322(5902), 717-720.
- Einstein, H. A., and E.-S. A. El-Samni (1949), Hydrodynamic forces on a rough wall, *Rev. Mod. Phys.*, 21(3), 520-527.
- Garcia, C., H. Cohen, I. Reid, A. Rovira, X. Úbeda, and J. B. Laronne (2007), Processes of initiation of motion leading to bedload transport in gravel-bed rivers, *Geophys. Res. Lett.*, 34, L06403, doi:10.1029/2006GL028865.
- Hofland, B., R. Booij, and J. Battjes (2005), Measurement of fluctuating pressures on coarse bed material, *J. Hydraul. Engrg.*, 131(9), 770-781.
- Garcia, C., H. Cohen, I. Reid, A. Rovira, X. Úbeda, and J. B. Laronne (2007), Processes of initiation of motion leading to bedload transport in gravel-bed rivers, *Geophys. Res. Lett.*, 34, L06403, doi:10.1029/2006GL028865.
- James, C. S. (1990), Prediction of entrainment conditions for nonuniform, noncohesive sediments, *J. Hydraul. Res.*, 28(1), 25-41.

- Jeffreys, H. (1929), On the transportation of sediment by streams, *Proc. Cambridge Philos. Soc.*, 25, 272-276.
- Kirchner, J. W., Dietrich, W. E., Iseya, F., and Ikeda, H. (1990), The variability of critical shear stress, friction angle, and grain protrusion in water-worked sediments, *Sedimentology* 37(4), 647–672.
- Kirchner, J. W., W. E. Dietrich, F. Iseya, and H. Ikeda (1990), The variability of critical shear stress, friction angle, and grain protrusion in water-worked sediments, *Sedimentology*, 37(4): 647–672.
- Komar, P. D., and Li, Z. (1988), Application of grain-pivoting and sliding analyses to selective entrainment of gravel and to flow-competence evaluations, *Sedimentology*, 35, 681-695.
- Lanczos, C. (1949) *The Variational Principles of Mechanics*. 418 pp., University of Toronto Press, Toronto.
- Lavelle, J. W. and H. O. Mofjeld (1897), Do critical stresses for incipient motion and erosion really exist?, *J. Hydraul. Eng.* 113(3), 370-385.
- Lu, S. and W. Willmarth (1973), Measurements of the structure of the Reynolds stress in a turbulent boundary layer., *J. Fluid Mech.*, 60, 481-511.
- Miller, M.C., I.N. McCave, and P.D. Komar (1977), Threshold of sediment motion under unidirectional currents, *Sedimentology*, 24, 507-527.
- Nezu, I. and H. Nakagawa (1993), *Turbulence in Open-Channel Flows*. 293pp. Taylor and Francis.
- Nino, Y., F. Lopez, and M. Garcia (2003), Threshold for particle entrainment into suspension, *Sedimentology*, 50, 247-263.
- Paintal, A. S. (1971), Concept of Critical Shear Stress in Loose Boundary Open Channels, *J. Hydraul. Res.*, 9(1), 91-113.
- Papanicolaou, A., P. Diplas, C. L. Dancy, and M. Balakrishnan (2001), Surface roughness effects in near-bed turbulence: Implications to sediment entrainment, *J. Eng. Mech.*, 127(3), 211-218.
- Papanicolaou, A. N., P. Diplas, N. Evaggelopoulos, and S. Fotopoulos (2002), Stochastic Incipient Motion Criterion for Spheres under Various Bed Packing Conditions, *J. Hydraul. Eng.*, 128(4), 369-380.

- Paphitis, D., M. B. Collins, L. A. Nash, and S. Wallbridge (2002), Settling velocities and entrainment thresholds of biogenic sands (shell fragments) under unidirectional flows, *Sedimentology*, 49, 211-225.
- Schmeeckle, M. W., J. M. Nelson, and R. L. Shreve (2007), Forces on stationary particles in near-bed turbulent flows, *J. Geophys. Res.*, 112, F02003, doi:10.1029/2006JF000536.
- Shields, A. (1936), Application of similarity principles and turbulence research to bed-load movement, Rep., No. 167, California Institute of Technology, Pasadena, CA.
- Shvidchenko, A. B., and G. Pender (2000), Flume study of the effect of relative depth on the incipient motion of coarse uniform sediments, *Water Resour. Res.*, 36(2), 619-628.
- Sumer, B. M., L. H. C. Chua, N.-S. Cheng, and J. Fredsoe (2003), Influence of Turbulence on Bed Load Sediment Transport, *J. Hydraul. Eng.*, 129(8), 585-596.
- Sutherland, A.J. (1967), Proposed mechanism for sediment entrainment by turbulent flows, *J. Geophysical Res.*, 72(24), 6183-6194.
- Torby, Bruce (1984). "Energy Methods". Advanced Dynamics for Engineers. HRW Series in Mechanical Engineering. United States of America: CBS College Publishing.
- Valyrakis M., Diplas P., Celik A. O., Dancey C. L. (2008), Investigation of evolution of gravel river bed microforms using a simplified Discrete Particle Model, *Proc. River Flow 2008*, Ismir, Turkey, 03-05 September 2008.
- Valyrakis M., P. Diplas, C. L. Dancey, K. Greer, and A. O. Celik (2010), The role of instantaneous force magnitude and duration on particle entrainment, *J. Geophysical Res.*, 115, F02006, doi:10.1029/2008JF001247.
- Valyrakis, M., P. Diplas, C.L. Dancey (2011a), Entrainment of coarse grains in turbulent flows: an extreme value theory approach, *Water Resources Research*, (under review).
- Valyrakis, M., P. Diplas, and C.L. Dancey (2011b), Entrainment of coarse particles in turbulent flows: an energy approach, *Physical Review E*, (in preparation).
- Vollmer, S., and M. G. Kleinhans (2007), Predicting incipient motion, including the effect of turbulent pressure fluctuations in the bed, *Water Resour. Res.*, 43, W05410, doi:10.1029/2006WR004919.
- White, C. M. (1940), The Equilibrium of Grains on the Bed of a Stream, *Proc. R. Soc. London A*, 174(958), 322-338. Wu, F.-C., and Y.-C. Lin (2002), Pickup Probability of Sediment under Log-Normal Velocity Distribution, *J. Hydraul. Eng.*, 128(4), 438-442.

- Yalin, M. S., and E. Karahan (1979), Inception of sediment transport, *J. Hydraul. Eng.*, 105(11), 1433-1443.
- Yang, C. T. (1972), Unit Stream power and sediment transport, *J. Hydraul. Div.*, 98, 1804-1826.
- Yang, C. T. (1992). A Force, Energy, Entropy, and Energy Dissipation Rate. Entropy and energy dissipation in water resources. V. P. Sing and M. Fiorentin. London, Kluwer Academic Publishers: 63-89.
- Zanke, U. C. E. (2003), On the influence of turbulence on the initiation of sediment motion, *Int. J. Sed. Res.*, 18(1), 17-31.

## Chapter 7. Conclusions

### Summary of major findings

Based on observations from a series of preliminary flume experiments at near incipient motion and uniform flow conditions, it is shown that peak values in the history of instantaneous drag forces are necessary but not sufficient to trigger particle entrainment. The duration of the peaking flow events is also shown to be relevant to the description of particle entrainment. A quantity that successfully captures the effect of both highly fluctuating magnitude of hydrodynamic forcing and duration of its application is impulse. The impulse criterion is formulated theoretically for both saltation and rolling modes of entrainment of a spherical particle.

A series of experiments imparting electromagnetic pulses for the displacement of a steel mobile particle are analyzed to demonstrate the application of the impulse criterion for particle entrainment. The applied pulse features vary in a controlled fashion so as to enable the identification of critical impulses, for various levels of particle mobility ranging from partial to complete displacement. Impulse is shown to be a versatile criterion which despite the variability of the flow features successfully incorporates the salient characteristics required to describe the dynamics of particle displacement.

The intermittent and extremal nature of occurrence of flow impulses and associated particle entrainment, at low mobility uniform flow conditions is statistically modeled utilizing distributions from Extreme Value Theory. Impulses are shown to follow the Frechet distribution which is associated with a power law relation for the frequency and magnitude of impulses. Such a relationship may serve as a particularly useful tool for the prediction of particle entrainment for given flow conditions. In addition to the body, the tail of the distribution of flow impulses or equivalently the distribution of the conditional exceedances above a high impulse threshold, are successfully modeled with the Generalized Pareto distribution, via implementation of the Peaks Over Threshold approach. A framework under which the utility of the above distributions may be extended and generalized by relating the distributions of the forces responsible for grain entrainment and those resisting it, is presented.

In addition to statistical modeling of the flow impulses, particle entrainment is treated as a survival process. Using the temporal history of particle entrainments obtained experimentally, it

is demonstrated that the Weibul or exponential distributions provide good fits to the empirical distribution of the interarrival time of particle entrainments.

In addition to the above statistical distributions, a neuro-fuzzy (ANFIS) algorithm is implemented to model the nonlinear dynamics of the flow-particle system leading to entrainment at low mobility flow conditions. Three distinct model architectures are developed, trained and tested using experimentally obtained synchronous measurements of local flow velocity and particle displacements as input-output pairs. These models incorporate different input flow characteristics, such as the magnitude (time representation) and energy content (wavelet representation) of the local instantaneous flow, at past time instants and different frequencies respectively, which are considered to be relevant to particle entrainment. The ability of the proposed models to generalize, simulate the dynamics of the system as well as their accuracy are evaluated based on a number of performance indices. These models are relatively transparent, allowing for knowledge extraction and interpretation of the fuzzy rules, which in this study show to validate the introduced hypothesis.

Similar to the impulse concept, a new criterion for identification of the incipient flow conditions is proposed, based on an energy perspective. It is demonstrated that a portion of the available energy of sufficiently energetic flow events is dissipated in performing mechanical work for the entrainment of individual particles. The efficiency with which energy is transferred towards particle entrainment is characterized by the energy efficiency coefficient. The critical energy criterion is theoretically formulated for the entrainment of spherical particles in saltation or rolling mode. The validity of this framework is shown via a series of low mobility experiments employing non-intrusive equipment to accurately acquire synchronous measurements of the entrainment instances of an individual particle by rolling in addition to the flow events triggering them. These measurements are also used to conduct a detailed trajectory analysis of the particle while being dislodged and link the rate of flow energy transfer to the exact particle response.

Finally, the derivation of the impulse and energy criteria from the fundamental principles of classical mechanics is demonstrated. The two concepts are compared with particular emphasis on the advantages of the energy criterion with regard to performance, utility and extensibility. High energy flow events, which are associated with coherent flow structures and lead to particle entrainment, are further investigated. Particle entrainment events are grouped into different

categories (rapid and slow particle response) based on the time required to complete the entrainment. Typical cases of highly energetic flow events before and during particle entrainment and their effect on the grain mobilization dynamics are provided. The role of single or sequence of peak sweep events is outlined.